ABSTRACT

Title of Document: AIR SIDE HEAT TRANSFER ENHANCEMENT IN HEAT EXCHANGERS UTILIZING INNOVATIVE DESIGNS AND THE ADDITIVE MANUFACTURING TECHNIQUE

Martinus Adrian Arie, Doctor of Philosophy, 2016

Directed By: Professor Michael Ohadi, Mechanical Engineering

Over the last decade, rapid development of additive manufacturing techniques has allowed the fabrication of innovative and complex designs. One field that can benefit from such technology is heat exchanger fabrication, as heat exchanger design has become more and more complex due to the demand for higher performance particularly on the air side of the heat exchanger. By employing the additive manufacturing, a heat exchanger design was successfully realized, which otherwise would have been very difficult to fabricate using conventional fabrication technologies. In this dissertation, additive manufacturing technique was implemented to fabricate an advanced design which focused on a combination of heat transfer surface and fluid distribution system. Although the application selected in this dissertation is focused on power plant dry cooling applications, the results of this study can directly and indirectly benefit other sectors as well, as the air-side is often the limiting side for in liquid or single phase cooling applications. Two heat exchanger designs were studied. One was an advanced metallic heat exchanger based on manifold-microchannel technology and the other was a polymer

heat exchanger based on utilization of prime surface technology. Polymer heat exchangers offer several advantages over metals such as antifouling, anticorrosion, lightweight and often less expensive than comparable metallic heat exchangers. A numerical modeling and optimization were performed to calculate a design that yield an optimum performance. The optimization results show that significant performance enhancement is noted compared to the conventional heat exchangers like wavy fins and plain plate fins. Thereafter, both heat exchangers were scaled down and fabricated using additive manufacturing and experimentally tested. The manifold-micro channel design demonstrated that despite some fabrication inaccuracies, compared to a conventional wavy-fin surface, 15% - 50% increase in heat transfer coefficient was possible for the same pressure drop value. In addition, if the fabrication inaccuracy can be eliminated, an even larger performance enhancement is predicted. Since metal based additive manufacturing is still in the developmental stage, it is anticipated that with further refinement of the manufacturing process in future designs, the fabrication accuracy can be improved. For the polymer heat exchanger, by fabricating a very thin wall heat exchanger (150μm), the wall thermal resistance, which usually becomes the limiting side for polymer heat exchanger, was calculated to account for only up to 3% of the total thermal resistance. A comparison of air-side heat transfer coefficient of the polymer heat exchanger with some of the commercially available plain plate fin surface heat exchangers show that polymer heat exchanger performance is equal or superior to plain plate fin surfaces. This shows the promising potential for polymer heat exchangers to compete with conventional metallic heat exchangers when an additive manufacturing-enabled fabrication is utilized.

Major contributions of this study are as follows:

(1) For the first time demonstrated the potential of additive manufacturing in metal printing of heat exchangers that benefit from a sophisticated design to yield a performance substantially above the respective conventional systems. Such heat exchangers cannot be fabricated with the conventional fabrication techniques.

(2) For the first time demonstrated the potential of additive manufacturing to produce polymer heat exchangers that by design minimize the role of thermal conductivity and deliver a thermal performance equal or better that their respective metallic heat exchangers. In addition of other advantages of polymer over metal like antifouling, anticorrosion, and lightweight.

Details of the work are documented in respective chapters of this thesis.

.

AIR SIDE HEAT TRANSFER ENHANCEMENT IN HEAT EXCHANGERS UTILIZING INNOVATIVE DESIGNS AND THE ADDITIVE MANUFACTURING TECHNIQUE

By

Martinus Adrian Arie

Dissertation submitted to the Faculty of the Graduate School of the
University of Maryland, College Park, in partial fulfillment
of the requirements for the degree of
Doctor of Philosophy
2016

Advisory Committee:
Professor Michael Ohadi, Chair
Professor Marino DiMarzo
Professor Hugh A. Bruck
Professor Amir Riaz
Professor Kyu Yong Choi

Dedication

To my parents who have helped, encouraged, and supported me always

Acknowledgements

First and foremost I would like to thank my advisor Dr. Michael Ohadi and my co-advisors Dr. Amir Shooshtari and Dr. Serguei Dessiatoun for their guidance, help, encouragement, and support for my research. I will carry what I learned from them with me throughout the rest of my life.

I would like to express my gratitude to Mr. David Hutton from Baltimore Air Coil Company for providing specification for the baseline heat exchanger which is quite helpful for the completion of this proposal. The author also wishes to thank Dr. Arun Muley and Mr. Doug H. Van Affelen from Boing Company for their advices during the duration of the project. Lastly, the author also thanks Mr. Frederick Claus from Stratasys for his help in fabrication of the metallic heat exchanger and Dr. Joshua Pearce from Pearce Research Group at Michigan Tech University for his assistance with the polymer heat exchanger fabrication.

Lastly, I am also grateful to my friends at Smart and Small Thermal Systems Laboratory (S2TS), especially Veena Venkoba Rao, David Deisenroth, Raphael Mandel, Stefan Bangerth, Xiang Zhang, Ning Yang, Christopher Sneeder, and Ratnesht Tiwari for providing a constructive and peaceful environment and also their helpful tips and suggestions regarding my research.

Table of Contents

List of Tables

List of Figures

Nomenclature

A	Area [m^2]
A_{base}	Base area [m^2]
A_{fin}	Fin surface area [m^2]
A_H	Heat transfer area [m^2]
a	Constant described in Eq. (30)
b	Constant described in Eq. (30)
C	Heat capacity [W/K]
C_r	Heat capacity ratio [-]
c_p	Specific heat [J/kgK]
COP	Coefficient of Performance [-]
$COP/\Delta T$	Normalized coefficient of performance [1/K]
D	Hydraulic diameter [m]
F	Flow maldistribution [-]
f	Darcy friction factor [-]
G	Mass flux [kg/sm^2]
H	Height [m]
h	Heat transfer coefficient [W/m^2K]
h_b	Base conductance ($h_b = Q/(A_{base}(T_{base} - T_{in}))$) [$W/m^2K$]
j	Colburn j-factor [-]
K	Microcahnnels non-uniformity [-]
k	Thermal conductivity [W/mK]
K_1	Constant described in Eq. (33)
K_2	Constant described in Eq. (34)
K_3	Constant described in Eq. (35)
L	Length [-]
m	Heat exchanger mass [kg]
$\dot{m}$	Mass flow rate [kg/s]
M	Constant described in Eq. (5)
N_{stc}	Total number of stack [-]
N_{seg}	Total number of segment [-]
N_{water}	Total number of water channels [-]
n	Total number of microchannel per pass in manifold microchannel HX [-]
ɳ	Constant to evaluate Wilson Plot [-]
N_{water}	The number of channels in the water-side [-]
NTU	NTU [-]
Nu	Nusselt number [-]
P	Pumping power [W]
p	Pressure [Pa]
p'	Normalized pressure $p' = \frac{p}{\rho v_{in}^2}$ [-]
Δp	Pressure drop [Pa]
Q	Heat flow rate [W]
$Q/m\Delta T$	Gravimetric heat transfer density [W/kgK]

$Q/V\Delta T$	Volumetric heat transfer density [W/m^{3}K]
R	Thermal resistance [K/W]
Re	Reynolds number [-]
Re_{nom}	Nominal Reynolds number [-]
r_{out}	Channel outer radius [m]
r_{in}	Channel inner radius [m]
S	Fin spacing ($S = t_{fin} + W_{chn}$) [m]
T	Temperature [C]
ΔT	Temperature difference between inlet air and water [C]
t	Thickness [m]
U	Overall heat transfer coefficient [W/m^{2}K]
U_X	Uncertainty of X [-]
U_y	Uncertainty of Y [-]
V	Volume [m^3]
$\dot{V}$	Volumetric Flow Rate [CFM]
v	Velocity [m/s]
v'	Dimensionless velocity $v' = v/v_{in}$ [-]
v_{in}	Velocity at the manifold channel entrance [m/s]
v_{chn}	Velocity at the microchannels [m/s]
W	Width [m]
x, y, z	Cartesian coordinate system [m]
x'	Dimensionless distance in x-axis direction $x' = \frac{x}{L_{tot,air}}$ [-]
X	Measures variables pertaining to Y [-]
Y	Calculated variable [-]
Z	Ratio of major axis of ellipse [-]

Greek Letters

β_1	Pressure regain coefficient [-]
β_2	Pressure loss coefficient [-]
Γ	Perimeter [m]
ε_{HX}	Heat exchanger effectiveness [-]
η_{fin}	Fin efficiency [-]
η_{HX}	Overall surface efficiency [-]
μ	Dynamic viscosity [kg/ms]
ρ	Density [kg/m3]

Subscripts

air	air-side
base	Base
bottom	bottom chapter
cal	Caloric
chn	Microchannel
conv	Convection
cond	Conduction

fin	Fin
front	frontal area
HX	heat exchanger
H	heat transfer area
in	inlet
mnd	Manifold
mnd-chn	manifold-channel
NU	non-uniform
no-flow	no-flow direction
out	Outlet
seg	Segment
solid	solid-side
stc	Stack
top	top chapter
tot	Total
U	uniform
water	water-side
wall	wall-side

Abbreviations

AM	Additive manufacturing
AlSi10Mg	Aluminum AlSi10Mg
BMI	Bismaleimide
CFD	Computational fluid dynamic
CNT	Carbon nanotube
DAQ	Data acquisition system
DMLS	Direct metal laser sintering
DOE	Design of experiment
HDPE	High density polyethylene
HX	Heat exchanger
LPFS	Louvered plate-fin surface
Man-Mchn	Manifold-microchannel
MAE	Mean absolute error
PDMS	Polydimethylsiloxane
PFPFS	Pin-fin plate-fin surface
PPFS	Plain plate-fin surface
PLA	Polylactic acid
PMMA	Poly(methyl methacrylate)
PPS	Polyphenylene sulfide
SS17-4	Stainless steel 17-4
SFPFS	Strip-fin plate-fin surface
SPSM	Single pass single manifold
Ti64	Titanium alloy (Titanium Ti-6Al-4V (Grade 5))
WFPFS	Wavy-fin plate-fin surface
VSC	Variable speed controller

Chapter 1: Introduction

1.1. Motivation and Background

Ambient air is the ultimate heat sink in various heat exchanger applications. Some examples of its applications are:

- Air to air heat exchangers (with application in space cooling, economizer, etc.)
- Air to liquid heat exchangers (with application in car radiators, HVAC, power plant cooling, etc.)
- Air to steam heat exchangers (with application in power plant cooling, heat pumps, refrigeration, etc)
- Air cooled heat sinks (with application in electronic cooling).

Even though it has numerous applications, the technology behind current conventional air-side heat exchangers, such as louvered fin, wavy-fin, strip-fin, and pin-fin, is based on decades old technology. New applications now demand higher heat transfer rates, lower pressure drops, and more compact systems which are challenging to achieve using conventional technology. As a result, there is a need for new advanced surfaces to enhance the performance of air-side heat exchangers. However, advanced heat transfer surfaces usually involve a complex geometry, which is challenging to fabricate using conventional methods. In the last few years, additive manufacturing has emerged as a new manufacturing technique that has shown several advantages over traditional methods. One of the main advantages is the ability to build 3-D objects layer-by-layer

from pre-programmed digital models, which makes it possible to construct these complex geometries which otherwise would be impossible using conventional methods. As a result, it is desirable to fabricate advanced heat exchangers using additive manufacturing. This dissertation investigates an additive manufacturing technique used to fabricate an advanced surface for an air-side heat exchanger applied to power plant cooling.

Currently, 99% of all power plant cooling in the U.S. is water cooling with breakdown as follows: 43% is once-through cooling, 42% is recirculation cooling using a cooling tower, and 14% use a cooling pond. The amount of water required for power plant cooling is tremendous. Currently over 41% of fresh water withdrawals in the U.S. are for power plant cooling. Another alternative to water cooling is dry cooling using air, which significantly reduces water consumption. However, only 1% of all power plants in the U.S. use dry cooling [1].

The use of freshwater for power plant cooling can have a detrimental environment effect, especially for the case of once-through cooling, as it increases the water temperature in the nearby rivers, lakes, or the ocean. To limit the environmental effect of the use of freshwater for power plant cooling, the federal government has implemented several regulations under the Clean Water Act that apply to both newly built power plants and existing power plants [2, 3]. The law requires new power plants to consider the best cooling technology available to minimize the plant's effect on the environment. By 2004 the law also included existing plants that withdraw more than 50 MGD of water and used at least 25% of it for cooling. The laws encourage plants to switch to recirculation cooling or dry cooling for the existing system. This regulation has significantly affected how power plant cooling systems are designed, as shown in Figure 1. Between the years

of 1950-1975, the majority of power plant cooling build was once-through cooling, but since 1975, the trend has switched to recirculating cooling. Since 2000, dry cooling has begun to be considered as another alternative.

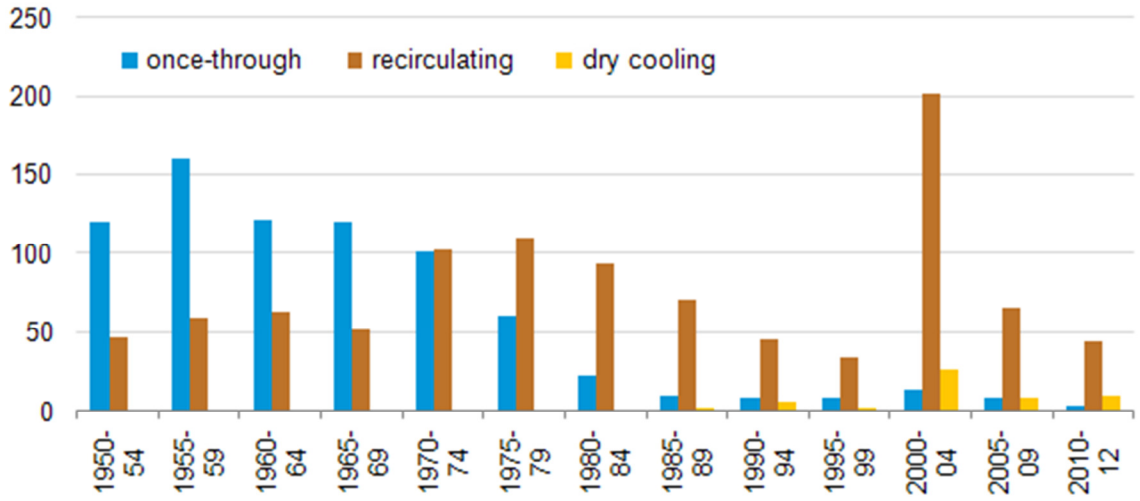

Figure 1: Types of power plant cooling systems built from 1950 to 2012 in the USA [4]

In addition, fresh water is becoming more difficult and expensive to get, especially in southwestern states like California due to long-time drought, which significantly increases the operational cost of water cooling power plants. Compared to water-cooled power plants, air-cooled power plants require only little or no water at all, which in turn significantly reduces operational costs and environmental effects. However, air-cooled plants are not without their drawbacks. The main drawback of air cooling is that air heat transfer coefficients are 20 times less than that of water. In top of that, air dry bulb temperature is also always higher than the wet bulb temperature. Because of those reasons, air-cooled systems are usually much larger in size than water-cooled systems in order to achieve the same heat transfer performance, which in turn requires much higher initial investment. In addition, air density is almost one thousand times lower than water; as a consequence, for the same mass flow rate, air requires much higher pumping power

than water. This can reduce the operational cost advantage if not addressed properly. As a result, in order for that air-cooling to become more appealing to the market as an alternative to water cooling, it is desirable to enhance air side heat transfer performance without significantly increasing the pumping power so that the cost of the air-cooled system can be reduced.

Air-cooled power plants can be separated into two configurations: air-cooled condenser power plants and hybrid air-cooled power plants as shown in Figure 2 and Figure 3, respectively. In air-cooled condensers, steam from the turbine is directly cooled down by air, as shown in Figure 2. In hybrid air-cooled power plants, steam is condensed with water, which is then cooled in an air-cooled heat exchanger. Even though more system installation is required for hybrid systems, these have their own advantage. The main advantage of hybrid cooling is that a cooling tower can be added to cover the periods during which air cooling is not sufficient to remove the heat. This is beneficial for regions with very dry summer times. Another advantage of hybrid air-cooled systems is that they can be retrofitted onto existing water-cooled power plants which use recirculating cooling. As depicted in the schematic in Figure 3, the retrofitting can be done by adding a secondary loop for the air-water heat exchanger without removing any existing systems. Because 42% of current water-cooled power plants utilize recirculating cooling, hybrid air-cooled power plants have great potential in the future of air-cooled power plants. As the air-side will always be the limiting factor for both configurations, the development of advanced air-side surfaces, which are studied in this dissertation, is beneficial for both configurations.

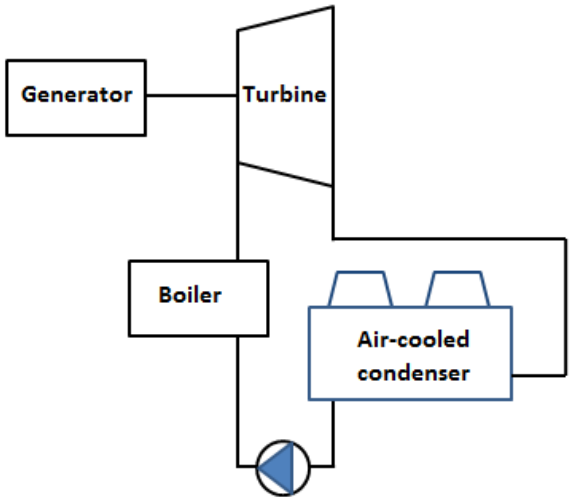

Figure 2: Air-cooled condenser power plant

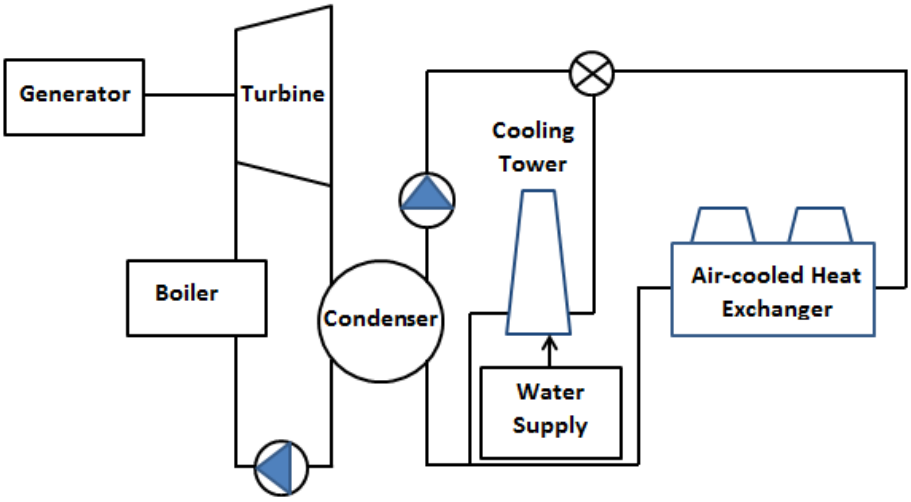

Figure 3: Hybrid air-cooled power plant

1.2. Dissertation Objective

The main objective of this dissertation is to design an air-water heat exchanger that yields significant performance enhancement compared to conventional heat exchangers for power plant cooling application. This can be accomplished by implementing advanced fabrication techniques, advanced heat transfer surfaces, and optimizing the design. By accomplishing this objective, air-cooled power plants can be more economically feasible. The advanced air-water heat exchanger can be directly implemented into the hybrid-air

cooled system. In addition, as the air side is also the limiting factor of the air-cooled condenser, the development of the advanced air-side heat exchanger will also benefit air-cooled condenser systems. Lastly, although this dissertation will focus on power plant cooling applications, the knowledge gained in this study can be applied to many other applications that use air as the heat transfer medium, such as HVAC, automotive (car radiator), and electronic cooling applications.

1.3. Approach

To accomplish the project objective, two types of advanced heat exchangers were studied. One is a metallic heat exchanger, based on manifold-microchannel technology, and the other is a polymer heat exchanger, based on prime surface technology. Metallic heat exchangers are the most common type of heat exchangers, especially for power plant cooling applications, due to their high thermal conductivity and structural strength. Polymer based heat exchangers, on the other hand, despite having lower thermal conductivity than metal, have shown several advantages compared to metallic heat exchangers in terms of their low weight and low cost, and their antifouling and anticorrosion properties.

To demonstrate the technology, two scaled down air-water heat exchangers were designed, optimized, fabricated, and experimentally tested, one for the advanced metallic design, and one for the advanced polymer design. The scaled down units were used for the testing because a full-scale power plant cooling heat exchanger is too expensive to build and would require a tremendous test setup. The heat exchanger was scaled up for application in air-cooled power plants based on the experimental data. The scaled up design was then compared with the baseline design based on conventional technology to

calculate how much improvement the advance design could yield. A flow chart showing the major steps performed to accomplish the dissertation objective is shown in Figure 4. A summary of each step will be provided in the following.

Literature review & design constraints and requirements:

1. **Literature review of state-of-the-art technology**

   A detailed literature study on the additive manufacturing technique and air-cooling technology was performed. The additive manufacturing literature study included different types of metallic additive manufacturing techniques, the latest developments in additive manufacturing, and some example work implementing additive manufacturing for heat exchanger fabrication. Next is the literature study on the air-cooling technology, which included conventional heat exchanger surface such as plain plate fin and wavy fin and advanced surfaces such as manifold-microchannel. Lastly, a detailed literature study of polymer heat exchangers was performed. The study included common types of polymer heat exchangers available in the literature.

2. **Define the design requirements and baseline**

   The design requirements for the heat exchanger, such as heat exchanger capacity, maximum allowable pressure drop, and mass flow rate, were defined based on standard specifications of power plant heat exchangers. In addition, a baseline design was selected based on the most common type of heat exchanger surface used for power plant cooling for comparison with the advanced design. Lastly,

several other conventional heat exchanger surfaces like plain plate fin and wavy fin were selected for additional comparison.

3. **Learn process, constraints, and limitations of additive manufacturing technique**

   A thorough study was performed on the additive manufacturing techniques used to fabricate both the metallic and polymer heat exchanger. The study included fabrication techniques, material compatibilities, and fabrication limitations such as minimum feature size, tolerance, and maximum fabrication size. The fabrication limitations and constraints learned in this step were implemented for the design optimization and selection.

Numerical Modeling and Optimization:

1. **Develop numerical simulation method**

   Before a design was selected for fabrication and testing, a numerical simulation was needed to predict the heat exchanger performance. For advanced metallic heat exchangers, a novel numerical method was developed to evaluate the performance of manifold-microchannel heat exchangers without having to run a CFD simulation of the full model. For the advanced polymer heat exchanger, CFD simulation was proposed to predict its performance, as its design is less complicated than the advanced metallic heat exchanger. Lastly, the performances of the conventional heat exchangers were solved based on analytical solution from the literature.

2. **Design optimization and down selection**

   Multi-objective optimizations were performed for the baseline, advanced metallic, and advanced polymer heat exchanger based on the design requirements previously defined. A design was selected which met all of the design requirements for each case. The optimum advanced metallic and polymer performances were compared with the optimized baseline design to calculate how much improvement was possible for the advanced designs.

3. **Design scale down**

   The selected heat exchanger design for both advanced metallic and polymer heat exchangers were scaled down so that they could be fabricated and experimentally tested.

Experimental Works and Scale Up

1. **Coupon HXs fabrication**

   The scaled down advance metallic and polymer coupon heat exchangers were fabricated by using additive manufacturing technique. A detailed evaluation was performed to evaluate the quality of the fabricated heat exchangers.

2. **Experimental testing**

   The fabricated coupon heat exchangers were experimentally tested in the lab. Their performances were compared with the numerical predictions to validate the proposed numerical methods.

3. **Scaling up**

   Based on the experimental results, both the metallic and polymer heat exchangers were scaled up to meet the design requirements for power plant cooling heat exchangers.

Performance Comparisons:

1. **Performance comparisons**

   The air-side performances of both the metallic and polymer heat exchangers were compared with the performances of the conventional heat exchanger surfaces. Lastly, the performances of the scaled up heat exchanger were also compared with the baseline's performance.

2. **Conclusion and future works**

   Finally, conclusions were derived based on what was learned in this study. In addition, some areas that still can be improved were recommended for future research in this area.

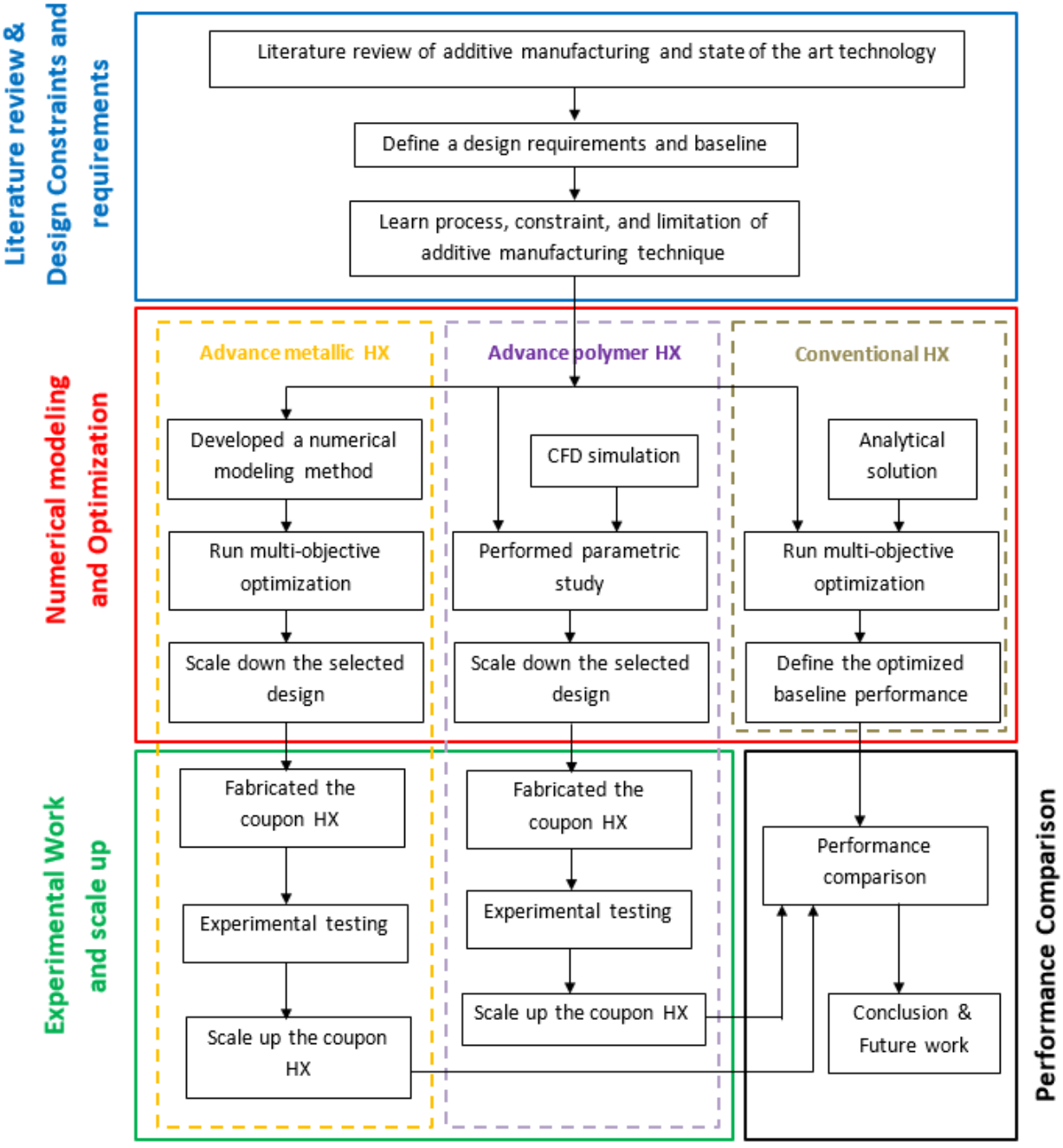

Figure 4: Flow chart of the project approach

1.4. Dissertation Layout

The layout of this dissertation is as follows. First a literature study of additive manufacturing processes, conventional and state-of-the-art air-side heat exchanger

technologies, and polymer heat exchanger development are presented in chapter 2. Then the design requirements and the conventional heat exchangers baseline are defined in chapter 3 (chapter 3.2 and chapter 3.3 respectively). In addition, in chapter 3, the concepts behind the designs of the advanced metallic and polymer heat exchanger surfaces are explained (chapter 3.4.1 and chapter 3.4.2 respectively). Chapter 4 discusses the fabrication method for both advanced metallic and polymer heat exchangers. The fabrication process and constraints are also discussed in detail. Next, the numerical method to evaluate the performance of advanced metallic, advanced polymer, and conventional heat exchangers is explained in chapter 5. Chapter 6 discusses the design optimization and the down selection process. Chapter 6.2 discusses the optimization method. Chapter 6.3 discusses the metallic heat exchanger optimization, its down selection, and scaling down process. Chapter 6.4 discusses the polymer heat exchanger sizing and scaling down. The experimental work on the scaled down coupon advanced metallic heat exchanger is discussed in chapter 7. The experimental results are then compared with numerical modeling and conventional heat exchanger performance. The experimental work on the scaled down coupon polymer heat exchanger is discussed in chapter 8. Details about the experimental results and comparison with conventional heat exchanger performance are discussed in chapter 8.6. Lastly the conclusion and recommendations for future work are presented in chapter 9.

Chapter 2: Literature Review

In this chapter the literature review on additive manufacturing techniques, conventional and state-of-the-art metallic heat exchangers, and polymer heat exchangers is presented. First, the most common types of additive manufacturing techniques, such as stereolithography, selective laser sintering, and fused deposition modeling, are discussed. In addition, any work done in implementing additive manufacturing for heat exchanger fabrication is discussed. The next section discusses metallic heat exchangers, including conventional heat exchanger surfaces such as plain plate-fin, louvered fin, wavy fin, offset fin, and pin-fin [5-8] and advanced surfaces such as oblique fin [9, 10] and manifold-microchannel [11-16]. Any work done to improve the heat transfer performance of conventional surfaces, such as by adding vortex generation [17, 18] or by using EHD pumping [19], is also discussed. In addition, a survey of common fabrication techniques for state-of-the-art heat exchangers will also be discussed, as well as their limitations. Lastly, several polymer based heat exchangers are discussed, such as polymer shell and tube heat exchangers [20-22], polymer hollow fiber heat exchangers [23-27], and polymer plate heat exchangers [28-31]. At the end of the chapter, tables summarizing the previous work in metal additive manufacturing, the use of additive manufacturing for heat exchangers fabrication, state-of-the-art heat exchangers, manifold-microchannel heat exchangers, polymer heat exchangers, and heat exchanger fabrication techniques are provided.

2.1. Additive Manufacturing

Additive manufacturing (AM) is an emerging technology which has shown significant advantages over traditional manufacturing technology such as casting, molding, and machining. Its main advantage is its ability to build 3-D object layer by layer from a pre-programed digital model, which makes it possible to construct much more complex geometries in a shorter period of time. Additive manufacturing has been incorporated in various fields as described in Ref. [32], especially in micro-electromechanical systems (MEMS) manufacturing [33-35] and the medical field [36-40], due to its ability to produce very small (on the order of a few microns) and complex geometries. There are multiple different additive process types such as sterolithography, selective laser sintering/melting, fused deposition modeling, laminated object manufacturing, laser chemical vapor deposition, inkjet printer, and many others as summarized in Refs. [41, 42]. This chapter discusses some of the metallic additive manufacturing techniques, including their resolution, strength, and weaknesses. In addition, the latest efforts to improve additive manufacturing fabrication quality will also be discussed. Lastly, some works in the literature that investigated using additive manufacturing to fabricate heat exchangers will be discussed.

Stereolithography is an additive manufacturing process which uses photopolymerization to form the 3-D model as shown in Figure 5. In this process, ultraviolet laser is applied to photopolymer resin to induce a polymerization process to bind molecules together. The process requires the use of photopolymer-resin, which is widely available on the market with different properties. Stereolithography has been shown to be successful in fabricating polymer [43-45], ceramic [43, 46, 47], or metal [47-49] objects. It has very

high resolution: structure as small as 1μm has been successfully fabricated [43]. However, its main disadvantage is that it requires post processing to remove the resin. The post processing can cause shrinkage on the printed object. Shrinkage as high as 28% is noted for metal stereolithography [48].

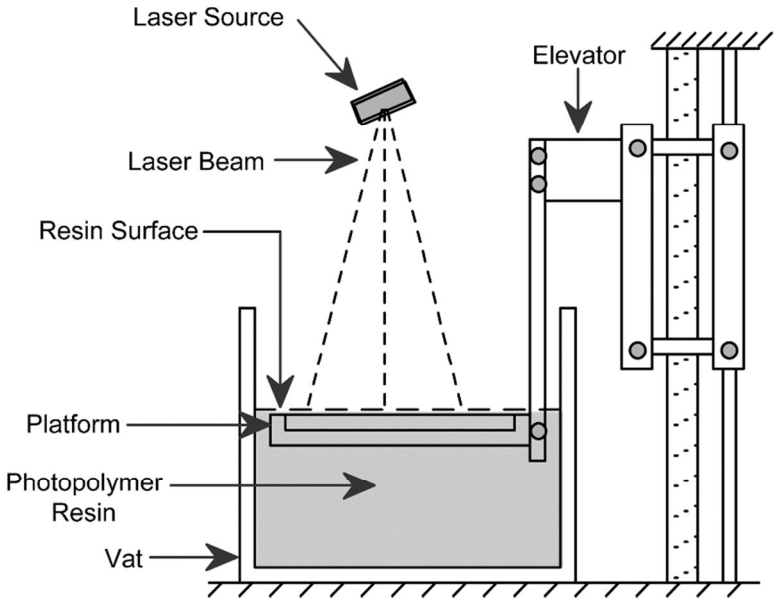

Figure 5: Stereolithography process [50]

Selective Laser Sintering (SLS) and Selective Laser Melting (SLM) are additive manufacturing techniques that use high power laser to fuse small particles of plastic, ceramic, metal, or gas powder to any desired 3-D shape, as shown in Figure 6. The major difference between SLS and SLM is that in SLS the powder is heated until it is fused together on the molecular level without melting the particle, while in the case of SLM, the powder is melted completely. SLM works well for mono-material, which only has one melting point. On the other hand, SLM works well for material that consists of a mix of different materials that do not have homogenous melting points, such as metal alloys. Although SLM and SLS are used mostly to build metallic structures [51-53], some work has shown the use of SLM or SLS for ceramic structure fabrication [54, 55]. Structures as

small as 30 μm have been successfully fabricated [41]. In addition, compared to stereolithography, SLS and SLM are less complex processes, as post processing are not needed. But, porosity can be a problem if it is not done properly [41]. In addition, the results are also highly dependent on the powder quality [56].

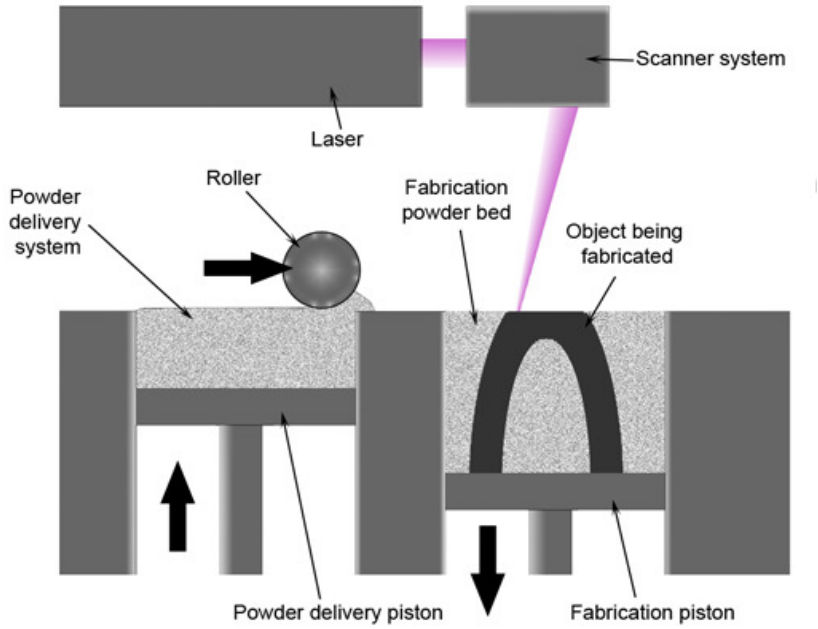

Figure 6: Selective laser sintering process [57]

Fused Deposition Modeling (FDM) is an additive manufacturing process that lays down material, like plastic filament, in layers as shown in Figure 7. Heat is applied to the nozzle to melt the material so that it can bind with material in the previous layer. Unlike stereolithography, SLS, or SLM, the FDM process does not use a laser to bind the material, which make the process less complex. In addition, by switching between one material to another, a multi-material structure can be fabricated. However, the main disadvantage of FDM is that the resolution of the process is limited by the nozzle size [36]. As a result, the resolution limit can be much higher than other additive manufacturing techniques. Vaezi et al. reported a resolution limit as high as 200 μm for

FDM [41]. FDM is mostly used to fabricate polymer structures, as shown in Refs. [36-38]. However, there has also been work in fabrication of composite (metal/polymer) structures using FDM as reported by Masood and Song [58].

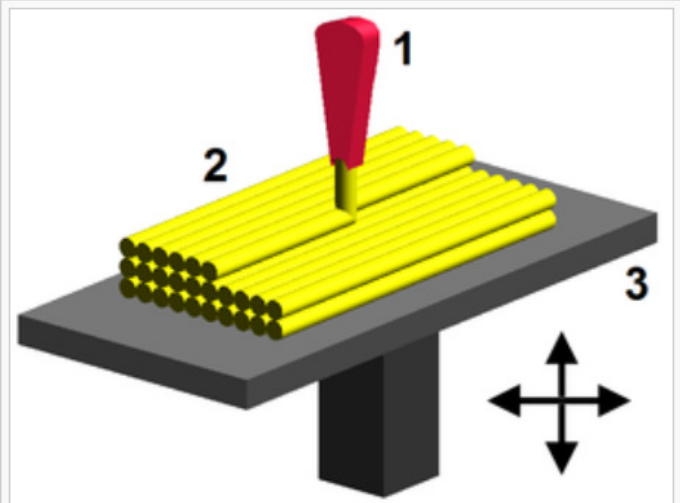

Fused deposition modelling: 1 – nozzle ejecting molten material, 2 – deposited material (modeled part), 3 – controlled movable table

Figure 7: Fused deposition modeling [59]

Laminated object manufacturing (LOM) is an additive manufacturing technique where layers of plastic, paper, or metal sheets are laminated/fused together using pressure and heat. A computer controlled laser is used to cut the sheets into the pre-programmed shape, as shown in Figure 8. This process was first developed by Helisys Inc. in California. In the literature, LOM has been used to fabricate ceramic structures [60-62] and metallic structures [60, 63]. Some of the strengths of LOM are that it uses cheap materials for fabrication such as plastic, paper, or metal sheets, and fabrication of very large structures is possible. Structures as big as 0.5 x 0.8 x 0.5 m can be fabricated, as reported in Ref. [64]. The disadvantage of LOM is that post-processing may be needed to

completely fuse each layer. The post-processing can cause significant shrinkage, warpage, delamination, and deformation as reported by Klosterman et al. [62].

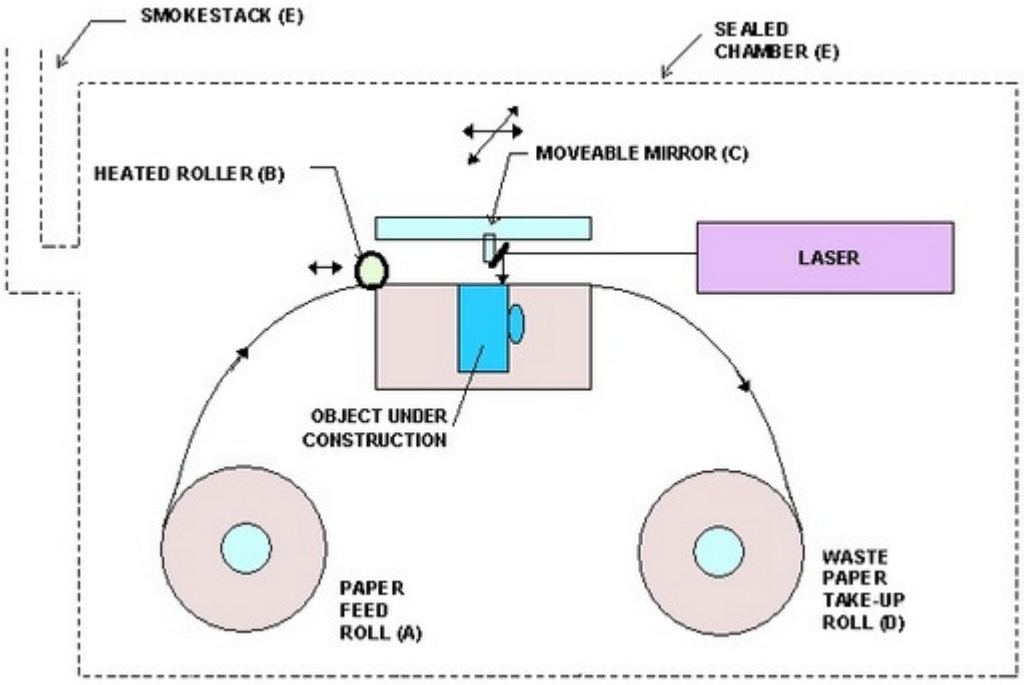

Figure 8: Laminated object manufacturing [65]

Laser Chemical Vapor Deposition (LCVD) is an additive manufacturing technique where a laser is used to locally heat the substance to initiate chemical vapor deposition. By controlling the laser, a 3-D structure can be formed. The use of LCVD to fabricate metallic [66-68] and ceramic [69-71] structures have been reported in the literature. The biggest advantage of this method is its capability to fabricate complex geometries with sizes as small as 1 μm [41]. Due to its low resolution limit, it has been used for semiconductor fabrication as reported in [72]. However, it is a highly complex process and due to the chemical reaction, the process needs to be done in a controlled atmospheric chamber.

Inkjet printing is an additive manufacturing technique based on inkjet technology where liquid material is deposited layer by layer and dried to form a 3-D structure. Inkjet printing is divided into two categories depending on the liquid viscosity: droplet on demand (DOD) and continuous inkjet (CIJ). The DOD technique is for low viscosity liquids, while CIJ is for high viscosity fluids. The liquid material used has viscosity of 2-10 mPas for the CIJ process or 10-100 mPas for DOD processes [41]. The main advantage of inkjet printing is that it is based on proven technology and it can be used on a wide range of materials. A summary of the liquid material applicable for inkjet printing can be found in Ref. [73]. The main disadvantage of inkjet printing is the fact that the droplet size is limited by the nozzle diameter as noted by Stringer and Derby [73]. This can reduce the resolution of the finished structure.

A summary of all additive manufacturing fabrication techniques discussed above is presented in Table 1, including the resolution, material compatibility, strength, and weakness of each technique.

Almost all of the additive manufacturing techniques available, including all of the methods summarized above, are based on an open loop system. However, by integrating sensors to monitor and control the process, a closed loop system can be created. The main advantage of a closed loop system is that the quality of the fabricated parts can be improved considerably compared to an open loop system. Several devices have been developed for detailed monitoring of the additive manufacturing process. High speed cameras and infra-red cameras are some of the most popular devices for monitoring the build quality in the middle of the fabrication process. However, most of the monitoring systems developed for additive manufacturing up until now have been used mainly to

better understand the process rather than to actively control the fabrication process [74]. There is only limited work in the literature involving a closed loop system, like works by Nassar et al., Ding et al., and Hagqvist et al. [75-77]

Nassar et al. proposed to build a closed loop temperature control system for an additive manufacturing process [75]. Their idea is to alter the build plan in real time based on the temperature reading. It was reported that by implementing such control a more uniform α-lath width and more uniform micro hardness was possible. Ding et al. proposed to build a closed loop control system to sense and control the powder flow rate and molten pool size for a robotized laser-based direct metal addition system [76]. By controlling those two variables a better fabrication quality can be achieved, as shown in Figure 9. Hagqvist et al. proposed the use of a resistance based sensor to measure the surface of the deposited layer of the fused deposition modeling method [77]. By controlling the wire feed rate based on the resistance reading, the stability of the deposition process was significantly improved. Flynn et al. pointed out the importance of closed loop feedback control in a hybrid additive and subtractive process, as the process consisted of two or more manufacturing processes on the same machine [78].

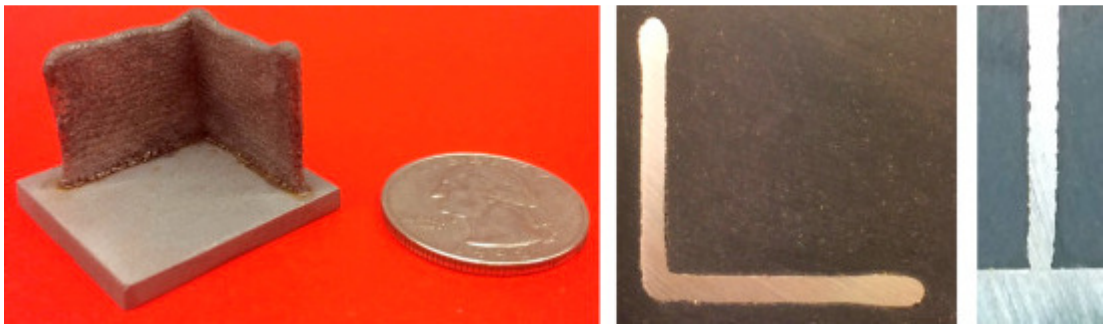

(a)

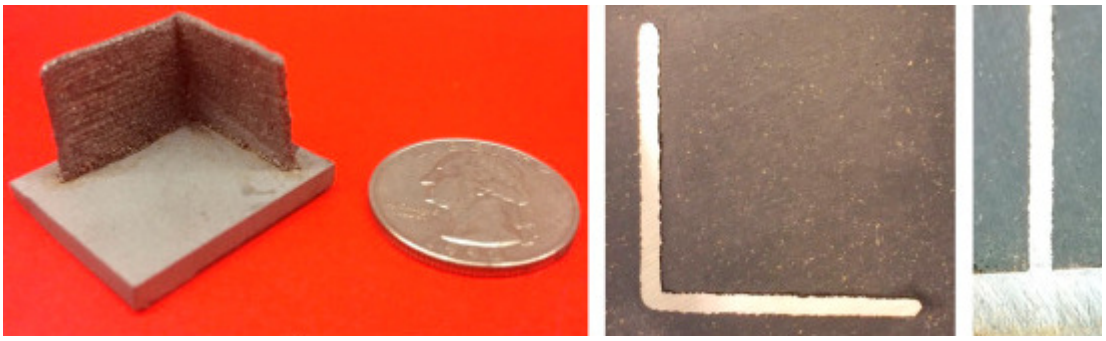

(b)

Figure 9: Fabrication quality of L-shape wall fabricated with or without control: (a) without control (b) with control [76]

Works in the literature show some success in the fabrication of complex heat exchangers using additive manufacturing techniques. The summary of such works are shown in Table 2.

One work by Tsopanos et al. showed successful fabrication of a micro cross-flow heat exchanger using the selective laser melting technique [53]. The heat exchanger was made out of stainless-steel 316L with an overall size of 15 mm x 15 mm x 15 mm. The heat exchangers consisted of rectangular channels in both side with fin thickness of 0.1 mm and fin height of 0.9 mm. Surface roughness was calculated in the range of 10 – 15 μm.

Kumar et al has shown succeed in fabrication of hexagonal periodic cellular structure for heat exchangers application [79]. Several structures were fabricated out of titanium alloy (Ti64) and Aluminum 6061 using Electron Beam Melting (EBM) technique. The influence of lattice orientation on the heat transfer and flow properties were evaluated.

Another work by Wong et al. showed the use of selective laser melting to fabricate complex heat sinks geometry out of aluminum [80]. Five heat sinks were fabricated with pin fins array, staggered rectangular array, staggered elliptical array, lattice array, and

rounded corners rectangular fin array. The lattice array heat sink, as shown in Figure 10, showed the highest heat transfer area per volume compared to other surfaces.

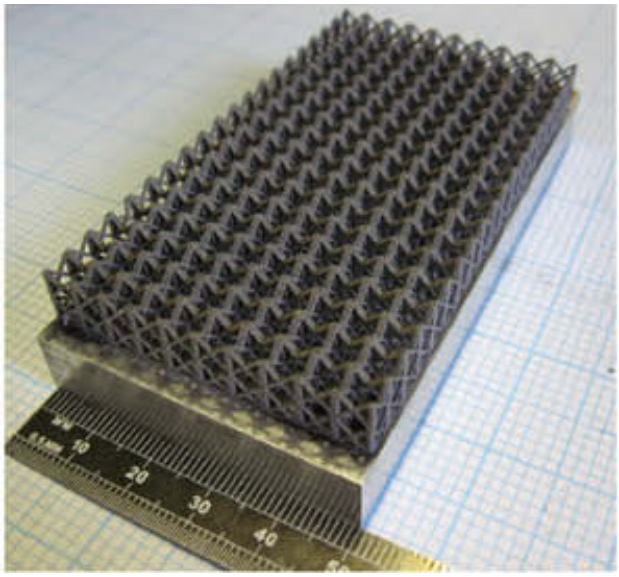

Figure 10: Lattice array heat sink [80]

Ramirez et al fabricated complex open cellular copper mesh and foams using electron beam melting [81]. The main application of those structures is for thermal management devices like heat exchanger. Detailed analysis of the fabricated structures was performed. The stiffness vs density and relative stiffness vs relative density plot of the fabricated mesh and foam were provided. The fabricated structure density was evaluated in the range of 0.73g/cm^3 to 6.67g/cm^3.

Hutter e al. fabricated a metal foam filled tubular heat exchanger out of aluminum using selective laser sintering for application in chemical production as shown in Figure 11 [82]. Higher heat transfer performance was observed compared to metal foam reactor fabricated using conventional method.

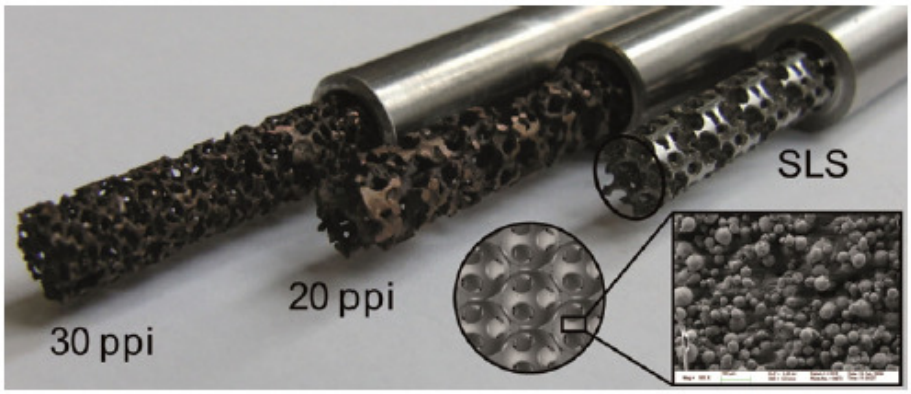

Figure 11: Metal foam filled tubular heat exchanger [82]

Cormier et al. fabricated an aluminum pyramidal fins arrays heat sink using cold spry technology [83]. Experimental testing was performed to evaluate its performance. Based on the experimental results, correlations linking Nusselt number with Reynolds number, fin height, and fin density were derived.

Another work by Cevallos showed the use of fused deposition modeling to successfully fabricate a webbed tube heat exchanger, as shown in Figure 12 [84]. Cold water flowed inside the tube, which then was heated by hot air which flowed around it. The thickness of the tube was 2 mm with an inner diameter of 5 mm. Cevallos also reported that porosity can cause leaks at the joint between the tubes and webbing. The porosity can be controlled by modifying the tool path used to print the heat exchanger. Heat transfer performance similar with plain plate fin heat exchanger was reported.

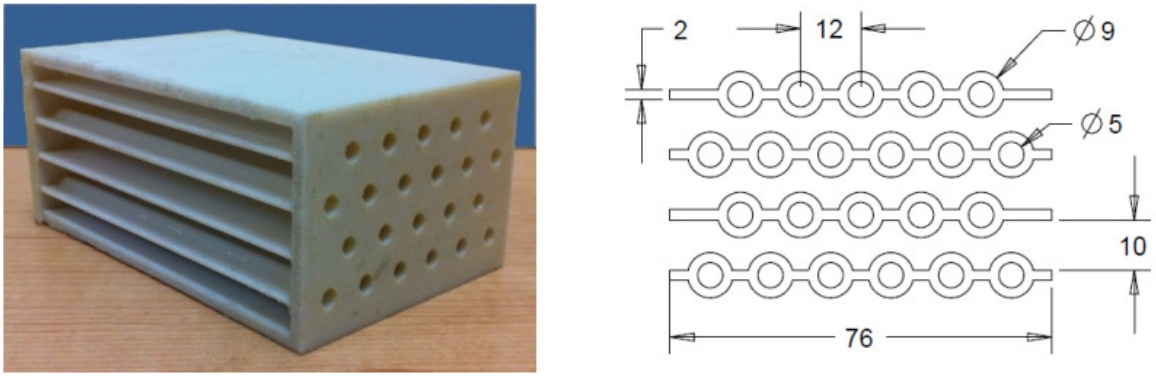

Figure 12: Webbed tube heat exchanger [84]

Another work by Thompson et al. successfully fabricated a titanium alloy (Ti64) flat-plate oscillating heat pipe with 1.53mm diameter channel using selective laser sintering [85]. Effective thermal conductivity of 110W/mK was recorded. However, through inspection of the fabrication quality revealed partially melted particle in the channels.

2.2. Metallic Heat Exchanger

2.2.1 Conventional Heat Transfer Surfaces

Conventional metallic heat exchangers utilize fins to increase heat transfer surface and reduce the size of the heat exchanger. The idea of fins was first introduced by Harper and Brown in 1922 [86]. Since then numerous works have been reported in the literature related to fins and extended surfaces. The most common type of fins are plain plate-fin, louvered fin, wavy fin, offset fin, and pin-fin, as summarized by Lays and London [5]. The heat transfer surfaces that utilized such fins structures are shown in Figure 13 for all five fin types.

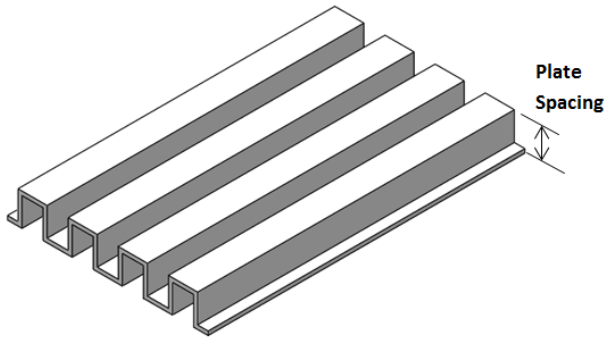

(a)

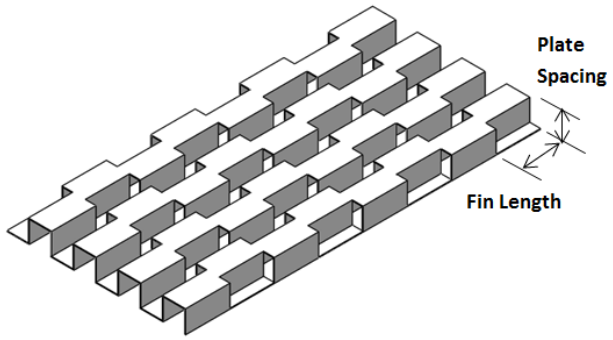

(b)

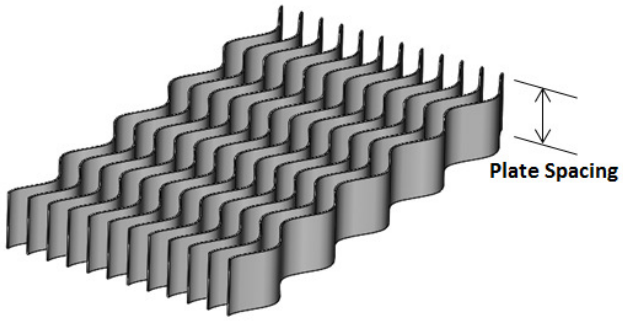

(c)

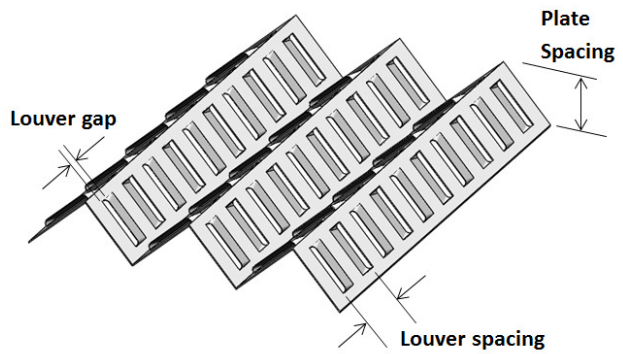

(d)

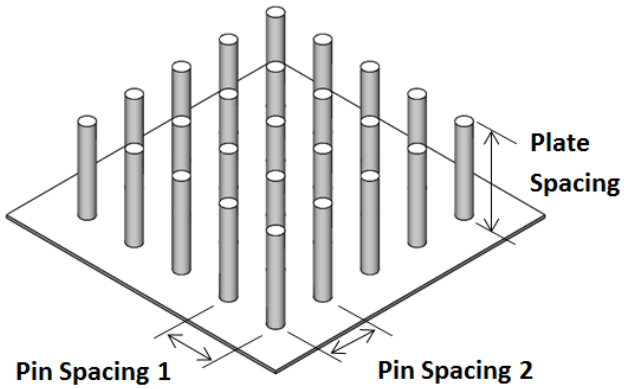

(e)

Figure 13: Conventional heat transfer surfaces: (a) Plain plate-fin surface (b) strip-fin plate-fin surface (c) wavy-fin plate-fin surface (d) louvered plate-fin surface (e) pin-fin plate-fin surface

Plain Plate Fins

The most basic and simplest type of fins is plain plate fins. Plain plate fins consist of rectangular fins extending on the flow length direction as shown in Figure 13(a). As the fins' geometry is constant in the flow direction, the flow most likely will reach hydrodynamically and thermally fully developed condition along the flow length. As a result, the pressure drop and heat transfer performance of the plain plate fin are the lowest compared to other types of fins. Plain plate fins are mostly used for cases where low pressure drop is desired or for cases with low Reynolds number [87].

Strip Fins

Strip fins (or sometimes called offset fin) are a rectangular fins cut into multiple small strips where every alternate strip is offset around 50% of the fin pitch as shown in Figure 13(b) [87]. The alternating fins disrupt the flow, which in turn causes the flow to be redeveloped along the flow length. This in turn enhances the heat transfer performance of the strip fins (by a factor of 1.5-4), but the redeveloping flow also causes a significantly higher pressure drop compared to plain pate fins [88]. Strip fins are commonly used for cases which require Reynolds number in the 500 to 10,000 range [88].

Wavy Fins

In the case of wavy fins, the fin is continuously folding across the flow length as shown in Figure 13(c). The heat transfer enhancement is caused by the Goertel vortices which develop along the flow length. However, such arrangement also increases pressure drop compared to plain plate fins. Three times increase in heat transfer is possible in Reynolds numbers around 6,000 to 8,000 compared to the smooth wall [87].

Louvered Fins

Louvered fins work by cutting the fin metal at an interval and turning the fins at 20^{o}-60^{o} degree relative to the flow direction as shown in Figure 13(d) [87]. Similar to strip fins, such arrangement disrupts the flow, which causes the flow to be redeveloped along the flow length, which in turn increases both heat transfer performance and pressure drop. Two or three times increase in heat transfer performance is possible compared to straight fins [89]. However, the ratio between friction factor and Colburn j-factor (j/f) is lower

than strip fin due to drag on the fin bend [90]. The operational Reynolds number for louvered fin is around 100 to 5,000 [88].

Pin Fins

Pin fins consist of an array of cylinder rods or wires attached to the wall as shown in Figure 13(e). The pins can be either circular or elliptical. The concept of pin fins is similar to strip fins and louvered fins where heat transfer enhances due to repeated boundary layer growth along the channel, which in turn also increases the pressure drop. It is usually used for the case of low Reynolds numbers where there is a strict limit in pressure drop [87].

2.2.2. State-of-the-Art Heat Transfer Surfaces

To meet the current demand of high heat transfer rate, low pressure drop, and more compact system, multiple works on performance enhancement of heat exchanger surface have been reported in the literature. The work can involve enhancement of existing conventional surfaces by way of by adding shaped reentrant cavities and internal ribs [91], vortex generation [17, 18], or by using EHD pumping [19] or a piezoelectric translation agitator (PTA) [92]. Other work developed a novel heat transfer surface such as by using porous media [93-95] or oblique fins [10] or by using impinging jets to enhance heat transfer rate [96, 97]. In this chapter, a summary of the literature review on the heat transfer enhancement will be reported.

Xia et al. proposed the heat transfer enhancement in a straight microchannel with fan-shaped reentrant cavities and internal ribs. The effect of relative rib height and Reynolds number (between 150 to 600) to the pressure drop and heat transfer performance was

studied. It was concluded that the combined effect of rib and cavity has better heat transfer performance than individual cavity only. 1.3-3 times of Nusselt number (Nu) and 6.5 times of f were reported compared to conventional microchannels [91].

Yang et al. rotated the fine surface of wavy-fin flat tubes that are commonly used in power plant cooling to prevent fouling in the heat exchanger. Higher heat transfer at the cost of higher pressure drop was recorded compared to the un-rotated surface. The results also showed that the buoyancy effect needs to be taken into account in the friction factor calculation for low Reynolds number calculation, but can be ignored in Nusselt number calculation [98].

Joardar and Jacobi added a winglet vortex generation to generate a vortex in the air side as shown in Figure 14. An experimental test was performed using a full scale wind tunnel. For a single row winglet arrangement, 16.5% to 44% increase in heat transfer coefficient at a cost of 12% increase in pressure drop was reported. For a three row vortex generation array, 29.9% to 68.8% increase in heat transfer coefficient with 26% increase in pressure drop was recorded [17]. A similar study was performed by Leu et al. which showed the effect of different vortex generation span angles by testing three different angles: 30^{o}, 45^{o}, and 60^{o}. The study reported that the 45^{o} span angle produced the highest heat transfer augmentation [18].

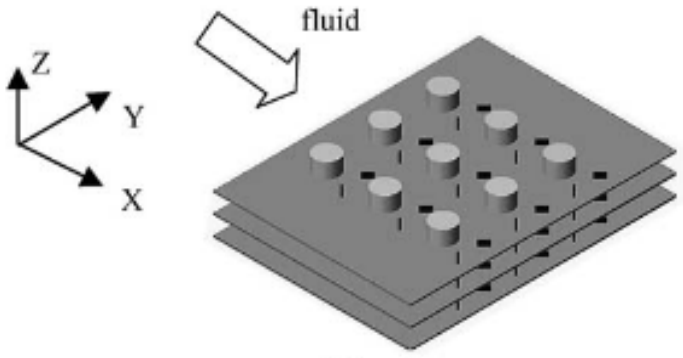

Figure 14: Plate fin heat exchanger with winglet vortex generation [18]

Another work involved a spiral fin-and-tube heat exchanger that was a fin and tube heat exchanger where the fin was twisting along the tube. Pongsoi et al. performed experimental work to study the effect of fin pitch on the heat transfer performance [99]. They reported that fin pitch effect was negligible on j factor at high Reynolds numbers (4,000-15,000), and its effect on pressure drop was also negligible at Reynolds numbers lower than 6,000. Another work by Tang et al. compared spiral fin-and-tube heat exchangers with plain fin-and-tube, vortex generation fin-and-tube, and slit fin-and-tube. This work showed that spiral fin-and-tube yield the highest Nusselt number and pressure drop compared to the other surfaces [100]. A j and f correlation for spiral fin-and-tube heat exchanger has also been reported by Pongsoi et al. [99].

Moore et al. performed an experimental study on novel air cooled enhancement for a 50 MW air-cooled solar power plant by using a multi-row circular finned tube bank or single row of rectangular plate finned tubes. The results showed that a single-row plate finned tube design, a four-row finned tube design, and a two-row circular finned tube design produced similar techno-economic performance and offered significant savings compared to other designs [101].

Yazdani and Yagoobi enhanced heat transfer by using electrohydrodynamic (EHD) conduction pumping. They reported fair heat transfer enhancement at low Reynolds number. However, they also noticed a significant pressure drop at high Reynolds numbers [19].

Yeom et al. utilized a piezoelectric translation agitator (PTA) to enhance the heat transfer performance in a narrow channel as shown in Figure 15. Based on the experimental results it is claimed that 55% increase in heat transfer coefficient was possible compared to the non-agitated states for PTA running at 961 Hz as its second resonance with a 1.4 mm displacement for a flow rate of 60 liters per minute. The pressure drop was recorded between 20 to 400 Pa for different operational conditions of the PTA and different flow rates [92].

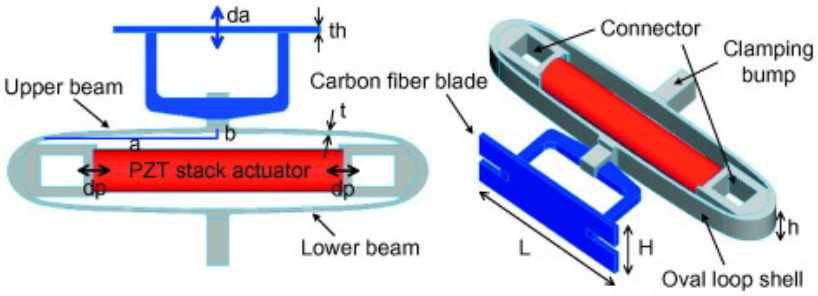

Figure 15: Piezoelectric translation agitator (PTA) [92]

Nawaz and Bock used metal foam in the air-side as replacement of conventional fin surface as shown in Figure 16 [93]. An increase in heat transfer coefficient was recorded due to the high porosity of the foam compared to conventional surfaces, but pressure drop also increased for the same reason. An f and Nu correlation for metal foam heat exchangers was also proposed based on the experimental results. Another work by Kim experimentally investigated the flow and convective heat transfer characteristics for

aluminum foam in an asymmetrically heated channel with three aluminum foams of various permeability and a porosity of 0.92 [102]. Experimental results indicated that the friction factor was much higher at the lower permeable aluminum foams while the significant enhancement in Nu was obtained. Another work by Ribeiro and Barbosa Jr. experimentally investigated crossflow microchannel condensers using metal foams as extended surfaces [94]. Decreasing the porosity and increasing the pore density resulted in higher values of friction factor. Due to the reduction of the surface efficiency with the pore density, the j-factor was highest for the sample with the highest porosity and the lowest pore density. In an effort to miniaturize thermal systems, Noh et al. conducted an experimental study on non-Darcy flow and heat transfer in an annulus with high porosity aluminum foams [95]. The results suggested that significant enhancement in Nusselt number was attained at the cost of increase in friction factor.

Figure 16: Metal foam heat exchanger [93]

Morimoto et al. proposed to use oblique wavy fin for heat transfer enhancement as shown in Figure 17 [10]. A series of numerical simulations was performed. The results showed that oblique wavy fins yield 1-2 and 1-1.3 times enhancement in Nu and j/f, respectively, compared to normal wavy fin surface. A similar work was done by Lee et al. for oblique

fin microchannels. The results show that the oblique configuration caused the flow to have thinner boundary layer thickness and secondary flow, which in turn enhanced heat transfer [9].

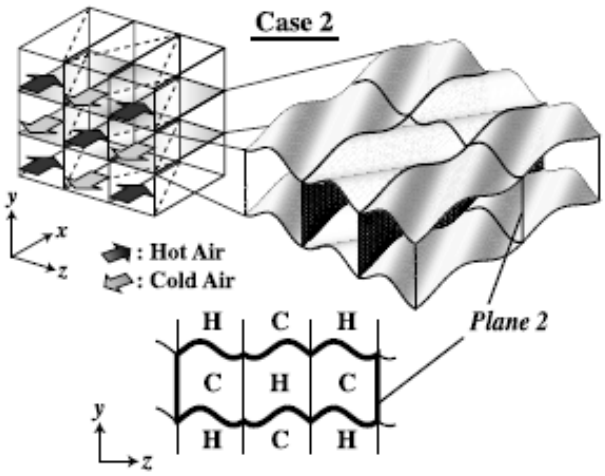

Figure 17: Oblique wavy fin [10]

Wong and Indran numerically investigated the fluid flow and thermal characteristics of an air-impinged plate fin heat sink to understand the effect of fillet profiles at the bottom of the plate fin. It was found that fillet profile enhanced the overall thermal performance of a plate fin heat sink, and the U-shaped channel profile was capable of achieving thermal enhancement as high as approximately 13% [96]. Mahalingam developed the design and thermal performance of a synthetic-air-jet-based heat sink for high-power dissipation electronics. The synthetic-jet heat sink dissipated ~ 40% more heat compared to steady flow from a ducted fan blowing air through the heat sink [97].

Although significant work has been reported in the literature to improve the performance of conventional heat transfer surfaces or to develop an advanced surface with higher performance than conventional surfaces, the increase in heat transfer performance is always accompanied by an increase in pressure drop. A summary of select previous air-

side heat exchanger enhancement is shown in Table 3. However, out of all of the advanced heat transfer surfaces proposed in the literature, manifold-microchannel technology shows the greatest promise to deliver significant improvement in heat transfer without significant pressure drop penalty.

2.2.3. Manifold Microchannels

Out of all of the proposed methods to enhance heat transfer performance, manifold-microchannels shows the most promising results, as they can significantly increase heat transfer coefficient without significant increase in pressure drop as reported in [12]. Manifold-microchannel heat exchangers can be perceived as an offspring of microchannel heat exchangers.

The idea of manifold-microchannel technology is to add a set of manifolds on top of the microchannels, as shown in Figure 18. The purpose of the manifold is to divide and deliver the flow into multiple microchannels as shown in the figure. Due to the short flow length on the microchannel, the flow will be in the developing region, which has higher heat transfer performance compared to fully developed flow. In addition, short flow length can also reduce pressure drop, which in turn, reduces the pumping power requirement. In order to further increase the effectiveness of the heat exchanger, the flow can be divided into a multi-pass system as shown in Figure 18(b). It has been shown by Cetegen that for the same heat transfer rate, multi-pass manifolding can reduce the single-phase pressure drop in a channel by a factor of N^2, where N is the number of channel segments [12].

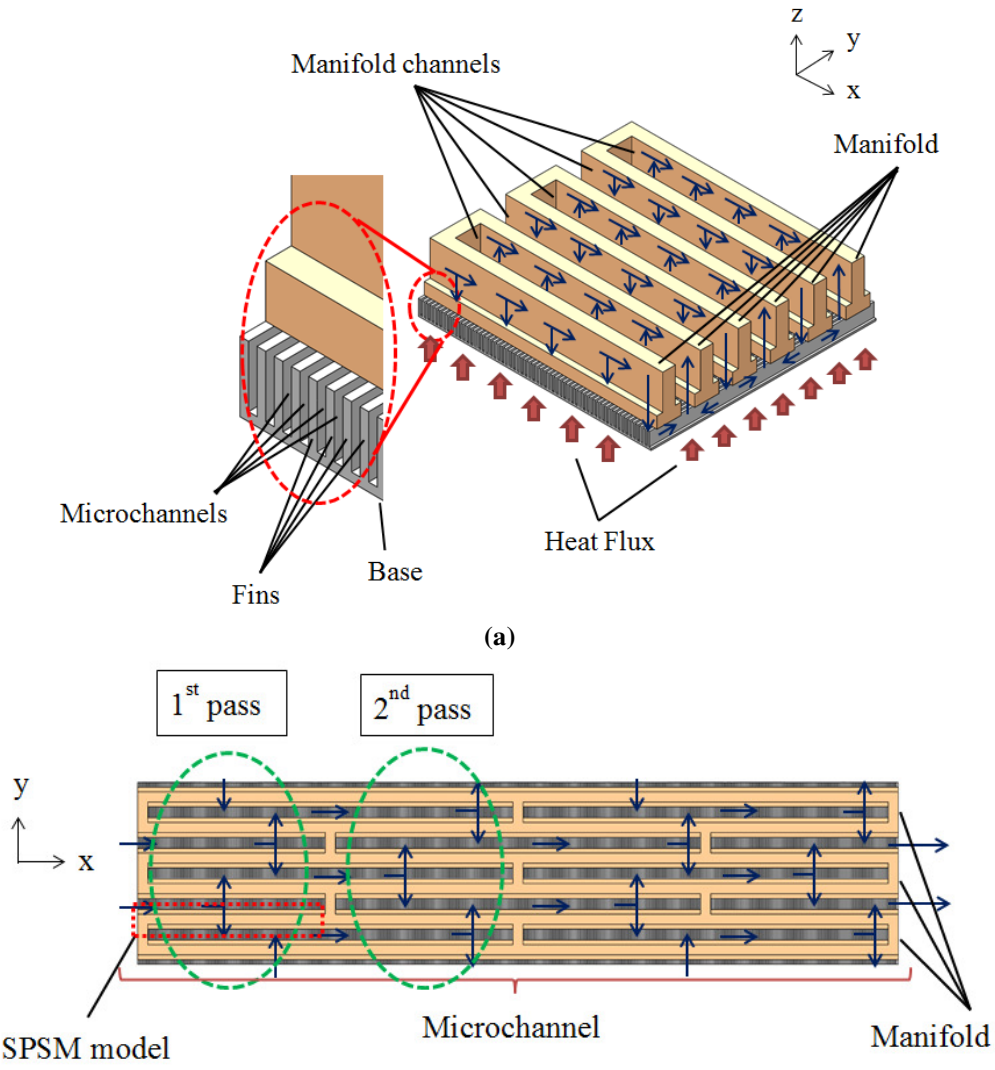

Figure 18: Manifold-microchannel plate heat exchanger: (a) partial 3-D view, (b) top view

Manifold-microchannel technology was first studied by Harpole and Eninger in 1991, who found that heat transfer coefficient on the order of 100 W/cm^{2}K and pumping power of 1 or 2 bar is possible for laminar flow in a manifold-microchannel heat exchanger [103]. Since then more work has been reported in the literature which shows the superiority of manifold-microchannel over conventional technology [12, 13, 15, 104-114]. A summary of some of the latest work on manifold-microchannel will be presented in the following.

Copeland et al. conducted a 3-D CFD simulation on manifold-microchannel heat sink using water as the working fluid and silicon fins and base [113]. The model considered only a single microchannel and assumed uniform laminar flow distribution in all channels as shown in Figure 19. Pressure drop in the range of 47 - 12,260 Pa and thermal resistance of 0.25 - 1.85 ^{o}C/W were observed for multiple different manifold channel pitches, microchannel widths, microchannel widths, and channel flow velocity combinations.

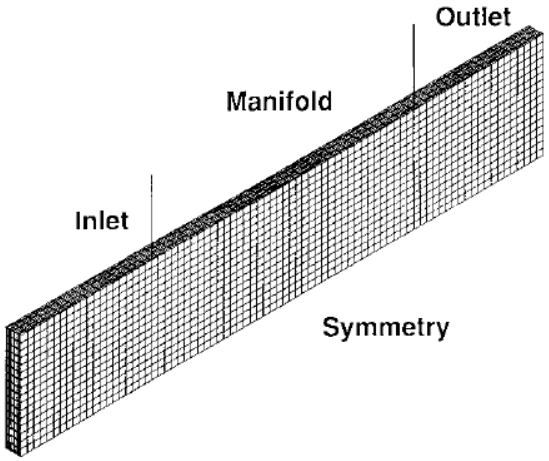

Figure 19: Single microchannel computational domain by Copeland et al. [113]

Kim et al. did experimental testing on manifold-microchannel for forced air cooling using a full model consisting of manifold and multiple microchannels [14]. The fin and base were made of silicon, and air was used as the working fluid with laminar flow configuration. The experiment revealed that 35% reduction on thermal resistance compared to microchannel heat sink was possible.

Ng and Poh also carried out a 3-D CFD simulation on a manifold-microchannel heat sink considering only a single microchannel and assuming uniform laminar flow distribution in all channels [114, 115]. The fins and base were made out of silicon, while water was

used as the working fluid. The effect of geometrical and flow properties on heat exchanger performances such as Nu, f, pressure drop, and thermal resistance, were investigated. Pressure drops between 45 - 10,209 Pa and thermal resistance of 0.53 - 6.66 ^{o}C/W were observed.

Ryu et al. also conducted a 3-D numerical optimization of a manifold-microchannel heat sink by optimizing heat transfer coefficient using CFD simulation [116]. The simulation considered a single manifold-microchannel segment with a portion of the inlet and outlet manifold channels as shown in Figure 20. The inlet and outlet manifold channels provided better flow distribution in the inlet and outlet of the microchannel. The fins were made out of copper, and water was used as the working fluid. The results showed that manifold-microchannel can reduce thermal resistance by half compared to traditional microchannel heat sinks and improve temperature uniformity on the channel.

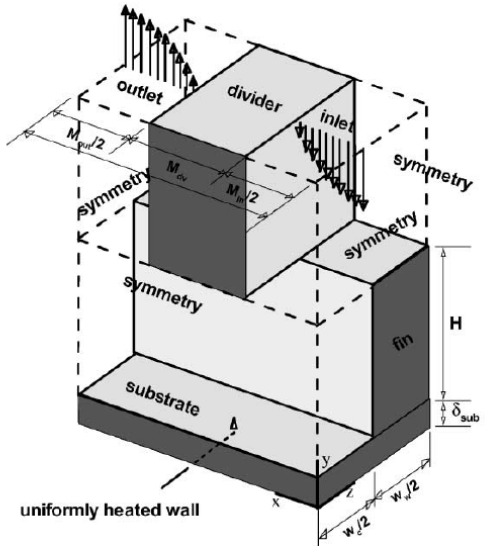

Figure 20: Single manifold-microchannel segment computational domain by Ryu et al. [116]

Wang et al. performed a 3-D CFD simulation on both the manifold and microchannel section of the heat exchanger [16]. The heat exchanger consists of 30 numbers of microchannels. The fin was fabricated out of copper and water was used as the working

fluid. The result showed that the manifold-microchannel design could increase heat transfer by 75% and delivered better temperature distribution compared to the microchannel heat sink.

Cetegen conducted 3-D numerical multi-objective optimization of a manifold-microchannel heat sink [12]. The simulation considered a single manifold-microchannel segment. Copper and water were used as the fin material and working fluid, respectively. The results showed that the manifold-microchannel heat sink can have 72% higher heat transfer coefficient than a traditional microchannel heat sink or 306% higher heat transfer coefficient than a jet impingement heat sink for the same pumping power. In addition, Cetegen also ran a single-phase and multi-phase heat transfer experiment using a manifold-microchannel which showed significant performance improvement of the manifold-microchannel over other state-of-the-art technology as shown in Figure 21.

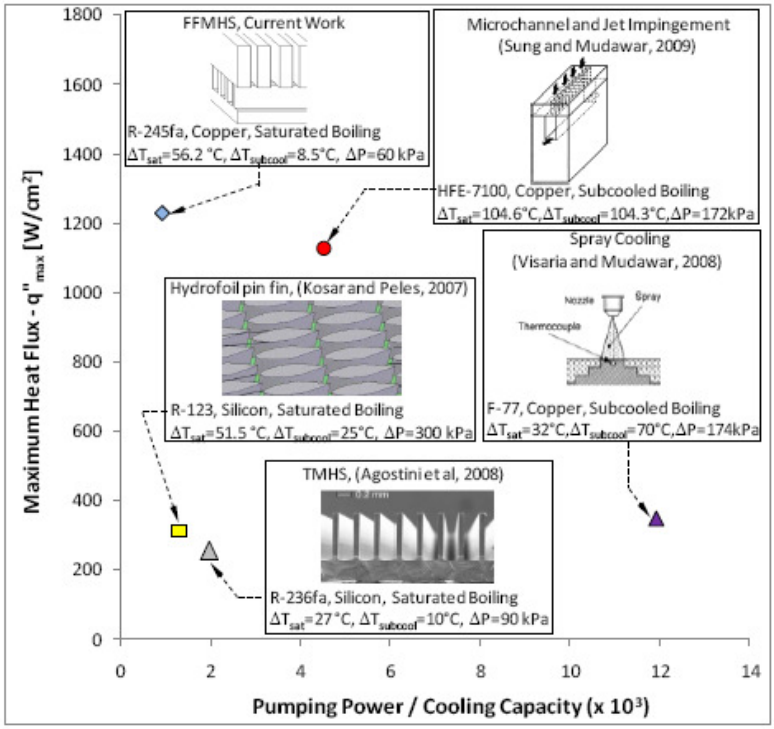

Figure 21: Performance comparison of manifold-microchannel (called FFMHS in the figure) with other state-of-the-art technology [12]

Kermani et al. did an experimental study on a manifold microchannel heat sink for concentrated solar cell cooling [117]. The fins and base were made out of silicon, while water was used as the working fluid. The experiment found that a heat transfer coefficient of 65.5 kW/m^{2}K can be achieved for flow rate of 1.1 g/s and heat flux of 75 W/cm^2.

Escher et al. conducted an experimental and numerical work on a manifold-microchannel heat sink using water as working fluid and silicon as the fin and base material [118]. In order to simplify the modeling problem, the microchannel section was considered as porous media with anisotropic permeability to account for resistance due to the microchannel. The result of the simulation to some degree agreed with experimental results, and it was found that thermal resistance of 0.09 cm^{2}K/W with corresponding pressure drop of 0.22bar as possible for a system with dimensions of 2 x 2 cm^2.

Boteler et al. carried out a numerical investigation on single-pass plate manifold microchannel heat exchanger that considered both the manifold and microchannel section for 2 to 20 microchannels, as shown in Figure 22, using commercial CFD software [15]. The result showed that the manifold-microchannel heat exchanger yielded a 97% reduction on pressure drop and better temperature distribution compared to a conventional microchannel heat sink.

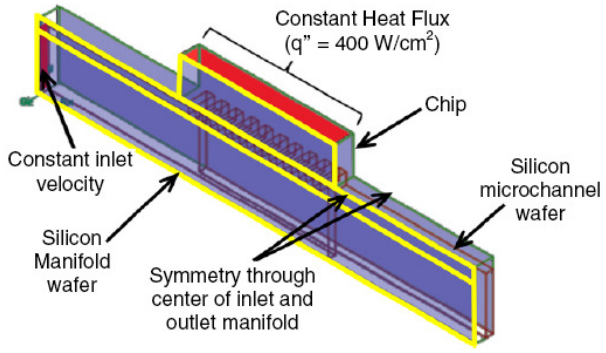

Figure 22: Single-pass plate manifold microchannel computational domain [15]

Kaijun and Zuo proposed the used of a manifold-microchannel for cooling of concentrated photovoltaic cells [119]. Experimental results showed that using water as the refrigerant, a heat transfer coefficient of 8236 W/m^2K was achievable with pressure drop of less than 3kPa. The concentrating photovoltaic cells surface temperature could be maintained below 6.3 °C.

Hu et al. studied the used of liquid metal (Galinstan) in a manifold-microchannel heat sink [120]. Numerical simulation was performed to compare the performance of the manifold-microchannel heat sink using water and liquid metal. The simulation results showed that liquid metal can enhance the heat transfer performance of manifold-microchannel heat sink at the cost of an increase in pressure drop.

Jha et al. implemented manifold-microchannel technology for an absorption cooling system [109]. A manifold-microchannel with 100 μm channel width and 600 μm channel height was experimentally tested using R134a as the refrigerant. An overall heat transfer coefficient of more than 10,000 W/m^2K was recorded with maximum pressure drop of 120 mbars and 100 mbars on the refrigerant and air side.

Arie et al. successfully developed a hybrid numerical method to predict the performance of manifold-microchannel heat exchangers with much lower computational time compared to full model CFD simulation [106]. The results showed good agreement with full model CFD simulation, but with more than 10 times reduction in computational time. Arie et al. also showed that manifold-microchannel plate heat exchangers yield significant performance improvement in Nusselt number and friction factor compared to chevron plate heat exchangers for three different chevron angle of 30^o, 45^o, and 60^o.

Andhare et al. studied the implementation of manifold-microchannels for low heat flux applications [121]. A manifold-microchannel pleat heat exchanger was successfully fabricated and tested for water-to-water heat transfer. The experimental results showed that overall heat transfer coefficient close to 20 kW/m^2K with pressure drop per length value of 5.85 bar/m was possible for flow rate as low as 20 g/s.

Zhou et al. studied the effect of different types of flow configuration on manifold-microchannel heat sinks for electronic cooling applications [122]. Several flow configurations, as shown in Figure 23, were numerically modeled and studied. The study showed that the base configuration yielded the most uniform performance in all modules. For configuration 2, the performances were non-uniform for the three modules, with the module closest to the outlet yielding the highest performance. For configuration 3, performances were similar with base case and were achieved with slightly more than half the coolant flow rate.

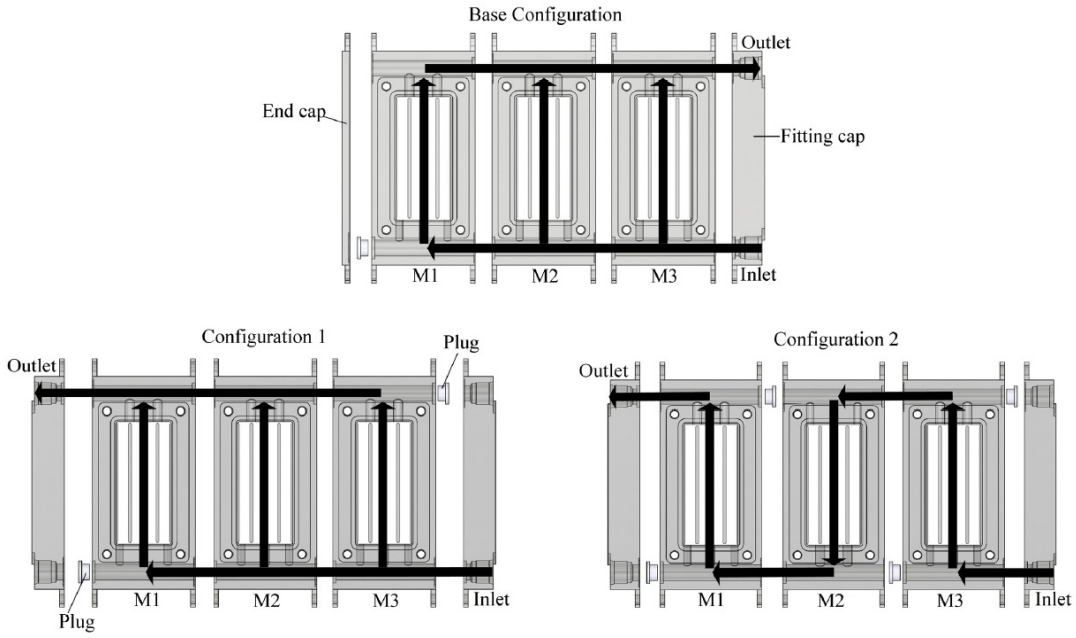

Figure 23: Several flow configurations for Zhou et al.'s study [122]

Mandel et al. also studied the implementation of manifold-microchannel for high heat flux electronic cooling applications [123]. The manifold-microchannel heat sink was successfully fabricated and tested. The results showed that by forcing thin film evaporation on the microchannel, a very high heat transfer coefficient of 40 kW/m^2K-140kW/m^2K at pressure drop of 10 kPa-50kPa were recorded for R245fa as the refrigerant.

The main challenge in the implementation of manifold-microchannel technology is to manufacture very small-scale microchannel sizes with high aspect ratio (ratio of fin height to thickness) and thin fins (hundreds of microns) using traditional manufacturing technology. A high aspect ratio fin is desirable for increasing the heat transfer area, and thinner fins can reduce the overall mass of the heat exchanger.

Conventional heat exchanger manufacturing involved fins fabrication using stamping or folding techniques, after which they are bonded to the base plate using methods like brazing [124-126]. Such techniques are not suitable for microchannel fabrication, however, which has small channel spacing (<1 mm) and fin spacing (<0.5 mm), as brazing a very small channel is a very challenging process.

The most common microchannel fabrication techniques involve lithography, laser exposure, electroplating, and molding. A summary of such techniques can be found in [127]. Several techniques have been recorded in the literature that can fabricate a very small fin size (<0.05 mm) with high aspect ratio (>10), but such techniques are mostly limited for non-metal fabrication, such as photolithography for silicon fin fabrication [118] or micro reverse wire-EDM for tungsten fin fabrication [128].

In the literature, several other works also have reported successful thin metallic fin fabrication with techniques such as molding (0.75 mm thickness recorded), hydroforming (0.36 mm thickness recorded), and micro-electroplating (0.01 mm thickness recorded), and chemical etching (0.08 mm thickness recorded) but with low aspect ratio (<2) [129-132]. CNC wire cutting has shown success in fabrication of metallic fins with aspect ratio as high as 12, but with fin thickness of only 0.44 mm [14]. Micro deformation shows success in fabricating metallic fins with fin thickness of 0.09 mm and aspect ratio of 4, but it is a slow and expensive technique [13].

Another challenge in manifold-microchannel fabrication is that the manifold and the microchannel sections must be manufactured separately due to the complexity of the geometry. Subsequently these sections must be then assembled to form a complete heat exchanger. The assembly process can be challenging and time consuming, especially in the case of large-scale heat-exchangers, which can consist of hundreds or thousands of manifold-microchannel layers. Brazing or welding both components together is a challenging task by itself, as the microchannels' size is on order of hundredths of microns, and improper brazing or welding can cause obstruction of the microchannels.

Additive manufacturing has shown promise in fabricating geometries which would otherwise is very challenging to fabricate using conventional techniques. Direct metal laser sintering (DMLS), one type of metal additive manufacturing technique first developed by EOS GmbH of Munich, Germany [133], has shown its ability to manufacture metallic fins as small as 150 μm [134]. In addition, using additive manufacturing can eliminate the need to build the manifold and microchannels separately, which can simplify the manufacturing process significantly. In this study,

additive manufacturing was implemented to fabricate a manifold-microchannel heat exchanger.

A table summarizing all of the recent work on manifold-microchannel heat exchangers is shown in Table 4. The summary of the manifold-microchannel heat exchanger fabrication techniques, including additive manufacturing techniques, is shown in Table 5.

2.3. Polymer Heat Exchangers

In addition to the advanced metallic based heat exchanger, a polymer based heat exchanger was also proposed as an advanced heat exchanger design. Although they have a lower thermal conductivity compared to metal, polymer based heat exchangers offer several advantages over metallic based heat exchangers such as low weight, low cost, low fouling, and good corrosion resistance. There are numerous works in the literature on polymer heat exchangers. A summary of the progress on the polymer heat exchangers can be found in [27, 135, 136]. Some of the most common polymer heat exchanger designs will be discussed in this chapter.

One of the most common types of polymer heat exchangers is a polymer shell and tube heat exchanger for liquid-liquid or condensing liquid-liquid heat transfer applications [20-22]. The heat transfer and pressure drop performance of polymer shell and tube heat exchangers was reported by Morcos and Shafey [20]. Due to low thermal conductivity of the polymer, the wall thickness is the limiting factor for this application. Liu et al. compared the performance of a polymer shell and tube heat exchanger with a metallic shell and tube heat exchanger and showed that the wall thermal resistance of the polymer heat exchanger is much higher than that of the metallic one [21]. In order for the

performance of the polymer heat exchanger to be comparable with the metallic one, the heat transfer area of the polymer heat exchanger needs to be much larger than the metallic one.

Another type of polymer heat exchanger is the polymeric hollow fiber heat exchanger [23-27]. It consists of hundreds to thousands of small polymer tubes bundled together at both ends to form a honeycomb structure, as shown in Figure 24. It is similar to the shell and tube heat exchanger but without the baffles and operates in either cross flow or parallel flow configuration. It can be used for liquid-to-liquid or condensing liquid-liquid heat transfer applications. In order to offset the low thermal conductivity of polymer, the heat transfer area per volume is increased by increasing the number of tubes per bundle. As many as 5000 tube per bundle was reported [27].

Figure 24: Hollow fiber heat exchanger [27]

Several works have proposed to use polymeric hollow fiber heat exchangers as a replacement for metallic shell and tube heat exchangers. One such work is by Zarkadas and Sirkar, who proposed to use a polymeric hollow fiber heat exchanger for a low

temperature/pressure application [23]. Heat transfer performance comparable to metallic shell and tube heat exchangers was reported. Another work by Song et al. proposed the use of a polymeric hollow fiber heat exchanger for a thermal desalination process [25]. Two to five times larger conductance/volume value is recorded compared to metallic heat exchangers. Yan et al. proposed to add a polypropylene (PP) net in the shell side to improve heat transfer performance of the polymeric hollow fiber heat exchanger [26]. A 30% increase in overall heat transfer performance is observed at the cost of 12% increase in pressure drop.

Another type of polymer heat exchanger wildly available on the market is the plate heat exchanger. An example of a polymer plate heat exchanger is shown in Figure 25. Several polymer plate heat exchangers have been commercially available, such as by AB Segerfrojd [137] and Ail Research [138]. A summary of commercially available polymer plate heat exchangers can be found in [27]. There has been significant research on plate polymer heat exchangers in the literature [28-31].

Figure 25: Polymer plate heat exchanger [139]

Burns and Jachuck examined the performance of a cross flow polymer plate heat exchanger for air/steam-liquid heat transfer applications where the water vapor through a non-condensable gas was used to heat the water [28]. Overall heat transfer coefficient in the range of 50-300 W/m^{2}K was reported. Cheng and Van Der Geld experimentally tested a polymer plate fin heat exchanger air-water and air/steam-water heat transfer application [29]. Overall heat transfer coefficient of 80-130 W/m^{2}K for air-water case was recorded. Harris et al. compared the performance of an air-water cross flow microchannel plate heat exchanger made out of nickle and poly(methyl methacrylate) (PMMA) [30]. The results showed that although the nickle heat exchanger had higher volumetric heat transfer density ($Q/(V\Delta T)$), the PMMA was superior in terms of gravimetric heat transfer density ($Q/(m\Delta T)$).

Above, some of the most common polymer heat exchangers have been discussed. Table 6 summarizing the polymer heat exchanger literature study. The biggest disadvantage of polymer over metal is its low thermal conductivity (thermal conductivity (k) ranging from 0.3-0.5 W/mK for polyethylene compared to 16 W/mK for stainless steel or 205 W/mK for aluminum), which can significantly reduce the thermal performance of polymer heat exchangers. Several approaches are being used to mitigate this disadvantage, such as improving the thermal conductivity by the use of a filler [140-145] or reducing the thickness [27].

Han and Fina have reported that up to 5 W/mK thermal conductivity is possible by using carbon nanotube (CNT) as a filler [140]. Wang et al. showed that with very high volume fractions (46%) and very long, well aligned CNT in a bismaleimide (BMI), thermal conductivity as high as 41W/mK is possible [141]. Beside carbon nanotubes, different

fillers have been investigated in several other works for their ability to enhance thermal conductivity. Khan et al. reported success in increasing the thermal conductivity of polyphenylene sulfide (PPS) from 0.22 W/mK to 1.94 W/mK with 22.4 vol% graphene nanoplatelets in PPS [142]. Another work by Balachander et al. shows that the thermal conductivity of polydimethylsiloxane (PDMS) can be increased by 30 times, to almost 5 W/mK, with <3 vol% gold nanotubes filler [143]. Development of higher thermal conductivity polymers, however, increases the cost of the material. In addition, adding a filler material can increase the weight of the material, as fillers like graphite and gold have higher densities than polymer.

The use of such enhanced materials for polymer heat exchangers has been reported on the literature. Robinson et al. reported the performance comparisons of a finned plate heat exchanger build out of polytetrafluoroethylene, carbon fiber-reinforced polyamide, and titanium [31]. The thermal performance of the carbon fiber-reinforced polyamide heat exchanger is 70% higher than the polytetrafluoroethylene heat exchanger, but it is still 28% lower than titanium heat exchanger. Another work by Dogruoz and Arik compared the figure of merit of heat sinks built out of different materials, including graphite filled PPS [146]. They reported a reasonably high figure of merit for the PPS based heat exchanger.

In the present study, a polymer heat exchanger based on prime surface technology was fabricated using a layer-by-layer line welding additive manufacturing technique of thin High Density Poly Ethylene (HDPE) sheets. Despite the advantages of additive manufacturing, work on the use of additive manufacturing for polymer heat exchanger fabrication is very limited. One known work in the literature is by Cevallos, who showed

that the performance of a webbed tube heat exchanger fabricated using fused deposition modeling yielded comparable performance to metallic heat exchangers in terms of pressure drop and heat transfer [84].

Table 1: Summary of additive manufacturing fabrication techniques

Process	Method	Resolution (μm)	Material	Strengths	Weaknesses
Micro-stereolithography (MSL)	Polymerization of photopolymer-resin via UV light	1	Polymer, ceramic, metal	• Very high resolution • Feature size < 1μm possible	• Metal/polymer mixed resin may have high viscosity • Shrinkage due to post processing
Selective laser sintering/melting	Sintering or melting fine powder via high temperature laser	30	Metal, ceramics	• Less complex process	• Difficult powder handling • Porosity (Sintering)
Fused deposition modeling	Continuous deposition of material in layers	200	Thermo-plastic	• Less complex process • Multi material possible	• Low resolution
Laminated object manufacturing process	Glue together layer of adhesive-coated material from a roll and cut it using laser	50	Ceramic and metal	• Cheap • Can fabricate very large structure	• Low resolution • Shrinkage, warpage, deformation due to post processing
Laser chemical vapor deposition process	Employ laser to convert gaseous reactant into solid layer	1	Metal, ceramic, semiconductor	• Very high resolution • Multi material possible	• Complex process • Slow process
Inkjet printing	Deposit liquid material layer by layer	20	Liquid material (μ=2-100mPas)	• Wide range of material	• Require support structure for micro fabrication • Droplet size limited by nozzle size

Table 2: Literature study on implementation of additive manufacturing in heat exchanger fabrication

Author	Year	Fabrication Process	Material	Major Finding
Tsopanos et al. [53]	2005	Selective Laser Melting	Stainless steel 316L	Micro cross-flow HX was fabricated out of stainless steel 316L. The HX was consist of rectangular channels in both side with fin thickness of 0.1 mm and fin height of 0.9 mm.
Kumar et al. [79]	2009	Electron Beam Melting (EBM)	Titanium alloy (Ti64) and Aluminum 6061	Hexagonal periodic cellular structures for heat exchangers application were successfully fabricated. The influence of lattice orientation on the heat transfer and flow properties were evaluated.
Wong et al. [80]	2009	Selective Laser Melting	Aluminum	Three novel heat sinks with a staggered elliptical array, a lattice array, and a rounded corners rectangular fin array were fabricated. The staggered elliptical array HX shows the highest performance
Ramirez et al. [81]	2011	Electron Beam Melting (EBM)	Copper	Complex open cellular copper mesh and foams were fabricated with application for thermal management devices like heat exchanger. Detailed analysis of the fabricated structures was performed.
Hutter et al. [82]	2011	Selective Laser Sintering	Aluminum	Metal foam filled tubular HX was fabricated and experimentally tested. Higher heat transfer performance was observed compared to metal foam reactor fabricated using conventional method.
Cormier et al. [83]	2014	Cold Spray Technology	Aluminum	Pyramidal fins arrays were fabricated. The effect of fin height and fin density was investigated. Correlations linking Nusselt number with Reynolds number, fin height, and fin density were derived.

Cevallos [84]	2014	Fused Deposition Modeling	Polycarbonate	A webbed tube HX with 2mm thick wall and 5mm inner diameter was fabricated. Similar heat transfer performance with plain plate fin HX was reported.
Thompson et al. [85]	2015	Selective Laser Melting	Titanium Alloy (Ti64)	A flat-plate oscillating heat pipe with 1.53mm diameter channel was fabricated. Partially melted particle was found in the channel. Effective thermal conductivity of 110W/mK was recorded.

Table 3: Summary of select previous air-side heat exchanger enhancement technologies

Author	Technology	Type of Study	Claim
Xia et al. [91]	Micro heat sink with fan-shaped reentrant cavities and internal ribs	Numerical	1.3-3 times and 6.5 times increase in Nu and f compared to microchannel, respectively.
Moore et al. [101]	A multi-row circular finned tube bank and a single row of rectangular plate finned tubes	Experimental	A single-row plate, a four-row finned tube design, and a two-row circular finned tube design produce similar techno-economic performance
Yang et al. [98]	Wave-finned flat tube where the fin surface rotates to be perpendicular	Numerical	The new wavy-finned configuration increase both pressure drop and heat flow rate
Yan and Sheen [8]	Finned-and-tube HX surface comparison using plain-plate-fin, wavy-fin, and louvered-fin	Experimental	Louvered fin has the highest j, f, and area goodness factor while wavy fin has the highest volume goodness factor
Wang et al. [6]	Louvered finned and tube	Experimental	A generalized heat transfer and pressure drop correlation for louvered fin and tube was proposed.
Joardar and Jacobi [17]	Plain-plate-fin HX using vortex generation	Experimental	Air-side heat transfer coefficient increases from 29.9% to 68.8% and 26% to 87.6% increase in pressure drop
Nawaz and Bock [93]	Plain plate-tube HX using metal foam	Experimental	j and f correlation for metal foam was developed
Pongsoi et al. [99]	Spiral fin-and-tube heat exchangers	Numerical & experimental	Literature review for spiral fin-and-tube heat exchangers (j and f correlation included)
Yazdani and Yagoobi [19]	EHD conduction pumping	Numerical	Heat transfer enhancement for low Reynolds number was noted
Morimoto et al. [10]	Oblique wavy walls	Numerical	1-2 and 1-1.3 times enhancement in Nu and j/f is possible compared to normal wavy fin

Table 4: Summary of manifold-microchannel literature survey

.

Authors	Year	Type of study	Application	Major finding
Harpole, G. M., and Eninger, J. E [147]	1991	Numerical work	Electronic cooling (liquid cooling)	Heat transfer coefficient in the order of 100 W/cm^{2}K and pressure drop of 100 kPa or 200 kPa were estimated.
Ryu et al. [116]	2003	Numerical work	Electronic cooling (liquid cooling)	Thermal resistances of 0.0196, 0.0232, and 0.031 ^{o}C/W were observed for pumping power of 2.56 W
Kermani et al. [112]	2009	Experimental work	Solar collector heat sink	Heat transfer coefficient of 65.5 kW/m^{2}K can be achieved for flow rate of 1.1 g/s and heat flux of 75 W/cm^2
Cetegen [12]	2010	Experimental and numerical work	Electronic cooling (Single phase liquid cooling & 2 phase cooling)	72% and 306% improvement in heat transfer coefficient were observed compared to microchannel heat sink and jet impingement heat sink, respectively, for the same pumping power
Escher et al. [118]	2010	Experimental and numerical work	Electronic cooling (liquid cooling)	Thermal resistance of 0.09 cm^{2}K/W with corresponding pressure drop of 0.22 bar was observed for a system of 2 x 2 cm^2
Boteler et al. [15]	2012	Numerical work	Electronic cooling (liquid cooling)	More uniform temperature distribution and 97% reduction of system pressure drop were detected compared to microchannel heat sink
Arie et al. [105]	2012	Numerical work	Liquid-liquid plate heat exchanger	A manifold-microchannel design with heat transfer rate of 56.7kW, pumping power of 138W, and volume of 4.25cm^3 was demonstrated.
Kaijun and Zuo [119]	2015	Experimental work	Liquid cooling of concentrating photovoltaic cells (CPC)	A heat transfer coefficient of 8236W/m^{2}K was achievable with pressure drop less than 3 kPa. The CPC surface temperate can be maintained below 6.3 ^{o}C.
Jha et al. [109]	2015	Experimental work	Liquid-liquid HX for absorption cooling system	Overall heat transfer coefficient of more than 10,000 W/m^{2}K was recorded with maximum pressure drop of 120 mbars and 100 mbars in the refrigerant and air side, respectively.
Arie et al. [106]	2015	Numerical Work	Liquid-liquid plate heat exchanger	Significant performance improvement in Nusselt number and friction factor compared to chevron plate heat exchanger was

				noted.
Mandel et al. [123]	2015	Experimental work	Electronic cooling (2 phase cooling)	A very high heat transfer coefficient of 40 kW/m2K-140 kW/m2K at pressure drop of 10 kPa-50 kPa was recorded
Andhare et al. [121]	2016	Experimental and numerical work	Liquid-liquid plate heat exchanger	Overall heat transfer coefficient close to 20 kW/m^{2}K with pressure drop per length value of 5.85 bar/m was possible for flow rate as low as 20 g/s

Table 5: Summary of microchannel fabrication techniques

Technique	Ref.	Minimum fin thickness	Maximum aspect ratio	Material	Bounding Needed?
Stamping/folding	[124-126]	50 µm	>10	Metal	Yes
Photolithography & deep reactive ion etching	[118]	12 µm	18.8	Silicon	Yes
Micro reverse wire-EDM	[128]	10 µm	30	Tungsten	Yes
Molding	[29]	750 µm	0.67	Metal – Al & Cu	Yes
Hydroforming	[28]	360 µm	1.5	Metal – stainless steel	Yes
Micro-electroplating	[30]	10 µm	1	Metal - nickle	Yes
CNC wire cutting	[14]	440 µm	12	Metal	Yes
Photochemical etching	[132]	80 µm	0.9	Metal	Yes
Micro Deformation	[13]	90 µm	10	Metal	Yes
Additive manufacturing (direct metal laser sintering (DMLS))	[134]	150 µm	10	Metal	No

Table 6: Summary of the polymer heat exchanger literature study

Authors	Year	Type of Heat Exchanger	Application Studied	Material	Major finding
Liu et al. [21]	2000	Shell and tube	Liquid-liquid HX	High temperature nylon, cross-linked polyethylene (PEX), and nickel	The wall thermal resistance in polymer HXs is significantly higher than nickel HX. Larger heat transfer area is needed to match the polymer HX performance with metallic HXs.
Harris et al. [30]	2000	Microchannel HX	Gas-liquid HX	Polymethylmethacrylate (PMMA)	The results show that although the nickle heat exchanger has higher ($Q/(V\Delta T)$), the PMMA HX was superior in term of ($Q/(m\Delta T)$.
Burns and Jachuck [28]	2001	Corrugated plate HX	Air/steam-liquid HX	Poly-ether-ether-ketone (PEEK)	Overall heat transfer coefficient in the range of 50-300 W/m^2K was reported
Song et al. [25]	2010	Polymeric hollow fiber HX	Desalination process	Polypropylene (PP)	2-5 times larger conductance/volume value is recorded compared to metallic HX
Robinson et al. [31]	2011	Finned plate HX	Gas-liquid HX	Polytetrafluoroethylene, carbon fiber-reinforced polyamide, and titanium	The thermal performance of the carbon fiber-reinforced polyamide HX is 70% higher than the polytetrafluoroethylene HX, but it is still 28% lower than titanium HX.
Yan et al. [26]	2014	Polymeric hollow fiber HX	Water-water HX	Polypropylene (PP)	Adding PP net in the shell side can improve the overall heat transfer coefficient by 30% at the cost of 12% increase in pressure drop
Cevallos [84]	2014	Webbed tube HX	Air-water HX	Polycarbonate	The first polymer HX successfully fabricated by AM. Similar heat transfer and pressure drop performance was noticed compared to metallic plain plate fin HX.

Chapter 3: Advanced and Conventional Heat Exchanger Designs

3.1. Introduction

This chapter discusses the design requirement baseline for the heat exchanger and also the conventional and advanced heat exchangers design. The conventional heat exchangers were based on the state of the art technology commonly used in power plant cooling. The conventional heat exchangers were used for baseline comparisons with the advanced design. For the advanced designs, two types of heat exchangers were proposed: one was a metallic heat exchanger utilizing manifold-microchannel technology and the other was a polymer heat exchanger utilizing prime surface technology.

3.2. Design Requirements

A design requirement baseline was derived based on Baltimore Aircoil Corporation's (BAC) and EPRI's power plant cooling specification for a 12.2 MW single cell heat exchanger unit [1, 148]. The detailed design flow rate, maximum pressure drop, and operational temperature are shown in Table 7.

Table 7: Design requirements

Variables	Baseline - specification
Q	12.2 MW
$\dot{m}_{air}$	608 kg/s
$T_{in,air}$	40 ^{o}C
$\dot{m}_{water}$	584 kg/s
$T_{in,water}$	67.5 ^{o}C
Δp_{air}	<200 Pa
Δp_{water}	<100 kPa
COP	172

3.3. Baseline Heat Exchanger

Based on the information provided by BAC, the most common type of fin surface used for power plant cooling is a wavy-fin surface. Kays and London [5] have provided friction factor (f) and Colburn j factor (j) vs. Reynolds number (Re) data for several commercially available wavy fin geometries. Wavy-fin s1144-38 W from Kays and London's database was chosen as the state of the art conventional heat transfer surface baseline, as its dimensions are closest to the current industrial fin geometry (based on BAC information) and its performance data is available in Keys and London [5].

The wavy-fin s1144-38W baseline is only applicable for power plant cooling applications, as different applications may use different types of fins. It is therefore of interest to also calculate the improvement that the advanced surface yields compared to other type of conventional fins such as louvered fins and plain plates fin. As a result, in addition to the baseline, 22 different types of commercially available plate-fin heat exchanger surfaces based on Keys and London's [5] database were selected for additional comparison. Some of the key geometrical specifications of these 22 surfaces are listed in Table 8, and the schematics drawings can be found in Figure 13. A more detailed geometry can be found in Ref. [5]. It should be noted that WFPFS 1 has the same dimensions as the wavy-fin s1144-38W. As a result, WFPFS 1's performance will also serve as the conventional heat exchanger performance baseline.

Table 8: Key geometrical specifications of conventional heat exchanger surfaces [5]

Plain Plate-Fin Surface (PPFS)		
Symbol	*Fin Pitch (fin/cm)*	*Plate Spacing (cm)*
PPFS 1	4.37	0.64
PPFS 2	5.94	1.06
PPFS 3	4.04	1.38
PPFS 4	5.82	0.84
PPFS 5	7.82	0.64

Louvered Plate-Fin Surface (LPFS)				
Symbol	*Fin Pitch (fin/cm)*	*Plate Spacing (cm)*	*Louvered gap (cm)*	*Louvered Spacing (cm)*
LPFS 1	2.39	0.64	0.14	0.95
LPFS 2	2.39	0.64	0.33	0.95
LPFS 3	4.37	0.64	0.10	1.91
LPFS 4	2.39	0.64	0.14	1.27
LPFS 5	4.37	0.64	0.14	1.27

Pin-fin Plate-Fin Surface (PFPFS)				
Symbol	*Plate Spacing (cm)*	*Pin Diameter (cm)*	*Pin Spacing 1 (cm)*	*Pin Spacing 2 (cm)*
PFPFS 1	0.61	0.10	0.32	0.32
PFPFS 2	1.01	0.10	0.24	0.30
PFPFS 3	1.91	0.08	0.15	0.15
PFPFS 4	1.30	0.17	0.50	0.60

Strip-Fin Plate-Fin Surface (SFPFS)			
Symbol	*Fin Pitch (fin/cm)*	*Plate Spacing (cm)*	*Fin Length (cm)*
SFPFS 1	4.8	1.23	0.24
SFPFS 2	4.37	0.64	0.64
SFPFS 3	4.70	0.60	1.27
SFPFS 4	7.77	0.13	0.25
SFPFS 5	5.49	0.95	0.32
SFPFS 6	6.15	0.64	0.32

Wavy-Fin Plate-Fin Surface (WFPFS)		
Symbol	*Fin Pitch (fin/cm)*	*Plate Spacing (cm)*
WFPFS 1	4.50	1.05
WFPFS 2	4.53	0.93

The conventional fin surface was applied to the air side while the water side consists of a series of rectangular channels in parallel in a cross-flow configuration as shown in Figure 26. The complete heat exchanger may be composed of several air and water side layers stacked vertically.

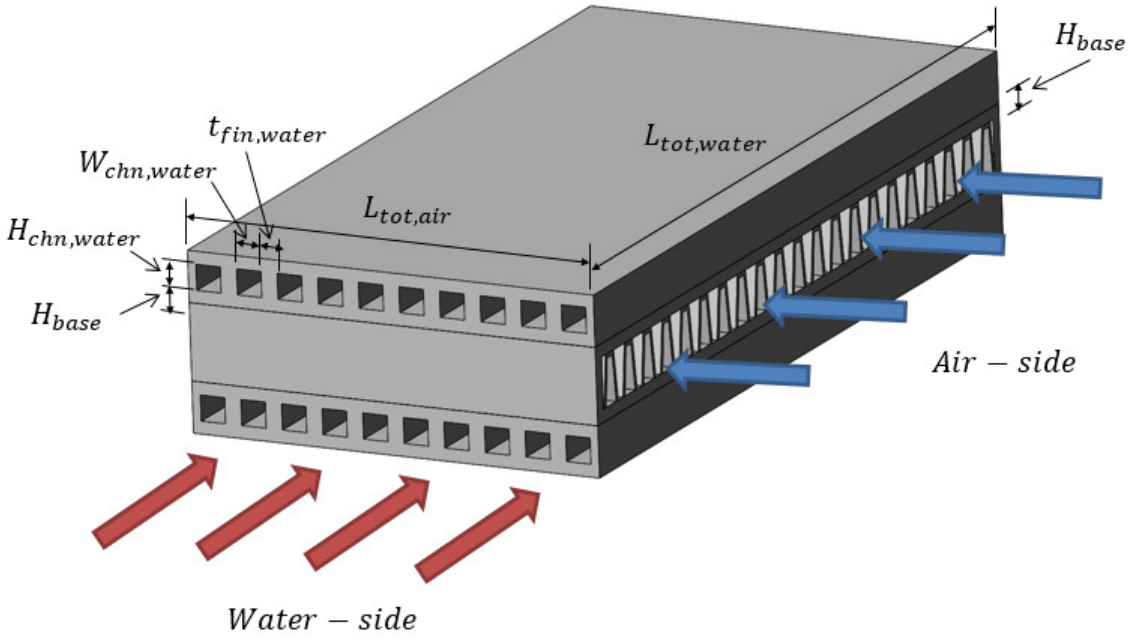

Figure 26: Conventional heat exchanger

3.4. Advanced Heat Exchanger Design

Two types of advanced heat exchangers (a metallic and polymer heat exchanger) were proposed to be studied as a possible replacement for the current state-of-the-art wavy-fin surface currently in used for power plant cooling as described previously. The metallic heat exchanger was based on manifold-microchannel technology, while the polymer heat exchanger was based on prime surface technology. A detailed description of both heat exchangers will be presented in this chapter.

3.4.1. Advanced Metallic Heat Exchanger

The advanced metallic heat exchanger consists of manifold-microchannel surface on the air-side and rectangular channels in the water-side as shown in Figure 27. The concept behind manifold-microchannel technology is that by adding manifolds on top of the microchannels, the flow length on the microchannels can be significantly reduced. This reduction in flow length can reduce the pressure drop, which in turn reduces pumping power requirement. In addition, short flow length can also force the flow to be in the

developing region, which has higher heat transfer performance compared to fully developed flow.

A manifold-microchannel was installed on the air side in order to maximize the heat transfer enhancement, as the air side's thermal resistance is generally much higher than the water side's. Both heat exchanger surfaces were combined in cross-flow arrangement as shown in Figure 27. The complete heat exchanger may be composed of several air and water side layers stacked vertically as shown in Figure 26(b).

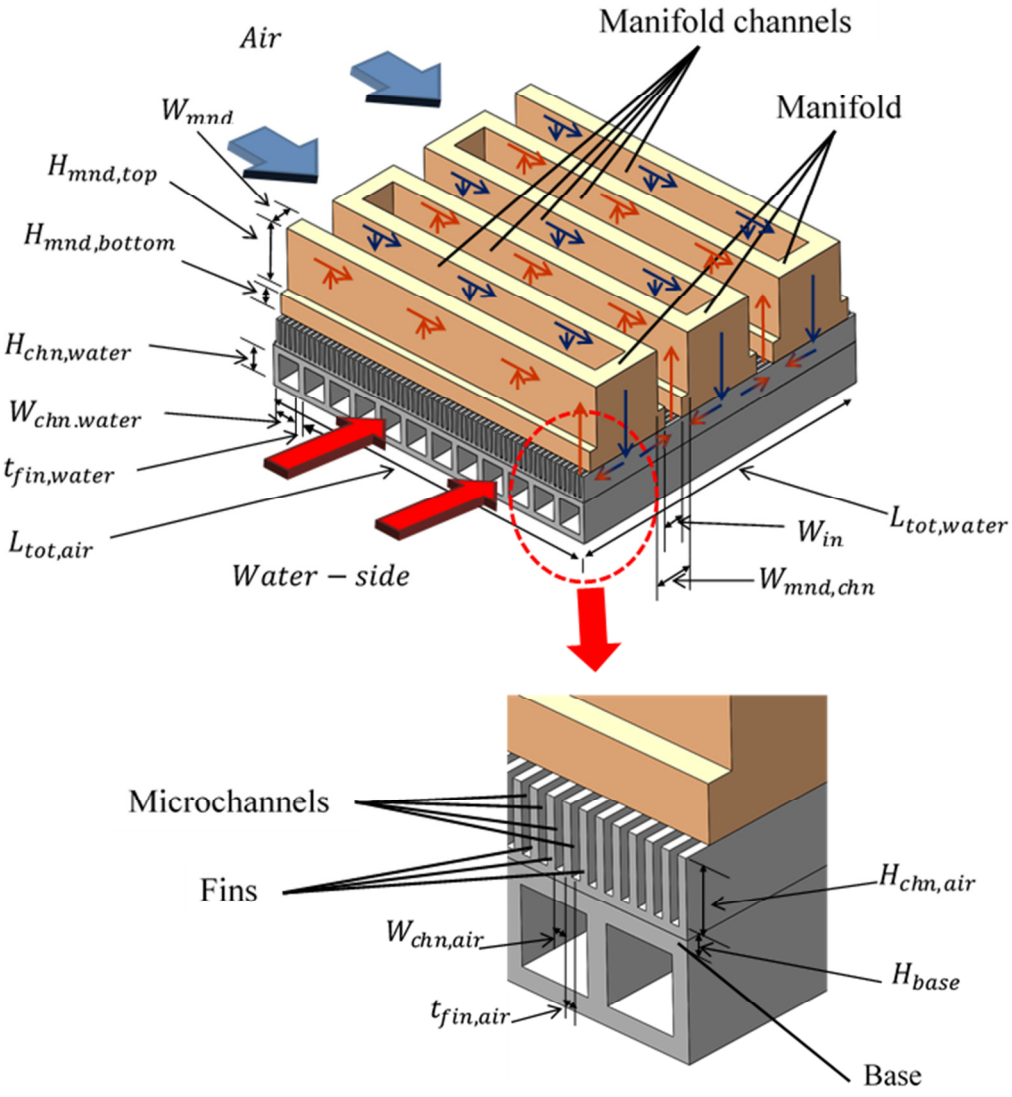

(a)

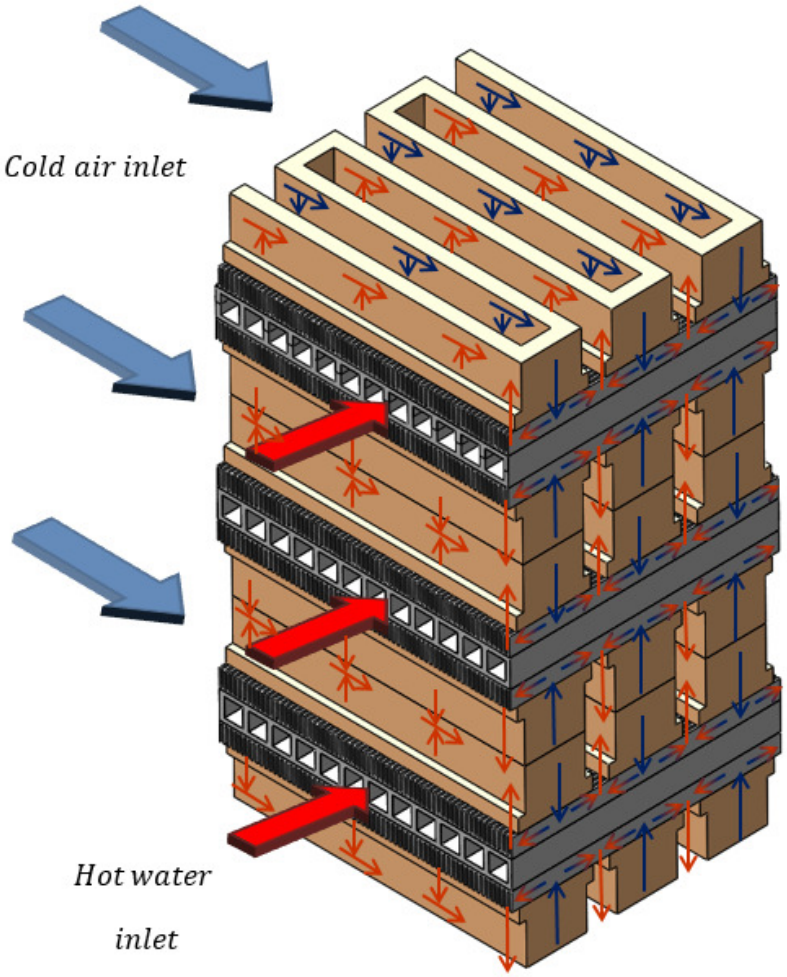

(b)

Figure 27: Manifold-microchannel heat exchanger (a) single layer (b) multi layers

3.4.2. Advanced Polymer Heat Exchanger

The advanced polymer heat exchanger consists of a prime surface heat exchanger. The prime surface polymer heat exchanger consists of water channels through which hot water flows to be cooled by air that flows through the gap between the water channels, as shown in Figure 28(a). Water channels were fabricated by welding two polymer sheets together using a layer-by-layer line welding additive manufacturing technique which was first introduced by Denkenberger et al. [149] out of thin High Density Poly Ethylene (HDPE) sheets. The location of the welding is shown in Figure 28(b). The heat exchanger can be fabricated by using different polymer materials depending upon the application

conditions such as temperature, pressure and chemical compatibility of the fluids. The wall thickness of the sheets is very small, and thus it is no longer a limitation in heat transfer, and thus does not require expensive polymer blends of higher thermal conductivity. The fabrication process of the heat exchanger will be discussed in detail later this dissertation.

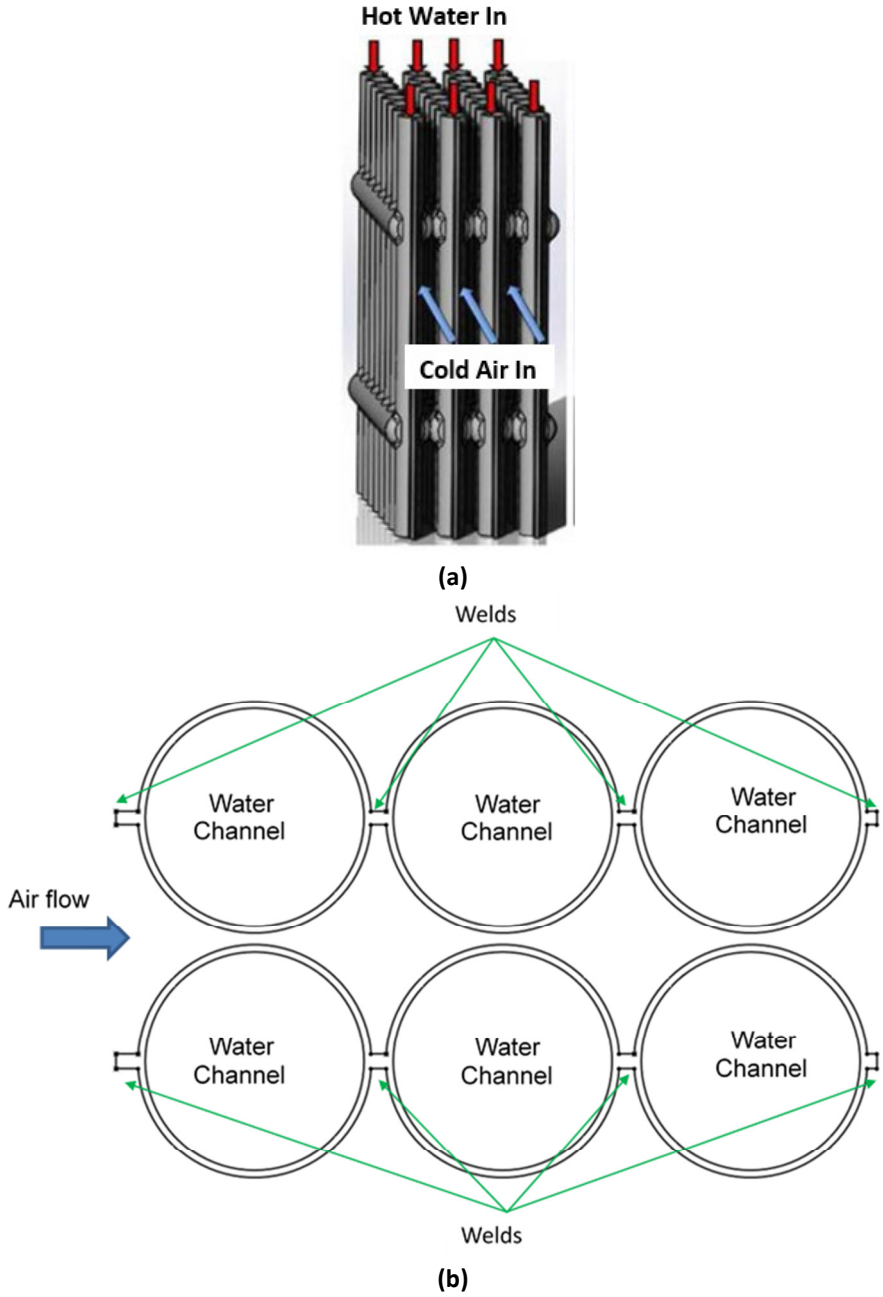

Figure 28: Prime surface heat exchanger (a) Isometric view (b) Cross-section view

3.5. Summary

In this chapter the design requirements for the heat exchanger were defined based on the power plant's cooling specifications for a 12.2 MW single cell heat exchanger unit. In addition, the heat exchanger designs for the conventional and advanced metallic and polymer heat exchangers were discussed in detail. Wavy-fin s1144-38W, from Kays and London's book, was selected as the baseline surface, as its geometry is the closest to that used for power plant cooling. In addition, for a broader comparison, 22 different types of commercially available plate-fin heat exchanger surfaces were introduced to be used for additional conventional heat exchanger comparisons. The advanced metallic heat exchanger consisted of a manifold-microchannel on the air side in cross flow configuration with rectangular channels on the water side. On the other hand, the advanced polymer heat exchanger was made of a prime surface heat exchanger. The thin wall characteristic makes it is less sensitive to thermal conductivity of the material, which makes it suitable for polymer heat exchangers which have low thermal conductivity. The fabrication method for both advance heat exchangers will be discussed in the next chapter.

Chapter 4: Fabrication Methods

4.1. Introduction

This chapter explains the metallic heat exchanger fabrication technique (direct laser metal sintering) and polymer heat exchanger fabrication technique (layer-by-layer line welded). The operating principles of the techniques, the machines used, and the limitations of the two techniques are discussed in detail.

4.2. Direct Laser Metal Sintering

4.1.1. Concept

Direct metal laser sintering (DMLS) is a metal based additive manufacturing process which uses a computer controlled laser to sinter metal powder based on a pre-programmed geometry to build a 3-D structure layer-by-layer as shown in Figure 29. DMLS is one of the most common additive manufacturing methods for metallic structures and was first developed by EOS GmbH of Munich, Germany [133]. Generally, DMLS consists of two platforms. The first platform is a powder dispenser platform to house the metal powder. The second platform is the build platform on which the 3-D structure is being built. After a layer of the 3-D structure is built, the powder dispenser platform rises up while the build platform lowers so that a new layer of powder can be distributed on top of the existing layer. A re-coater arm is used to uniformly distribute the metal powder as shown in Figure 29. The metal powder is sintered using the laser, as shown in Figure 29. Lenses focus the laser beam while a scanning mirror controls the location where the laser will hit the powder based on the pre-programmed geometry. The process is repeated until the entire 3-D structure is built.

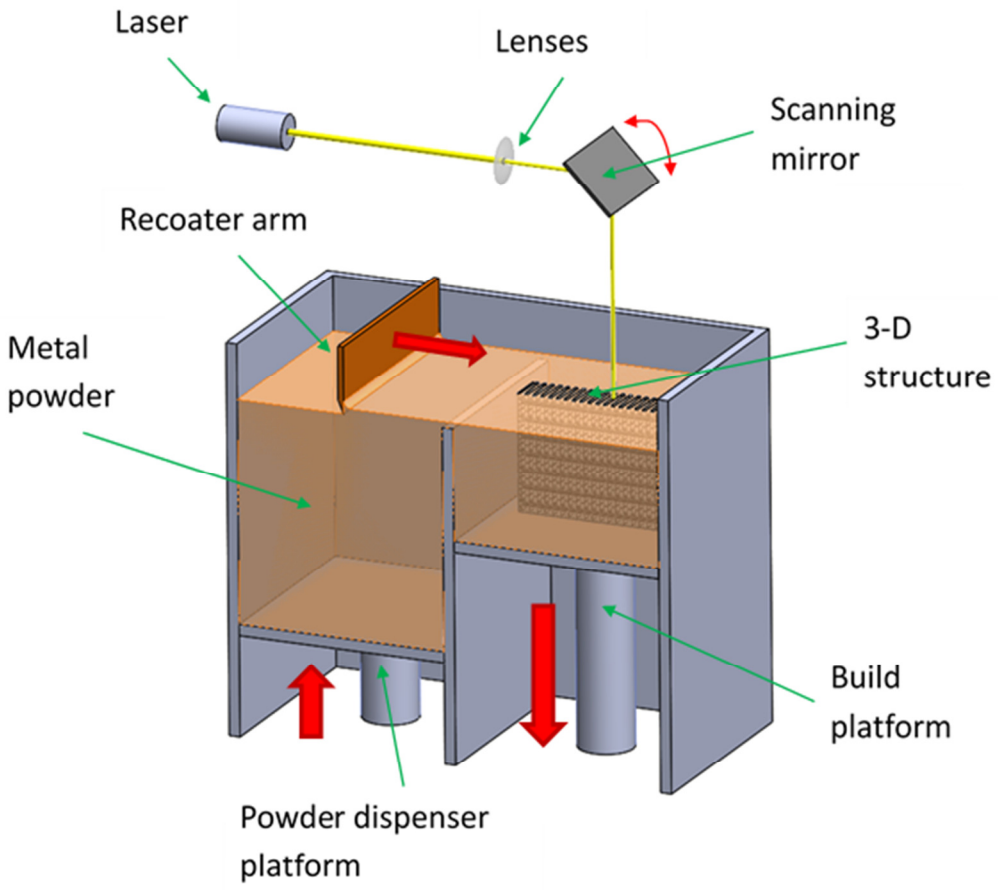

Figure 29: Direct metal laser sintering component

4.2.2. Machine

Figure 30 shows the actual DMLS machine used by Stratasys. The building chamber is where the fabrication process occurs. The chamber is closed when the process is running to limit the outside interference (like dust) and for safety measures due to the high-power laser used for fabrication. In order to avoid oxidation of the metal powder during the sintering process, the build chamber is usually filled with gases like argon. A computer is built into the machine where the 3-D digital model can be installed and the entire fabrication process can be controlled.

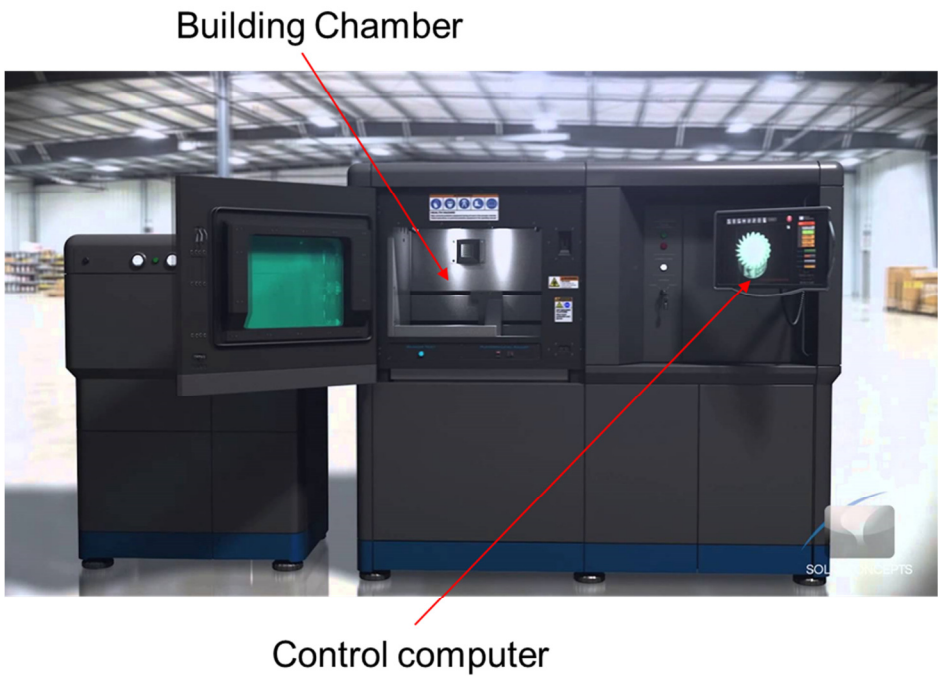

Figure 30: Direct metal laser sintering machine [150]

4.2.3. Material Compatibility and Fabrication Limitations

As DMLS is still a new technology, not all metal can be processed using DMLS. Currently, stainless steel, aluminum, Inconel, and titanium are the most common types of metal used for DMLS. Table 9 lists metals compatible with the DMLS process based on the three top DMLS companies: Stratasys, Proto Labs, and Laserwise (part of 3D Systems). Stainless steel has a good anticorrosion and high temperature resistance which make it suitable for heat exchange. Aluminum and aluminum alloy is a common heat exchanger material for air-to-air heat exchangers in HVAC application. However, its reaction with non-treated water limits its application for air-water heat exchangers. In addition, titanium and its alloys has started to receive higher attention to be implemented for heat exchanger fabrication due to its relatively lower density than stainless steel (60%), favorable corrosion resistance, and better material strength. Lastly, stainless-steel,

titanium and Inconel are suitable for high temperature heat exchangers, due to their high melting points.

Table 9: Direct metal laser sintering – Material compatibility

	Stratasys [151]	Proto Labs [152]	Layerwise (3D Systems) [153]
Stainless steel 17-4	X	X*	
Stainless steel 316L	X	X*	X
Aluminum AlSi10Mg	X	X	X
Inconel 625	X		
Inconel 718	X	X*	X
Pure titanium Ti			X
Titanium Ti64	X	X	X
Cobalt chrome CoCrMo	X	X*	X
Tungsten (pure)			X
Tantalum (pure)			X

* For high precision machine

A list of the fabrication limitations and tolerances is given in Table 10 based on Stratasys, Proto Labs, and Layerwise data. Under normal resolution, the minimum feature size that can be fabricated using DMLS is 300 μm. However, by using a high resolution machine, the feature size can be further reduced to 150 μm. For heat exchangers, the smaller the fins the better their performance, as smaller fins can reduce the overall mass. As a result, due to DMLS's good compatibility with common heat exchanger materials and its capability to fabricate very thin fins, it shows promise to be incorporated for advanced heat exchanger fabrication.

Table 10: Direct metal laser sintering – Fabrication limitation and tolerance

	Stratasys [154, 155]	**Proto Labs [152]**	**Layerwise (3D Systems) [156]**
Layer thickness	*Normal resolution:* 40µm	*Normal resolution:* 30µm *High resolution:* 20µm	N/A
Minimum feature size	*Normal resolution:* 300µm *High resolution*: 150µm	*Normal resolution:* 300µm *High resolution:* 200µm	120µm
Tolerance	*First inch*: ±127µm *Thereafter*: ±50µm	*Normal resolution:* ±76µm *High resolution:* ±76µm	±50µm
Maximum size	N/A	*Normal resolution:* 246mm x 246mm x 274mm *High resolution:* 88mm x 88mm x 73mm	N/A

4.3. Layer-by-layer Line Welded Additive Manufacturing Technique

4.3.2. Machine

The polymer heat exchanger was fabricated from High Density Polyethylene (HDPE) sheets using the layer-by-layer line welded additive manufacturing technique. The laser welder apparatus consists of a computer controlled welding laser that can be moved on the x-, y-, and z-axes, a motor to position the laser, frames to support the laser and motors, and a printer bed where the polymer sheets are placed. The z-direction movement of the laser is necessary for better control of the laser focus, especially for the case of printing a ticker heat exchanger stack. The 3-D printer machine, including all of its components, is shown in Figure 31(a), while a zoomed-in view of the welding laser is shown in Figure 31(b). The 3-D printer machine was custom made by our partner in Pearce Research Group in Michigan Tech University (MTU). The polymer heat exchanger was fabricated entirely at MTU.

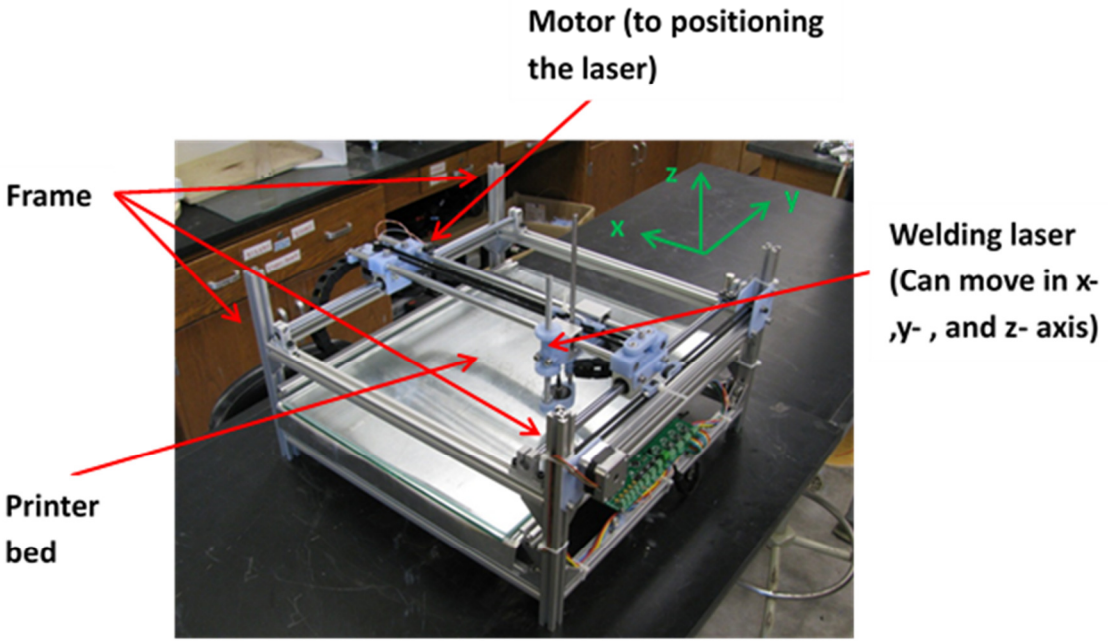

(a)

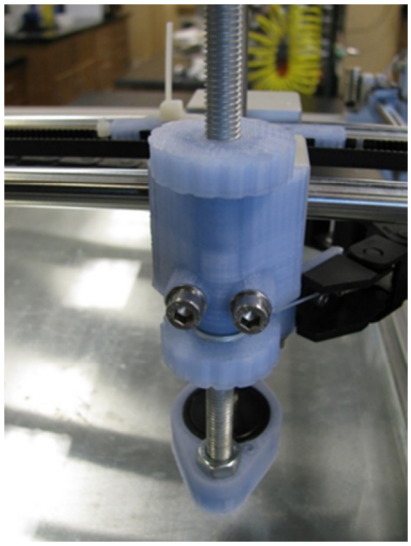

(b)

Figure 31: Polymer HX 3-D printer (a) Complete laser welder apparatus (b) Zoomed-in view of the welding laser

4.3.1. Fabrication Process

Summarizing the fabrication process. First, two layers of HDPE sheets were set on top of each other. Then, water channels were formed by welding both layers together based on a pre-programed digital model for the water channel as shown in Figure 32(a). The water

channel welding pattern shown in Figure 32(a) is for a case where there are two passes on the water side (water is cooled down by air side twice). Then a third polymer layer was added on top of the bounded layer. Air channels were then formed by welding the second and third layer based on a pre-programed digital model for the air channel welding pattern as shown in Figure 32(b). The process was repeated, alternating between water channel welding and air channel welding, as shown in Figure 33 for the case of heat exchanger which consists of 8 layers. It should be noted that the laser power was adjusted so that the welding only occurred on the top two layers. A more detailed explanation of the layer-by-layer line welded additive manufacturing technique can be found in [149].

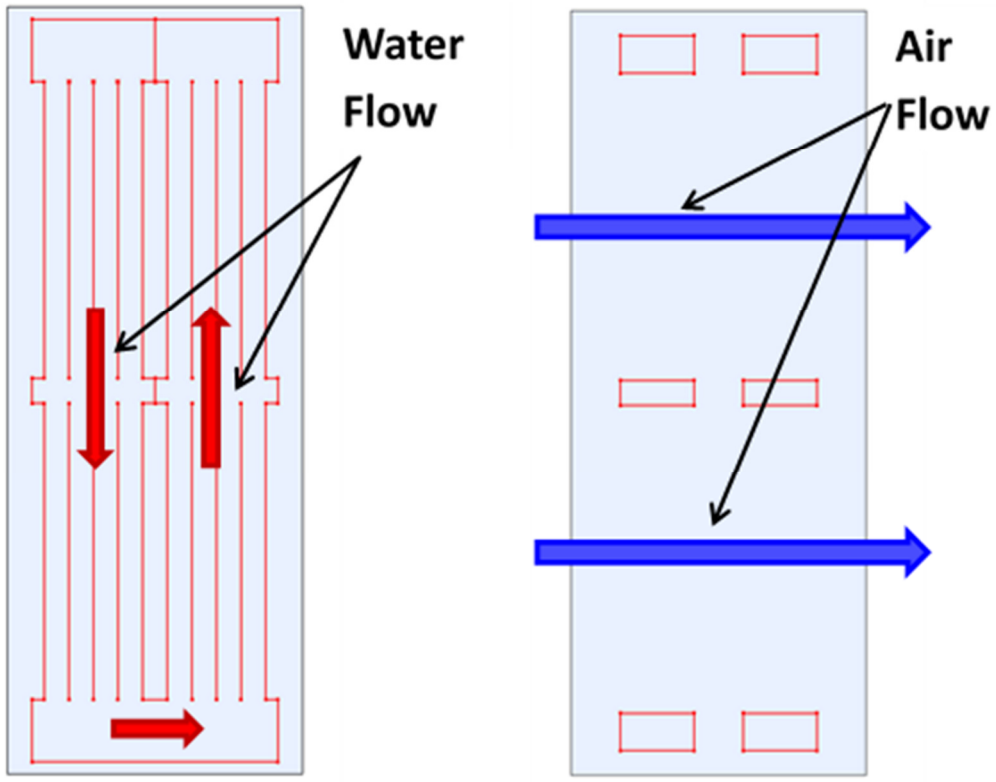

Figure 32: Welding pattern for the prime surface polymer HX (a) For water channel (b) For air channel

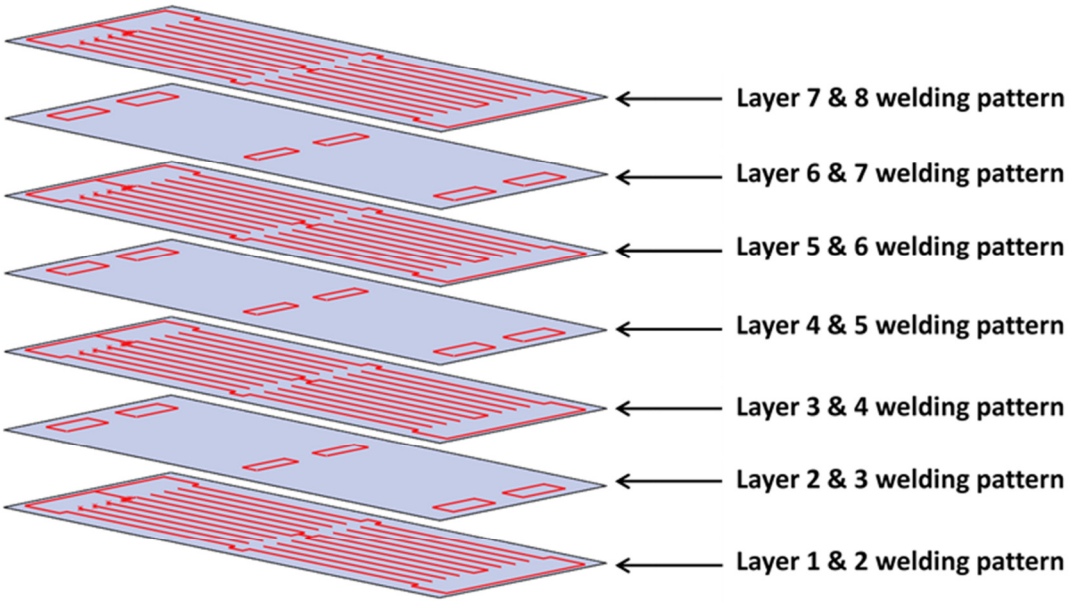

Figure 33: Welding pattern in the stacked polymer heat exchanger

So that water can be distributed to all heat exchanger layers, holes were created on the heat exchanger header as shown in Figure 34(a). In addition, in order to install the pipe that supplies and collects the water for the heat exchanger, pipe bearings were used as shown in Figure 34(a). The pipe bearing was made out of HDPE so that it could be welded to the heat exchanger body. As the water flows to the heat exchanger, the heat exchanger will expand as shown in Figure 35. The eight-layer design will produce a polymer heat exchanger with four stacks (each stack consists of two layers) as shown in Figure 35. The air-channel is formed from the gap between the water channels as shown in Figure 35 (b).

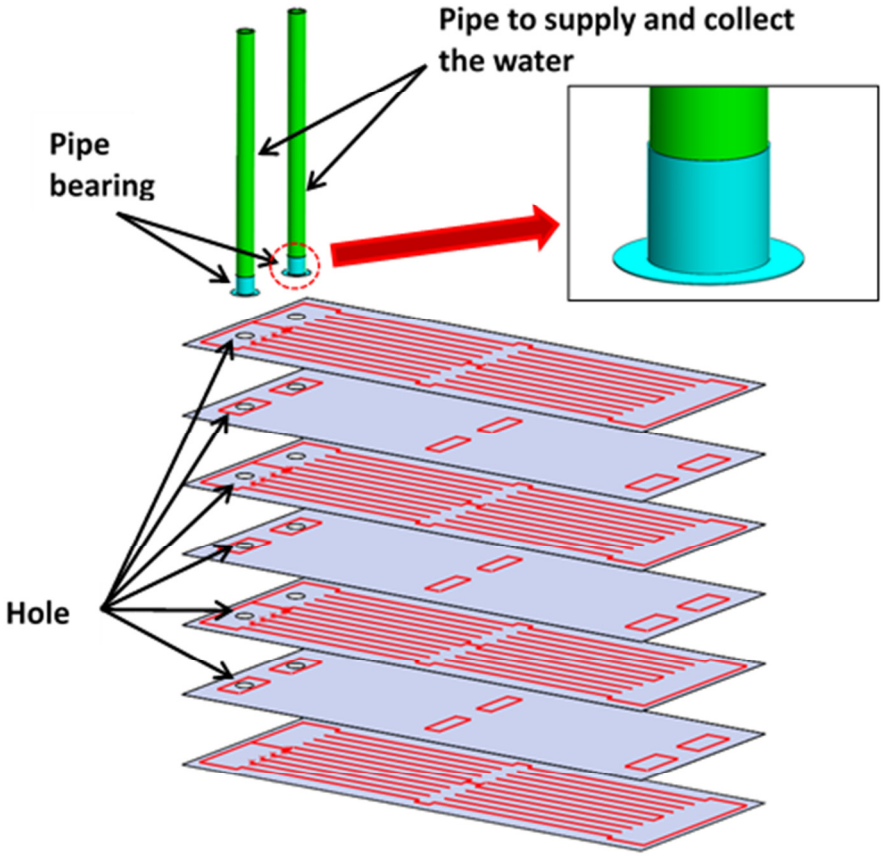

(a)

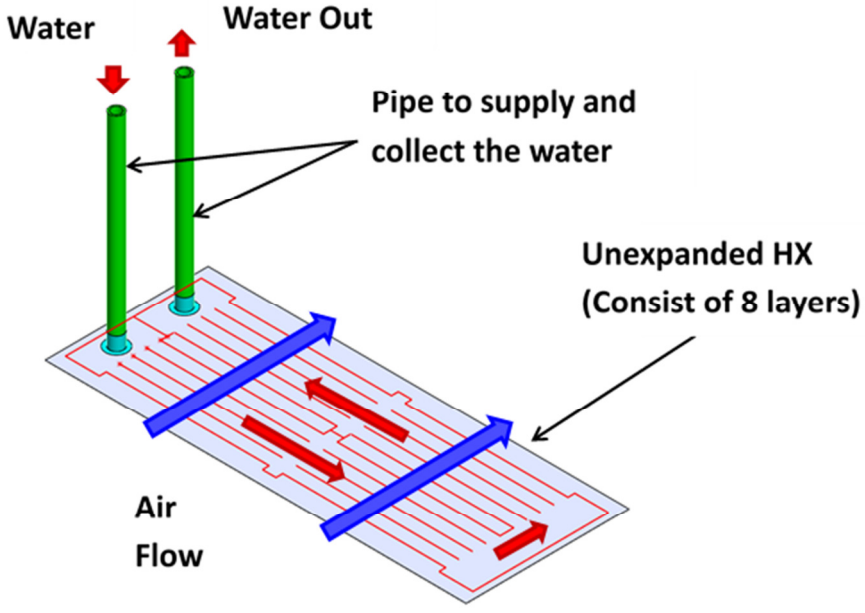

(b)

Figure 34: Assembly of the unexpanded polymer HX: (a) Exploded view (showing welded line) (b) Combined view

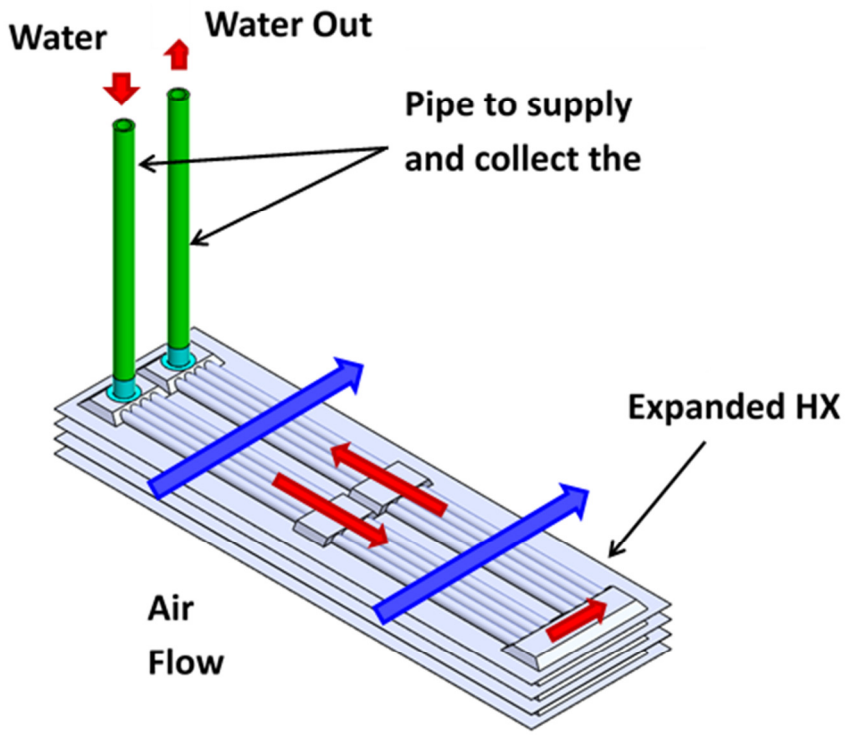

(a)

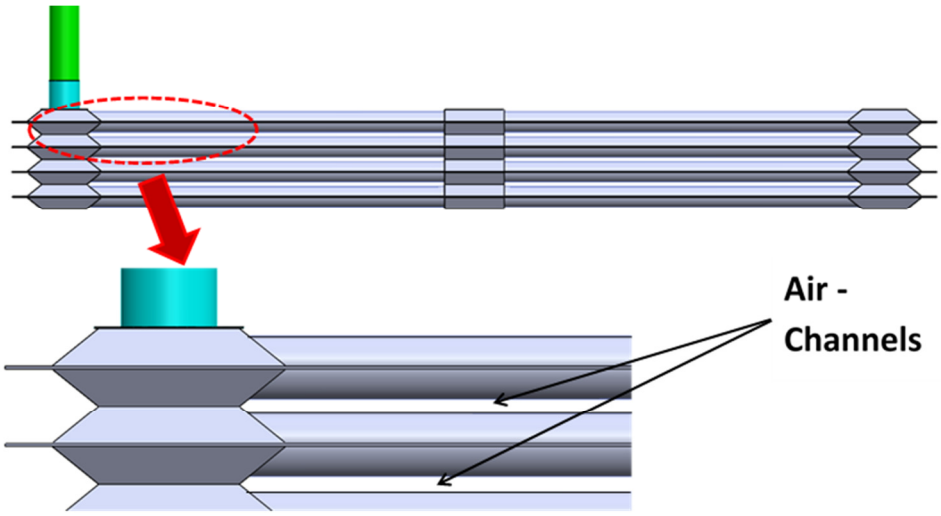

(b)

Figure 35: Assembly of expanded polymer HX: (a) Isometric view (b) Side view

The minimum distance between welding lines needed to be at least 2 mm for precise fabrication. As a result, the minimum water channel diameter that could be fabricated as 1.27 mm.

4.4. Summary

This chapter discussed the direct laser metal sintering method, the fabrication method for the advanced metallic heat exchanger; and the layer-by-layer line welded additive manufacturing technique, the fabrication method for the advanced polymer heat exchanger. The discussion included the components of the printers and the operating principles behind both techniques. In addition, the design constraints of both methods were also discussed.

Chapter 5: Numerical Method

5.1. Introduction

In this chapter, the numerical modeling method used to evaluate the heat transfer and pressure drop performance of the conventional heat exchanger, the manifold-microchannel heat exchanger, and the polymer heat exchanger are discussed in detail.

5.2. Conventional Heat Exchanger

The performances of the conventional heat exchanger (capacity (Q), heat exchanger effectiveness (ε_{HX}), coefficient of performance (COP), and gravimetric heat transfer density ($Q/m\Delta T$)) were solved by first evaluating the individual performance of both the water and air sides. On the water side, heat transfer coefficient (h_{water}) and pressure drop (Δp_{water}) of the rectangular channel were calculated after solving Nusselt number (Nu) and friction factor (f) using available correlations [157]. The corresponding heat transfer coefficient and pressure drop can then be calculated as:

$$h = Nu\frac{k}{D} \tag{1}$$

$$\Delta p = f\frac{L}{D}\frac{\rho v^2}{2} \tag{2}$$

Thereafter, the water-side thermal resistance due to convection ($R_{conv,water}$) can be calculated as (please refer to Figure 26 for geometrical variables description):

$$\frac{1}{R_{conv,water}} = h_{water}(L_{tot}W_{chn}N)_{water} + \eta_{fin,water}h_{water}(L_{tot}H_{chn}N)_{water} \tag{3}$$

where N_{water} is the number of channels on the water side, and $\eta_{fin,water}$ is the water-side fin efficiency calculated as [158]:

$$\eta_{fin,water} = \frac{tanh\left(\frac{MH_{chn,water}}{2}\right)}{\left(\frac{MH_{chn,water}}{2}\right)} \tag{4}$$

$$M = \sqrt{\frac{2h_{water}}{k_{solid}t_{fin,water}}} \tag{5}$$

On the air side, heat transfer and pressure drop were calculated using Colburn j factor (j) and friction factor (f) vs. Reynolds number (Re) test data for common compact heat exchanger surfaces as described by Kays and London [5]. The air-side thermal resistance due to convection ($R_{conv,air}$) can be calculated as:

$$R_{conv,air} = \frac{1}{h_{air}\eta_{HX,air}A_{H,air}} \tag{6}$$

where h_{air} is air-side heat transfer coefficient, $A_{H,air}$ is air-side heat transfer area, and $\eta_{HX,air}$ is overall surface efficiency of airside heat exchanger surface calculated as:

$$\eta_{HX,air} = \left[1 - \frac{A_{fin}}{A_H}\left(1 - \eta_{fin}\right)\right]_{air} \tag{7}$$

where $\frac{A_{fin}}{A_H}$ is the ratio of fin surface area to the total heat transfer area and $\eta_{fin,air}$ is air-side fin efficiency.

The combined heat transfer characteristics of the air and water sides were evaluated using the $\varepsilon - NTU$ method for an unmixed cross-flow heat exchanger by first calculating the

overall heat transfer coefficient (U), where U is calculated as a function of water-side and air-side convection thermal resistances and base conduction thermal resistance (R_{cond}) as:

$$U = \frac{1}{\left(R_{conv,air} + R_{conv,water} + R_{cond}\right)A_{base}} \tag{8}$$

$$R_{cond} = \frac{H_{base}}{k_{solid}A_{base}} \tag{9}$$

where A_{base} is the base area ($A_{base} = L_{tot,water}L_{tot,air}$).

Then, NTU, the heat exchanger effectiveness (ε_{HX}), and heat exchanger capacity (Q) were calculated as [158]:

$$NTU = \frac{UA_{base}}{\min(C_{water}, C_{air})} \tag{10}$$

$$\varepsilon_{HX} = 1 - exp[(1/C_r)NTU^{0.22}\{\exp[-C_r(NTU)^{0.78}] - 1\}] \tag{11}$$

$$Q = \varepsilon_{HX}[\min(C_{water}, C_{air}) \times \left(T_{in,water} - T_{in,air}\right)] \tag{12}$$

where $C_{water} = \dot{m}_{water}c_{p,water}$, $C_{air} = \dot{m}_{air}c_{p,air}$, and $C_r = \frac{\min(C_{water},C_{air})}{\max(C_{water},C_{air})}$.

Lastly, the coefficient of performance (COP) and gravimetric heat transfer density ($Q/m\Delta T$) of the heat exchanger were evaluated as:

$$Q/m\Delta T = \frac{\mathrm{Q}}{m(T_{in,water} - T_{in,air})} \tag{13}$$

$$COP = \frac{Q}{\left(\frac{\Delta p_{air}\dot{m}_{air}}{\rho_{air}} + \frac{\Delta p_{water}\dot{m}_{water}}{\rho_{water}}\right)} \tag{14}$$

where m is the total mass of the heat exchanger and $\dot{m}$ is mass flow rate.

5.3. Manifold-Microchannel Heat Exchanger

5.3.1. Heat Exchanger Capacity Evaluation (Control volume method)

This section presents a control volume method to evaluate the capacity (Q), effectiveness (ε_{HX}), coefficient of performance (COP), and gravimetric heat transfer density ($Q/m\Delta T$) of a cross flow manifold-microchannel heat exchanger based on the known information on air-side and water-side inlet temperature ($T_{in,air}$ & $T_{in,water}$), base conductance ($h_{b,air}$ & $h_{b,water}$), mass flow rate ($\dot{m}_{air}$ & $\dot{m}_{water}$), and pressure drop (Δp_{air} & Δp_{water}). Base conductance is defined as heat capacity over base area (A_{base}) times the absolute values of temperature difference between the base (T_{base}) and inlet fluid (T_{in}) as shown below:

$$h_b = \frac{Q}{A_{base}|T_{base} - T_{in}|} \tag{15}$$

where $A_{base} = L_{tot,air} \times L_{tot,water}$.

First, on the water side, the performances of heat transfer coefficient (h_{water}) and pressure drop (Δp_{water}) of the rectangular channel were calculated by solving its corresponding Nusselt number (Nu) and friction factor (f) value using available correlations [157] and Eqs. (1)-(2) as for the case of conventional heat exchanger. Thereafter, the water-side base conductance ($h_{b,water}$) can be calculated as:

$$h_{b,water} = \frac{1}{R_{water} A_{base}} \tag{16}$$

$$R_{water} = R_{conv,water} + R_{cal,water} + \frac{R_{cond}}{2} \tag{17}$$

where $R_{conv,water}$ and R_{cond} are water-side convection thermal resistance and base conduction thermal resistance, which were evaluated using Eq. (3) and (9) respectively. It should be noted that the base thermal conduction resistance is divided into two parts. Half is considered as part of water-side total thermal resistance in Eq. (17), while the other half is included in air-side total thermal resistance. Lastly, unlike the calculation for U, which is based on the log mean temperature difference between the two fluids, base conductance calculation requires a caloric resistance ($R_{cal,water}$) term, as it is based on the temperature difference between inlet fluid and the base temperature. The caloric resistance represents the additional thermal resistance due to the change in the fluid temperature, as it is flow through the channel. It relates the inlet fluid temperature to the average fluid temperature. The water-side caloric resistance is calculated as:

$$R_{cal,water} = \frac{1}{2\dot{m}_{water} c_{p,water}} \tag{18}$$

For the air-side, a modified form of hybrid method developed by Arie *et al.* [106] was utilized to evaluate the air-side base conductance ($h_{b,air}$) and pressure drop (Δp_{air}) in the manifold-microchannel heat exchanger. A detailed description of the modified hybrid method will be explained in chapter 5.3.2.

The cross-flow ε-NTU method used to calculate the conventional heat exchanger capacity cannot be used to evaluate the capacity of the manifold-microchannel heat exchanger (Q).

This is because for the case of the manifold-microchannel, both water and air temperatures are constant in the y direction (Figure 36). As the majority of the heat transfer occurs on the microchannels, the heat transfer in the manifold can be assumed to be negligible. As a result, the air temperature in the manifold channel can also be assumed to be constant. As the feeding air temperature from the manifold channel to the microchannel is constant along the manifold channel flow length (the y direction in Figure 36) and the inlet water temperature is uniform in the y direction, both the air and water temperatures are always constant in the y direction. This condition is not purely a cross-flow arrangement in which the temperature varies in both the x and y directions. For this reason, a method based on energy and mass balances was developed to evaluate the capacity of the manifold-microchannel heat exchanger. The main assumption for this method is that the flow is uniformly distributed in all manifold channels, so that the performance of all stacked layers, in the z direction, is identical.

The heat exchanger capacity (Q) was calculated by first calculating the heat capacity in each stack (Q_{stc}). To do the calculation, first a single stack of the heat exchanger needs to be divided into N_{seg} segments, each consisting of a full inlet manifold channel and two half exit manifold channels as shown in Figure 36. By dividing the heat exchanger into multiple small segments, the base temperature in each segment can be assumed to be constant, so that an energy balance can be drawn to relate water-side and air-side base conductance as shown in Eqs. (21) and (22), which will be explained below. This assumption is valid, as both air and water temperatures are constant in the y direction, as mentioned previously, and the x direction length per segment is short. Heat flow rate for each segment can be calculated by performing an energy balance on that segment. In this

analysis it is assumed that the heat transfer in the x direction between two adjacent segments is negligible as compared to heat transfer in the z direction between the air- and water-sides. The detailed steps for the capacity, effectiveness, coefficient of performance, and gravimetric heat transfer density calculation are as follows:

1. Set i=1, $T_{in,water,1} = T_{in,water}$ and $T_{in,air,1} = T_{in,air}$
2. Perform an energy balance on the segment i by solving Eqs. (19)-(22) to solve for heat capacity (Q_i), air exit temperature ($T_{out,air,i}$), water exit temperature ($T_{out,water,i}$), and base temperature ($T_{base,i}$) corresponding to segment *i,* where $h_{b,water}$ and $h_{b,air}$ are known variables corresponding to air-side and water-side base conductance calculated previously, and N_{stc} is total number of stacks.

$$Q_i = \frac{\dot{m}_{water}}{N_{stc}} c_{p,water}\left(T_{in,water,i} - T_{out,water,i}\right) \tag{19}$$

$$Q_i = \frac{\dot{m}_{air}}{N_{seg} \times N_{stc}} c_{p,air}\left(T_{out,air,i} - T_{in,air,i}\right) \tag{20}$$

$$Q_i = h_{b,water} \frac{A_{base}}{N_{seg}} \left(T_{in,water,i} - T_{base,i}\right) \tag{21}$$

$$Q_i = h_{b,air} \frac{A_{base}}{N_{seg}} \left(T_{base,i} - T_{in,air,i}\right) \tag{22}$$

3. Update i value: $i = i + 1$
4. Set $T_{in,water,i} = T_{out,water,i-1}$ and $T_{in,air,i} = T_{in,air}$
5. Repeat steps 2-4 until $i = N_{seg}$
6. Calculate the total capacity for each stack as: $Q_{stc} = \sum_{i=1}^{N_{seg}} Q_i$

7. Calculate the total capacity of the heat exchanger as: $Q = N_{stc}Q_{stc}$.
8. Calculate the heat exchanger effectiveness, coefficient of performance, and gravimetric heat transfer using Eq. (12)-(14).

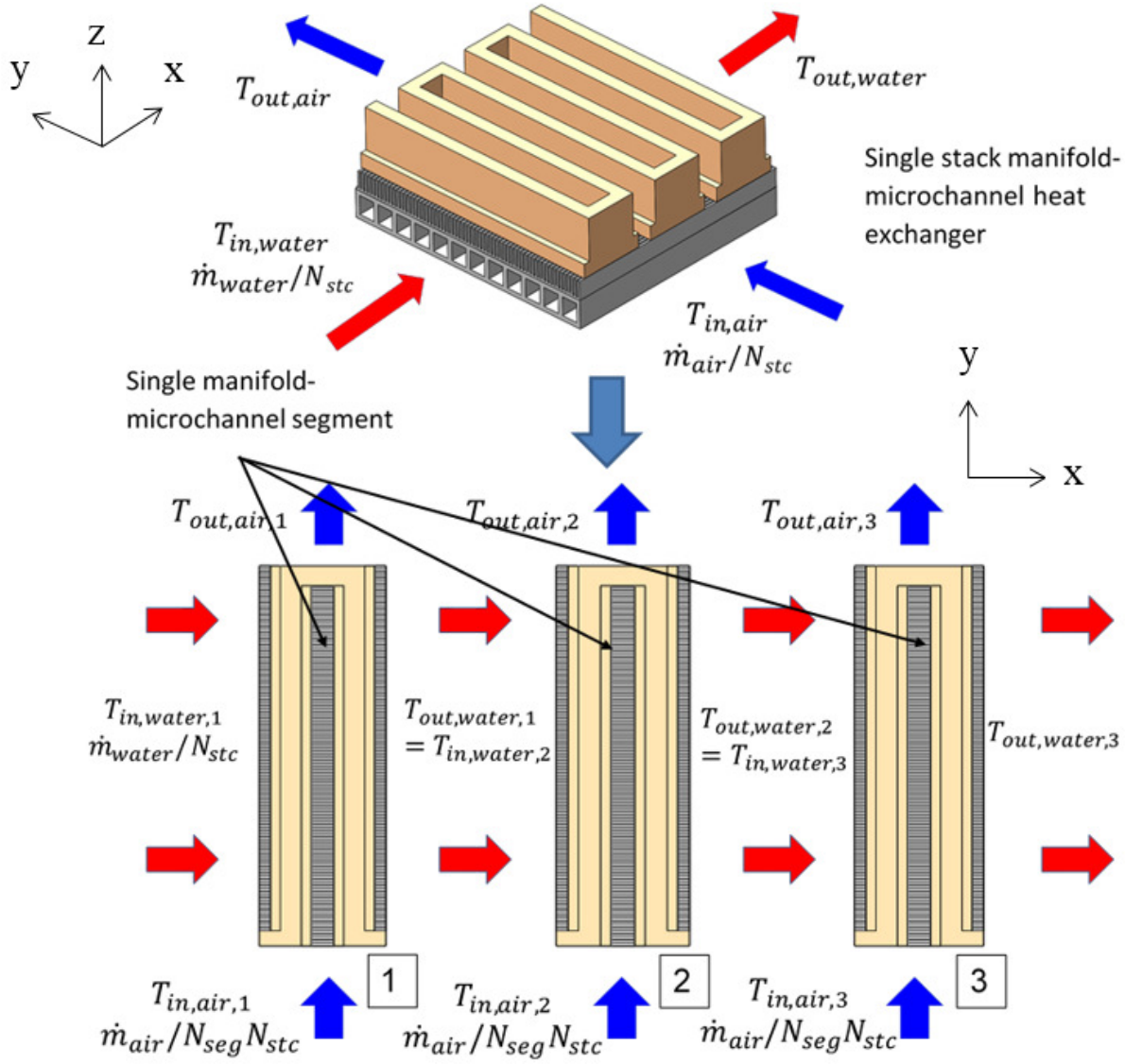

Figure 36: Control volumes for performance evaluation of cross flow manifold-microchannel heat exchanger

5.3.2. Modified Hybrid Method

For the air-side, Arie *et al.* has developed a hybrid method capable of evaluating the air-side base conductance ($h_{b,air}$) (listed as base heat transfer coefficient in Arie *et al.*) and pressure drop in manifold-microchannel heat exchanger in much shorter time than a full CFD simulation, which makes it suitable for optimization problem where hundreds of different geometries need to be evaluated [106]. Based on the method, a single manifold-microchannel model CFD simulation, as shown in Figure 37, was utilized to evaluate air-side base conductance of the manifold-microchannel heat exchanger. The main assumptions are uniform flow distribution in all microchannels and that heat transfer in manifold can be neglected compared to the heat transfer in the microchannels (but the pressure drop cannot). To assure a uniform flow distribution in the microchannels, a constraint is imposed to limit the ratio between the standard deviation of the flow in all microchannels and its mean value to be less than 30%. For the pressure drop calculation, the pressure drop across the microchannel was evaluated by a single manifold-microchannel model CFD simulation, while the pressure drop in the manifold channels was evaluated by solving the 1-D differential equation derived from momentum and mass balance equations in manifold channels (see Ref [106] for further details). To be noted, even though the single manifold-microchannel model in Figure 37 includes the inlet and exit manifold channel, their function is to limit the entrance and exit effect to the flow in the microchannel. The calculation of pressure drop in the manifold channel is more complex due to the deceleration and acceleration of the flow in the inlet and exit manifold channel because of the diverging and combining flow to and from the microchannel all across the manifold channels.

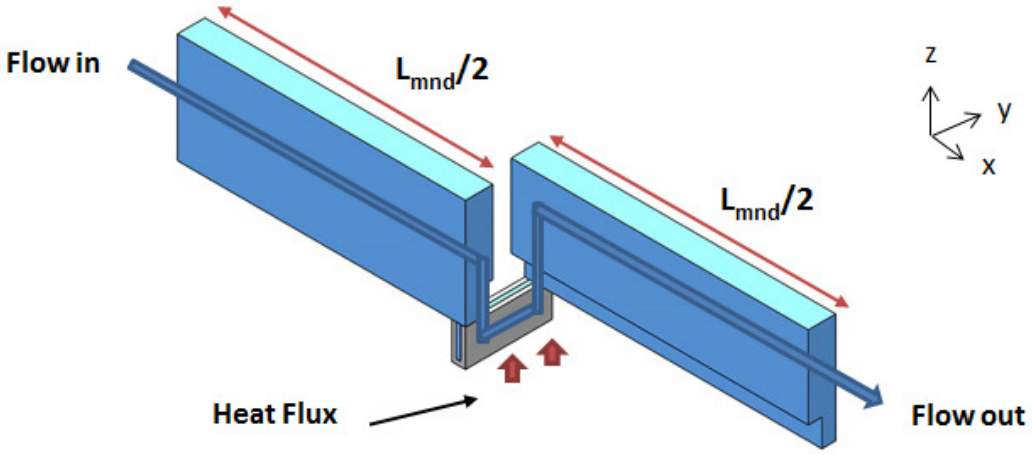

Figure 37: Single manifold-microchannel model.

The hybrid method used to calculate the manifold pressure drop assumes that the inertia term in the momentum equation in the manifold channel can be ignored in comparison with the frictional term [106]. This assumption holds for the case of low Reynolds numbers where the friction term is more dominant than the inertia term, but as the flow becomes turbulent the effect of the inertia term can no longer be ignored. A study using five full CFD models has shown that for the case of Reynolds numbers between 3,000 to 8,000, ignoring the inertia term can cause on average about 25% deviation in pressure drop calculation. As a result, a modified hybrid method was developed that considers the effect of the inertia term. However, due to the assumption that the heat transfer is mainly happening in the microchannels and the flow distributes evenly in all microchannels, this modification in the manifold-channel momentum equation will not affect the way heat transfer performance in the microchannel is calculated. As a result, the air-side base conductance calculation remains unchanged.

By considering the effect of the inertia term, normalized mass balance and momentum equations on the inlet manifold channel (subscript 1) and exit manifold channel (subscript

2) can be derived as shown in Eqs. (23) - (27) by assuming one-dimensional flow in both manifold channels:

$$\frac{dv_1'}{dx'} = -\frac{2nA_{chn}}{v_{in}A_{mnd}}v_{chn} \tag{23}$$

$$\frac{dv_2'}{dx'} = \frac{2nA_{chn}}{v_{in}A_{mnd}}v_{chn} \tag{24}$$

$$2v_1'\frac{dv_1'}{dx'} + \frac{dp_1'}{dx'} + \left(\frac{(fRe)_{mnd,1}\Gamma_{mnd}L_{tot,air}\mu}{2A_{mnd}\rho D_{mnd}v_{in}}\right)v_1' + \frac{2A_{chn}n\beta_1}{A_{mnd}}v_{chn}'v_1{}' = 0 \tag{25}$$

$$2v_2'\frac{dv_2'}{dx'} + \frac{dp_2'}{dx'} + \left(\frac{(fRe)_{mnd,2}\Gamma_{mnd}L_{tot,air}\mu}{2A_{mnd}\rho D_{mnd}v_{in}}\right)v_2' - \frac{2A_{chn}n\beta_2}{A_{mnd}}v_{chn}'v_2{}' = 0 \tag{26}$$

$$v_1' + v_2' = 1 \tag{27}$$

where v_{in} and v_{chn} is the inlet fluid velocity to the manifold channel and average flow velocity in the microchannels respectively, Γ_{mnd} is manifold channel perimeter, n is the total number of microchannels per pass, A_{mnd} and A_{chn} are manifold channel and microchannel cross section areas, respectively, p_1' and p_2' are normalized pressure ($p' = \frac{p}{\rho v_{in}^2}$) at the inlet and exit manifold channels, respectively, and v_1' and v_2' are normalized velocities ($v' = v/v_{in}$) at the inlet and exit manifold channels, respectively. Note the subscripts 1 and 2 are represented as inlet manifold channel and exit manifold channel, respectively. Lastly, as a mass conservation between the inlet and exit manifold channels, the sum of the normalized velocities in both manifold channels must be equal to one, as shown in Eq. (27).

The main difference between this set of equations and those originally given in Arie et al [106] is the additional inertia terms appeared as the last term in the momentum Eqs. (25) - (26) where β_1 and β_2 are pressure regain and loss coefficient. In addition, unlike for the

case of laminar flow where $(fRe)_{mnd}$ depends only on aspect ratio between width and height of the manifold channel, for turbulent flow $(fRe)_{mnd}$ is a function of both aspect ratio and flow rate in its respective manifold channel. As the velocity in the inlet and exit manifold channel are not the same, $(fRe)_{mnd}$ terms in the inlet and exit manifold channels must be evaluated separately. $(fRe)_{mnd}$ is solved using Petukhov's correlation [159] for smooth turbulent flow, where f is given as:

$$f = \left(0.79ln\left(Re_{D_{mnd}}\right) - 1.64\right)^{-2} \tag{28}$$

By combining Eqs. (25) - (27), v_1', can be expressed as:

$$\begin{aligned} 2\frac{dv_1'}{dx'} + \frac{d(\Delta p_{12})'}{dx'} & \\ - \left(\frac{\Gamma L_{mnd}\mu}{2A_{mnd}\rho D_{mnd}v_{in}}\right)\left((fRe)_{mnd,2}(1 - v_1') - (fRe)_{mnd,1}v_1'\right) & \\ - \frac{2A_{chn}n}{A_{mnd}}v_{chn}'(v_1'(\beta_2 - \beta_1) - \beta_2) = 0 & \end{aligned} \tag{29}$$

where $\Delta p'_{12}$ ($\Delta p'_{12} = p'_2 - p'_1$) is normalized pressure drop between inlet manifold channel (surface 1) and exit manifold channel (surface 2) as seen in Figure 38, which can also be expressed in the form of $(fRe)_{12}$, friction factor times Reynolds number between both manifold channel surfaces.

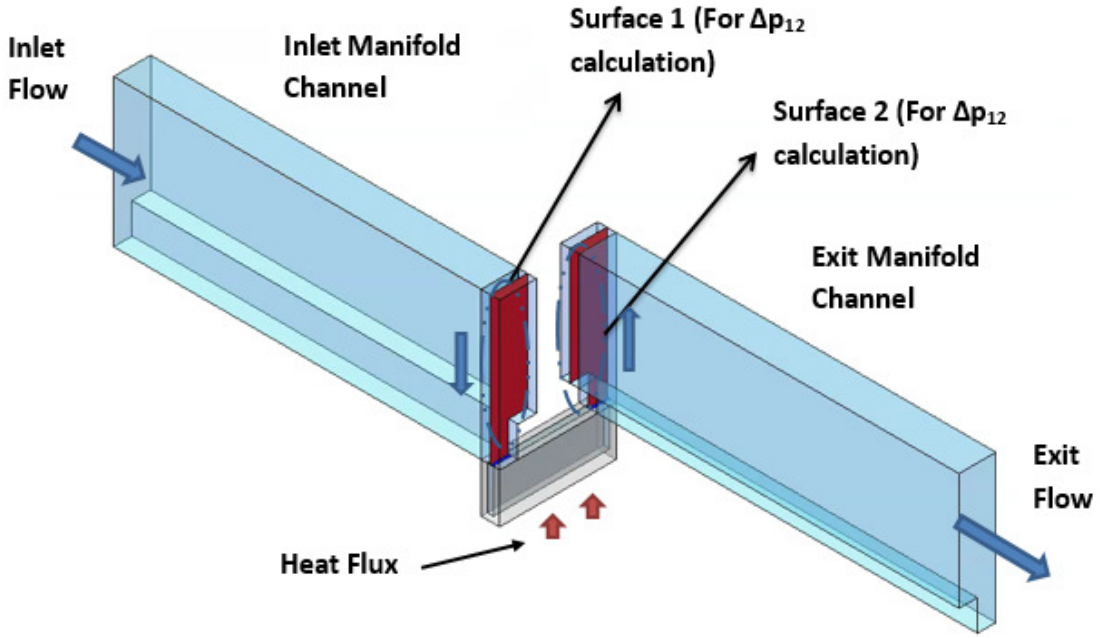

Figure 38: Single manifold-microchannel model control volume

Based on our previous investigation, as a first order approximation for the range of parameters in our study, there is a linear relationship between $(fRe)_{12}$ and flow velocity in the microchannel (v_{chn}) in the form as:

$$(fRe)_{12} = av_{chn} + b \tag{30}$$

where a and b are two geometry dependent constants which are calculated from a CFD simulation of single manifold-microchannel model by calculation of $(fRe)_{12}$ for two different v_{chn} values (see Ref [106] for further details). Eq. (30) can then be expressed in term of $\Delta p'_{12}$ and v'_{chn} as:

$$\Delta p'_{12} = \left(a(v'_{chn})^2 + b\frac{v'_{chn}}{v_{in}}\right)\left(\frac{2L_{chn}\mu}{D_{chn}^2\rho}\right) \tag{31}$$

where L_{chn} is the microchannel flow length defined as $L_{chn} = t_{mnd} + W_{mnd-chn}$ and D_{chn} is hydraulic diameter of the microchannel defined as $D_{chn} = \frac{2W_{chn}H_{chn}}{W_{chn}+H_{chn}}$. (Note: the derivation of the geometrical variables are shown in Figure 27)

By combining Eqs. (23), (29), and (31), a new ordinary-differential equation that governs the normalized velocity at inlet manifold (v_1') is calculated as:

$$\frac{d^2v_1'}{dx'^2}\left(K_3\frac{dv_1'}{dx'}-1\right)+2K_1\frac{dv_1'}{dx'}-K_1K_2\left((fRe)_{mnd,2}(1-v_1')-(fRe)_{mnd,1}v_1'\right) + K_1\frac{dv_1'}{dx'}(v_1'(\beta_2-\beta_1)-\beta_2)=0 \tag{32}$$

where:

$$K_1 = \left(\frac{2nA_{chn}\rho v_{in}}{A_{mnd}}\right)\left(\frac{D_{chn}^2}{2\pi L_{chn}b}\right) \tag{33}$$

$$K_2 = \frac{\Gamma_{mnd}L_{mnd}\mu}{2A_{mnd}\rho D_{mnd}v_{in}} \tag{34}$$

$$K_3 = \left(\frac{a}{b}\right)\left(\frac{A_{mnd}v_{in}}{nA_{chn}}\right) \tag{35}$$

The boundary condition of the differential equation is as follows:

$$v_1'(x'=0)=1 \text{ and } v_1'(x'=1)=0 \tag{36}$$

Note that if $\beta_1$and β_2 are set to zero (i.e. setting zero inertia term), Eq. (32) is reduced to the form proposed by Arie et. al. [106] for the case of laminar flow in the manifold channels. For the manifold-microchannel heat exchanger, the values of $\beta_1$and β_2 are set to 1 (for the case of short spacing between branches, which is appropriate for manifold-microchannel where the spacing between each channel is very short) and -0.8 (for large

diameter ratios between manifold channel and microchannel), respectively, as mentioned by Bajura [160]

The differential equation in Eq. (32) can be solved numerically using a Matlab toolbox. Thereafter, the microchannel velocity (v_{chn}) can be evaluated by inserting the v_1' expression back to Eq. (23), and pressure at the inlet manifold channel (p_1) can be calculated by inserting the v_1' and v_{chn}' expressions back into Eq. (25). Lastly, the total pressure drop (Δp_{tot}) is calculated as the sum of the total pressure drop along the inlet manifold ($\Delta p_1 = p_1(x' = 0) - p_1(x' = 1)$) and the pressure drop at the last microchannel (Δp_{chn}) as:

$$\Delta p_{tot} = \Delta p_1 + \Delta p_{chn}(x' = 1) \tag{37}$$

The single manifold-microchannel simulations were solved using commercial CFD code Fluent 14.5 and mesh generation software Gambit 2.4.6. There were two goals of this modeling. The first was to determine the heat transfer coefficient, which was calculated by assuming the mass flow rate is uniformly distributed over all microchannels. The second goal was to determine coefficients *a* and *b* given in Eq. (30). To do so, it is necessary to calculate pressure drop (or $(fRe)_{12}$) for two different microchannel velocities (v_{chn}) and determine those coefficients.

The computational domain and boundary condition of the single manifold-microchannel model are shown in Figure 39. The manifold channel inlet was set to mass flow rate boundary condition and constant inlet temperature. The manifold channel outlet boundary condition was set to a constant pressure. The boundary condition on the base was set to a uniform constant temperature. To reduce the computational domain, only a half chapter of the manifold was modeled, and symmetry boundary condition was applied. Before the

simulation was started, a grid independency study was performed to find the minimum computational element number that provides less than 1% error while limiting the computational time. It was concluded that about 250,000 computational elements could be sufficient for this purpose.

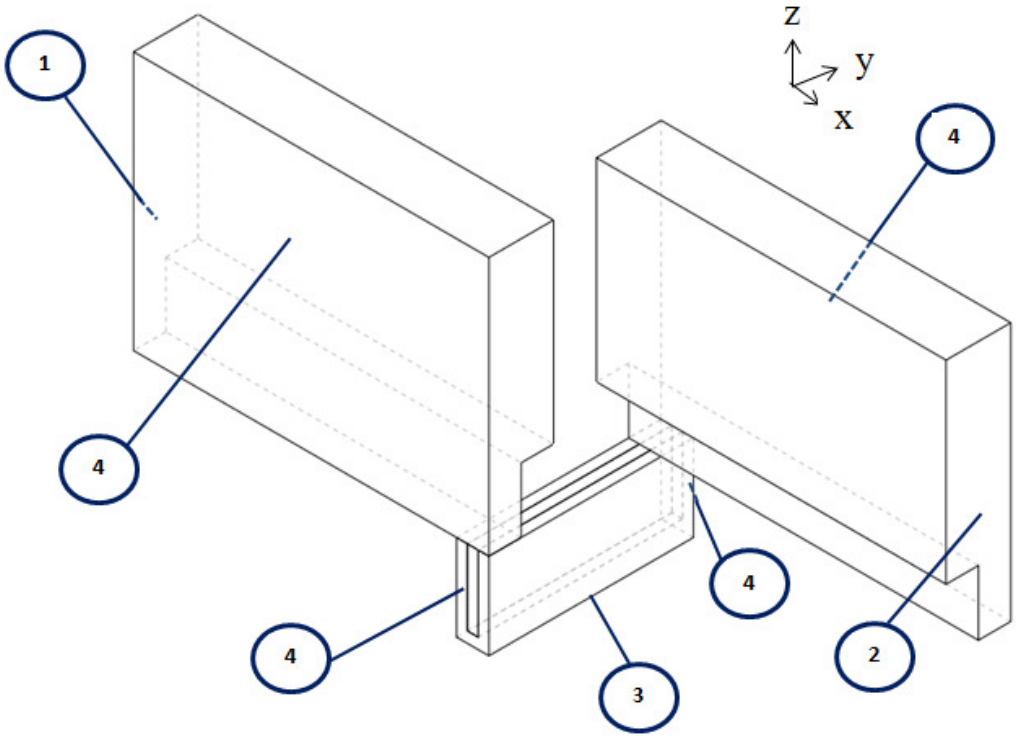

Figure 39: Computational domain and boundary conditions: mass flow inlet and constant temperature (1), constant pressure outlet (2), constant surface temperature (3), symmetry plane (4), and insulated wall surface for all other boundaries

5.3.3. Modified Hybrid Method Validation

In order to validate the pressure drop calculation using the modified hybrid method, five complete single pass single manifold (SPSM) models were created with 2,500,000 elements each and solved numerically using commercial CFD software Fluent 14.5 (Figure 40 shows an example of one of the SPSM models). By using the modified hybrid

method the number of element size can be reduced by a factor of 10, which significantly reduces computational time. Pressure drop between inlet and outlet for each one of the models was calculated for Reynolds numbers varying from 1,000 to 8,000 to be compared with the corresponding values calculated using the hybrid method and modified hybrid method. The calculated pressure drops using all three methods are compared in Figure 41 for one of the selected models.

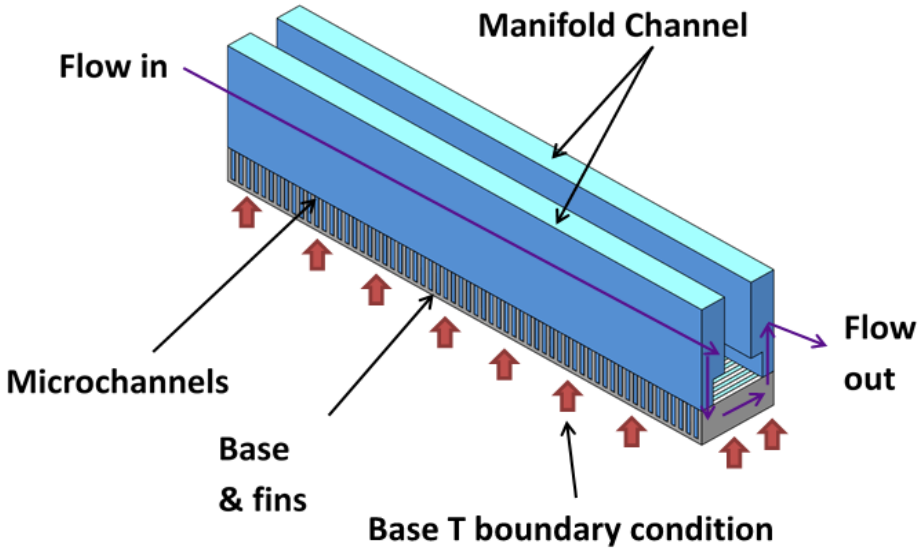

Figure 40: SPSM model for full CFD simulation

Comparing the results shown in Figure 41, pressure drop calculated using the modified hybrid method shows good agreement with pressure drop calculated using full CFD modeling of the SPSM model. In the laminar region, pressure drops calculated using all three methods are close to each other. This is because at low Re, the pressure drop is dominated by the friction force, causing the hybrid method results to be close to the ones obtained by the full CFD method. But as Re increases, the inertia effect becomes significant, which causing deviation in pressure drop calculations. The modified hybrid method, which takes into account the inertia effect, shows better accuracy at large Re. A

similar trend is noted for the other four models. From this study it was concluded that on average, for the range of Re between 1,000 to 8,000, the accuracy of pressure drop calculation can be improved from 20% to 5% by switching from the hybrid method to the modified hybrid method.

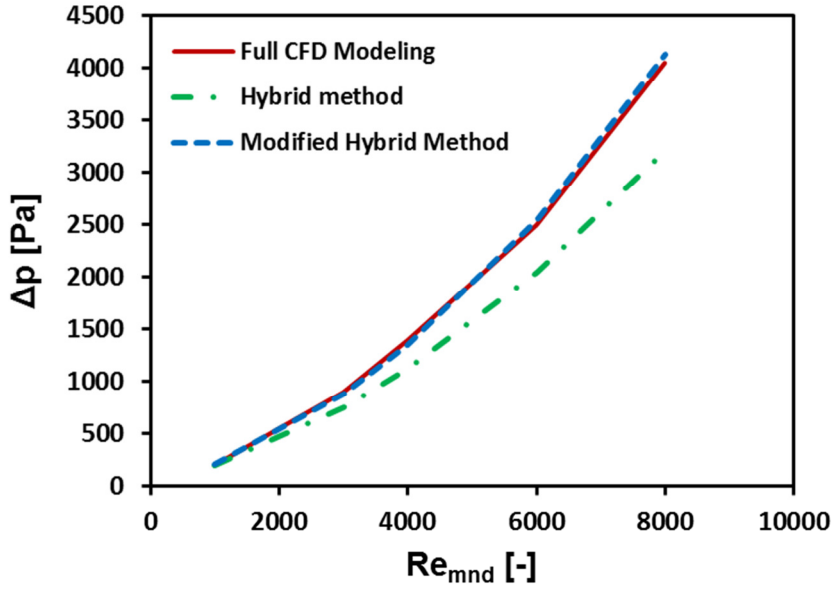

Figure 41: Full CFD modeling versus hybrid and modified hybrid methods

For further validation, the modified hybrid method and hybrid method results were compared with experimental data for the case of the manifold-microchannel plate heat exchanger as mentioned in [106]. The comparison plot is shown in Figure 42. Comparing the experimental data to the modified hybrid method results, on average there is a 24% deviation between both results. This is an improvement compared to the hybrid method, which yielded 31% deviation compared to the experimental data. As mentioned in [106], there are other factors such as imperfections in microchannel fabrication and non-uniform flow in all manifold channels that can cause the deviation between the numerical and experimental results. Considering these factors, it can be concluded that

the modified hybrid method can improve pressure drop prediction for the manifold-microchannel heat exchanger over the hybrid method.

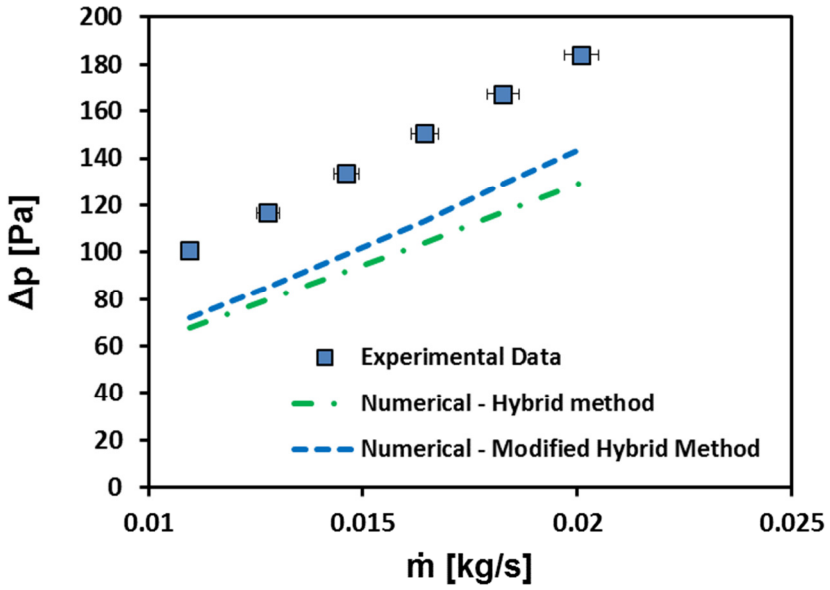

Figure 42: Experimental vs. numerical

5.4. Polymer Heat Exchanger

Since there is no analytical method in the literature to evaluate the performance of the polymer heat exchanger shown in Figure 28, the heat exchanger was simulated using a CFD model of a single layer as shown in Figure 43. For such purpose commercial CFD software (Fluent 14.5) and a mesh generation code (Gambit 2.4.6) were used.

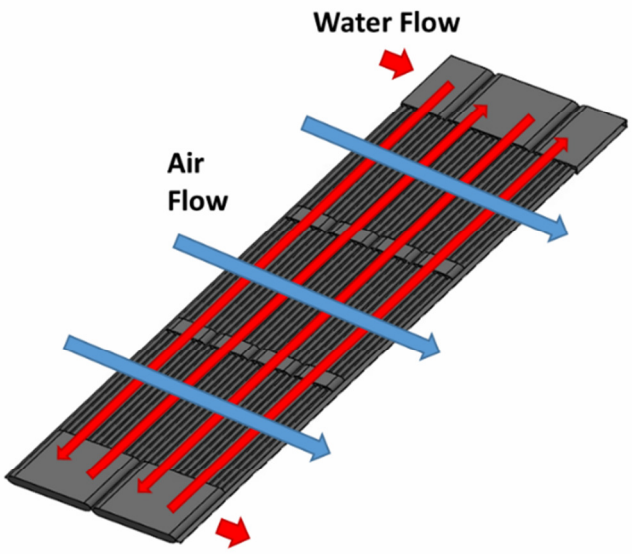

Figure 43: Single layer polymer heat exchanger

5.5. Summary

In this chapter the numerical modeling to compute the performances of both the conventional and advance heat exchangers were discussed in detailed. The conventional heat exchanger performances were calculated using an analytical correlation and ε-NTU method. For the manifold-microchannel heat exchanger (advanced metallic), the modified hybrid method was derived to evaluate air-side performance, while the overall heat exchanger capacity was evaluated using a control volume method. Lastly, for the polymer heat exchanger, CFD simulation was performed to evaluate its performance.

Chapter 6: Design Optimization and Selection

6.1. Introduction

In this chapter multi-objective optimization was performed for both the conventional and advanced metallic heat exchangers (manifold-microchannel heat exchanger) to find optimum designs that met all of the design requirements as listed in chapter 3.2. The first purpose of this optimization was to compare the performance of the manifold-microchannel with conventional heat exchangers. The second purpose was for design down selection. An optimum design that met all of the design requirement was selected and scaled down so that it could be fabricated and tested in the lab. For the polymer heat exchanger, a parametric study was performed to calculate a geometry that met all of the performance requirements, and then similarly the selected design was scaled down for fabrication and testing.

6.2. Optimization Method

6.2.1. Conventional Heat Exchanger Optimization

A combination of an Ɛ-constrained and genetic algorithm was utilized for the conventional heat exchanger optimization. The Ɛ-constrained method is based on converting a multi-objective problem into a single-objective constrained optimization problem by setting all but one of the objectives as constraints. The method has been widely used, such as in [161-163]. The single objective problems were then solved using the genetic algorithm. The genetic algorithm is a meta-heuristic approach which adapts the principle of natural evolution into the optimization process. The method is based on crossover and mutation of the populations where only superior offspring is kept. The process is repeated for several generations until only the most superior offspring is left on

the population. The method was first developed by John Holland in the 1970 [164], and since then it has become one of the most widely used optimization methods [12, 165-168]. By running the optimization code multiple times and updating the value of the constraints after every iteration, the optimized solution of the multi-objective optimization can be obtained. For the optimization process, the performances of the conventional heat exchanger were solved using the method explained in chapter 5.2.

6.2.2. Manifold-microchannel Heat Exchanger Optimization

Unlike conventional heat exchanger surfaces where the performance can be evaluated using available analytical correlations, the manifold-microchannel heat exchanger evaluation required solving the modified hybrid method, which involved solving a CFD simulation as previously explained in chapter 5.3.2. Solving the CFD simulation can be several orders of magnitude longer than the analytical solution solver. As a result, in order to cut computational times, approximation-assisted optimization was applied for the optimization process. This method reduces the number of CFD simulations by using a metamodel derived from sampling results to predict the behavior of the system. The method is divided into the following four main stages:

1. *Design of Experiment (DOE)*: The purpose of DOE is to obtain a limited number of sampling data across the feasible domain for the metamodel. The space filling method developed by Aute et al. [169], which is based on the maximum entropy method, was used to select the initial sampling points. The DOE was run for the manifold-microchannel on the air side, and the water side, which consists of rectangular channels, can be solved easily using an analytical solution. For each

sampling point, the objective functions were directly calculated using the modified hybrid method.

2. *Metamodel creation*: The metamodel works as an approximation function to predict the response of the system at unobserved points over the feasible domain by using the known information at the sampling points obtained from the DOE (observed points). The Kriging-based metamodel was chosen because of its ability to solve non-linear problems that depend on multiple variables. Kriging-based metamodels have been widely used to approximate a system behavior as used in [12, 170-173]. Dace, a Kriging-based metamodel toolbox developed by Lophaven et al. [174], was utilized for this purposed. The number of required CFD simulations can be significantly reduced by the use of metamodel approximation. For example, 200,000 numbers of solutions (unobserved points) can be provided by the metamodel based on just 1,000 sampling points (observed points). The metamodel was created to predict the manifold-microchannel performance based on the sampling points solved using the modified hybrid method.
3. *Multi-objective optimization*: The multi-objective optimization was performed using the Ɛ-constrained and genetic algorithm, the same method explained in chapter 6.2.1., by using the metamodel function as an input for the air-side performances (manifold-microchannel), while the water-side performances (rectangular channels) were solved using analytical solutions. The overall performances of the heat exchanger were solved using the methods explained previously in chapter 5.3.1.

4. *Metamodel validation:* Since the metamodel is an approximation of the system behavior, the optimum points obtained must be validated. This validation was performed by calculating the actual air-side performance of the optimum points using the modified hybrid method. Then, the optimum points were recalculated using the actual air-side performance rather than the one predicted by the metamodel. Thereafter, the Mean Absolute Error (MAE) was calculated with respect to optimum points calculated based on the predicted air-side performance. In the case of large MAE, the air-side metamodel was recreated by including the validation points as additional sampling points and repeating the steps 2-4 of the process, from which a new set of optimum points was calculated. By adding additional sampling points, the metamodel prediction becomes more accurate for the next iteration. The process was repeated until a sufficiently low MAE was obtained. For this optimization, the MAE was targeted to be less than 3% for all of the objective functions. This value is an arbitrary criterion chosen because for smaller target ranges the amount of required sampling points will increase significantly and the optimization process becomes computationally expensive.

   A flowchart summarizing the optimization methodology is reported in Figure 44.

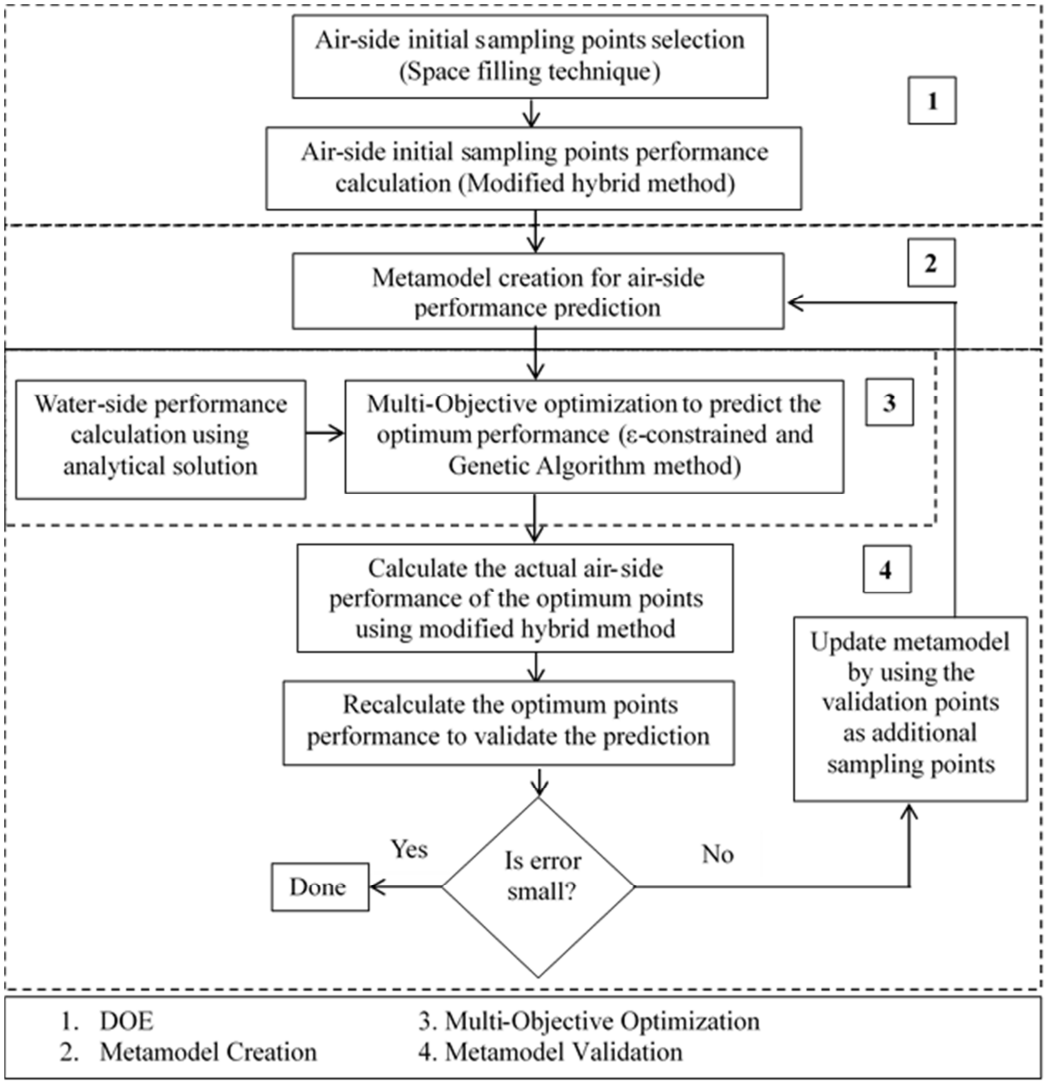

Figure 44: Optimization flow-chart

6.3. Metallic Heat Exchanger Design Optimization

6.3.1. Optimization Objectives and Constraints

The optimization objective is to maximize gravimetric heat transfer density $[Q/(m\Delta T)]$ and normalized coefficient of performance $[COP/\Delta T]$, where m is mass of the heat exchanger, ΔT is temperature difference between inlet water and air ($\Delta T = T_{in,water} - T_{in,air}$), and COP is coefficient of performance. The coefficient of performance is

normalized with respect to temperature difference between inlet water and air (ΔT) so that its results are independent of temperature boundary conditions.

The heat exchanger material is stainless steel, as it is one of the most common material for air-water heat exchanger. The geometrical and flow constraints for both conventional and manifold-microchannel heat exchangers are listed in Table 11, while the performance constraints are the same as those listed previously in Table 7. Please refer to Figure 26 and Figure 27 for descriptions of each geometrical variable of the conventional and manifold-microchannel heat exchanger, respectively. For the conventional heat exchanger, the air-side geometry is fixed to the 22 commercially available surfaces as shown previously in Table 8. On the other hand, the manifold-microchannel heat exchanger geometrical constraints (both air and water sides) are adopted from the manufacturing limits of direct metal laser sintering (DMLS). For a fair comparison, the same water-side constraints as the manifold microchannel heat exchanger are applied for the water-side conventional heat exchanger constraints.

Out of all the geometrical constraints listed, air-side fin thickness ($t_{fin,air}$) and manifold thickness (t_{mnd}) are the most important variables, as both directly affect heat exchanger mass. Both variables should be as small as possible to minimize heat exchanger mass. However, manufacturing very thin fins can be challenging. To study the effect of fin thickness manufacturing constraints on heat exchanger performance, three different fin thickness limits are considered: $t_{fin,air} > 0.3$ mm (based on the recommended limit for safe manufacturing), $t_{fin,air} > 0.15$ mm (based on the technological limit), and $t_{fin,air} > 0.05$ mm (based on future technology projection). Three different manifold thickness limits are also considered: $t_{mnd} > 0.5$ mm (based on the recommended limit for safe

manufacturing), $t_{mnd} > 0.3$ (based on the technological limit), and $t_{mnd} > 0.15$ mm (based on future technology projection). The manufacturing limits are adopted based on information provided by one of the manufacturers [134].

The optimizations were run for five different combinations of microchannel fin thickness and manifold thickness as shown in Table 12. Case 3 (Man-Mchn 3) is the baseline case when both thickness are at the technological limit. Case 1 and Case 2 (Man-Mchn 1 & 2), are for the case when the microchannel fin thickness or manifold thickness are less than the technological limit to study the future technology projection. Lastly, Case 4 and Case 5 (Man-Mchn 4 & 5), are for the case when the microchannel fin thickness or manifold thickness is higher than the technological limit to study the performance penalty if the fins need to be made thicker for more robust manufacturing.

It should be noted that the manifold thickness limitation is higher than that of fin thickness. The reason for this is that the height of the manifold ($H_{mnd,top}$) needs to be larger than the microchannel height ($H_{chn,air}$) to accommodate the larger flow rate. A fin with a large aspect ratio between its height and thickness is more difficult to build. As a result, the manifold needs to be thicker than the microchannel fins.

Lastly, as the modified hybrid method proposed in chapter 5.3. is working under the assumption of uniform flow in all microchannels. A constraint to limit the flow maldistribution is needed. A factor, F, defined as the ratio of the standard deviation of mass flow rate among all the microchannels to the mean microchannel mass flow rate (Eq. (39)), was introduced to investigate the uniformity of the mass flow rate over all of the microchannels.

$$F = \frac{\sqrt{\frac{1}{n}\sum_{i=1}^{n}\left(\dot{m}_{chn,i} - \overline{\dot{m}_{chn}}\right)^2}}{\overline{\dot{m}_{chn,i}}} \tag{38}$$

From the definition of F, it was concluded that the higher its value, the larger the maldistribution. In order to minimize maldistribution, F was constrained to be less than 0.3.

Table 11: Optimization constraints

	Conventional HX	**Manifold-Microchannel HX**
Air-Side		
$Re_{mnd,air}$	100-8,000	
$H_{chn,air}$	—	0.2-5 mm
$W_{chn,air}/t_{fin,air}$	—	1-5
$W_{chn,air}$	—	0.05-0.5 mm
$W_{mnd-chn}$	—	0.4-6 mm
$H_{mnd,top}$	—	1-10 mm
n	—	50-1000
$W_{in}/W_{mnd-chn}$	—	0.1-0.9
$t_{fin,air}$	—	≥ (0.05, 0.15, 0.3) mm
$H_{mnd,bottom}$	—	0.3 mm
t_{mnd}	—	≥ (0.3, 0.5, and 0.7) mm
H_{base}	0.3 mm	
Water-Side		
Re_{water}	25-10,000	
$H_{chn,water}$	1-25 mm	
$W_{chn,water}$	0.5-25 mm	
$t_{fin,water}$	0.2-5 mm	
$L_{tot,air}$	20-200 mm	
$L_{tot,water}$	0.2-12 m	

Table 12: Manifold-microchannel optimization cases

Symbol	**Microchannel fin thickness limit (mm)**	**Manifold thickness limit (mm)**
Man-Mchn 1	0.05	0.3
Man-Mchn 2	0.15	0.15
Man-Mchn 3	0.15	0.3
Man-Mchn 4	0.15	0.5
Man-Mchn 5	0.3	0.3

6.3.2. Optimization Results - 12.2 MW Heat Exchanger

The manifold-microchannel heat exchanger optimization results are shown in Figure 37 for all five cases as defined in Table 12. Each data point corresponds to a certain heat exchanger optimized design independent from neighboring points. As expected, the results indicate that with increasing compactness of the heat exchanger (i.e. higher $Q/(m\Delta T)$), the required pumping power increases as well (i.e. $COP/\Delta T$ reduces). Comparison of the results for different microchannel fin thicknesses (cases 1, 3, and 5) clearly shows that the heat exchanger performance is improved significantly with thinner fins, as thinner fins equal less mass, although thinner fins reduce fin efficiency as well. Reducing the microchannel fin thickness from 150 µm to 50 µm can yield 20-40% increase in $Q/(m\Delta T)$ for the same $COP/\Delta T$. But, increasing the thickness to 300 µm reduces $Q/(m\Delta T)$ by 40-60%. A similar trend is also observed for manifold thickness (cases 2, 3, and 5), for the same reason. Reducing the manifold thickness from 300 µm to 150 µm increases $Q/(m\Delta T)$ by 10-30% for the same $COP/\Delta T$. However, increasing the thickness to 500 µm causes 10-30% reduction in $Q/(m\Delta T)$. Currently, case 3 is the limit of the design that can be built using current additive manufacturing technology based on DMLS technology. However, as additive manufacturing technology is one of the fastest growing technologies, it is expected that its manufacturing limitations will improve in the near future. These projected manufacturing limits will allow for the manufacturing of thinner fins, which will yield a significant performance improvement.

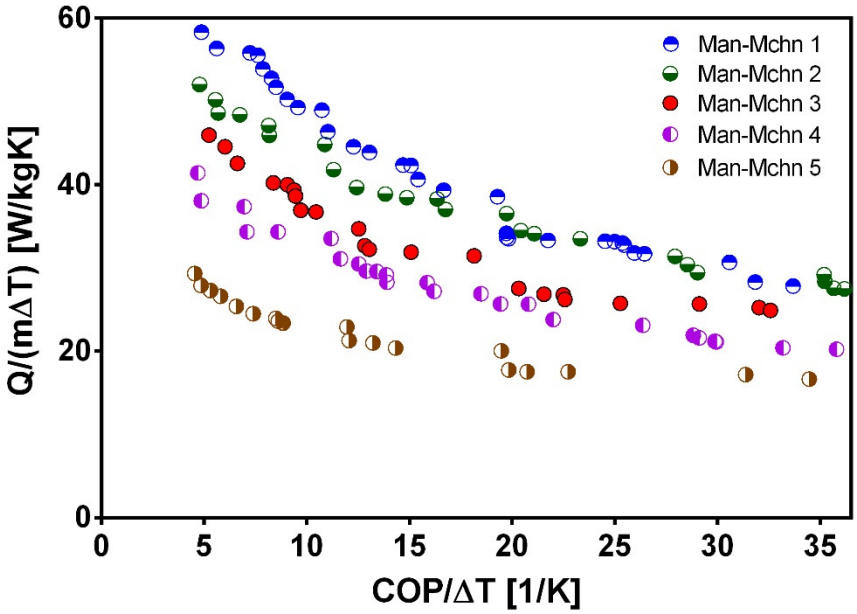

Figure 45: Manifold-microchannels optimization results: the effect of fin and manifold thicknesses

The optimization results for conventional heat exchangers are shown in Figure 46 for all surfaces. Comparing the optimizations results for all conventional surfaces (Figure 46 (a)-(e)), the strip-fin-plate-fin surface (SFPFS) heat exchanger shows the highest performance, followed by the pin-fin-plate-fin-surface (PFPFS) heat exchanger, and then by the wavy-fin-plate-fin-surface (WFPFS) heat exchanger. The louvered-plate-fin-surface (LPFS) heat exchanger performance is similar to the plain-plate-fin-surface (PPFS) heat exchanger in low $COP/\Delta T$. However, for higher $COP/\Delta T$, LPFS is superior. The optimization results for conventional heat exchangers results are directly compared with manifold-microchannel case 3 results, which are also shown in Figure 46 (a)-(e). Comparing the performance of the manifold-microchannel and conventional heat exchanger, the manifold-microchannel outperforms almost all of the conventional surfaces studied for the entire range of $COP/\Delta T$. Only the strip-fin case 6 (SFPF 6) has performance close to the manifold-microchannel. However, strip-fins are not the type of

heat transfer surface used for power plant cooling. The most common type of surfaces used for power plant cooling are plain surface and wavy-fin surface, all of which have significantly lower performance than the manifold-microchannel.

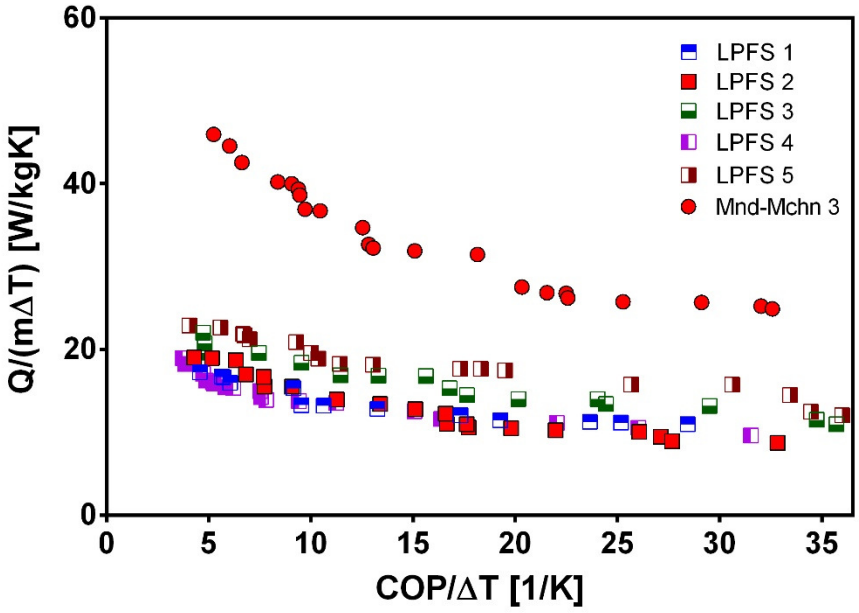

(a)

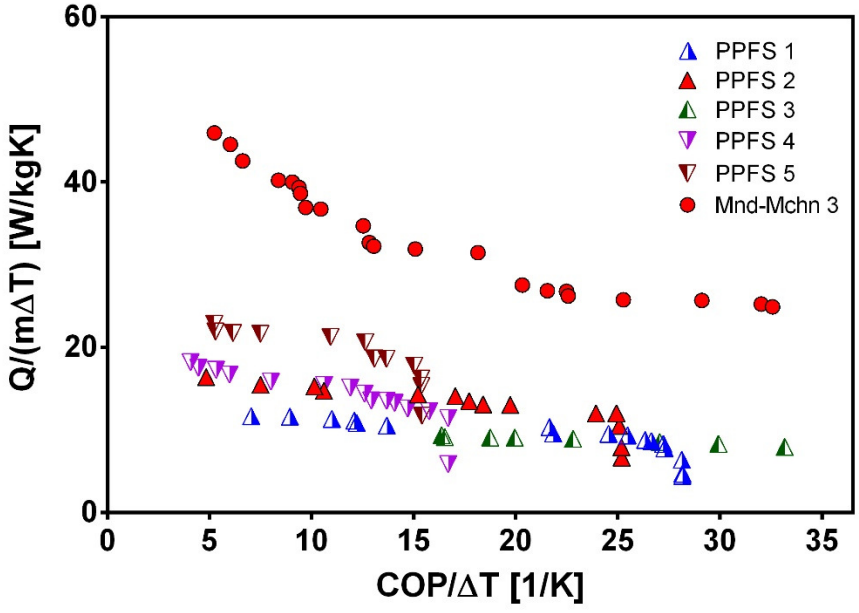

(b)

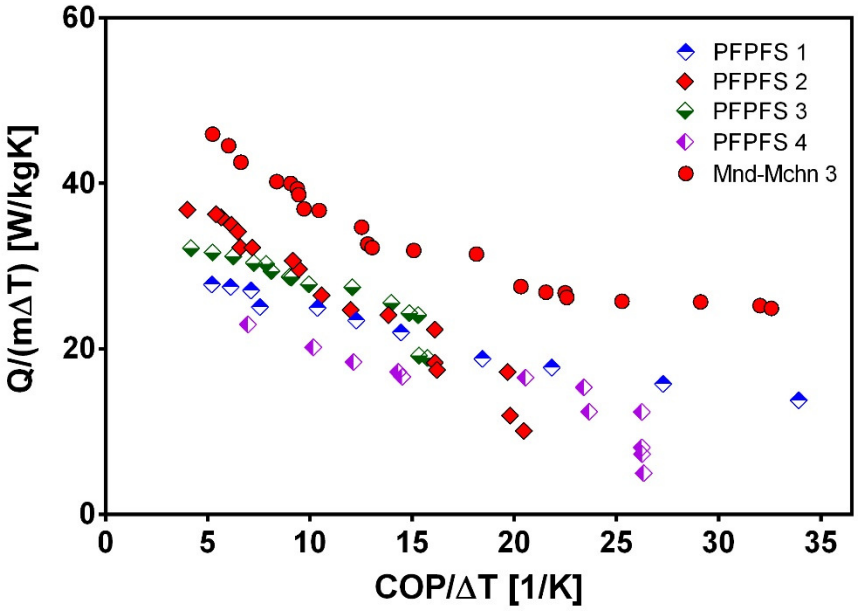
PFPFS 1
PFPFS 2
PFPFS 3
PFPFS 4
Mnd-Mchn 3
Q/(mΔT) [W/kgK]
COP/ΔT [1/K]
0
20
40
60
0
5
10
15
20
25
30
35

(c)

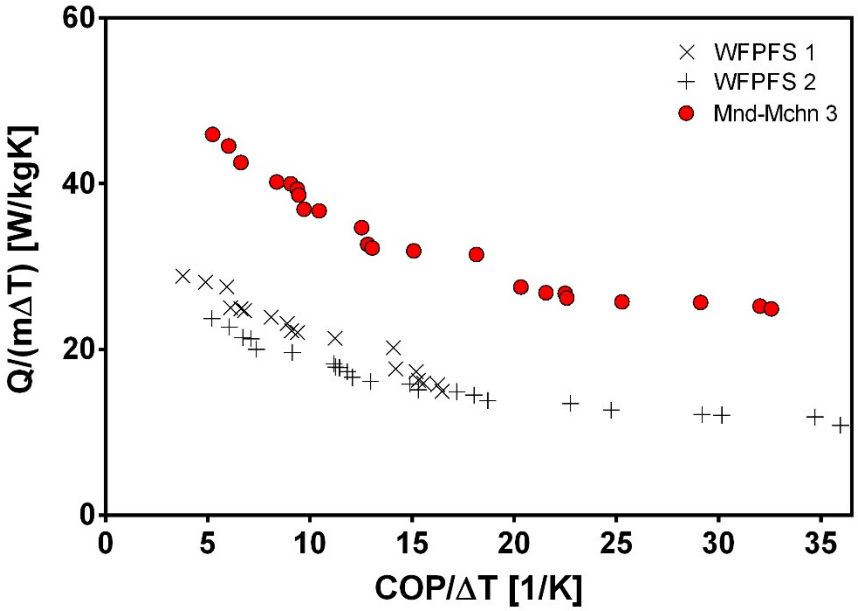
WFPFS 1
WFPFS 2
Mnd-Mchn 3
Q/(mΔT) [W/kgK]
COP/ΔT [1/K]
0
20
40
60
0
5
10
15
20
25
30
35

(d)

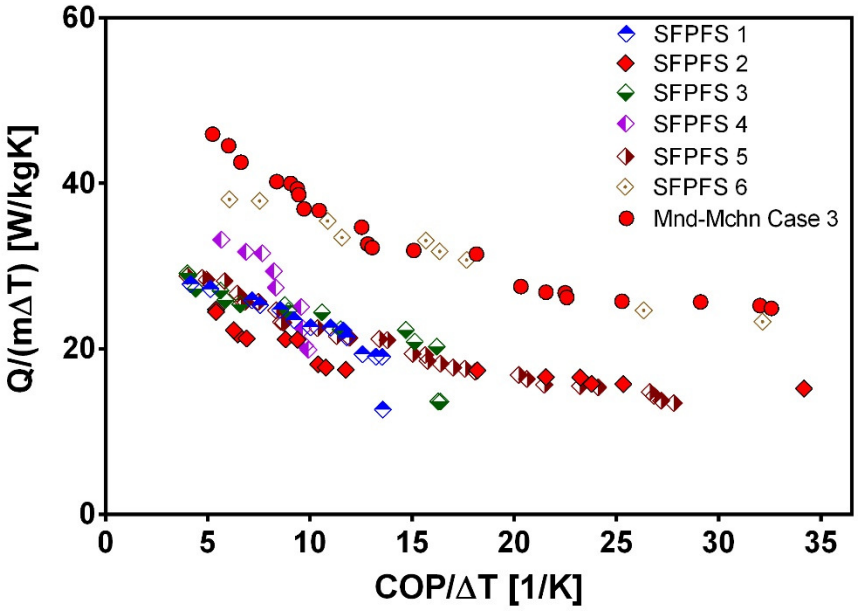

(e)

Figure 46: Optimization results of manifold-microchannel HX versus conventional HXs: (a) Louvered plate-fin surface HX, (b) Plain plate-fin surface HX, (c) Pin-fin plate-fin surface HX, (d) Wavy-fin plate-fin surface HX, (e) Strip-fin plate-fin HX

In order to get a better picture of how much improvement the manifold-microchannel yields with respect to the conventional heat exchangers, Table 13 compares all five manifold-microchannel cases with the best surface case for each conventional surface type. The percent improvement is calculated based on the improvement in $Q/(m\Delta T)$ for the case of $COP/\Delta T = 6.25$ (estimated based on a practical COP value for power plant cooling HX from EPRI with ΔT =27.5C [1]). The table shows that the manifold-microchannel outperformed conventional heat exchanger in almost all cases. PFPFS and SFPFS outperformed manifold-microchannel cases 4 and 5, which are cases in which the manufacturing limit is set higher than the actual limit. All conventional air-side geometries studied are inferior to manifold-microchannel case 3, in which the design is based on the technological limit. Additionally, WFPFS can only outperform manifold-microchannel case 5. This table clearly shows that for power plant cooling applications,

air-water manifold-microchannel heat exchanger built by current additive manufacturing technology limitation still outperforms other conventional heat exchangers. As additive manufacturing is a fast growing technology, it is expected that a smaller fin and manifold size can be built in the future which will yield further performance enhancement, as shown by cases 1 and 2.

Table 13: Percent improvement of $Q/(m\Delta T)$ in manifold-microchannel HX compared to conventional HXs for $COP/\Delta T = 6.25$

	Man-Mchn 1	Man-Mchn 2	Man-Mchn 3	Man-Mchn 4	Man-Mchn 5
PPFS	156	122	95	58	17
LPFS	158	124	97	59	18
PFPFS	59	38	21	-2	-27
SFPFS	47	27	12	-10	-33
WFPFS	109	81	59	29	-5

Man-Mchn 3 design at $COP/\Delta T = 6.25$ was selected as the manifold-microchannel heat exchanger design to be scaled down, fabricated, and experimentally tested, as this design met all the design requirements as specified in Table 7 and it yielded the highest performance enhancement based on the current technological limit. For comparison purposes, WFPFS 1's performance at $COP/\Delta T = 6.25$ was also selected as the baseline design performance, as WFPFS 1's air-side geometry is the closest to the actual air-side geometry for power plant cooling heat exchangers as discussed in chapter 3.3.

The performance comparison of the down selected manifold-microchannel and baseline (WFPFS 1) heat exchanger is shown in Table 14 below. Comparing the specifications for the two designs, for the same capacity (Q), heat exchanger effectiveness (ε), and COP, the manifold-microchannel heat exchanger mass (m) and volume (V) is significantly lower, 50% and 37% respectively, compared to the baseline design. As a result, substantial improvement in volumetric heat transfer density ($Q/V\Delta T$) and gravimetric

heat transfer density ($Q/m\Delta T$) is projected compared to the baseline wavy-fin. Even though water-side pressure drop in manifold-microchannel heat exchanger is significantly higher than its corresponding value for the baseline heat exchanger, the overall COP of manifold-microchannel is slightly higher. This is due to the decrease in air-side pressure drop. As air density is much lower than water, the decrease in the air-side pressure drop is enough to overcome the pumping power increase due to the increase in the water-side pressure drop.

Table 14: Performance comparison for full-scale (12.2 MW) metallic heat exchangers

	Manifold-microchannel heat exchanger	**Baseline (WFPFS 1)** heat exchanger	**% Variation**
Q [MW]	12.2	12.2	-
$Q/(V\Delta T)$ [W/m^{3}K]	54,599	27,217	**+101**
$Q/(m\Delta T)$ [W/kgK]	42.5	26.7	**+59**
COP	182	171	-
COP_{air}	208	183	-
ε_{HX}	72%	73%	-
V [m^3]	8.13	16.3	**-50**
m [kg]	1.04×10^4	1.66×10^4	**-37**
Δp_{water} [Pa]	12,335	5050	**+144**
Δp_{air} [Pa]	104	121	**-14**

6.3.3. Scaled Down Model

So that the optimized heat exchanger could be fabricated and tested, the heat exchanger had to be scaled down. As a result, the optimized heat exchanger was scaled down to a 1 kW unit. For scaling down the 12.2 MW heat exchanger unit, the optimization was re-run by fixing the air-side geometry as the optimum geometry calculated for the 12.2 MW unit. It should be noted that the primary focus in the subscale 1 kW unit was to evaluate the performance of the air-side of the metallic heat exchanger. For optimization purposes,

unlike for the case of wavy-fin surface, the manifold-microchannel airflow length was kept fixed (i.e. the air-side length of 1 kW unit was required to be the same as its 12.2 MW unit counterpart). This constraint was enforced to make sure geometrical similarity between the full-scale and subscale heat exchangers was preserved. This in turn allowed us to use the 1 kW unit experimental results on Nusselt number (Nu) and friction factor (f) for future re-evaluation of the full-scale heat exchanger performance and savings. If we had not imposed this restriction and allowed the airflow length for the 1 kW unit to be determined by optimization, then the flow distribution in the manifold channels of 1 kW unit and 12.2 MW unit would have been completely different, and scaling up the experimental results would be challenging. This was not an issue for the baseline heat exchanger because as long as the airflow is fully developed in wavy channels, the Colburn j-factor and friction factor experimental data are independent from the airflow length.

In total there were three variables that were allowed to vary for the optimization of the 1 kW unit: air-side Reynolds number ($\mathrm{Re_{air}}$), water-side Reynolds number ($\mathrm{Re_{water}}$), and water-side flow length ($\mathrm{L_{water}}$). The upper and lower limit constraints for those variables were the same as those listed in Table 11. For higher experimental measurement accuracy, it was desired that the air-side thermal resistance of the 1 kW unit dominate the water-side. As a result, the strip-fin s110-1974 from Kays and London's database [5] was used for the water-side of the 1 kW design, as it could deliver lower thermal resistance compared to the rectangular channel used in the 12.2 MW design. Moreover, so that the air-side thermal resistance was much more dominant than the water-side, the water flow rate to heat capacity ratio ($\dot{m}_{water}/Q_{tot}$) was increased 5 times with respect to the full

scale case, and an additional constraint was added to limit the ratio between the water-side and air-side thermal resistances ($\frac{R_{water}}{R_{air}}$) to less than 0.1. As the heat transfer performance was dominated by the air-side and there was no water-side geometrical similarity between the full scale and subscale units, the air-side COP was more of interest than the overall COP. As a result, COP constraints for the 1kW unit were calculated based on air-side COP. Lastly, for easier additive manufacturing and an even flow distribution, it was also desired that the air-side cross sectional area (Calculated as $L_{water} \times L_{no-flow}$) be a square. As a result, another constraint was added so that no flow length ($L_{no-flow}$) was equal to the water-side flow length (L_{water}). The operating conditions and performance constraints for the 1 kW heat exchanger are shown below:

Table 15: Operating conditions and performance constraints for 1 kW heat exchanger

Parameter	Value
Q [kW]	1kW
$\dot{m}_{air}$ [kg/s]	0.0498
$\dot{m}_{water}$ [kg/s]	0.239
$T_{in,air}$ [^{o}C]	40
$T_{in,water}$ [^{o}C]	67.5
COP_{air} [-]	>183 (= $COP_{air,full-scale}$ [baseline])
Δp_{air} [Pa]	<200
Δp_{water} [kPa]	<100
$\frac{R_{water}}{R_{air}}$	<0.1
$L_{no-flow} = L_{water}$	
$L_{air,1kW} = L_{air,12.2MW}$ (only for manifold-microchannel heat exchanger)	
Material: Stainless steel	

Besides being used to determine Nu and f factor for scaling up the 12.2 MW unit, the scaled down 1 kW HX can be considered as a standalone heat exchanger, which can have many applications in other fields including HVAC, and electronics cooling. For this reason, we have compared the 1 kW baseline and advanced manifold-microchannel units

performances'. The baseline was scaled down by applying the same constraints as listed in Table 15. The results are shown in Table 16 below. Comparing the results for the two units, the manifold-microchannel has significantly lower mass and volume compared to the wavy-fin for the same or higher capacity, effectiveness, and air-side COP (COP_{air}): 56% and 49% reduction in mass and volume, respectively. As a result, noteworthy improvements in heat transfer density ($Q/V\Delta T$) and gravimetric heat transfer density ($Q/m\Delta T$) are possible compared to the wavy-fin. However, compared to the baseline wavy-fin unit, there was a drastic increase in water side-pressure drop of the manifold-microchannel unit. This is because, for the same water-side flow rate, there was a substantial reduction in water-side cross-sectional area (Calculated as $L_{tot,air} \times L_{tot,no-flow}$) in the manifold-microchannel heat exchanger units compared to the wavy-fin units (3.18dm^2 vs. 9.67dm^2). In addition, the manifold-microchannel heat exchanger's water-side flow length is also longer, which also contributes to higher water-side pressure drop. As the COP constraint is calculated based on the air-side COP, a design with higher water-side pressure drop still could be selected by optimization process.

Table 16: Performance comparison for 1 kW metallic heat exchangers

	Manifold-microchannel	**Baseline (Wavy-fin)**	**% Variation**
Q [kW]	1	1	-
Q/(VΔT) [W/m^{3}K]	79051	34500	**+129%**
Q/(mΔT) [W/kgK]	58.7	29.7	**+98%**
COP	116	177.6	**-**
COP_{air}	203.3	182.9	**-**
ε_{HX}	74.3%	72.6%	**-**
$L_{tot,no-flow}$ [m]	0.146	0.111	**-**
$L_{tot,water}$ [m]	0.142	0.109	**-**
$L_{tot,air}$ [m]	0.0219	0.0871	**-**

$V\ [dm^3]$	0.46	1.054	**-56%**
m [kg]	0.62	1.224	**-49%**
Δp_{water} [Pa]	15994	681	**+2248%**
Δp_{air} [Pa]	107.4	118.3	**-9%**

The geometry for the 1 kW manifold-microchannel is shown in Figure 47. The heat exchanger is 14.6 cm long on the water-side, 2.23 cm long on the air-side and 14.2 cm in no flow direction. Detailed dimensions of the fins and manifolds are shown in Figure 47(b). Similarly, the geometry for the 1 kW wavy-fin is shown in Figure 48. This heat exchanger is 10.9 cm long on the water side, 8.71 cm long on the air side and 11.2 cm in no flow direction. Detailed dimensions of the fins are shown in Figure 48(b).

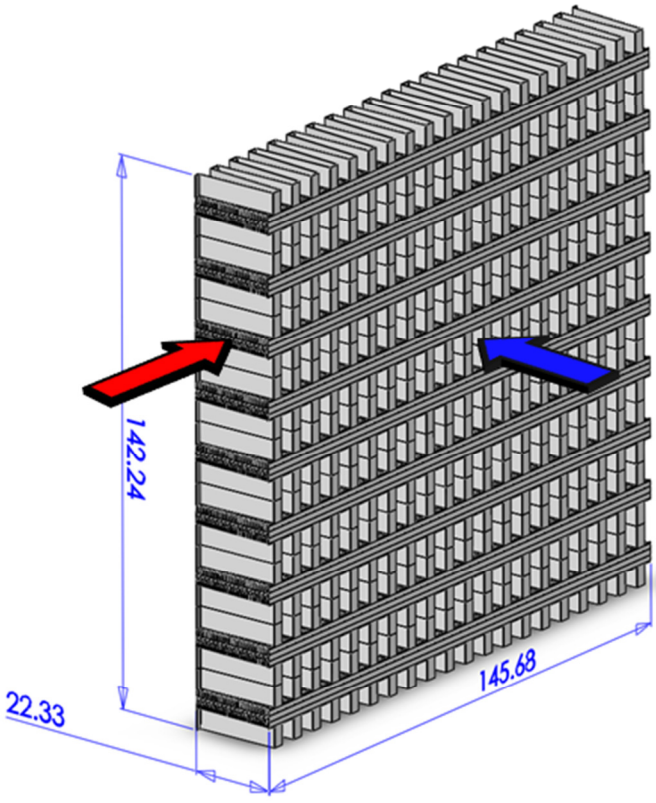

(a)

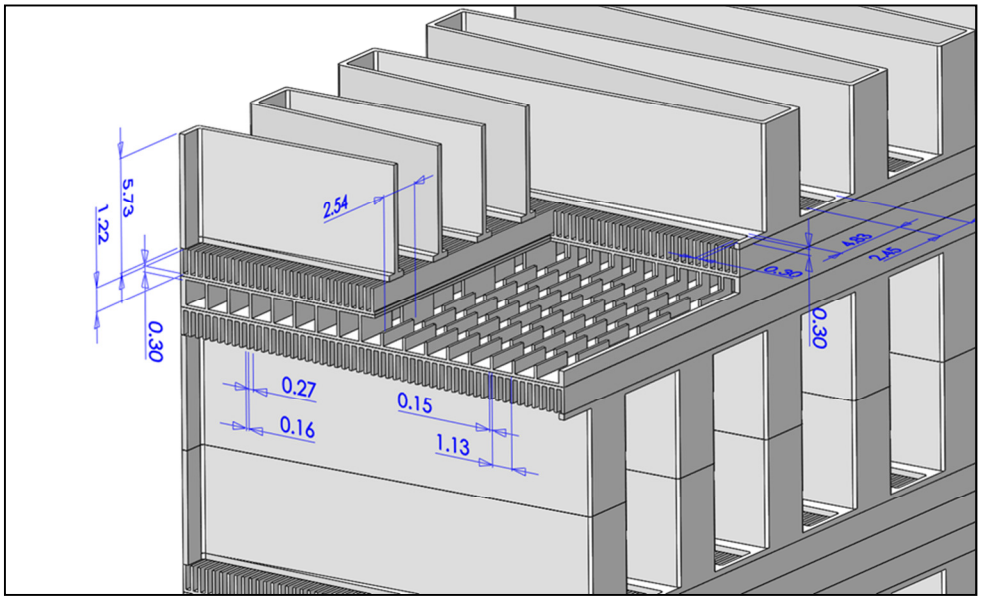

(b)

Figure 47: CAD drawings of the optimized manifold-microchannel heat exchanger (all dimensions are in mm)

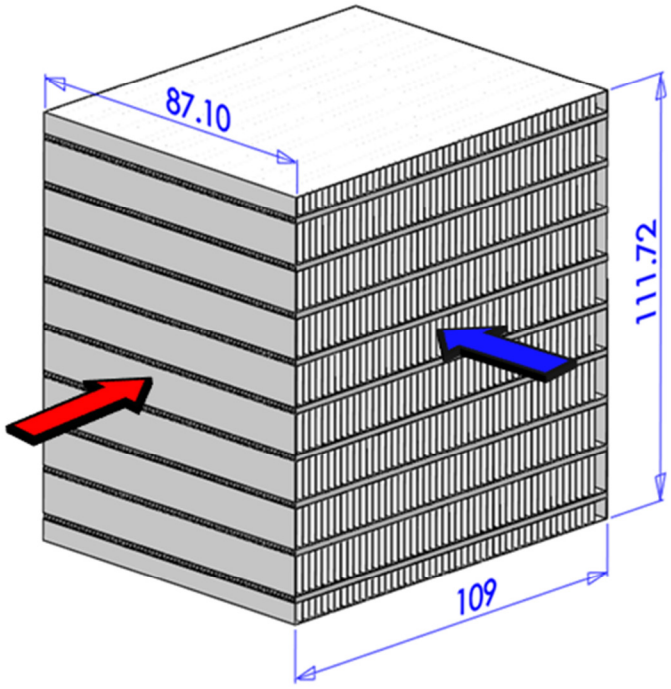

(a)

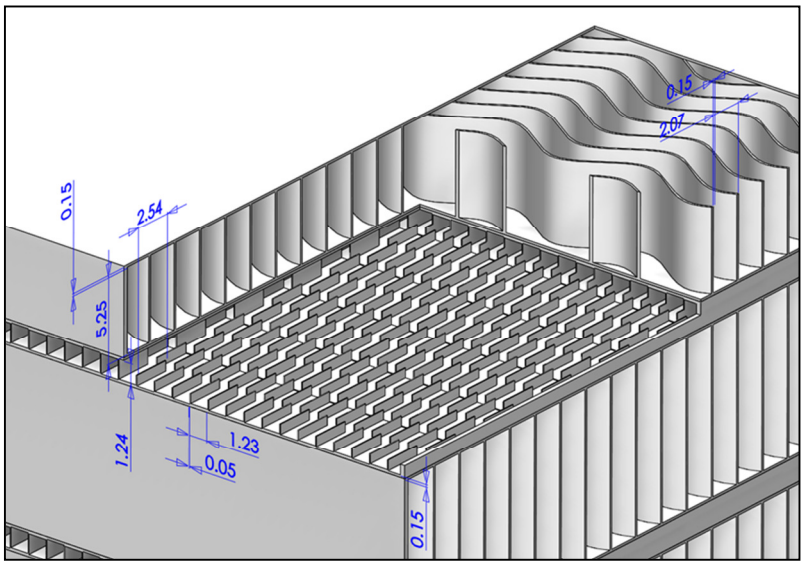

(b)

Figure 48: CAD drawings of the baseline heat exchanger (all dimensions are in mm)

6.4. Polymer Heat Exchanger Design Optimization

6.4.1. 12.2 MW Unit Sizing

The conceptual design was first constructed based on Michigan Tech University's polymer fabrication experience and the process manufacturing constraints. Welding patterns for the polymer sheets are shown in Figure 49, where B.1 is the welding pattern that forms the water channels and B.2 is the welding pattern that forms the air channels. In order to make the heat exchanger as compact as possible, the water channel dimensions were based on the smallest channel size that could be fabricated using laser welding technique. In addition, in order to increase heat exchanger effectiveness, a multi pass system was employed where water is forced to re-enter the heat exchanger multiple times, as shown in Figure 49.

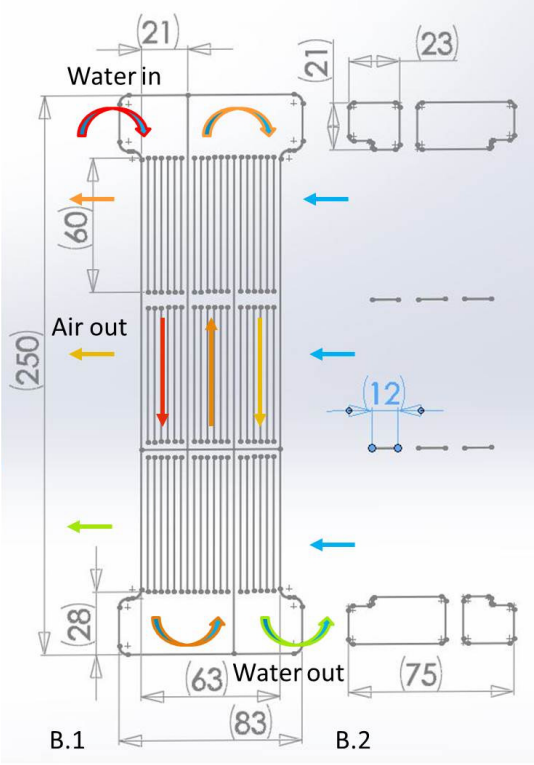

Figure 49: Welding pattern for polymer HX

In order to meet the specifications listed in Table 7 for the 12.2 MW unit, a parametric study was performed by varying the mass flow rate in each layer, spacing between the layers, and number of passes to find a design that met all of the specifications. A design that met all the performance requirements was selected, which was then compared to the optimized 12.2 MW metallic baseline heat exchanger for the same capacity, COP, effectiveness, and mass flow, rate as shown in Table 17 below. From comparison of the two designs, it can be concluded that polymer heat exchangers drastically reduce the heat exchanger mass (87%) in spite of increasing the volume by 14% when compared to the metallic heat exchanger. Moreover, a significant improvement on the gravimetric energy density of the polymer heat exchanger over metallic wavy-fin heat exchanger can be achieved at the expense of a reduction in volumetric heat transfer density.

Table 17: Performance comparison for 12.2 MW polymer heat exchanger

	Polymer heat exchanger	Baseline (Wavy-fin)	% Variation
Material	High density Polyethylene	Stainless Steel	N/A
Q [MW]	12.2	12.2	-
$Q/(V\Delta T)$ [W/m^{3}K]	23866	27217	**-12%**
$Q/(m\Delta T)$ [W/kgK]	208	26.7	**+680%**
COP	170	171	**-**
ε_{HX}	73.4%	73%	**-**
V [m^3]	18.59	16.3	**+14%**
m [kg]	2.14×10^3	1.66×10^4	**-87%**
Δp_{water} [Pa]	1632	5050	**-68%**
Δp_{air} [Pa]	130	121	**+9%**

6.4.2. Scaled Down Model

Like the case of the metallic heat exchanger, the polymer heat exchanger also needed to be scaled down. A scaled down 1kW unit was calculated by keeping the geometry the same as that of the 12.2 MW unit and adjusting the mass flow rate and number of passes to match the specification of the 1 kW unit as listed in Table 15. The 1 kW polymer heat exchanger results are shown in Table 18 and compared with the optimized 1 kW metallic wavy-fin heat exchanger evaluated at the same mass flow rate. Comparing both designs, a weight saving of 86% was possible for the polymer heat exchanger, while its volume increased by 47%. There was a slight reduction on the air-side COP compared to the wavy-fin unit due to a slight increase in the air-side pressure drop. However, the capacity and effectiveness of the polymer heat exchanger was also slightly higher than the wavy-fin unit. A design adjustment can be performed to increase the air-side COP by reducing the capacity and effectiveness to the desired levels.

Table 18: Performance comparison for 1 kW polymer heat exchanger

	Polymer heat exchanger	Baseline (Wavy-fin)	% Variation
Material	High density Polyethylene	Stainless Steel	N/A
Q [kW]	1.04	1	-
$Q/(V\Delta T)$ [W/m^3K]	24150	34500	**-30%**
$Q/(m\Delta T)$ [W/kgK]	218	29.7	**+634%**
U [W/m^2K]	68.8	403	**-83%**
COP	105	177.6	-
COP_{air}	172	183	-
ε_{HX}	77%	72.58%	-
$L_{tot,no-flow}$ [m]	0.0952	0.111	-
$L_{tot,water}$ [m]	0.25	0.109	-
$L_{tot,air}$ [m]	0.0658	0.0871	-
# of stack	34	9	-
V [dm^3]	1.54	1.05	**+47%**
m [kg]	0.174	1.22	**-86%**
Δp_{water} [Pa]	16,214	681	**+2381%**
Δp_{air} [Pa]	134	118.3	**+15%**

The CAD drawings for the 1 kW polymer heat exchanger unit, including its dimensions, are shown in Figure 50. Figure 50 (a) and (b) show the top and bottom view of a single heat exchanger layer, including the water and airflow directions. Water enters the heat exchanger from the side and then the flow passes through the heat exchanger four times (four passes) as shown in Figure 50 (b). For each pass, heat is extracted from the water into the air, which flows perpendicular to the water flow, creating a cross-flow configuration as shown in the figure. In total 34 layers were needed to achieve 1 kW performance. The size of the full model geometry was 25 cm on the water-side, 6.58 cm on the air-side, and 9.52 cm height as shown in Figure 50 (c). The water channel is positioned in a staggered configuration from one layer to another as shown in Figure 50 (d).

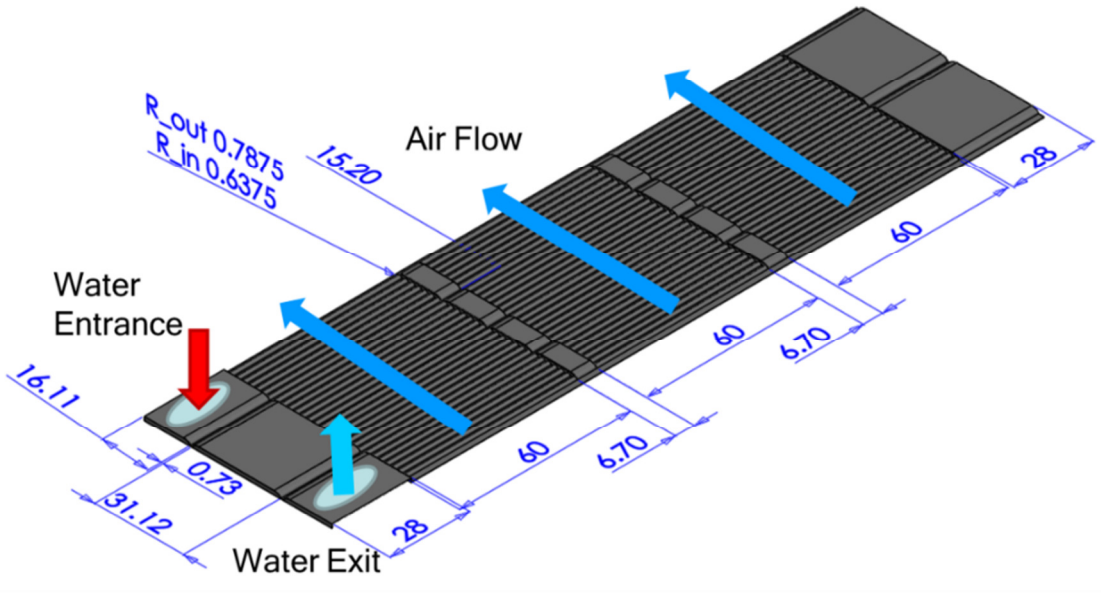
R_out 0.7875
R_in 0.6375
15.20
Air Flow
28
60
Water
Entrance
60
6.70
16.11
0.73
60
6.70
31.12
28
Water Exit

(a)

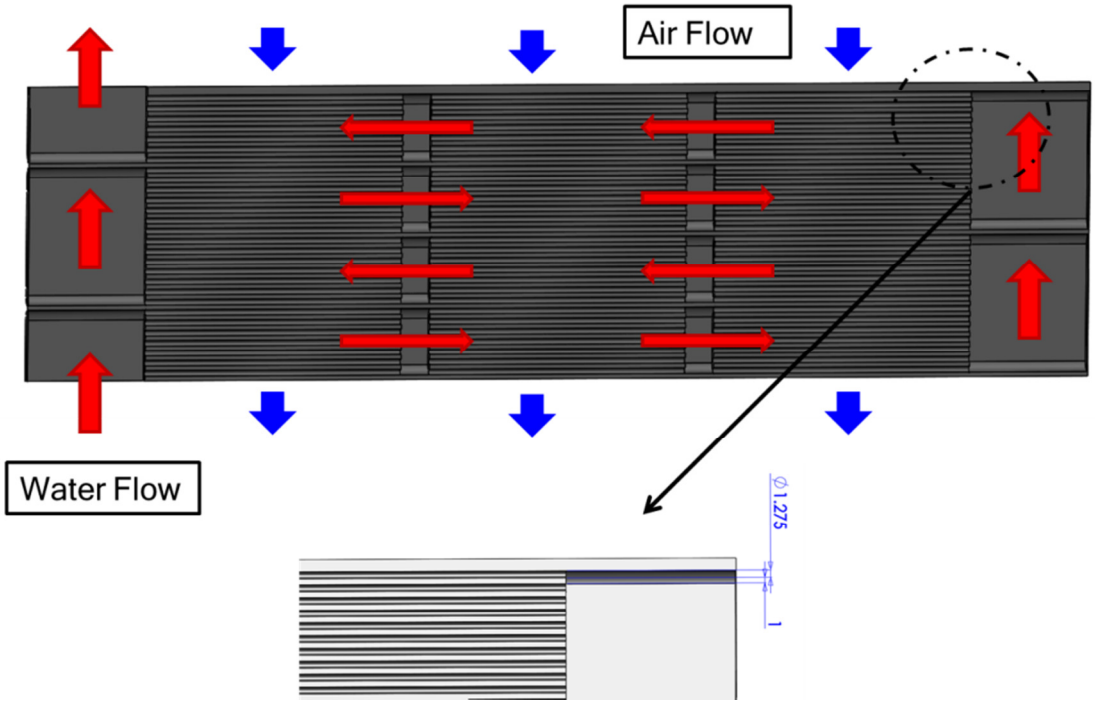
Air Flow
Water Flow
Ø1.275
1

(b)

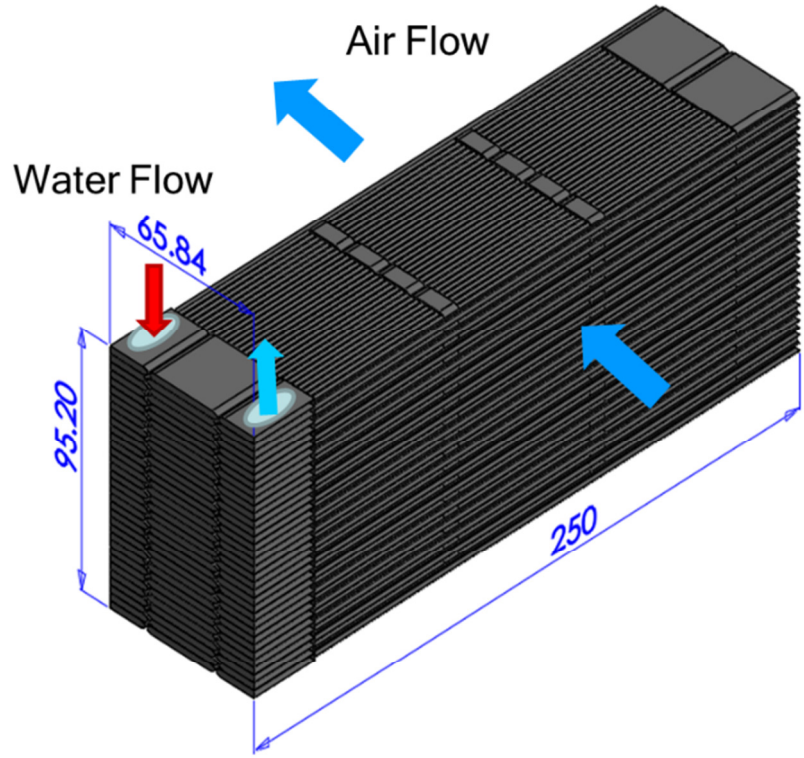

(c)

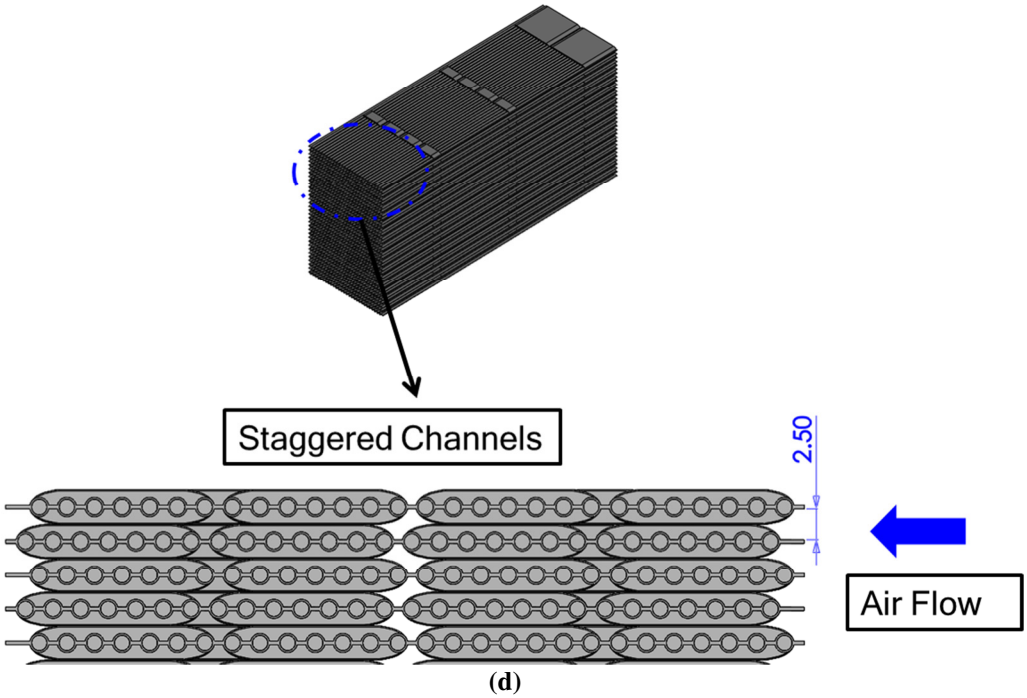

(d)

Figure 50: CAD drawings of the 1 kW polymer heat exchanger (a) Single layer top view, (b) Single layer bottom view, (c) Full model geometry, (d) staggered flow configuration (all dimensions are in mm)

6.5. Summary

In summary, in this chapter multi-objective optimization was performed to compared the performance of the manifold-microchannel and conventional heat exchangers. The results show that the manifold-microchannel performance was significantly superior to the conventional heat exchangers like wavy fin, louvered fin, plain plate fin, pin fin, and strip fin. Compared to the baseline, significant mass and volume reduction was noted for manifold-microchannel heat exchanger (37% and 50% respectively). The optimization results also show that if the fin thickness can be reduced from 150 μm to 50μm, an even larger mass reduction is possible. For the case of the polymer heat exchanger, more than 80% reduction in mass is possible compared to the baseline at the price of slight increase in volume (14%). Lastly, the advanced metallic and polymer heat exchangers were scaled down for fabrication and experimental testing.

Chapter 7: Performance Characterization of Advanced Metallic Heat Exchanger

7.1. Introduction

This chapter discusses the performance characterization of the coupon manifold-microchannel heat exchangers (advanced metallic). The coupon heat exchanger geometry was based on the scaled down design proposed in chapter 6 with some design adjustments based on suggestions from the supplier. After fabrication, the fabricated coupon heat exchangers were analyzed to evaluate the fabrication quality. Thereafter, experimental work was performed to evaluate the heat exchanger's performances. The experimental results were then compared with the numerical results and conventional heat exchanger's performance. Lastly, the heat exchanger was scaled up to 12.2 MW for comparison with the baseline.

7.2. Heat Exchanger Geometry and Fabrication

7.2.1. Heat Exchanger Geometry and Performance

Based on suggestion from the supplier, a few design modifications are needed. First, in order to be able to use the high precision printing machine, the 1 kW heat exchanger previously proposed need to be scaled down even further to 150 W. The 150 W heat exchanger was a portion of the 1 kW manifold-microchannel heat exchanger proposed in chapter 6.3.3. The sizing process is based on the assumption that the heat exchanger capacity is proportional with volume. As a result, the 150 W heat exchanger was a portion of the 1 kW heat exchanger (with approximately 1/7 in volume) as shown in Figure 51. This assumption can be justified as the water temperature is only varied by 1 °C for the 1 kW unit. The CAD drawing of the heat exchanger is shown in Figure 52

while the geometrical variables of both the air and water sides are shown in Table 19. The size of the air-water heat exchanger is 24.9 mm x 44.3 mm x 61.7 mm. In order to achieve the 150 W performance, the same mass flux is applied in both the air and water sides as the one proposed for the 1 kW unit.

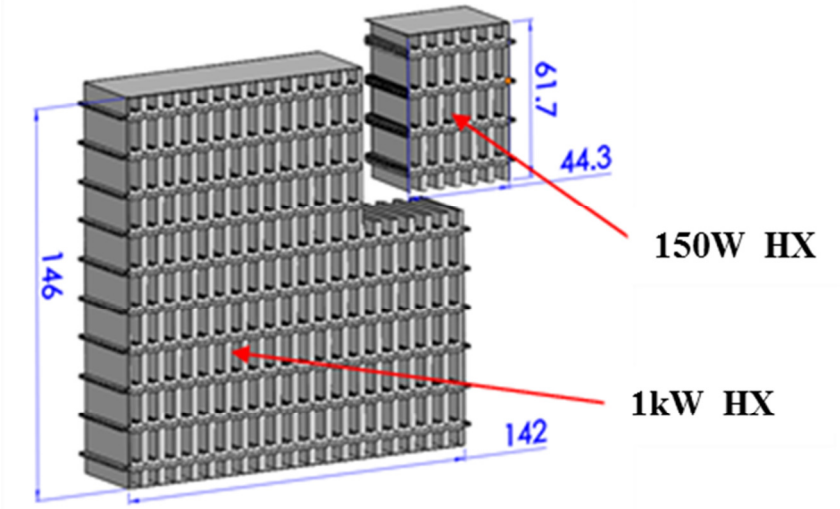

Figure 51: Scaling down of 150 W heat exchanger (All unit in mm)

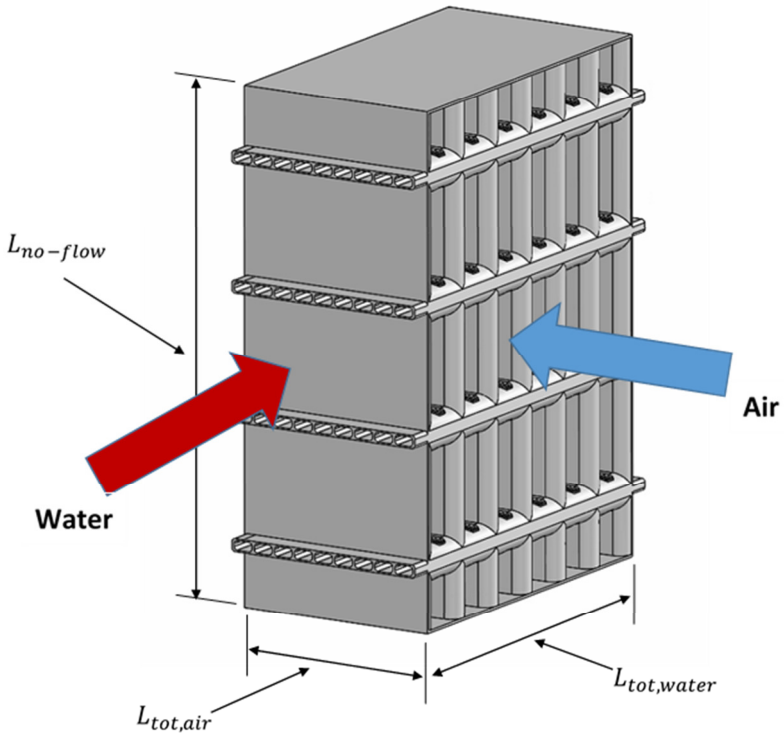

(a)

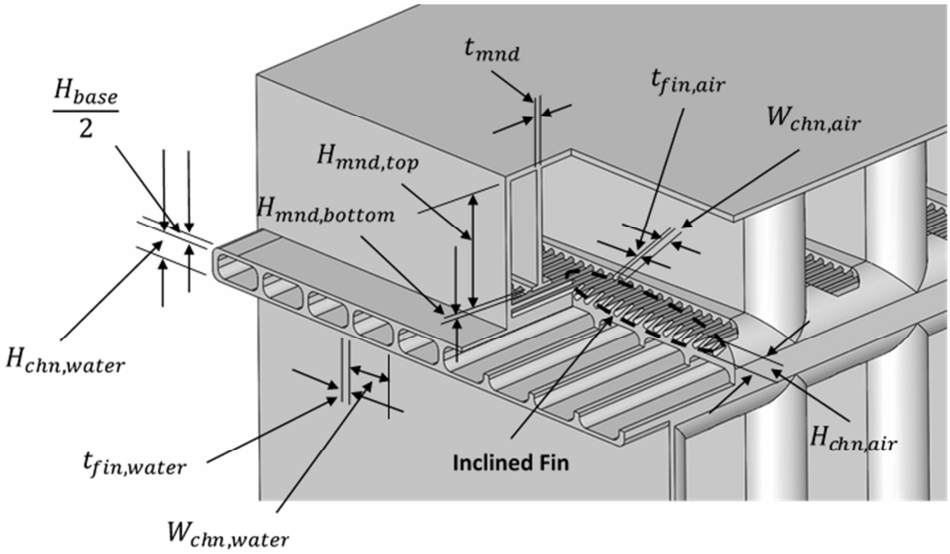

(b)

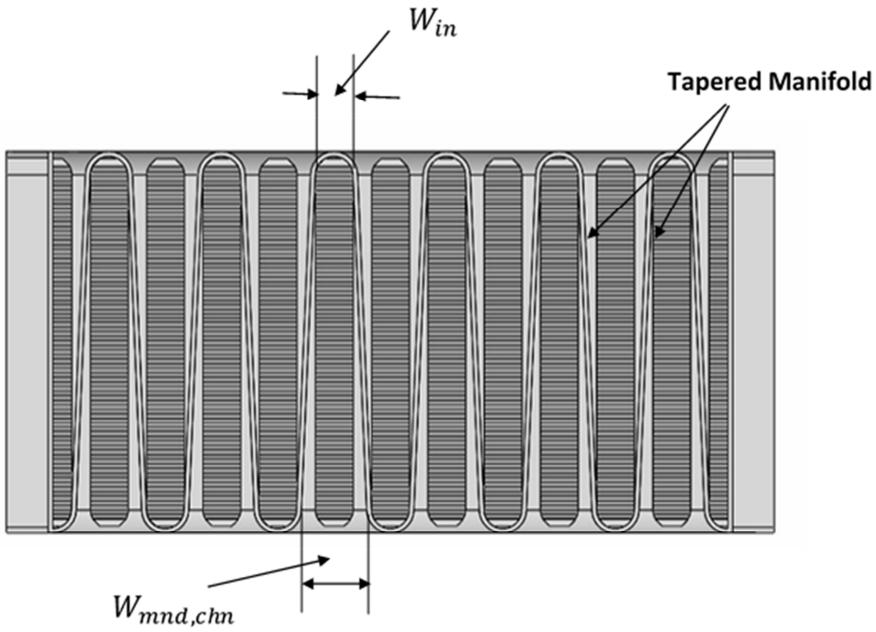

(c)

Figure 52: Heat exchanger geometry: (a) full-view, (b) cross-section view, (c) top view (all dimensions in mm)

Table 19: Geometrical and flow variables for the 150 W HXs

Air-Side	
$H_{chn,air}$	1.2 mm
$t_{fin,air}$	0.15 mm
$W_{chn,air}$	0.27 mm
$W_{mnd-chn}$	4.24 mm
W_{in}	2.45 mm
$H_{mnd,bottom}$	0.3 mm
$H_{mnd,top}$	5.43 mm
t_{mnd}	0.3 mm
n	39
H_{base}	0.3 mm
$\dot{m}_{air}$	6.23g/m^{2}s
Water-Side	
$H_{chn,water}$	1.14 mm
$W_{chn,water}$	2.4 mm
$t_{fin,water}$	0.318 mm
$\dot{m}_{water}$	100g/m^{2}s
Overall	
$L_{tot,air}$	24.78 mm
$L_{tot,water}$	44.3 mm
$L_{no-flow}$	61.74 mm

For the second modification, the air-side fins had be inclined at a 45^o angle as shown in Figure 53 and Figure 52(b). As a general rule, printing of a layer which is not supported by the lower layer can lead to overhang issue. In general DMLS method has a small allowance for unsupported overhangs. One way to overcome this issue is to adopt self-supporting structures with inclined angles 45^o or higher [175]. In our design in order to avoid unsupported air-side fin strcture, these fins need to be inclined 45^o. For the third modification, in order to ease the pressure drops and provide better control of flow maldistribution, the manifold design was modified from a straight manifold to a tapered manifold as shown in Figure 52(c). The manifold-channel flow area now varied with respect to the amount of flow in the channel. This means that for supply manifold channels, as more flow was diverted into microchannels along the air flow length, the

cross section area of manifold channel was reduced. As seen in Figure 52(c), at the inlet of the manifold channel, the cross sectional area was the largest where the mass flow rate was the highest, while as the manifold cross sectional area tapers, gradually more fluid passes through the microchannels where the actual heat transfer takes place. For the exit manifold the opposite process happens, in which the cross sectional area of the manifold channel gradually increases as more flow exits the microchannels and flow rate increases. For the last modification, in order to avoid overhang issue during the fabrication, the strip-fin was replaced with plain plate fin.

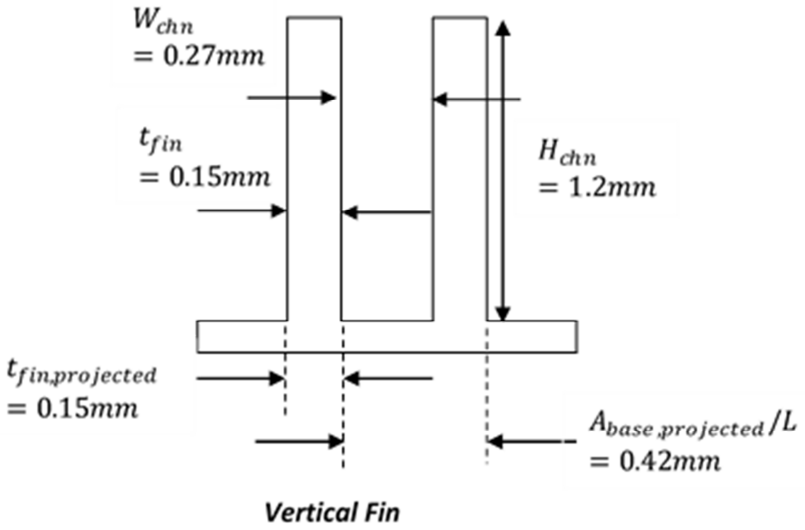

Vertical Fin

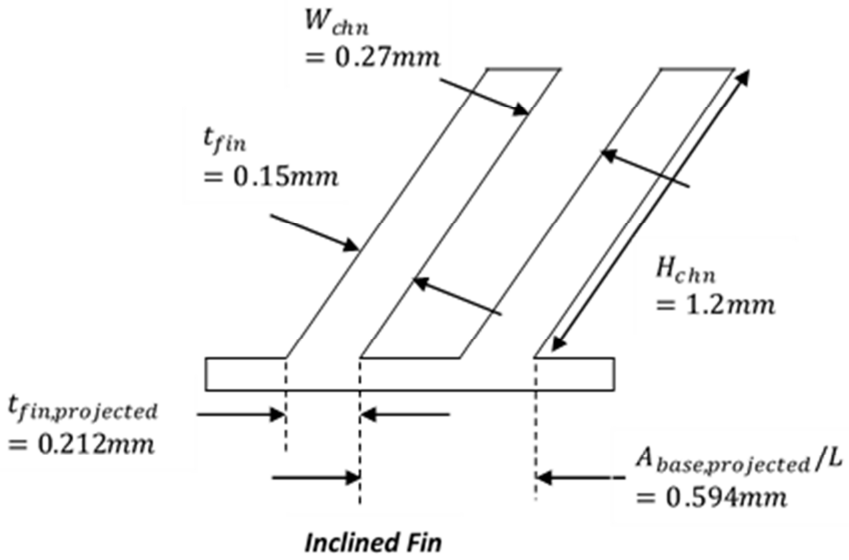

Figure 53: Vertical fin and inclined fin

In order to study the effect of the incline fin and tapered manifold on the heat exchanger performance, three single pass single manifold models (SPSM), which each consisted of inlet manifold channel, exit manifold channel, fins, and microchannels, were created for CFD simulation of the air-side performance with inclined fin and/or tapered manifold as shown in Figure 54. The first model simulated a case of inclined fin with flow direction on the direction of the fins (Case 1 Figure 54(a)). As this case was intended to study the effect of incline fin, a straight manifold was used. The second model was to simulate a case of inclined fin with flow direction against the direction of the Figure 54(b)). Similarly, a straight manifold was used for the second case. The third model combined the inclined fin and tapered manifold as shown in Figure 54 (Case 3(c)). For the flow direction, flow against the direction of the fin was selected. To calculate the overall performance of the heat exchanger, the same control volume method explained in chapter 5.3.1 was employed. The air-side performances were evaluated by using SPSM CFD simulation rather than the modified hybrid method.

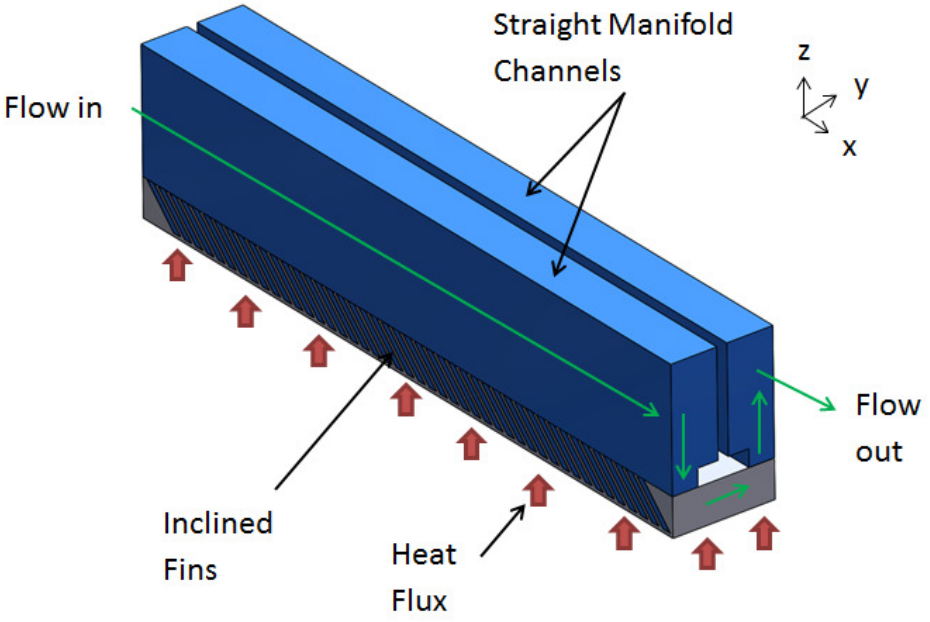
Straight Manifold
Channels
z
y
x
Flow in
Flow
out
Inclined
Fins
Heat
Flux

(a)

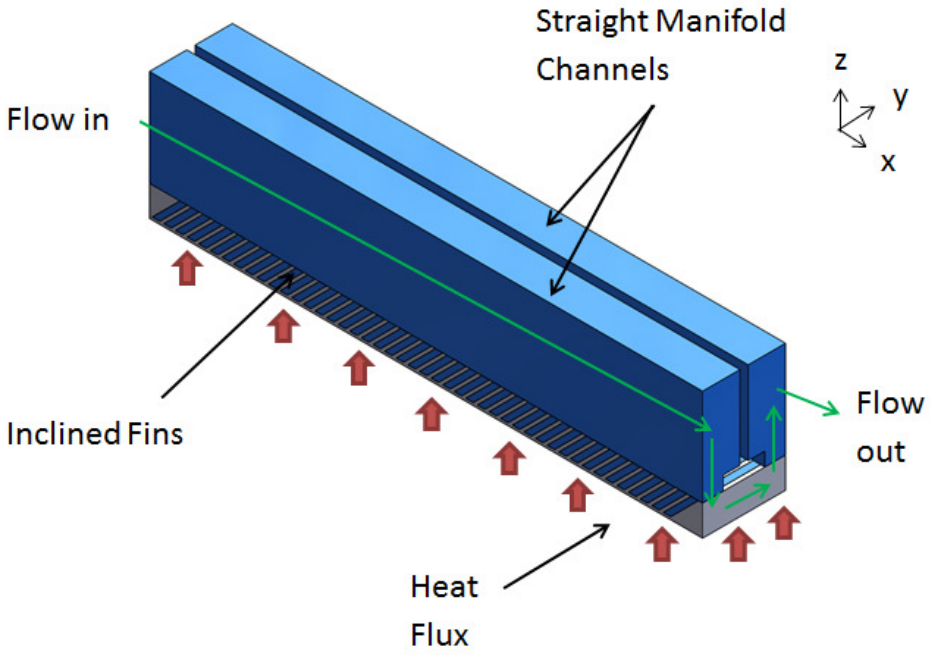
Straight Manifold
Channels
z
y
x
Flow in
Inclined Fins
Flow
out
Heat
Flux

(b)

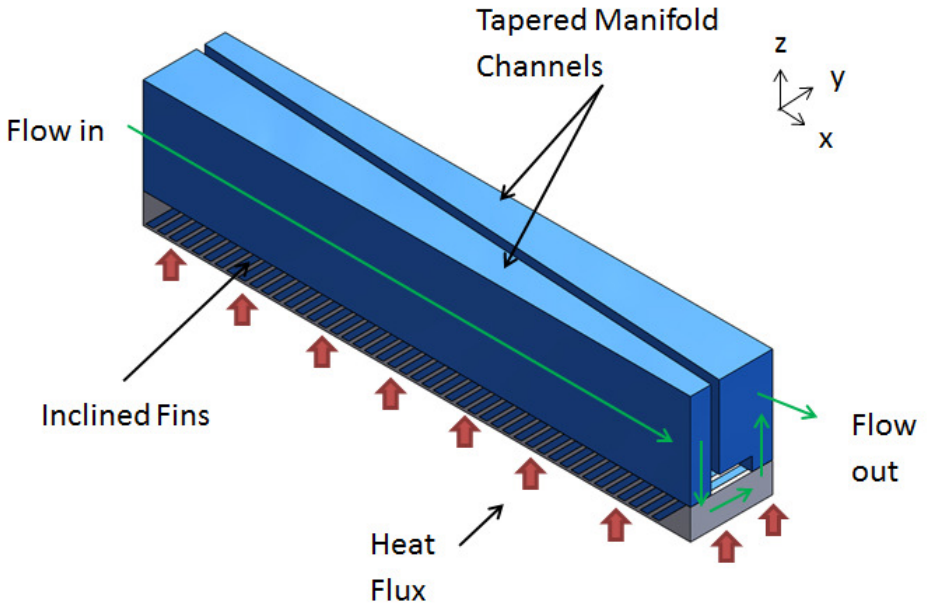

(c)

Figure 54: Inclined fin and tapered manifold simulation cases: (a) Case 1 – inclined fin & straight manifold with flow on the direction of the fins (b) Case 2 – inclined fin & straight manifold with flow against the direction of the fins (c) Case 3 – inclined fin & tapered manifold with flow against the direction of the fins

The simulation results of all three cases are shown in Table 20 compared with the performance of the original design of vertical fin and straight manifold. Comparing the heat transfer performance, a reduction in heat exchanger capacity (Q) is noted for the inclined fin design (cases 1 and 2) compared to the original design. This is because, unlike the case of the vertical fin where the projected fin thickness ($t_{fin,projected}$) is equal to the actual fin thickness (t_{fin}), for the case of inclined fin the projected fin thickness was always higher than the actual fin thickness, as shown in Figure 53. As a result, for the same actual fin thickness and flow length, the number of fins per inch for the incline fin design as always lower than the case of vertical fin. This caused a reduction in the heat transfer area, which in turn reduced the heat exchanger capacity. For the same reason, the air-side pressure drop performance of cases 1 and 2 with vertical fin and straight manifold case was higher than the original case with vertical fin design. As the

number of fins per inch decreases, for the same total mass flow rate and total air–side length, the amount of flow that goes to each microchannel will increase, which in turn increases the pressure drop.

Comparing the performance of case 1 and case 2, there is no significant difference between both cases. The only noticeable difference is that case 2 yields 5% higher heat transfer capacity than case 1. Comparing the effect of the tapered manifold (case 3) to the straight manifold in case 2 (Both case 2 and 3 use the same inclined fin configuration), only minor pressure drop reduction was noticed (6%). This is because this geometry does not produce high flow maldistribution, as the geometry was optimized by setting an upper limit constraint on flow maldistribution. Lastly, as most of the heat transfer occurred on the microchannels, the heat transfer performance was also not affected by the tapered manifold design as shown in the table.

Table 20: Performance comparison of the inclined fin and tapered manifold

	Original (Vertical fin & straight manifold)	Case 1	% Diff 1	Case 2	% Diff 2	Case 3	% Diff 3
Q [kW]	0.15	0.13	-14%	0.135	-11%	0.135	-11%
Q/(VΔT) [W/m^{3}K]	76.6	68.7	-11%	71.4	-7%	71.4	-7%
Q/(mΔT) [W/kgK]	47.8	44.6	-7%	46.3	-3%	46.3	-3%
ε_{HX} [%]	81.3	70.9	-15%	74	-11%	74	-11%
$L_{tot,air}$ [mm]	24.78	24.78	-	24.78	-	24.78	-
V [dm^3]	0.071	0.069	-3%	0.069	-3%	0.069	-3%
m [kg]	0.114	0.106	-7%	0.106	-7%	0.106	-7%
Δp_{water} [Pa]	802	802	0%	802	0%	802	0%
Δp_{air} [Pa]	112	152	30%	153	31%	143	25%

Although the numerical method previously developed in chapter 5 was for the case of vertical fins and straight manifold design, the method can still be applied to inclined fin and tapered manifold designs with high accuracy if a number of conditions are met. The

first condition is that the flow maldistribution should be low. As the main function of the tapered manifold is to reduce flow maldistribution, for cases where maldistribution is already low, the tapered manifold will not significantly affect the performance. This is the case for the proposed geometry, as previously discussed. The second condition requires that the microchannel hydraulic diameter, flow length, and heat transfer area for both the vertical and inclined fins not be significantlly different. To achive that the microchannel geometrical parameters, including height (H_{chn}), width (W_{chn}), and fin thickness (t_{fin}) for both vertical and inclined fins, need to be defined as shown in Figure 53 for both the vertical and inclined fins. Consequently, the microchannel pressure drop and heat transfer performance calculation based on the hybrid method can still be valid using vertical fin models. In order to prove the above assumptions, the performance comparison of the hybrid method to the full CFD model of case 3 is shown in Table 21. Both heat conductance and pressure drop calculated using the hybrid method were only 8% and 5% different, respectively, compared to their equivalent values calculated based on full CFD simulation.

Table 21: Performance comparison – hybrid method for inclined fin and tapered manifold

	Hybrid method	Case 3	% Diff 3
Q [kW]	0.126	0.135	**7%**
$h_{air}[W/m^2K]$	578	628	**8%**
Q/(VΔT) [W/m^{3}K]	66.6	71.4	**7%**
Q/(mΔT) [W/kgK]	43.2	46.3	**7%**
ε_{HX} [%]	70.9	74	**4%**
V [dm^3]	0.069	0.069	**0%**
m[kg]	0.106	0.106	**0%**
Δp_{water} [Pa]	802	802	**0%**

7.2.2. Fabricated Heat Exchanger Evaluation

For evaluation of the fabrication quality and repeatability, seven small coupons were fabricated from different material as shown in Figure 55. Three coupons were fabricated out of titanium alloy (Ti64), two coupons were fabricated out of stainless steel (SS17-4), and one coupon was fabricated out of aluminum (Alsi10Mg) and Inconel 718. The microscopic view of the coupons were shown in Figure 56. Analyzing the fins and microchannel quality, some of the channels were partially obstructed especially for the case of Inconel 718. The fin thickness and microchannel width for all seven coupons and the requested dimensions were compared in Table 22. Most of the fins were fabricated close to 300µm thickness compared to requested thickness of 150µm. Titanium alloy coupons show the best fabrication quality although with poor repeatability. This analysis show that significant fabrication inaccuracy was observed in all of the coupons and HXs which may affecting the heat exchanger performances.

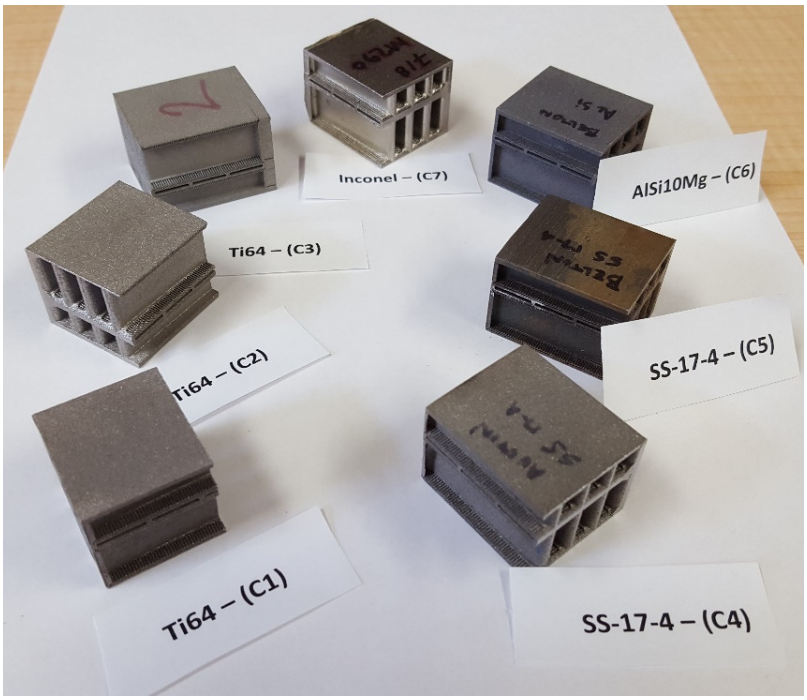

Figure 55: Coupons heat exchangers for fin evaluations

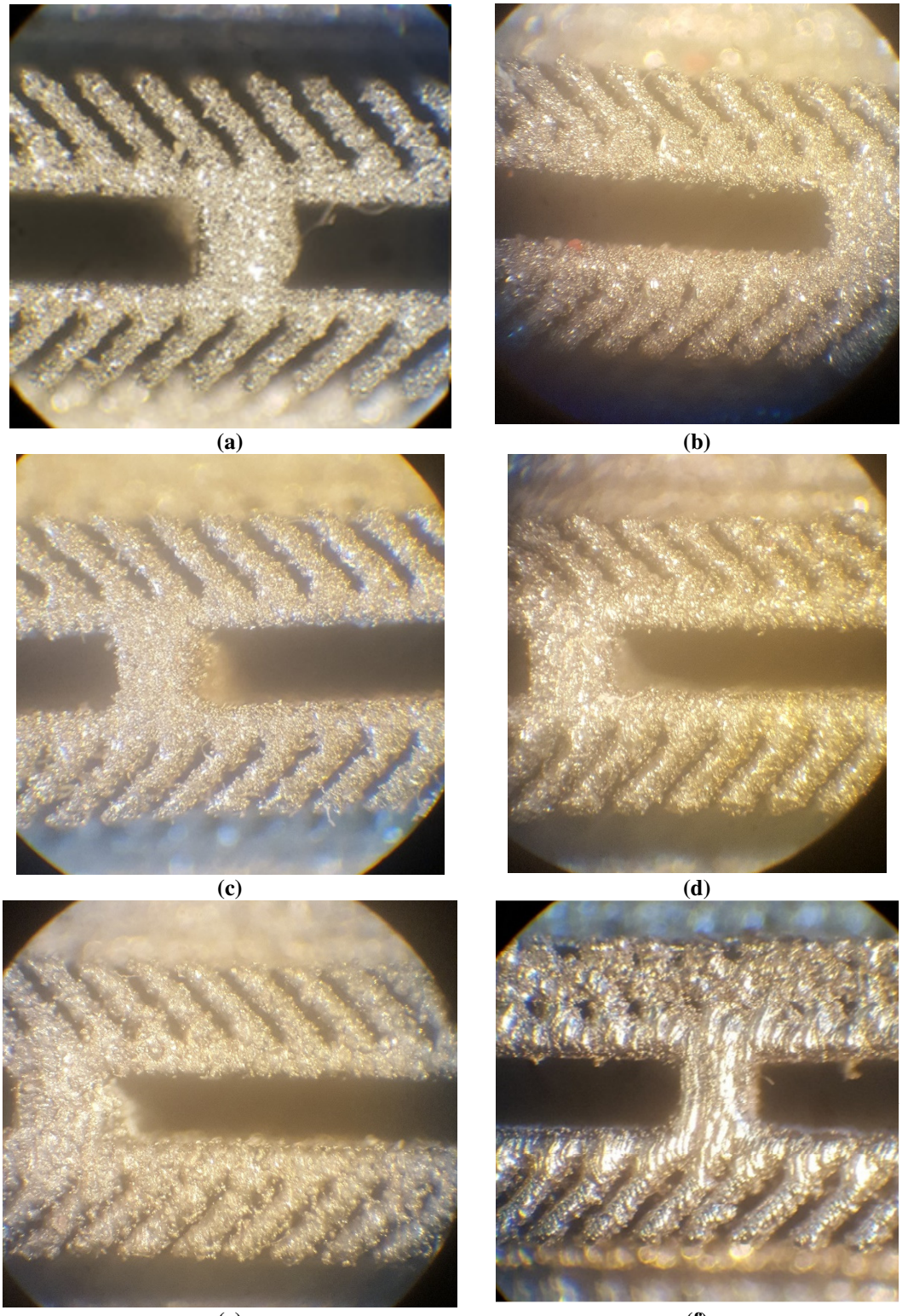

Figure 56: Microscopic view of the fins and microchannels of the coupons (a) Ti64 – C1 (b) Ti64 – C3 (c) SS-17-4 – C4 (d) SS-17-4 – C5 (e) AlSi10Mg – C6 (f) Inconel 718 – C7

Table 22: Coupons heat exchanger fin dimensions

	W_{chn}[μm]	t_{fin} [μm]
Requested	270	150
Ti64 – C1	150	260
Ti64 – C2	80	340
Ti64 – C3	130	290
SS-17-4 – C4	120	300
SS-17-4 – C5	110	310
AlSi10Mg – C6	90	330
Inconel 718 – C7*	130	290

** Not taking into account the clogged channel*

The 150W heat exchanger was built out of three different materials: titanium alloy (Ti64), stainless steel (SS17-4), and aluminum (AlSi10Mg). Stainless steel is one of the most common materials for air-water heat exchangers. On the other hand, although aluminum is not often used for air-water heat exchanger due to its reaction with water, aluminum is often used for other air-based heat exchanger applications like air-to-air heat exchangers. As the main focus of this project as on air-side enhancement, it is also in our interest to study aluminum-based heat exchangers. Lastly, the main reason for the use of titanium alloy as one possible material for metallic heat exchanger fabrication was because titanium alloy is lighter than stainless steel (60% in density), and it also has better material strength than stainless steel. In addition, titanium is one of the most abundant materials on earth next to aluminum, iron, and magnesium.

In total five heat exchangers were successfully fabricated from three different materials: two from titanium alloy, two from stainless steel, and one from aluminum, using the direct metal laser sintering (DMLS) technique as shown in Figure 57.

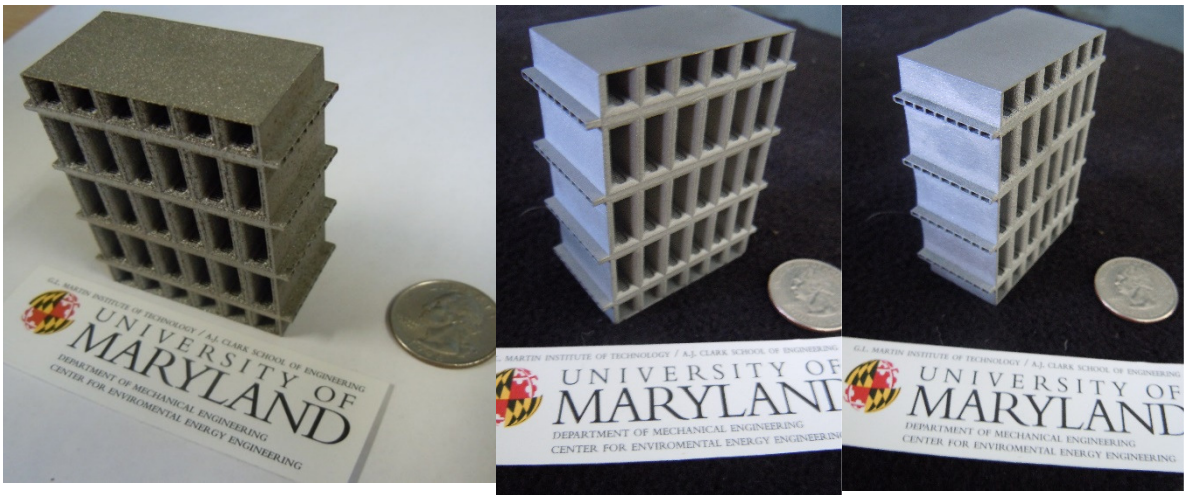

(a) (b) (c)

Figure 57: Fabricated test coupons core (a) Titanium alloy (b) Stainless steel (c) Aluminum

In order to assess the fabrication quality, the overall dimensions ($L_{tot,air}$, $L_{tot,water}$, and $L_{no-flow}$) and mass (m) of all prototypes were measured and compared with the original design dimensions and expected mass. Table 23 summarizes the percentage of deviation between actual fabricated and design dimensions of the heat exchangers. Comparing the overall dimensions, a good agreement is seen between the fabricated and original design dimensions for all heat exchangers. However, in terms of mass, there is a significant deviation between the expected and fabricated heat exchangers for the case of stainless steel and aluminum alloy prototypes. The deviation in mass could be due to fabrication inaccuracy in some of the variables as previously shown.

Table 23: % Variation of the requested and fabricated dimensions of the test coupon HX

	Ti64 - 1	Ti64 - 2	SS17-4 - 1	SS17-4 - 2	AlSi10Mg
$L_{tot,air}$	0.16%	1.69%	1.81%	0.04%	1.81%
$L_{tot,water}$	0.36%	0.00%	0.85%	1.48%	0.38%
$L_{no-flow}$	0.10%	0.26%	0.79%	0.15%	0.29%
m	5.79%	9.09%	45.28%	35.85%	19.14%

In order to assess the quality of the fabricated microchannels and fins, the Ti64-2 heat exchanger was cut in the middle using wire EDM technique. Since cutting the heat exchanger will damage the test section, it was cut after the experimental testing was finalized. The microscopic view of the fins and microchannels is shown in Figure 58. The fin thickness was measured at 235±40 μm, while its microchannel width was measured at 185±30 μm, as compared to the requested fin thickness and microchannel width of 150 μm and 270 μm, respectively. In addition, partial obstruction was also noticed in some of the channels which blocked about half the channel, as shown in Figure 58. Lastly, it was also noticed that there was geometrical non-uniformity in both microchannels and fin sizes in all of the channels. Up to 20% deviation from average values was noticed for both variables. These fabrication inaccuracies are not surprising by noting that the technology is still in its infancy stage and requires further effort to overcome technological challenges, especially in areas of process precision and consistency.

Re-calculating the mass of the heat exchanger based on $W_{chn,air} = 185\mu m$ and $t_{fin,air} = 235\mu m$, the percentage of deviation between the fabricated and anticipated masses can be reduced to only 1.5% as oppose to 9.1% calculated based on $W_{chn,air} = 270\mu m$ and $t_{fin,air} = 150\mu m$ as previously reported. This confirms that the cause of the mass deviation as previously reported is due to the inaccuracy in the fabrication.

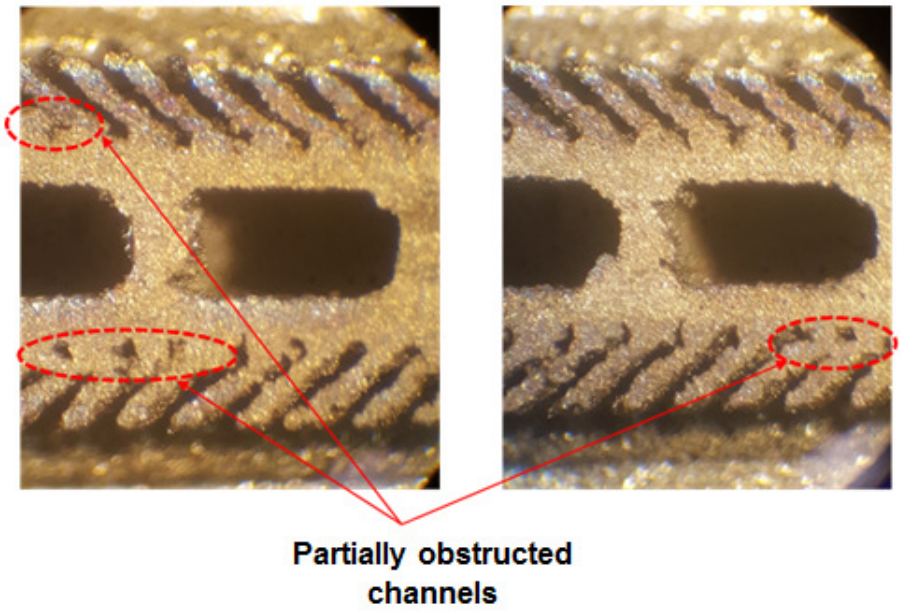

Figure 58: Microscopic view of the fins and microchannels of Ti64-2

The assembly test sections for the titanium and stainless-steel heat exchangers are shown in Figure 59. Water and air headers were added to distribute the water and air flow to the HX cores. Both headers were manufactured by 3-D printing using nylon.

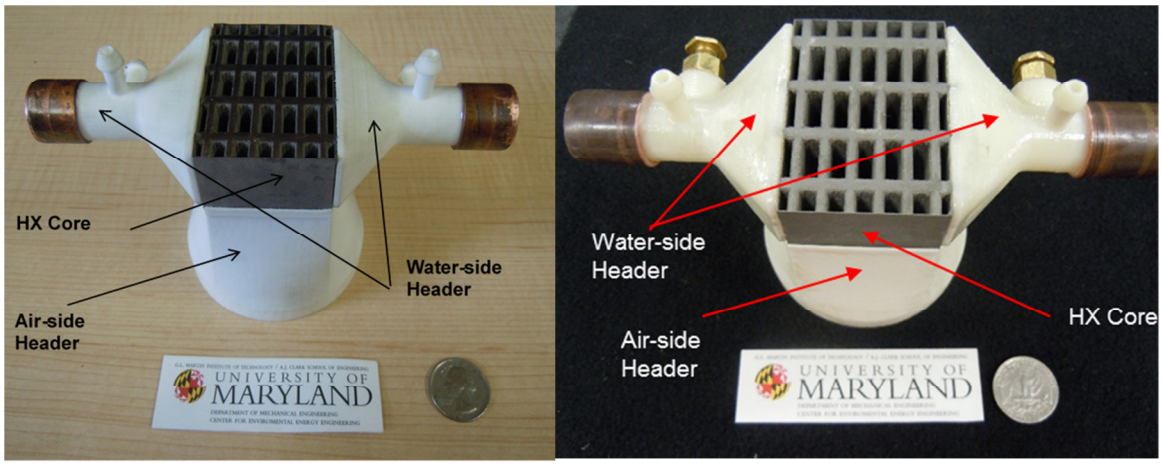

(a) (b)

Figure 59: Assembly test section (a) Titanium alloy (b) Stainless steel

7.3. Experimental Setup

A schematic diagram of the experimental test setup is shown in Figure 60. The air-side flow path consisted of an open loop with a blower to drive the air flow. To control the

air-side mass flow rate, a Variable Speed Controller (VSC) was used to control the amount of voltage supplied to the blower. A heat exchanger was used on the air side to control the air temperature before it entered the test section. On the other hand, the water-side flow path consisted of a closed loop with a chiller to drive and control the water temperature. On both sides, flow meters, differential pressure transducers, and thermocouples were used to measure the mass flow rate, pressure drop, and temperature, respectively. Due to the low temperature difference in the inlet and outlet of the water side (<1 ^{o}C), a differential thermopile was utilized to measure the change in water temperature. The reading data was collected using a data acquisition (DAQ) system connected to a computer. The assembled experimental test setup is shown in Figure 61 with the test section shown attached at the end of the air flow path.

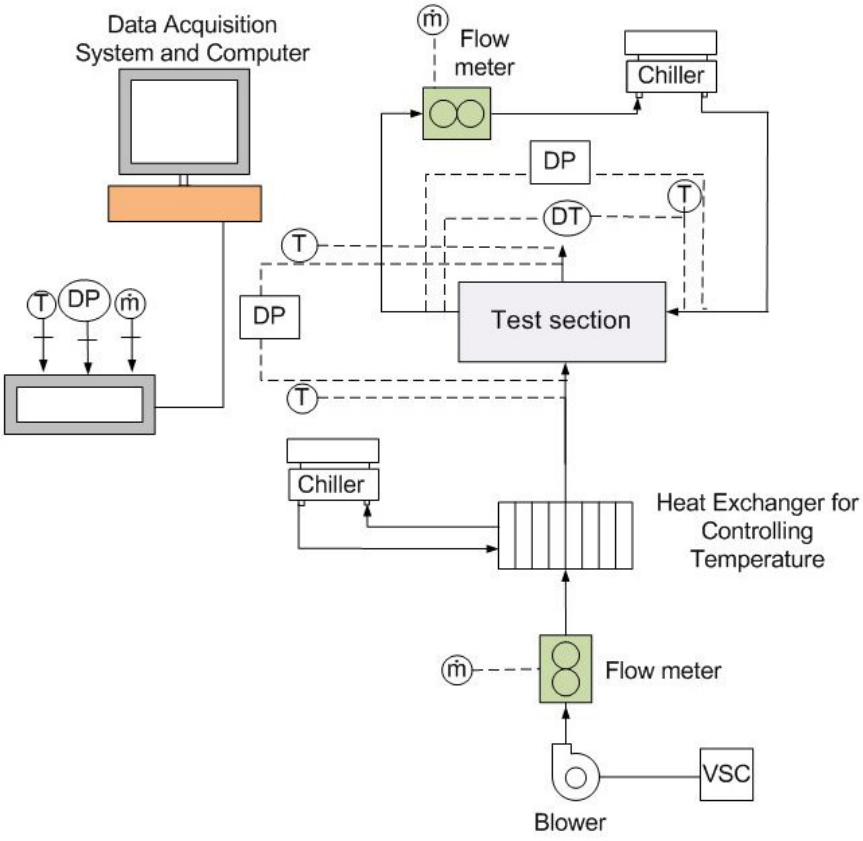

Figure 60: Schematic diagram of the experimental test setup

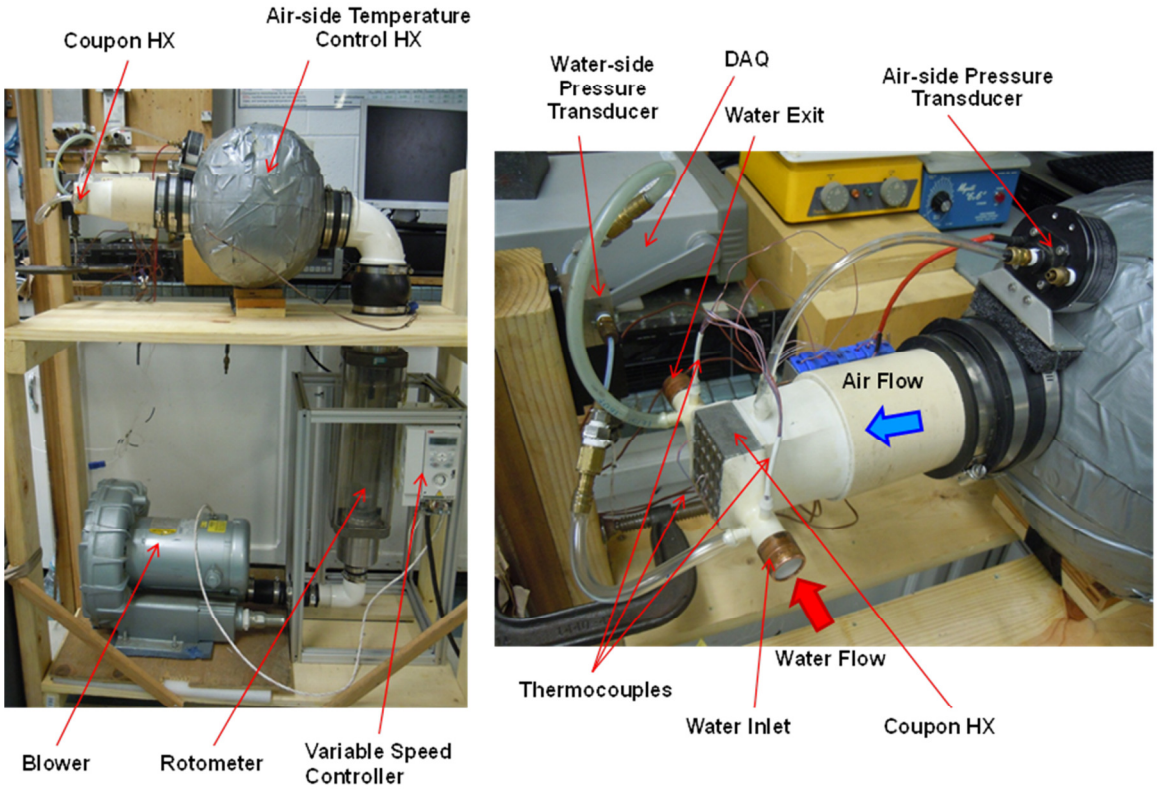

Figure 61: Assembled experimental test setup

7.4. Experimental Method and Data Reduction

The experiments were performed for the conditions shown in Table 6. The water-side inlet temperature ($T_{in,water}$) was set at 32.5 ^{o}C. In order to achieve a larger temperature difference between inlet air and water temperature, the air-side inlet temperature ($T_{in,air}$) was set at 5 ^{o}C. The experiment was performed twice: first by varying the water-side flow rate while keeping the air-side flow rate constant and second by keeping the water-side flow rate constant while varying the air-side flow rate. The purpose of the water-side flow variation was to obtain a Wilson plot to evaluate water-side convective thermal resistance ($R_{conv,water}$). For this purpose the water-side volumetric flow rate ($\dot{V}_{water}$) was varied from 0.025 L/s to 0.2 L/s while the air-side volumetric flow rate ($\dot{V}_{air}$) was kept constant at 5.9 L/s. On the other hand, when air-side volumetric flow rate was varied

from 1.89 L/s to 18.9 L/s, the water-side flow rate was kept constant at 0.1 L/s. At each flow rate variation, air-side inlet temperature ($T_{in,air}$), air-side exit temperature ($T_{out,air}$), water-side inlet temperature ($T_{in,water}$), water-side temperature difference (ΔT_{water}), air-side pressure drop (Δp_{air}), water-side pressure drop (Δp_{water}), and air-side and water-side mass flow rate ($\dot{m}_{air}$ and $\dot{m}_{water}$) were measured and recorded.

Table 6: Experimental conditions

Temperature Boundary Condition	
$T_{in,air}$	5°C
$T_{in,water}$	32.5°C
Varying Air-side	
$\dot{V}_{water}$	0.1 L/s
$\dot{V}_{air}$	1.89-18.9 L/s
Varying Water-side	
$\dot{V}_{water}$	0.025-0.2 L/s
$\dot{V}_{air}$	6.23 L/s

In order to evaluate the heat exchanger performance, heat exchanger capacity (Q), air-side base conductance ($h_{b,air}$), air-side heat transfer coefficient (h_{air}), overall heat transfer coefficient (U), and heat exchanger effectiveness (ε_{HX}) had to be evaluated.

First, the heat exchanger capacity was calculated for both the air- and water- sides as shown in Eqs. (39) - (40) below. The energy balance between both sides was found to be within 1-18% of each other. For consecutive calculations, the heat exchanger capacity (Q) was evaluated as the average of air-side (Q_{air}) and water side (Q_{water}) capacity as shown in Eq. (41).

$$Q_{air} = \dot{m}_{air} c_{p,air} (T_{out,air} - T_{in,air}) \tag{39}$$

$$Q_{water} = \dot{m}_{water} c_{p,water} (T_{in,water} - T_{out,water}) \tag{40}$$

$$Q = 0.5(Q_{air} + Q_{water}) \tag{41}$$

Next, the water-side wall conductance ($h_{b,water}$) can be evaluated as:

$$h_{b,water} = \frac{1}{A_{base}(R_{conv,water} + R_{base} + R_{cal,water})} \tag{42}$$

$$R_{cal,water} = \frac{1}{2\dot{m}_{water} c_{p,water}} \tag{43}$$

$$R_{base} = \frac{H_{base}/2}{k_{solid} A_{base}} \tag{44}$$

where $R_{cal,water}$ and R_{base} are water side caloric and conductive base thermal resistances, respectively and $R_{conv,water}$ is the water-side convective thermal resistance calculated using Wilson plot of UA (Overall heat transfer area times area) v.s. v_{water}^{η} where $\eta = 0.8$ as described in Ref. [176].

In chapter 5.3.1, a method to relate the capacity of a cross flow manifold-microchannel heat exchanger (Q) with air-side and water-side base conductance ($h_{b,air}$ & $h_{b,water}$), mass flow rate ($\dot{m}_{air}$ & $\dot{m}_{water}$), and inlet temperature ($T_{in,air}$ & $T_{in,water}$) was described. Using the same method, air-side base conductance can be back calculated using the known water-side base conductance, heat exchanger capacity, air-side and water-side mass flow rate and inlet temperature.

After calculating the air-side base conductance, the air-side heat transfer coefficient can then be calculated. The air-side base conductance can be derived as:

$$h_{b,air} = \frac{1}{A_{base}(R_{conv,air} + R_{base} + R_{cal,air})} \tag{45}$$

$$R_{cal,air} = \frac{1}{2\dot{m}_{air} c_{p,air}} \tag{46}$$

$$R_{conv,air} = \frac{1}{h_{air} \eta_{HX,air} A_{H,air}} \tag{47}$$

$$\eta_{HX,air} = 1 - \frac{A_{fin,air}}{A_{H,air}} \left(1 - \eta_{fin,air}\right) \tag{48}$$

$$\eta_{fin,air} = \frac{tanh\left(M_{air} H_{chn,air}\right)}{\left(M_{air} H_{chn,air}\right)} \tag{49}$$

$$M = \sqrt{\frac{2h_{air}}{k_{solid} t_{fin,air}}} \tag{50}$$

where $R_{conv,air}$ is air-side convection resistance, $R_{cal,air}$ is air-side caloric resistance, $A_{H,air}$ is air-side heat transfer area, $A_{fin,air}$ is air-side fins area, $\eta_{HX,air}$ is air-side overall surface efficiency, and $\eta_{fin,air}$ is air-side fin efficiency. By using Eqs. (45) - (50), the air side heat transfer coefficient (h_{air}) was calculated using the previously calculated air-side base conductance, air-side mass flow rate, and air-side geometry.

The overall heat transfer coefficient (U) then can be calculated as:

$$U = \frac{1}{A_{base}(R_{conv,air} + 2 * R_{base} + R_{conv,water})} \tag{51}$$

where $R_{conv,air}$ is air-side convective thermal resistance as described in Eq. (6). It should be noted that the overall heat transfer coefficient calculated here is based on the base heat transfer area.

Lastly the heat exchanger effectiveness (ε_{HX}) can be evaluated as:

$$\varepsilon_{HX} = \frac{Q}{\min(C_{water}, C_{air})\left(T_{in,water} - T_{in,air}\right)} \tag{52}$$

where $C_{water} = \dot{m}_{water} c_{p,water}$, $C_{air} = \dot{m}_{air} c_{p,air}$.

For repeatability analysis, the experiments were run twice for each heat exchanger. The heat transfer and pressure drop performances were evaluated to be within 5% for both runs.

7.5. Uncertainty Analysis

Uncertainty propagation analysis was performed to calculate the inaccuracy in the heat exchanger performance ($Q, h, h_b, U, \Delta p, \varepsilon_{HX}$) due to inaccuracy in the measurements. A list of measurement equipment is shown in Table 24 with their corresponding accuracies. Based on the method explained in NIST Technical Note 1297 [177], the uncertainty of calculated quantity Y (U_Y) which is a function of $X_1, X_2, \ldots, X_N$ with uncertainty of $U_{X_1}, U_{X_2}, \ldots, U_{X_N}$ can be calculated as:

$$U_Y = \sqrt{\sum_i \left(\frac{\partial Y}{\partial X_i}\right)^2 U_{X_i}^2} \tag{53}$$

Using this method the uncertainties for all heat exchanger performance parameters ($Q, h, h_b, U, \Delta p, \varepsilon_{HX}$) were calculated, and the error bars are included in the results presented in the next sections.

Table 24: List of measurement equipment and their accuracy

Equipment Function	Equipment Name	Accuracy
Air-side flow rate	Fischer Porter F Rotameter (Model#: 10A4557SS)	$\pm 2\%$
Water-side flow rate	Endress Hauser PromassF (Model#: 82Fit331582)	$\pm 0.1\%$
Temperature	T type thermocouple	$\pm\ 0.5^{o}C$
Air-side pressure drop	Setra pressure transducer (Model#: 239)	0.14% FS of 5 inch H20 (For Δp < 1kPa) 0.14% FS of 50 inch H20 (For Δp > 1kPa)
Water-side pressure drop	Validyne P55 general purpose pressure transducer (Model#: P55D 4-N-1-36-S-4-S)	0.25% FS of 35kPa

7.6. Experimental Results

7.6.1. Heat Transfer Performance

The heat transfer performances of all five heat exchangers are shown in Figure 62 for the case of varying air-side flow rate while keeping the water flow rate of 0.1 L/s. The results are plotted as a function of air-side flow rate and Reynolds number (Re_{air}), which is calculated as [5]:

$$Re_{air} = \frac{DG_{air}}{\mu_{air}} \tag{54}$$

$$D = 2 * \frac{H_{chn,air} W_{chn,air}}{H_{chn,air} + W_{chn,air}} \tag{55}$$

Where G is mass flux on the microchannels and $H_{chn,air}$ and $W_{chn,air}$ are microchannel height and width as defined in Table 19.

The heat transfer performances of the heat exchangers built from the same material (Ti64 – 1 with Ti64 – 2 and SS17-4 – 1with SS17-4 – 2) were compared. As shown in Figure 62, the performance of both Ti64 heat exchangers are very close to each other (within 10%). On the other hand, the performance deviation between both stainless steel heat exchangers is much higher.

The capacity (Q) of the coupon heat exchangers is shown in Figure 62 (a) for temperature difference between inlet air and water of 27.5 °C. The graph shows heat exchanger capacity up to 200 W, 300 W, and 400 W are possible for Ti64, SS17-4, and AlSi10Mg heat exchangers, respectively. Figure 62 (b) shows that overall heat transfer coefficients (U) of 75-1100 W/m^{2}K, 100-1700 W/m^{2}K, and 100-3000 W/m^{2}K were reported for Ti64, SS17-4, and AlSi10Mg heat exchangers, respectively. Heat exchanger effectiveness (ε_{HX}) up to 92%, 95%, and 99% was observed for Ti64, SS17-4, and AlSi10Mg heat exchangers, respectively, as shown in Figure 62 (c). Air-side heat transfer coefficient (h_{air}) and base conductance $(h_{b,air})$ results were shown in Figure 62 (d) and (e). Air-side heat transfer coefficient in the range of 100-450 W/m^{2}K, 100-600 W/m^{2}K, and 100-900 W/m^{2}K were observed for Ti64, SS17-4, and AlSi10Mg heat exchangers, respectively. For the base conductance, air-side base conductance in the range of 200-1000 W/m^{2}K, 200-1500 W/m^{2}K, and 200-2000 W/m^{2}K were observed for Ti64, SS17-4, and AlSi10Mg heat exchangers, respectively.

Analyzing the overall trend, heat exchanger capacity, overall heat transfer coefficient, air-side base conductance, and air-side heat transfer coefficient all increase as Reynolds number increases. This trend is as expected, as for the case of flow in the developing

region, increasing flow rate leads in an increase in heat transfer coefficient which subsequently increase both the heat exchanger capacity and overall heat transfer coefficient.

Comparing the performance of the five heat exchangers, the aluminum heat exchanger yielded the highest Q, U, ε_{HX}, and $h_{b,air}$ followed by the stainless-steel heat exchangers and titanium alloy heat exchangers. Such trend was expected as aluminum has the highest thermal conductivity (k=174W/mK) followed by stainless-steel (k=13W/mK), and titanium alloy (k=6.7W/mK) [178-180]. However, due to manufacturing inaccuracy and partial clogging as mentioned previously, heat exchanger prototypes fabricated from different materials delivered different heat transfer coefficients despite the fact that all five of them were based on the same original geometry. Otherwise, heat transfer coefficient obviously should not depend on the material property.

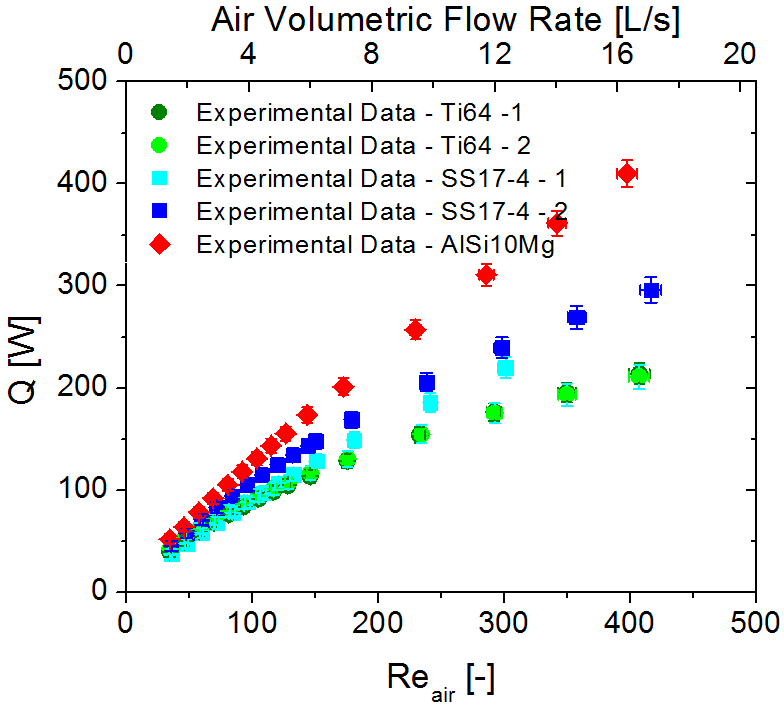

(a)

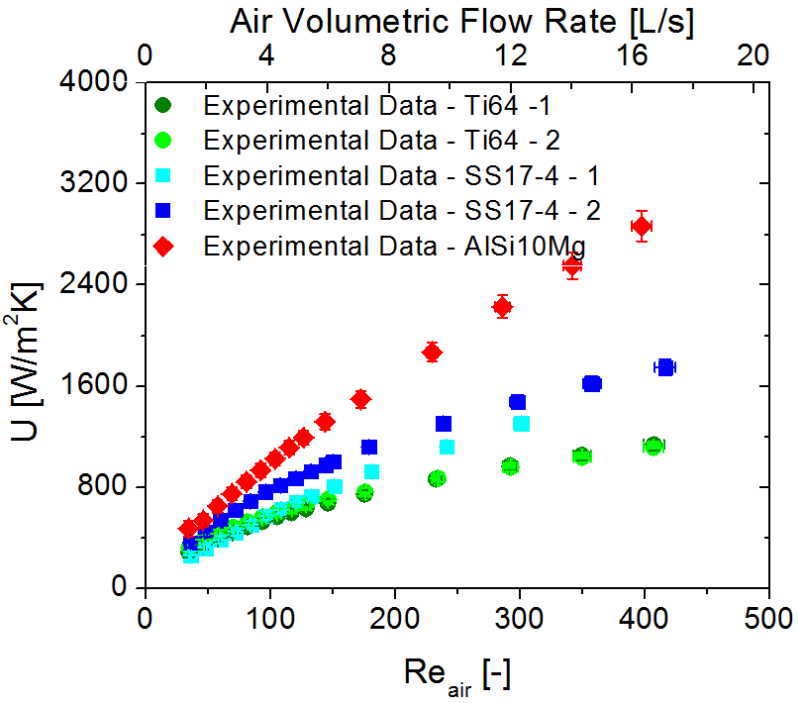
Air Volumetric Flow Rate [L/s]
0
4
8
12
16
20
4000
3200
2400
1600
800
0
U [W/m²K]
Experimental Data - Ti64 -1
Experimental Data - Ti64 - 2
Experimental Data - SS17-4 - 1
Experimental Data - SS17-4 - 2
Experimental Data - AlSi10Mg
0
100
200
300
400
500
Re air [-]

(b)

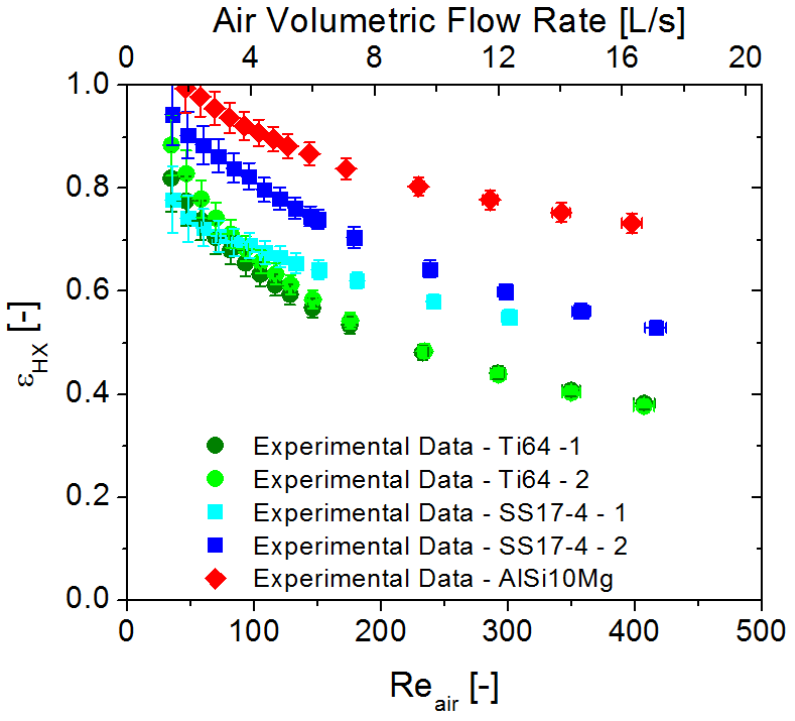
Air Volumetric Flow Rate [L/s]
0
4
8
12
16
20
1.0
0.8
0.6
0.4
0.2
0.0
ε HX [-]
Experimental Data - Ti64 -1
Experimental Data - Ti64 - 2
Experimental Data - SS17-4 - 1
Experimental Data - SS17-4 - 2
Experimental Data - AlSi10Mg
0
100
200
300
400
500
Re air [-]

(c)

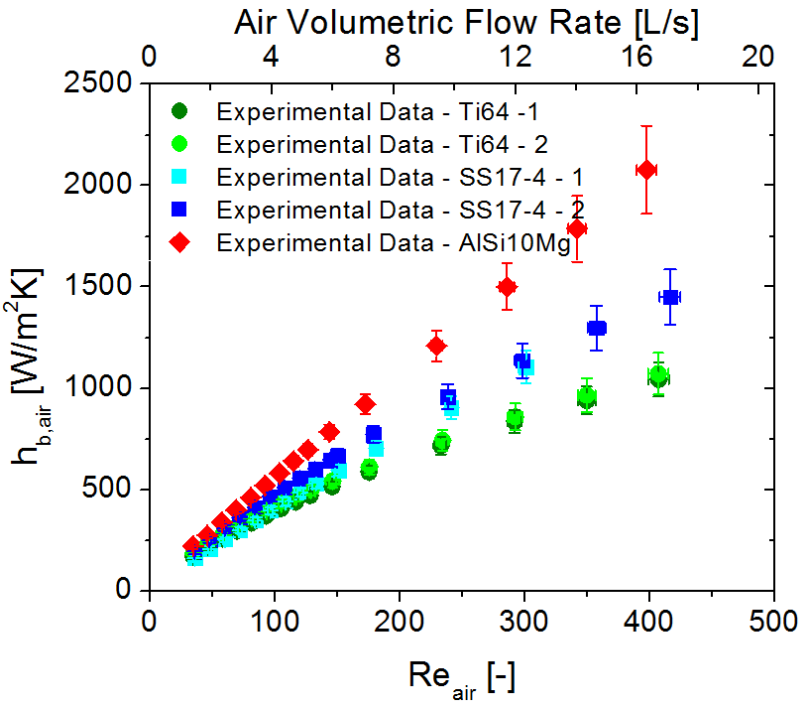

(d)

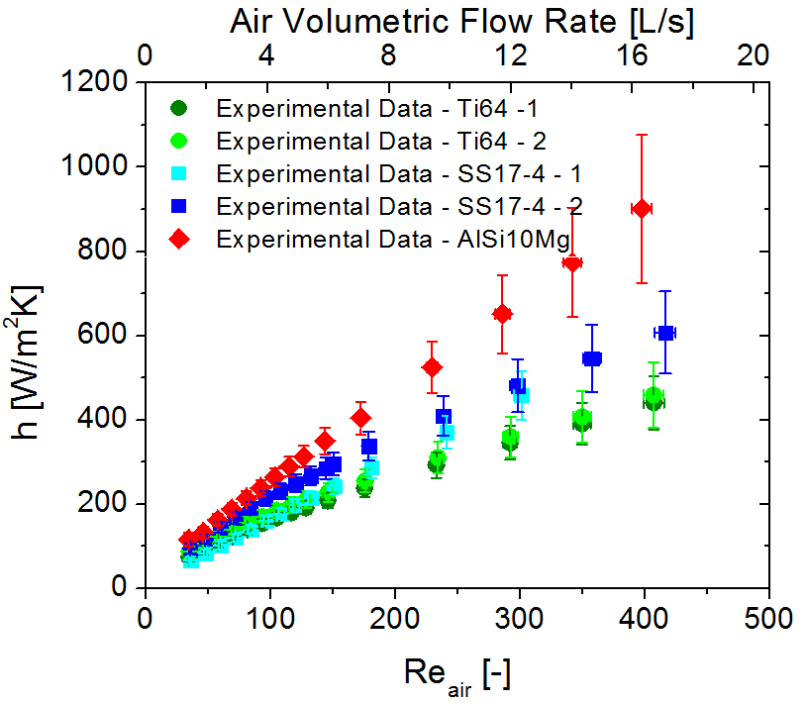

(e)

Figure 62: Heat transfer performance (for constant water flow rate of 0.1L/s): (a) Heat exchanger capacity, (b) Overall heat transfer coefficient, (c) Heat exchanger effectiveness, (d) Air-side base conductance, and (e) Air-side heat transfer coefficient

The overall heat transfer coefficient performance as a function of water-side Reynolds number and flow rate are presented in Figure 63 as evaluated at the air-side design point ($\dot{V}_{air}$ = 6.23 L/s). The same equation as derived in Eqs. (54)- (55) can be used to evaluate the water-side Reynolds numbers by using water-side geometry and flow rate. Analyzing the trend, it can be seen that overall heat transfer coefficient is not significantly affected by water side mass flow rate. This shows that the air-side thermal resistance is much more dominant than the water-side. Only at low Reynolds number (Re_{water}<1500) does water flow rate shows some effect on the overall heat transfer coefficient.

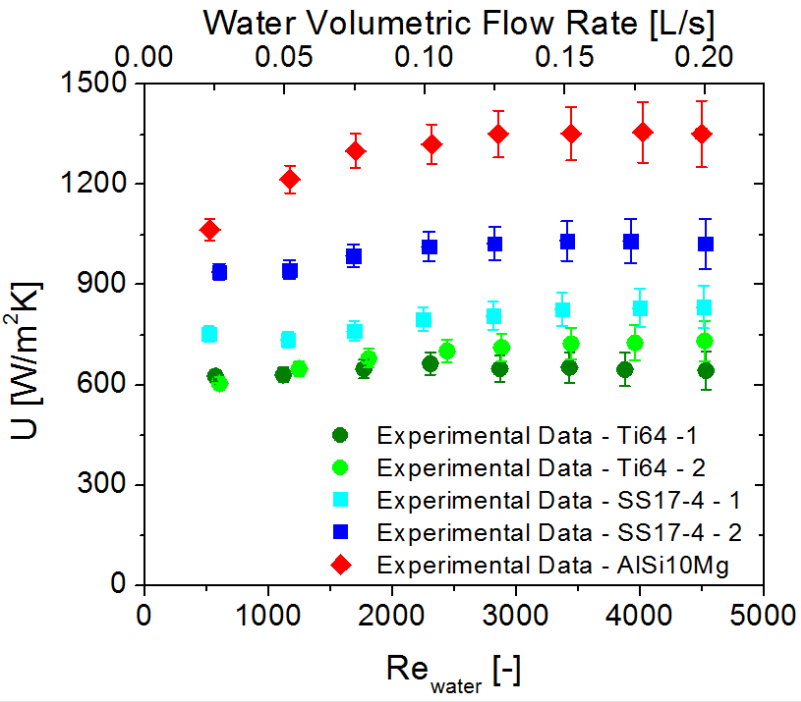

Figure 63: Heat transfer performance (for constant air flow rate of 6.23 L/s): Overall heat transfer coefficient

7.6.2. Pressure Drop Performance

The air-side pressure drop for all five coupon heat exchangers (Δp_{air}) is shown in Figure 64 as a function of air-side Reynolds number and flow rate. The trend is as expected where pressure drop increases as a function of flow rate. However, comparing the performance of all five heat exchangers, difference performances were noted for some of them. Both titanium alloy heat exchangers' pressure drop performances were similar, in the range of 50-2000 Pa. However, there was significant difference between the pressure drops of the stainless-steel heat exchangers. Pressure drop of SS17-4 – 2 heat exchanger was in the range of 200-7000 Pa, while the pressure drop of the SS17-4 – 1 heat exchanger was more than double that of SS17-4 – 2. Lastly the pressure drop of AlSi19Mg heat exchanger was close to the SS17-4 – 2 heat exchanger in the range of 200-7000 Pa. As for the case of heat transfer coefficient, this variation can only result from manufacturing inaccuracies (in fin thickness and microchannel width) and partial clogging on some of the channels. Looking at the trend, titanium alloy shows the most promise to be manufactured by 3-D printing as it yields the lowest pressure drop (lowest manufacturing inaccuracy), while SS17 – 1 shows the worst fabrication quality, as its pressure drop is significantly higher than the other surfaces.

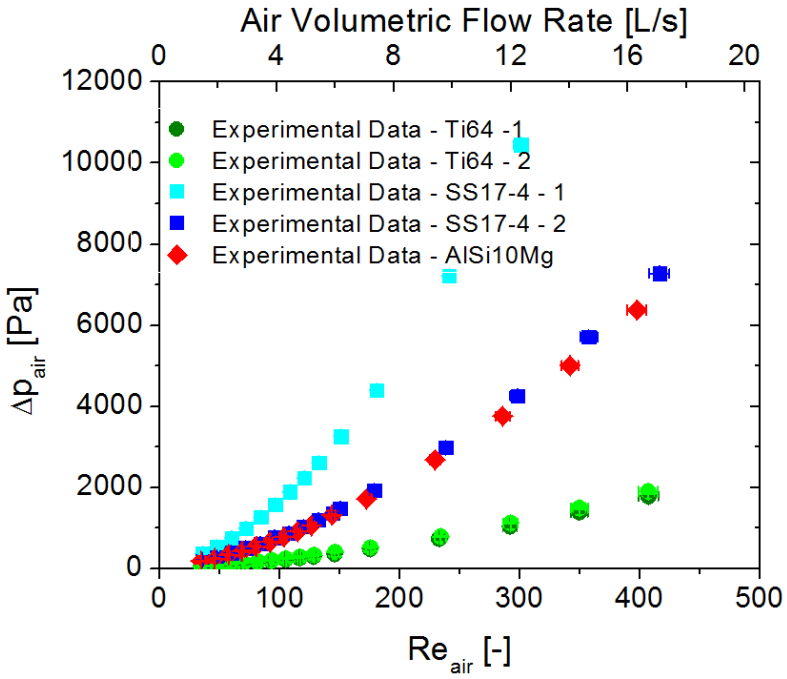

Figure 64: Air-side performance: Air-side pressure drop

7.6.3. Comparison with Numerical Results

The air-side base conductance and pressure drop were compared with the numerical method mention in chapter 5.3. The performance comparison was performed for the Ti64-2 heat exchanger, as its actual fin and microchannel sizes are known. The comparison between the numerical and experimental results are shown in Figure 65. Compared to the numerical values of the actual fins size (t_{fin}=235µm), there is a slight drop in the base conductance and slight increase in pressure drop. The average percentage error between the numerical and experimental results is calculated as 18% and 12% for pressure drop and base conductance, respectively, for Reynolds number in the range of 250 to 400. One of the possible causes of the deviation is due to microchannel geometrical non-uniformity, as reported in chapter 7.2.2. Another possible cause is clogging in some of the microchannels. Clogging can reduce the flow area and heat transfer area, which in turn can increase pressure drop and reduce base conductance. Compared to the predicted values, if the fin thickness and microchannel width were

fabricated properly at 150 µm and 270 µm as requested, there was significant increase in pressure drop as shown in Figure 65(b) due to significant reduction in the flow area.

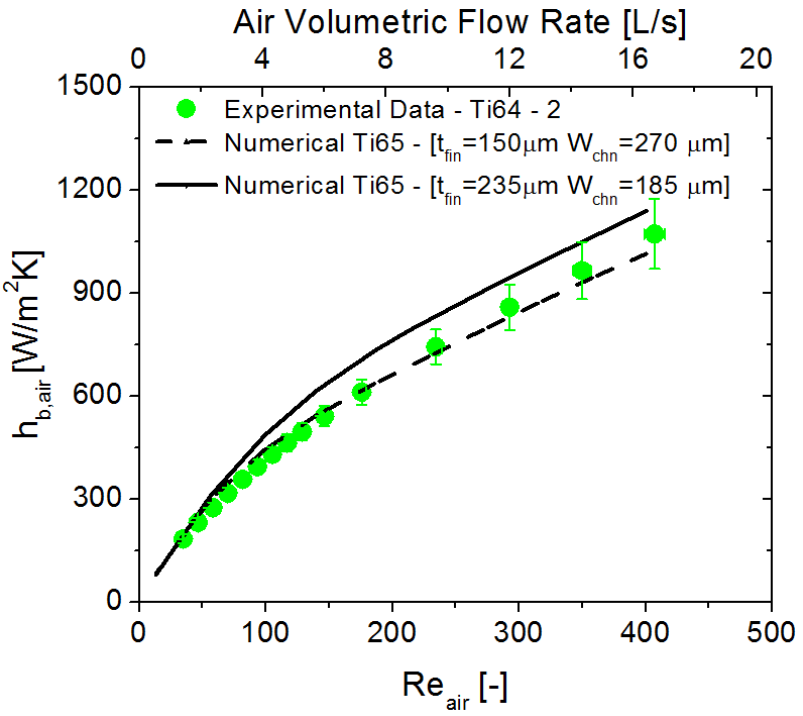

(a)

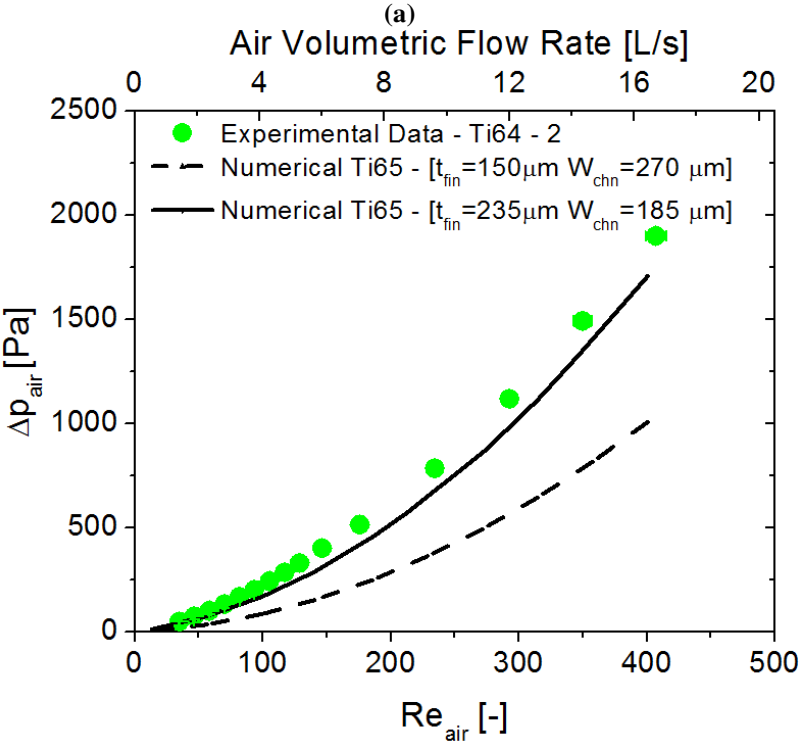

(b)

Figure 65: Comparison between experimental and numerical results of Ti64-2 HX (a) $h_{b,air}$ (b) Δp_{air}

7.6.4. Effect of Microchannel Non-uniformity on Heat Exchanger Performances

A study was performed to examine the effect of the microchannel geometrical non-uniformity on the heat exchanger performances (pressure drop and heat transfer). Evaluating the impact of all geometrical non-uniformities on performances of the heat exchanger can be challenging without performing a full size CFD simulation of the entire heat exchanger. However, a full size CFD modeling of the manifold-microchannel heat exchanger with non-uniform microchannels is a challenging process, as it consisted of approximately 40 microchannels. But, for a simple case of a non-uniform manifold-microchannel heat exchanger which only has two variations in the microchannel width, half of the channels sizes are $W_{chn,1}$ and the other half are $W_{chn,2}$, its performance prediction can be significantly simplified. Figure 66 shows an example of a non-uniform manifold-microchannel heat exchanger where the first three microchannels have widths of $W_{chn,1}$ and the last three microchannels have widths of $W_{chn,2}$.

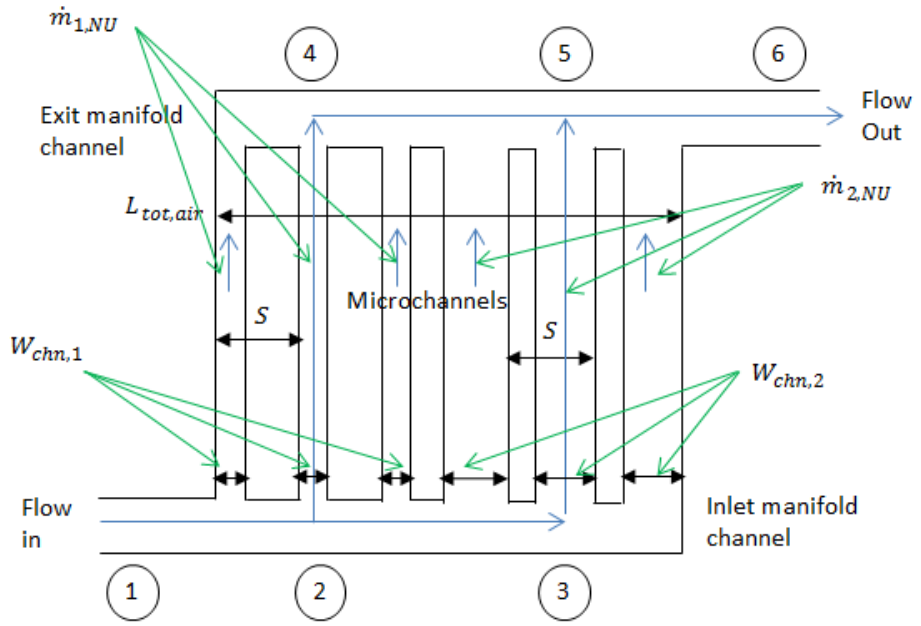

Figure 66: Manifold-microchannel heat exchanger with non-uniform microchannels

A method to predict the pressure drop performance of a non-uniform manifold-microchannel heat exchanger using the performance of uniform manifold-microchannel heat exchangers was discussed here. The uniform manifold-microchannel heat exchanger performance can be evaluated without having to model the entire heat exchanger by using the modified hybrid method proposed in chapter 5.3.2. As a result, using the proposed method, the performance of the non-uniform manifold-microchannel heat exchanger can be evaluated without having to model the full heat exchanger as well. As the non-uniform manifold-microchannel heat exchanger has two microchannel width variations, as shown in Figure 66, two uniform manifold-microchannel heat exchangers: one with microchannel width of $W_{chn,1}$ (Label as HX1) and the other with microchannel width of $W_{chn,2}$ (Label as HX2), as shown in Figure 67 were required. So that the uniform manifold-microchannel heat exchangers model can represent the non-uniform model (labeled as HX3), all other geometrical variables beside the microchannel widths have to be the same for HX1, HX2, and HX3. Lastly, in order to maintain the same total length ($L_{tot,air}$) and number of microchannels (n) for all the heat exchangers, the fin spacing (S), as shown in Figure 66 and Figure 67, must always be set to be constant for all heat exchangers.

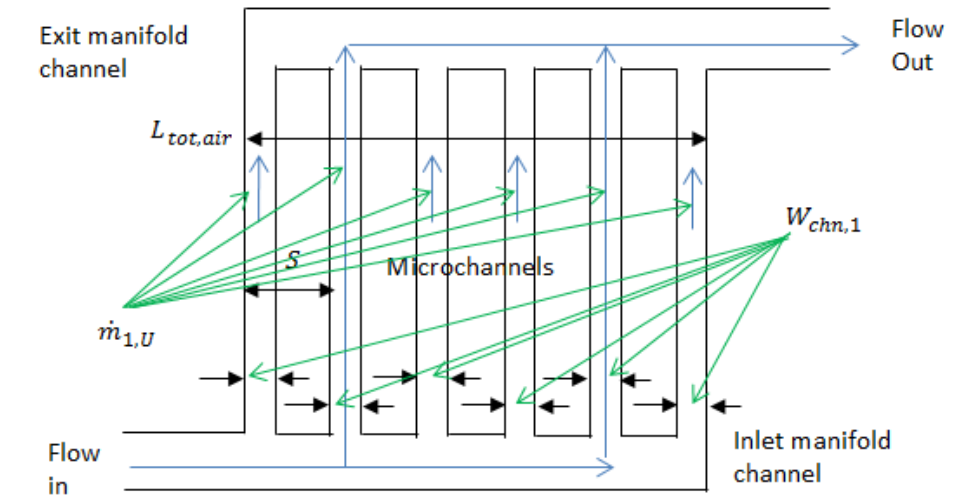

(a)

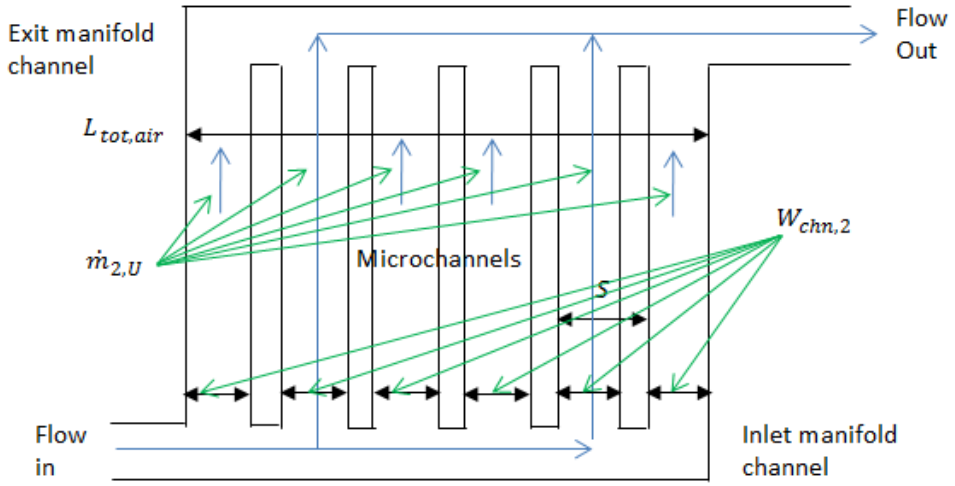

(b)

Figure 67: Manifold-microchannel heat exchanger with uniform microchannels (a) With microchannel width of $W_{chn,1}$ (b) With microchannel width of $W_{chn,2}$

So that the performance of the uniform manifold-microchannel heat exchanger (HX1 & HX2) can represent the non-uniform manifold-microchannel heat exchanger's (HX3) performance, an equation that relates the mass flow rate and pressure drop of all heat exchangers needs to be derived. For the non-uniform manifold-microchannel heat exchanger, it is assumed that the flow maldistribution is only caused by the non-uniformity on the microchannel size. This is a valid assumption as the manifold-microchannel heat exchanger that was fabricated and tested in the current work was

designed for low maldistribution. As a result, the microchannel non-uniformity that accidently happened due to fabrication inaccuracy is the only factor that could have caused flow maldistribution. Based on this assumption, there are two different flow rates in the microchannels. The first flow rate, $\dot{m}_{1,NU}$, is for the case of microchannel width of $W_{chn,1}$ and the second variation, $\dot{m}_{2,NU}$, is for the case of microchannel width of $W_{chn,2}$ as shown in Figure 66. In order for HX1 and HX2 to represent HX3 performance, the mass flow rate per channel in HX1 ($\dot{m}_{1,U}$) needs to be equal to $\dot{m}_{1,NU}$ and mass flow rate per channel in HX2 ($\dot{m}_{2,U}$) need to be equal to $\dot{m}_{2,NU}$ as shown in Eq. (56) and (57). For visualization of $\dot{m}_{1,U}$ and $\dot{m}_{2,U}$ please refer to Figure 67.

$$\dot{m}_{1,U} = \dot{m}_{1,NU} \tag{56}$$

$$\dot{m}_{2,U} = \dot{m}_{2,NU} \tag{57}$$

$\dot{m}_{1,NU}$ and $\dot{m}_{2,NU}$ can be related to the known value of the total mass flow rate of the non-uniform manifold-microchannel heat exchanger ($\dot{m}_{tot,NU}$) as:

$$\dot{m}_{1,NU}\frac{n}{2} + \dot{m}_{2,NU}\frac{n}{2} = \dot{m}_{tot,NU} \tag{58}$$

where n is total number of microchannels. By combining Eq. (58) with Eqs. (56) and (57), Eq. (58) can also be rewritten as:

$$\dot{m}_{1,U}\frac{n}{2} + \dot{m}_{2,U}\frac{n}{2} = \dot{m}_{tot,NU} \tag{59}$$

In addition, for manifold-microchannel, the total pressure drop calculation (Δp) should be independent from the flow path ($\Delta p = \Delta p_{16} = \Delta p_{12} + \Delta p_{24} + \Delta p_{46} = \Delta p_{13} + \Delta p_{35} + \Delta p_{56}$) as shown in Figure 66. As a result, so that the pressure drop for the non-uniform manifold-microchannel heat exchanger can be represented by the pressure drop of the

uniform manifold-microchannel heat exchanger, the total pressure drop in all three heat exchangers: HX1 (Δp_{HX1}), HX2 (Δp_{HX2}), and HX3 (Δp_{HX3}), needs to be set as equal as shown in Eq. (60). The main assumption is that the pressure drop in the microchannel is more dominant than the pressure drop in the manifold channels. As a result, although all three heat exchangers can have different mass flow rates in the manifold channels, its effect on the total pressure is not significant.

$$\Delta p_{HX1} = \Delta p_{HX2} = \Delta p_{HX3} \tag{60}$$

By finding the mass flow rate combination of the HX1 and HX2 which satisfies Eq. (59) and (60), the pressure drop and microchannel flow rate distribution of the non-uniform manifold-microchannel heat exchanger can be evaluated.

Base conductance can be evaluated by dividing the non-uniform manifold-microchannel heat exchanger into segments each with the same microchannel size. The non-uniform heat exchanger shown in Figure 66 consists of two segments with microchannel size of $W_{chn,1}$ and $W_{chn,2}$ in parallel. By assuming that there is no heat transfer between each segment, the overall base conductance (h_b) can be evaluated using a thermal circuit analysis as:

$$\frac{1}{R_{tot}} = \frac{1}{R_1} + \frac{1}{R_2} \tag{61}$$

$$R_{tot} = \frac{1}{h_b A_{base}} \tag{62}$$

$$R_1 = \frac{1}{h_{b,1} A_{base}/2} \tag{63}$$

$$R_2 = \frac{1}{h_{b,2} A_{base}/2} \tag{64}$$

where $h_{b,1}$ and $h_{b,2}$ are base conductance for segments with microchannel size of $W_{chn,1}$ and $W_{chn,2}$ respectively. The base conductance in each segment can be evaluated using a CFD simulation of the single manifold-microchannel model as proposed in chapter 5.3.2. For the mass flow rate input, the mass flow rate per channel ($\dot{m}_{1,NU}$ and $\dot{m}_{2,NU}$) previously calculated can be used.

Lastly, a variable K is defined to represent the non-uniformity of the microchannel size as the ratio between the microchannel with variation and its average value as:

$$K = \frac{\left|W_{chn,1} - W_{chn,2}\right|}{0.5(W_{chn,1} + W_{chn,2})} \tag{65}$$

To be noted, the actual manifold-microchannel design consisted of 39 channels, as microchannel non-uniformity was evaluated by assuming two channels, so the K value may not represent the actual microchannel non-uniformity. But, it may represent the extreme case when half of the channels size are $K/2$ % larger than average and the other half is $K/2$ % smaller than the average.

The effect of the microchannel non-uniformity on the heat exchanger performance is shown in Figure 68 for both pressure drop and base conductance. Analyzing the figure, microchannel non-uniformity (R) causes an increase in pressure drop and decrease in base conductance, which in overall reduces the heat exchanger performance. As microchannel non-uniformity increases, the numerical results get closer to the experimental results. This confirms that microchannel non-uniformity is one of the possible causes of the deviation between the numerical and the experimental results. As discussed in chapter 7.2.2., up to 20% deviation in microchannel size was noticed ($K = 0.4$) for the Ti64-2 test coupon. Comparing the performance for the case of

$K = 0.4$ with the experimental results, some deviation was still noticed. This deviation may be due to partial obstruction on some of the channels, as channel obstruction can reduce the flow area and heat transfer area, which in turn can increase pressure drop and reduce base conductance. These results show that the numerical method previously proposed in Chapter 5 can predict the performance of the manifold microchannel heat exchanger with high accuracy.

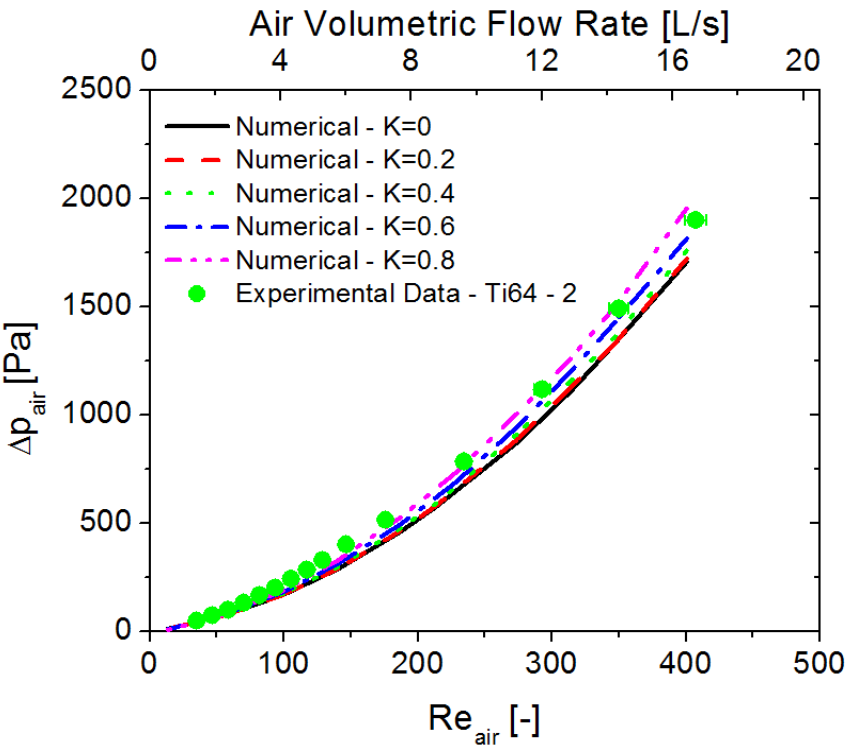

(a)

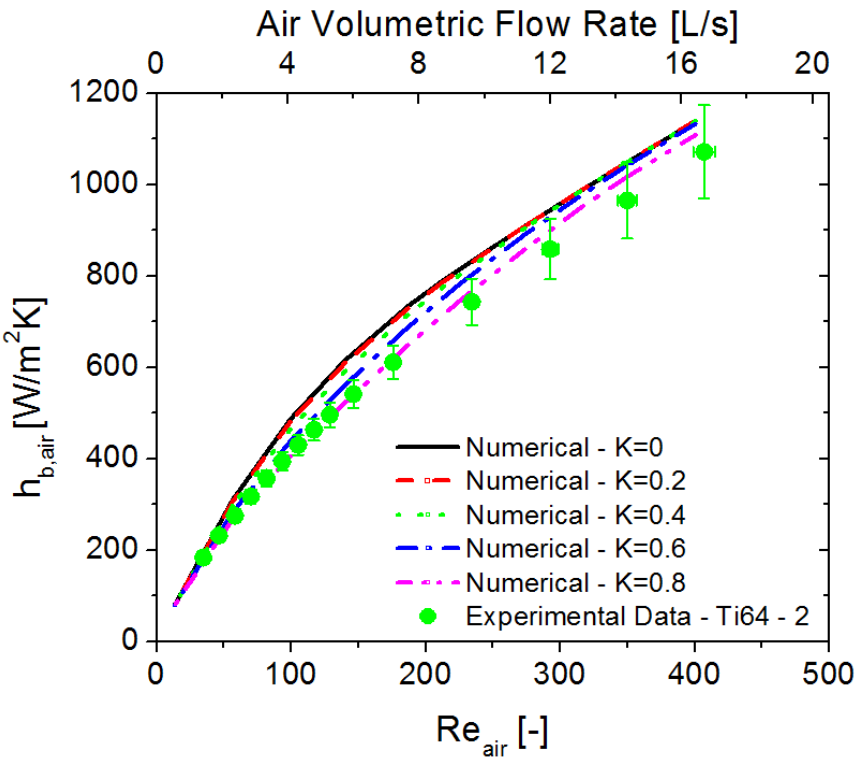

(b)

Figure 68: Effect of the microchannel non-uniformity on the heat exchanger performance: (a) Pressure drop, (b) Base conductance

7.6.5. Comparison with Conventional Technology

The manifold-microchannel performance was then compared with the conventional surface performance (wavy fin, plain plate fin, louvered fin, pin fin, and strip fin) in term of pressure drop (Δp_{air}), base conductance ($h_{b,air}$), and heat transfer coefficient (h_{air}). The conventional surface geometries were based on the best surface from the optimization results stated in chapter 6.3.2 at design specification of $COP/\Delta T = 6.25$.

The performance comparison for aluminum alloy (AlSi10Mg) manifold-microchannel heat exchanger surface with the conventional surfaces is shown in Figure 69. A plot showing the performance prediction if the fins can be fabricated properly at 150 μm is also included. Comparing the air-side base conductance in Figure 69 (a), for the same pressure drop, the manifold microchannel yielded higher performance over plain plate fin, louvered fin, and pin fin at the region of high pressure drop, Δp_{air}>500Pa. However,

at low pressure drop, Δp_{air}<500Pa, its performance is equivalent to louvered fin and pin fin. Comparing the air-side heat transfer coefficient in Figure 69(b), manifold-microchannels yield superior performance over most of the conventional surfaces at the region of Δp_{air}>750Pa. Up to 40% improvement is possible compared to wavy fins for the same pressure drop. At low pressure drop ($\Delta p_{air} < 500$Pa), the manifold-microchannel is still superior to wavy fin, plain plate fin, and louvered fin. But, it is inferior to pin fin and strip fin. If 150 μm fins can be fabricated, both base conductance and heat transfer coefficient can be significantly improved. Manifold-microchannel performance will be superior to all conventional surfaces for the entire pressure drop range. Compared to wavy fin, up to 105% and 95% improvement in base conductance and heat transfer coefficient is possible for the same pressure drop. A summary of the percentage improvement of aluminum alloy manifold microchannel conventional surfaces is shown in Table 25.

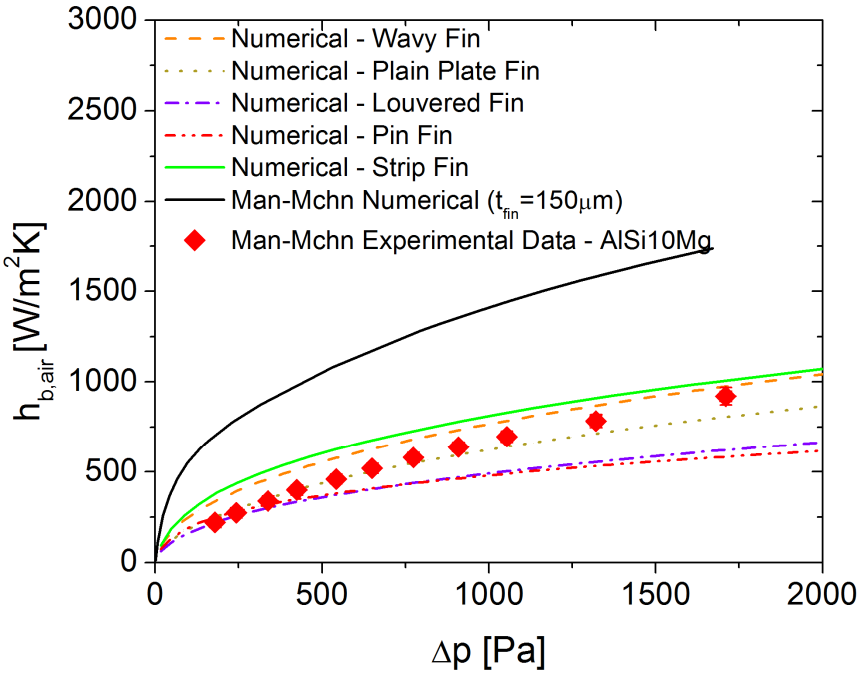

(a)

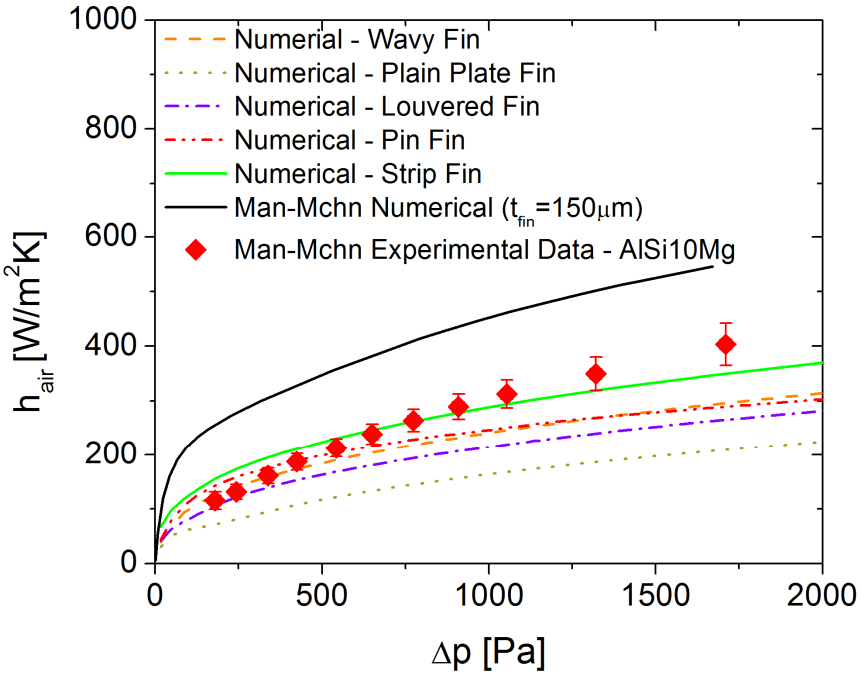

(b)

Figure 69: Performance comparison between AlSi10Mg manifold-microchannel HX with conventional HX: (a) $h_{b,air}$ $vs.$ Δp_{air} (b) h_{air} $vs.$ Δp_{air}

Table 25: % improvement of AlSi10Mg manifold-microchannel over conventional HX for $100 < \Delta p_{air} < 2000$

Conventional Surface	% Improvement for $h_{b,air}$		% Improvement for h_{air}	
	AlSi10Mg	AlSi10Mg – $t_{fin} = 0.15mm$ (Num)	AlSi10Mg	AlSi10Mg – $t_{fin} = 0.15mm$ (Num)
Wavy-fin	-30% to -5%	75% to 105%	-10% to 40%	75% to 95%
Plain Plate-fin	-5% to 15%	115% to 175%	55% to 95%	145% to 225%
Louvered-fin	5% to 50%	175% to 215%	10% to 55%	95% to 125%
Pin-fin	-10% to 60%	185% to 200%	-20% to 45%	65% to 80%
Strip-fin	-40% to -5%	70% to 85%	-30% to 20%	45% to 55%

The performance comparison for stainless steel (SS17-4 - 1 and SS17-4 - 2) manifold-microchannel heat exchanger surfaces with the conventional surfaces is shown in Figure 70. A graph showing the predicted performance if 150 μm fins can be successfully fabricated was also included on the figures. Analyzing the graphs, the SS17-4 - 1 heat exchanger, which by far shows the worst fabrication quality, shows lower performance

compared to all conventional surfaces. On the other hand, SS17-4 - 2 heat exchanger shows better performance than conventional surfaces at the high pressure drop region.

When the air side pressure drop is higher than 1000 Pa, for the same pressure drop, SS17-4 – 2 manifold-microchannel performance is superior to all conventional surfaces in terms of base conduction as shown in Figure 70(a). Comparing the heat transfer coefficient in Figure 70(b), SS17-4 – 2 manifold-microchannel yields superior performance over all of the conventional surfaces except strip fin at the region of Δp_{air} >1000Pa. Compared to wavy fin and plain plate fin, up to 10% and 50% improvement in heat transfer coefficient is possible for the same pressure drop, respectively. However, at low pressure drop ($\Delta p_{air} <$ 500Pa), the SS17-4 – 2 heat exchanger shows superior performance only over plain plate fin surface. If 150 μm fins can be fabricated, SS17-4 – 2 manifold-microchannel performance will be superior to all conventional surfaces for the entire pressure drop range. Compared to wavy fin, up to 140% and 95% improvement in base conductance and heat transfer coefficient is possible for the same pressure drop. A summary of the percentage improvement of the stainless steel manifold microchannel conventional surfaces is shown in Table 27.

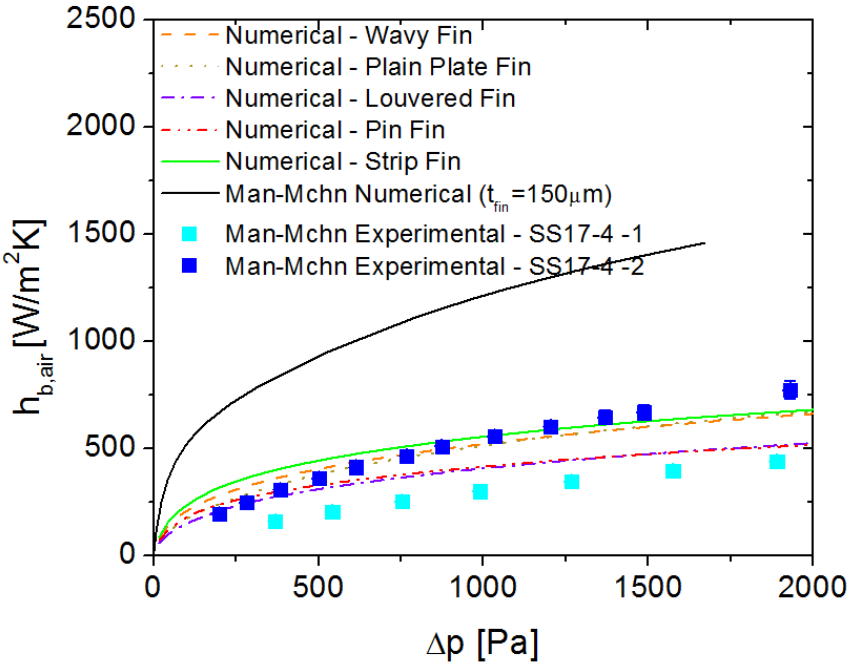

(a)

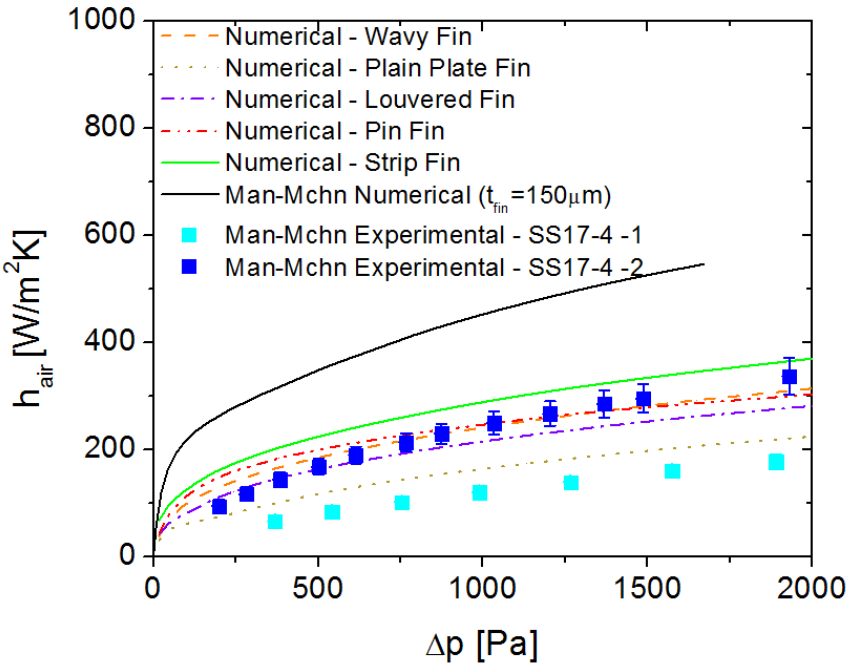

(b)

Figure 70: Performance comparison between SS17-4 manifold-microchannel HX with conventional HX: (a) $h_{b,air}$ $vs.\Delta p_{air}$ (b) h_{air} $vs.\Delta p_{air}$

Table 26: % improvement of SS17-4 manifold-microchannel over conventional HX for $100 < \Delta p_{air} < 2000$

	% Improvement for $h_{b,air}$			% Improvement for h_{air}		
	SS17-4 - 1	**SS17-4 - 2**	**SS17-4 – $t_{fin} = 0.15mm$ (Num)**	**SS17-4 - 1**	**SS17-4 – 2**	**SS17-4 – $t_{fin} = 0.15mm$ (Num)**
Wavy-fin	-55% to -30%	-25% to 20%	130% to 140%	-60% to -40%	-20% to 10%	75% to 95%
Plain Plate-fin	-50% to -30%	-15% to 15%	125% to 175%	-30% to -20%	30% to 50%	145% to 225%
Louvered -fin	-40% to -15%	5% to 50%	190% to 225%	-50% to -35%	-10% to 20%	95% to 125%
Pin-fin	-45% to -10%	-10% to 50%	185% to 200%	-65% to -40%	-30% to 10%	65% to 80%
Strip-fin	-60% to -30%	-35% to 15%	110% to 125%	-65% to -50%	-35% to -10%	45% to 55%

The performance comparison between experimental results of both titanium alloy (Ti64 - 1 and Ti64 - 2) manifold-microchannel surface with the conventional surfaces is shown in Figure 71. A graph of performance prediction if 150 μm fins can be successfully fabricated is also included in the figures. Analyzing the graphs, for the same pressure drop, manifold-microchannel yields significant improvement in base conductance and heat transfer coefficient over all conventional surfaces despite reduction in performance due to manufacturing inaccuracy. Compared to the wavy fins, 45% - 100% and 15% - 50% improvement in base conductance and heat transfer coefficient is possible for pressure drop between 100 to 2000 Pa respectively. Compared to the plain plate fins, 70% - 95% and 95% - 120% improvement in base conductance and heat transfer coefficient is possible. If 150 μm fins can be fabricated as requested, larger improvement can be achieved: 135% to 150% and 75% to 95% for base conductance and heat transfer

coefficient, respectively, compared to wavy fin. A summary of the percentage improvement of aluminum alloy manifold microchannel conventional surfaces is shown in Table 27.

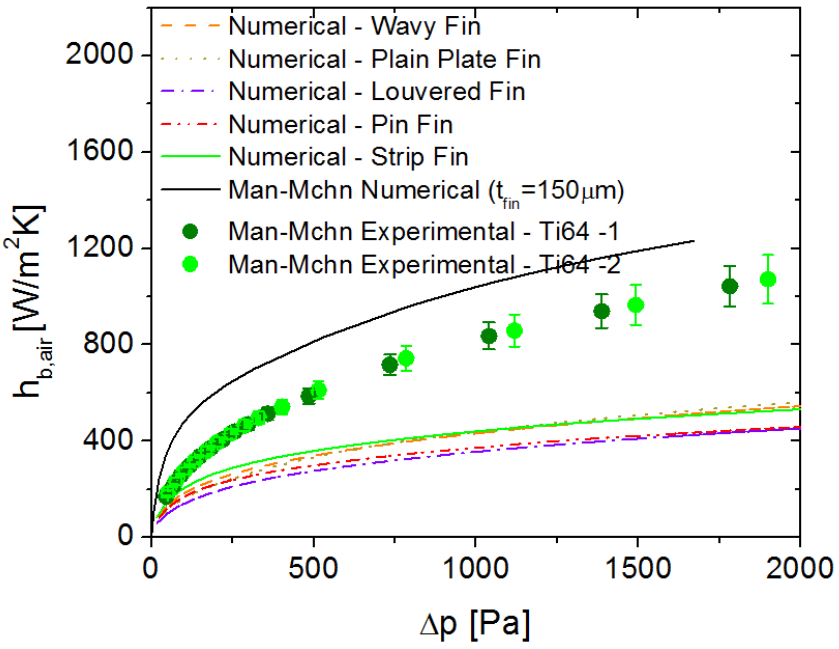

(a)

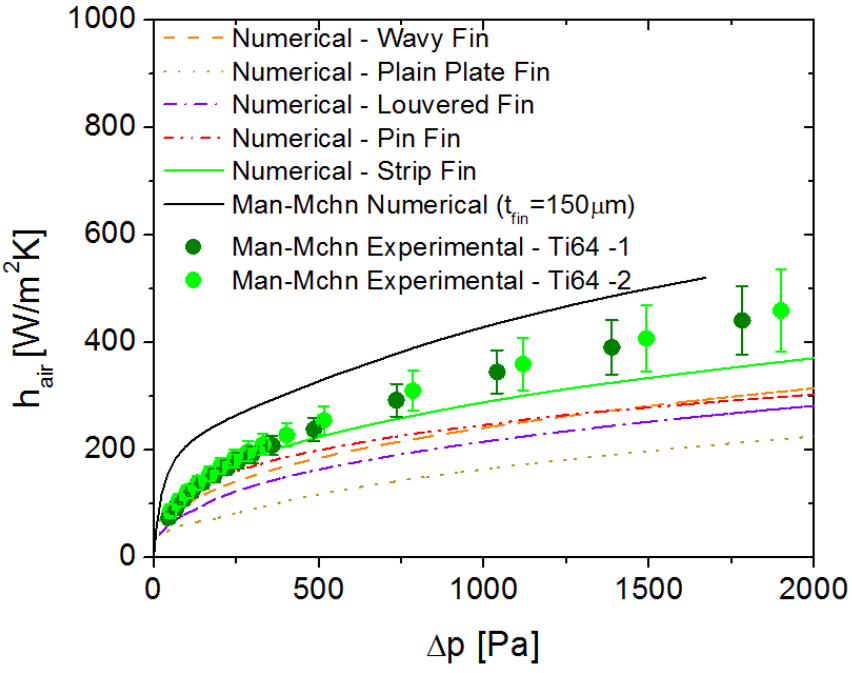

(b)

Figure 71: Performance comparison between Ti64 manifold-microchannel HX with conventional HX: (a) $h_{b,air}$ $vs.\Delta p_{air}$ (b) h_{air} $vs.\Delta p_{air}$

Table 27: % improvement of Ti64 manifold-microchannel over conventional HX for $100 < \Delta p_{air} < 2000$

	% Improvement for $h_{b,air}$			% Improvement for h_{air}		
	Ti64 - 1	**Ti64 - 2**	**Ti64 – $t_{fin} = 0.15mm$ (Num)**	**Ti64 - 1**	**Ti64 - 2**	**Ti64 – $t_{fin} = 0.15mm$ (Num)**
Wavy-fin	45% to 100%	50% to 100%	135% to 150%	15% to 50%	20% to 50%	75% to 95%
Plain Plate-fin	70% to 95%	70% to 95%	130% to 175%	95% to 110%	105% to 120%	145% to 225%
Louvered-fin	90% to 140%	95% to 140%	185% to 220%	35% to 65%	45% to 65%	95% to 125%
Pin-fin	60% to 140%	60% to 140%	175% to 185%	1% to 55%	5% to 55%	65% to 80%
Strip-fin	30% to 105%	30% to 105%	125% to 130%	1% to 25%	1% to 25%	45% to 55%

7.6.6. Scaled Up Performance Model and Mass Saving Estimations

In order to calculate how much mass saving is possible for power plant cooling application by incorporating the manifold-microchannel concept, the titanium alloy heat exchanger, which has the most favorable performance out of the three tested materials, was scaled up to a 12.2 MW unit suitable for power plant cooling. To scale up the test coupon to a full scale 12.2 MW module, the optimization process was re-run. The air-side heat conductance and pressure drop were evaluated using experimental results instead of CFD simulation. For scaling up, the air-side geometry was kept unchanged and only Reynolds number and water-side geometry were allowed to vary. A summary of the geometrical constraints is shown in Table 28, while the performance constraints are the same as those shown in Table 7.

Table 28: Geometrical constraints for scaled up 12.2 MW HX

Air-Side	
Re_{air}	100-8,000
Water-side	
Re_{water}	25-10,000
$H_{chn,water}$	1-25 mm
$W_{chn,water}$	0.5-25 mm
$t_{fin,water}$	0.2-5 mm
Combined Geometry	
$L_{tot,water}$	0.2-12 m

A curve fit method was employed to create correlations for air side Nusselt number (Nu) and friction factor (f) with respect to Reynolds number (Re) based on the experimental results for the region of Δp_{air}<200Pa. The Nusselt number and friction factor were previously defined in Eqs. (1) and (2) respectively, where D is the hydraulic diameter as described by Eq. (55). The Nusselt number and friction factor correlations for the Ti64-2 heat exchanger are divined as:

$$Nu = -1.70 \times 10^{-8} Re^3 + 5.17 \times 10^{-6} Re^2 - 6.10 \times 10^{-4} Re + 5.28 \times 10^{-2} \quad (66)$$

$$f = -3.36 \times 10^{-6} Re^3 + 1.02 \times 10^{-3} Re^2 - 1.11 \times 10^{-1} Re + 6.17 \quad (67)$$

where Reynolds number (Re) was evaluated using Eq. (54).

The scaled up manifold-microchannel heat exchanger was compared with the baseline stainless steel wavy fin heat exchanger. For further comparison two additional graphs are also included: conventional titanium alloy wavy fin heat exchanger and numerically optimized manifold-microchannel heat exchanger with fin thickness of 150 μm. The mass for all heat exchangers was normalized with the mass of the baseline heat exchanger (wavy fin SS17-4) at the operation condition of COP=172, as shown in Figure 72.

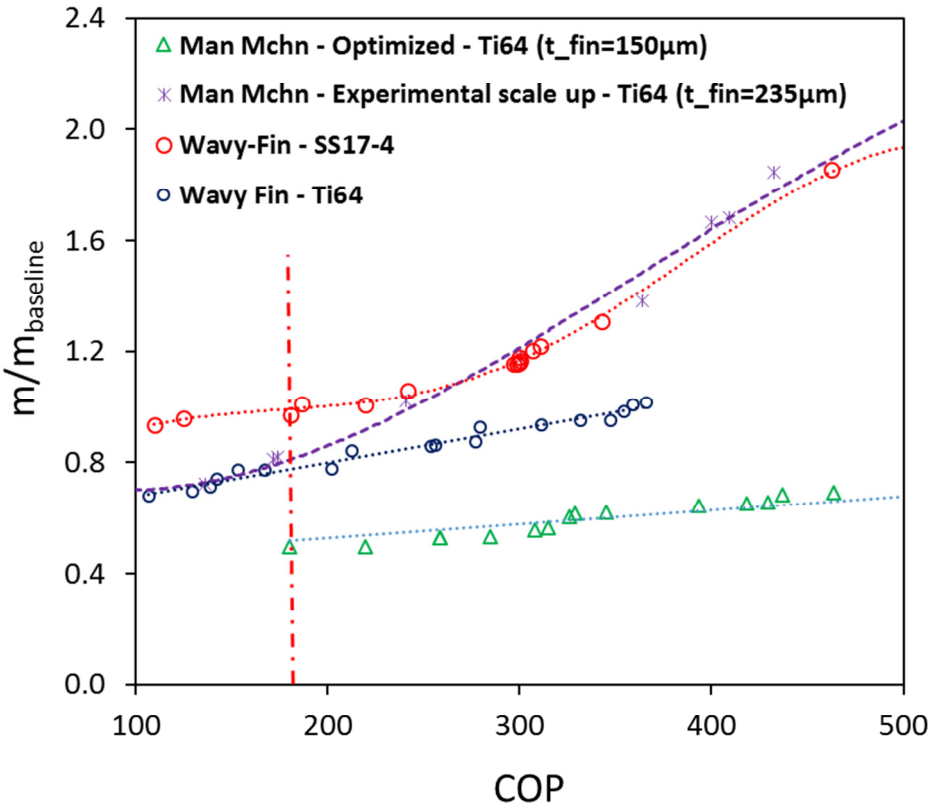

Figure 72: 12.2 MW scaled up heat exchangers: mass saving vs. COP

Comparing the manifold-microchannel experimentally scaled up heat exchanger with the baseline (stainless steel wavy fin) at the operation condition, it can be seen that 20% mass reduction is possible. If the comparison with conventional wavy fin is performed for the same build material of titanium alloy the Ti64-2 manifold-microchannel heat exchanger has equivalent mass with the Ti64 conventional wavy fin. These results indicate that for the scaled up designs based on experimental data from test coupons there is about up to 20% mass saving depending on the material of baseline wavy fin (i.e. stainless steel vs. titanium alloy). However, the results do not reflect the potential mass saving possible by refining the fabrication technology. In order to have a better picture of the potential of the technology, optimization was performed on the manifold-microchannel design. The results indicate that if the fin thickness can be reduced from 235 µm to 150 µm and the

design is optimized, 50% reduction of mass is possible compared to the conventional stainless steel wavy fin heat exchanger or 30% reduction in mass compared to the conventional titanium alloy wavy fin heat exchanger. This suggests that future efforts should be focused on reducing additive manufacturing production uncertainty and increasing printing resolution. This goal can be achieved through better control of 3D printing parameters and settings.

7.7. Summary

In summary, five coupon heat exchangers were successfully fabricated out of three different materials: stainless steel, aluminum, and titanium alloy, and then experimentally tested. Inspection of the fabricated heat exchangers revealed that the fabricated fin sizes were much bigger than requested. In addition, partial obstruction was noticed on some of the channels. This caused the heat exchanger performance to deviate from the initially predicted performance. Out of the three materials, titanium alloy heat exchangers showed the most promise. Compared to the wavy-fin baseline, 45% to 100% and 15% to 50% improvement in base conductance and heat transfer coefficient is possible for pressure drop between 100 to 2000 Pa, respectively. If the proposed dimensions can be built, an even larger improvement is possible. As the scaled up heat exchanger was no longer optimized due to the need to modify the design to meet the new fabrication constraints and also due to fabrication inaccuracy, the scaled up results did not show significant improvement compared to the baseline. If the fabrication inaccuracy can be reduced and the optimized design is used, 30% reduction in mass is possible compared to the baseline. As the numerical modeling has been successfully validated by the experimental, the prediction of 30% reduction is valid.

Chapter 8: Performance Characterization of Advanced Polymer Heat Exchanger

8.1. Introduction

This chapter discusses the performance characterization of the polymer heat exchanger. First, in order to test the water channel expansion process, a polymer heat exchanger was fabricated with only 4-5 layers based on the proposed design. Based on the lessons learned from the expansion process, the polymer heat exchanger design was modified. Thereafter, the modified polymer heat exchanger was fabricated and experimentally tested. The experimental results were then compared with the numerical results and conventional heat exchangers performance. Lastly, the heat exchangers were scaled up to 12.2 MW for comparison with the baseline.

8.2 Heat Exchanger Geometry and Fabrication

8.2.1. First Fabrication Attempt – Proposed Design

In order to study the water channel expansion process, the proposed 1 kW polymer heat exchanger discussed in chapter 6.4.2 was reduced in size. The coupon heat exchanger consisted of only 4-5 layers out of the 34 layers originally proposed for the 1 kW unit. The heat exchanger was fabricated out of High Density Polyethylene (HDPE) sheets using the layer-by-layer laser welding additive manufacturing technique. The fabricated polymer heat exchanger is shown in Figure 73(a). Observation confirmed that all of the layers were welded properly.

To expand the water channels, high pressure air was applied to the channel via a nozzle, shown in Figure 73(a). However, the expansion process turned out to be unsuccessful, as most of the channels did not expand and as the air pressure increased the welding line

break instead, as shown in Figure 73(b). We suspect that the constraint we had previously on the allowable minimum water channel was too small to allow a proper expansion. In order to ease the expansion process, the polymer heat exchanger was modified by increasing the water channel diameter to 6.5 times bigger than the one originally proposed. A new design is proposed and will be discussed in the following chapter.

(a)

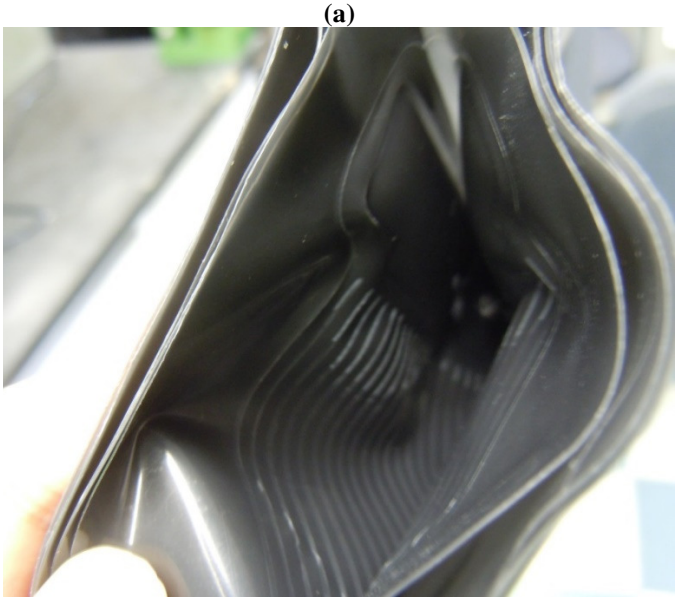

(b)

Figure 73: Fabricated polymer heat exchanger (proposed design): (a) Before expansion (b) After expansion

8.2.2. Second Attempt – Modified Polymer Heat Exchanger with Enlarged Channels

The new polymer heat exchanger was design with significantly larger channel size (6.5 times) to ease the expansion process. As the main purpose of this unit is to validate the fabrication process, only one layer was fabricated. A CAD drawing of the fabricated polymer heat exchanger and its dimensions is shown in Figure 74(a), showing the welding line of the water channel. Figure 74(b) shows how the heat exchanger will look if it can be expanded properly.

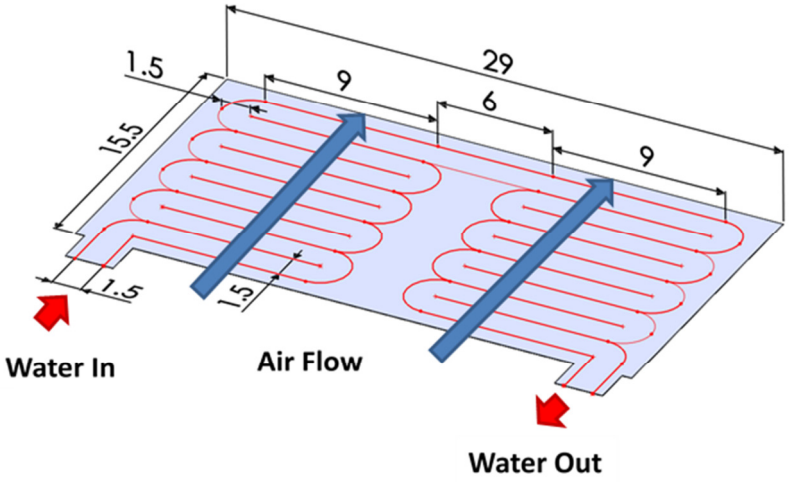

(a)

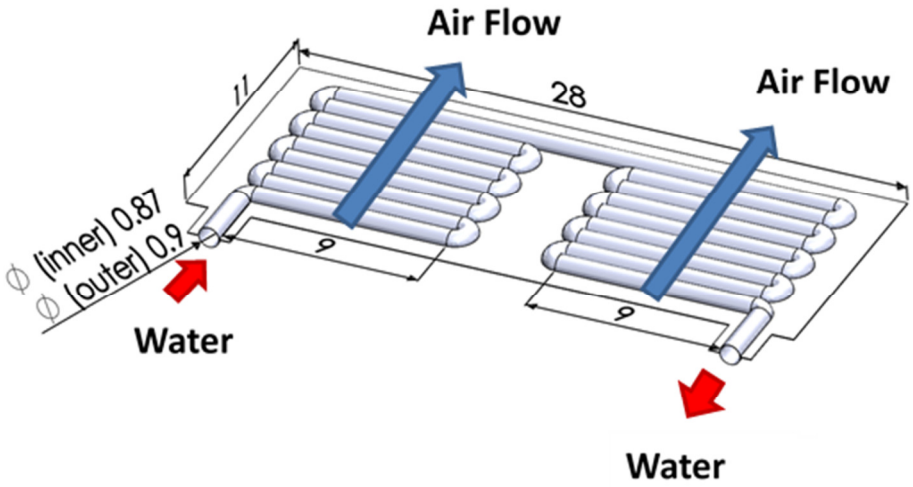

(b)

Figure 74: Modified polymer heat exchanger (a) Unexpanded (b) Expanded (all dimensions in cm)

The fabricated polymer heat exchanger, which consists of a single layer only, is shown in Figure 75(a). A similar expansion test was performed. Unlike the proposed design, the water channel in the modified design was successfully expanded. The expanded heat exchanger is shown in Figure 75(b). This confirmed our initial suspicion that the reason that our proposed design did not expand properly is because the water channel was too small to allow proper expansion.

(a)

(b)

Figure 75: Fabricated polymer heat exchanger: (a) Unexpanded (b) Expended

Since this modified design was successfully expanded, experimental testing was performed to evaluate its performance. A header was created to accommodate the air flow and to serve also as housing for the polymer heat exchanger core, as shown in Figure 76(a). The header was fabricated using 3-D printing made out of polylactic acid (PLA). The assembled test section is shown in Figure 76(b), which shows the unexpanded polymer heat exchanger inserted into the header. The gap between the heat exchanger and the header serves as the air channel. The water channel was then connected with pipes to supply and collect the water as shown in Figure 76(b). It should be noted that the header was needed only to determine the heat transfer in the prototype and will not be required in a heat exchanger with multiple stacks of polymer layers.

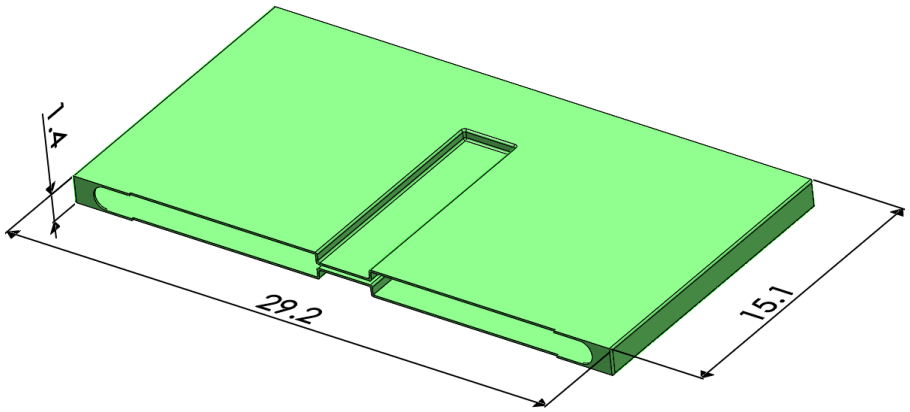

(a)

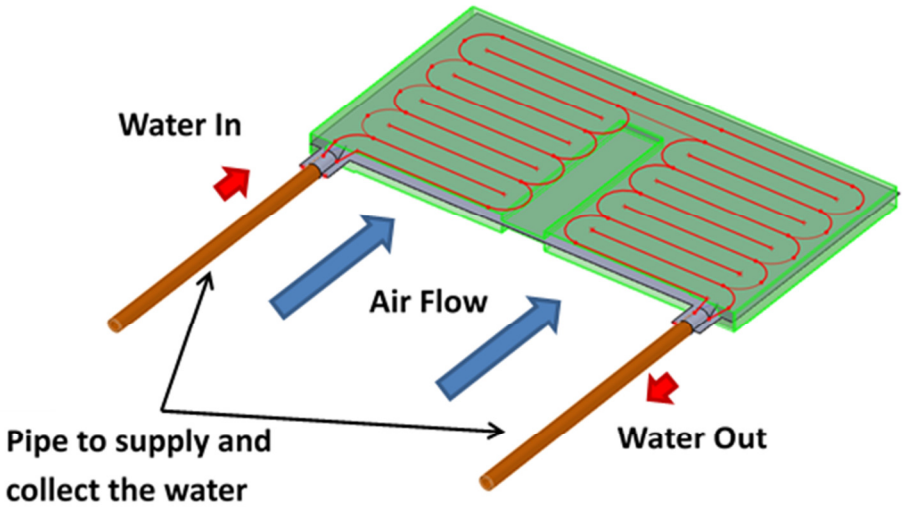

(b)

Figure 76: Polymer heat exchanger and its header: (a) Header design, (b) Assembled test section (unexpanded) (all units in cm)

The assembled unit of the expanded heat exchanger is shown in Figure 77(a). Due to expansion of the channel, the overall size of the expanded heat exchanger is significantly reduced compared to the unexpanded one, as shown in Figure 76(b). The gap between the heat exchanger core and the header which served as the air channel is shown in Figure 77(b). Since the channel took a tubular shape after the expansion of the polymer, the air gap between the test section and header was not uniform. The channel gap varied from 0.6 cm to 0.15 cm depending on the curvature of the water channel. Lastly, in order to fix the position of the heat exchanger core, small cylindrical rods were added as a support to the heat exchanger core as shown in Figure 77(a) and (b).

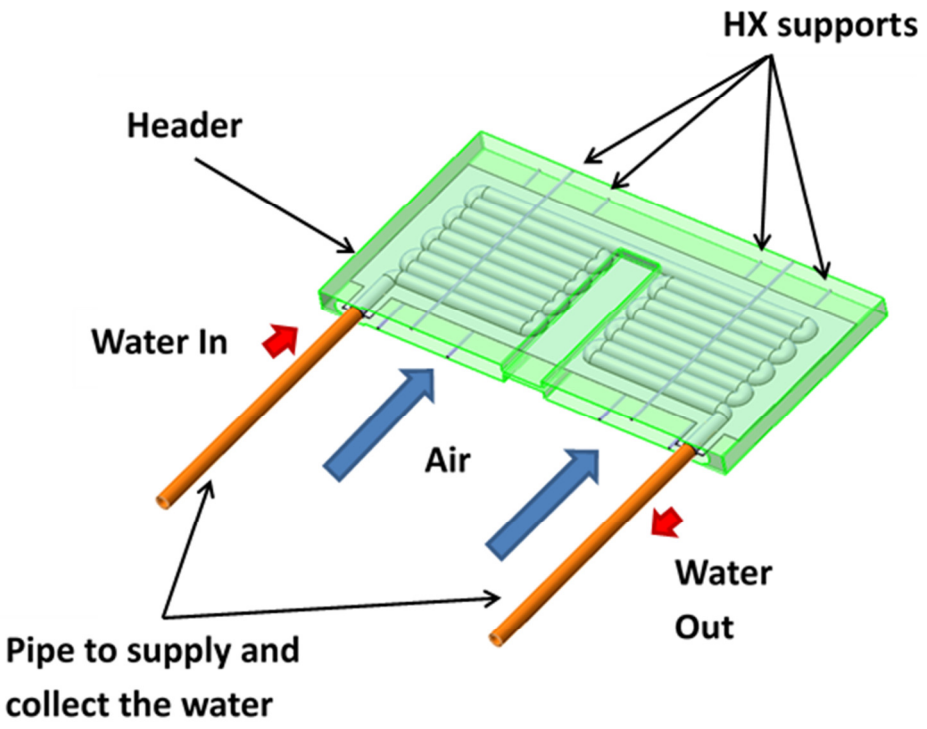

(a)

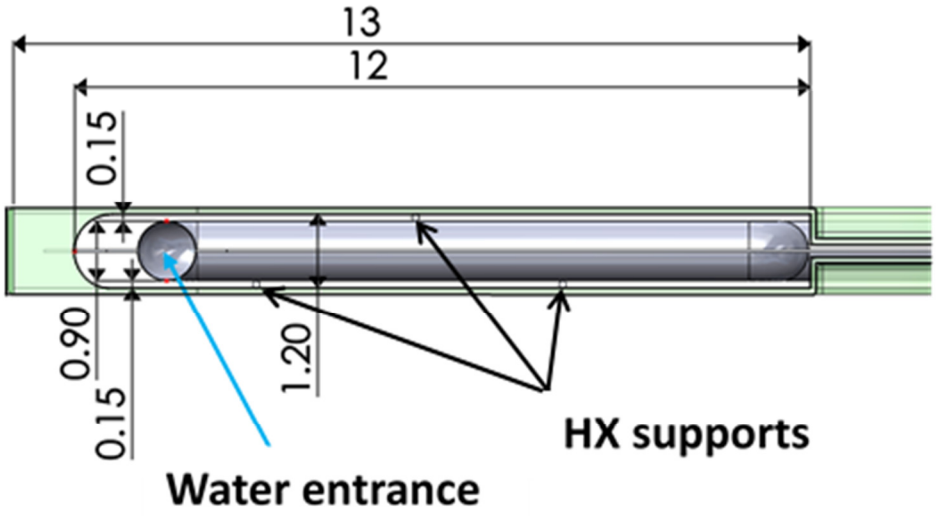

(b)

Figure 77: Polymer heat exchanger with header: (a) Assembled chapter (expended), (b) Front view of the assembled chapter (expended) (all units in cm)

The assembled polymer heat exchanger with the header is shown in Figure 78(a). Lastly, a second header was added to distribute the flow to the heat exchanger. The second

header was also fabricated using 3-D printing made out of polylactic acid (PLA). The final assembly of the polymer heat exchanger test section is shown in Figure 78(b).

(a)

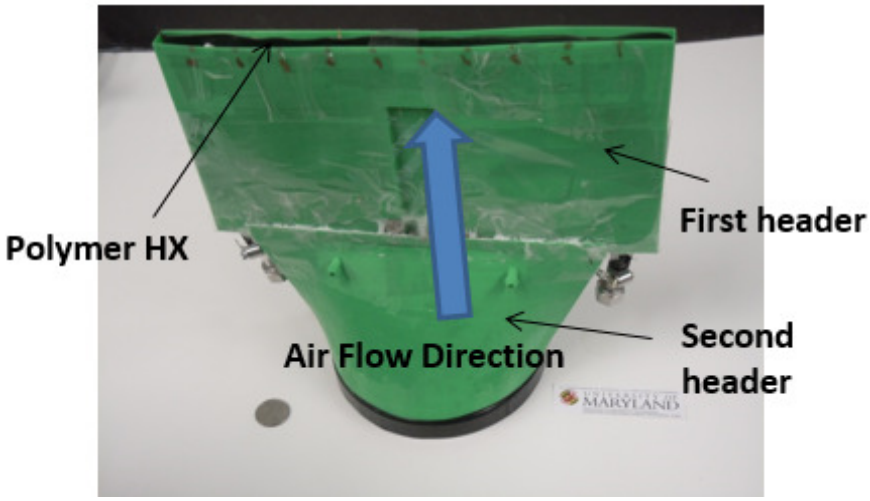

(b)

Figure 78: Polymer heat exchanger with header

8.3. Experimental Test Setup

The schematic diagram of the experimental test setup is shown in Figure 79. The air-side flow path consisted of an open loop with a heat exchanger to control the air temperature,

a blower to drive the flow, and a flow meter to measure the flow rate. The polymer heat exchanger was installed on the end of the loop as shown in Figure 80. In order to control the flow rate of the blower, a Variable Speed Controller (VSC) was used. The water-side flow path consisted of a closed loop with a chiller to control the water temperature and a Coriolis flow meter to measure the water flow rate. To evaluate the performance, differential pressure transducers and thermocouples were used to measure the pressure drop and temperature, respectively, on both sides. Due to very low temperature difference (0.5 to 1.5 °C) in the inlet and outlet of the water-side, a thermopile was utilized to measure the differential temperature of inlet and outlet of the water. Instrument data was collected using a data acquisition system (DAQ).

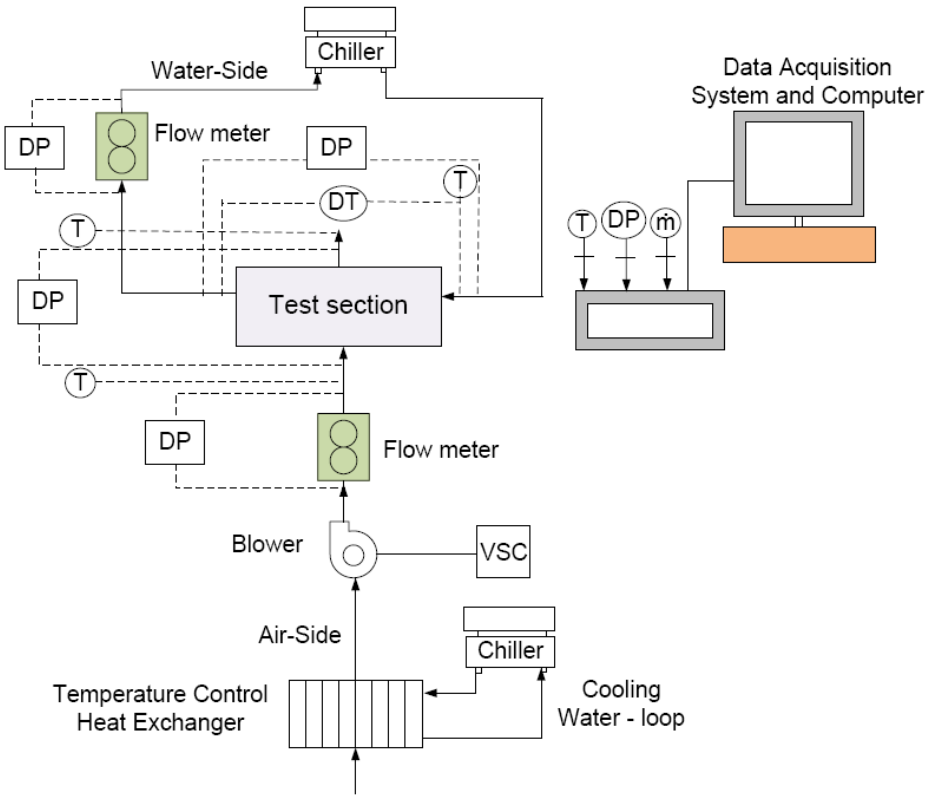

Figure 79: Experimental setup schematic diagram

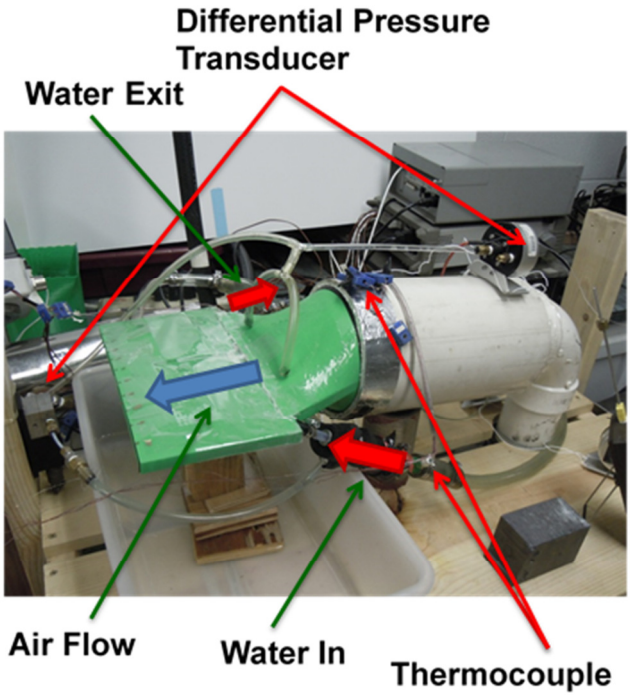

Figure 80: Zoomed in view of the test section

8.4. Experimental Method and Data Reduction

The experiments were performed for the conditions shown in Table 29. Inlet air and water temperatures were fixed at 22.5 ^{o}C and 50 ^{o}C respectively. The experiments were run for varying air-side and water-side flow rates. Air-side volumetric flow rate ($\dot{V}_{air}$) was varied from 3 L/s to 24 L/s while keeping water volumetric flow rate ($\dot{V}_{water}$) constant at 12.5 mL/s. Similarly, water-side volumetric flow rate was varied between 7 mL/s to 21 mL/s while keeping airside volumetric flow rate constant at 20 L/s. Air-side inlet and exit temperatures ($T_{in,air}$ and $T_{out,air}$), air-side pressure drop (Δp_{air}), water-side pressure drop (Δp_{water}), water-side inlet temperature ($T_{in,water}$), temperature difference between water inlet and outlet (ΔT_{water}), and air-side and water-side mass flow rate ($\dot{m}_{air}$ and $\dot{m}_{water}$) were recorded for each case.

Table 29: Experimental conditions for polymer heat exchanger testing

Temperature Boundary Condition	
$T_{in,air}$	22.5°C
$T_{in,water}$	50°C
Flow Rate Boundary Condition (Air side variation)	
$\dot{V}_{water}$	12.5 mL/s
$\dot{V}_{air}$	3-24 L/s
Flow Rate Boundary Condition (Water side variation)	
$\dot{V}_{water}$	7-21 mL/s
$\dot{V}_{air}$	20 L/s

To evaluate the performance of the heat exchanger, the heat transfer performance indicators like heat exchanger capacity (Q), overall heat transfer coefficient (U), air-side heat transfer coefficient (h_{air}) and heat exchanger effectiveness (ε_{HX}) had to be calculated. The heat exchanger capacity was evaluated on both the air and water sides as shown in Eqs. (68) and (69). The energy balance between both sides was found to be within 1-24% of each other. The average of air-side and water-side heat exchanger capacity (Eq. (70)) is used for further estimation of the heat transfer coefficients:

$$Q_{air} = \dot{m}_{air} c_{p,air} (T_{out,air} - T_{in,air}) \tag{68}$$

$$Q_{water} = \dot{m}_{water} c_{p,water} (T_{in,water} - T_{out,water}) \tag{69}$$

$$Q = 0.5(Q_{air} + Q_{water}) \tag{70}$$

In order to evaluate the overall heat transfer coefficient, the heat exchanger was divided into 18 identical segments as shown in Figure 81. In each segment, the air-side and the water side was at cross flow configuration. Before the overall heat transfer coefficient can be calculated the heat exchanger effectiveness in each segment need to be calculated first.

By definition, heat exchanger effectiveness (ε_{HX}) is the ratio between heat exchanger capacity over the minimum of the heat capacity (C) of the two fluids times the temperature difference between the two fluids $\left(\varepsilon_{HX} = \frac{Q}{\min(C_{hot}, C_{cold})(T_{hot,in} - T_{cold,in})}\right)$. Bergman et al. has shown that for any heat exchanger, the effectiveness depends only on the fluid mass flowrate, overall heat transfer coefficient times area, and heat exchanger configuration [158]. As each of the 18 segments is identical in geometry, mass flow rate input, and also heat exchanger configuration (Cross flow), heat exchanger effectiveness is the same in each segment. As a result, the heat exchanger segment effectiveness ($\varepsilon_{HX,seg}$) can be derived as a function of known information of the air-side and water-side inlet temperatures, mass flow rates of air and water, and the heat exchanger capacity as shown in Eqs. (71)-(74):

$$Q_i = \dot{m}_{water} c_{p,water} \left(T_{in,water,i} - T_{out,water,i}\right) \text{ for } i\text{=1:18} \tag{71}$$

$$Q_i = \frac{\dot{m}_{air}}{2} c_{p,air} \left(T_{out,air,i} - T_{in,air,i}\right) \text{ for } i\text{=1:18} \tag{72}$$

$$\varepsilon_{HX,seg} = \frac{Q_i}{\min(C_{water}, C_{air})\left(T_{in,water,i} - T_{in,air,i}\right)} \text{ for } i\text{=1:18} \tag{73}$$

$$Q = \sum_{i=1}^{18} Q_i \tag{74}$$

where Q_i is the capacity of each segment and C is heat capacity derived as: $C_{water} = \dot{m}_{water} c_{p,water}$ and $C_{air} = \frac{\dot{m}_{air}}{2} c_{p,air}$ as only half of air flow rate passes over each segment as shown in Figure 81.

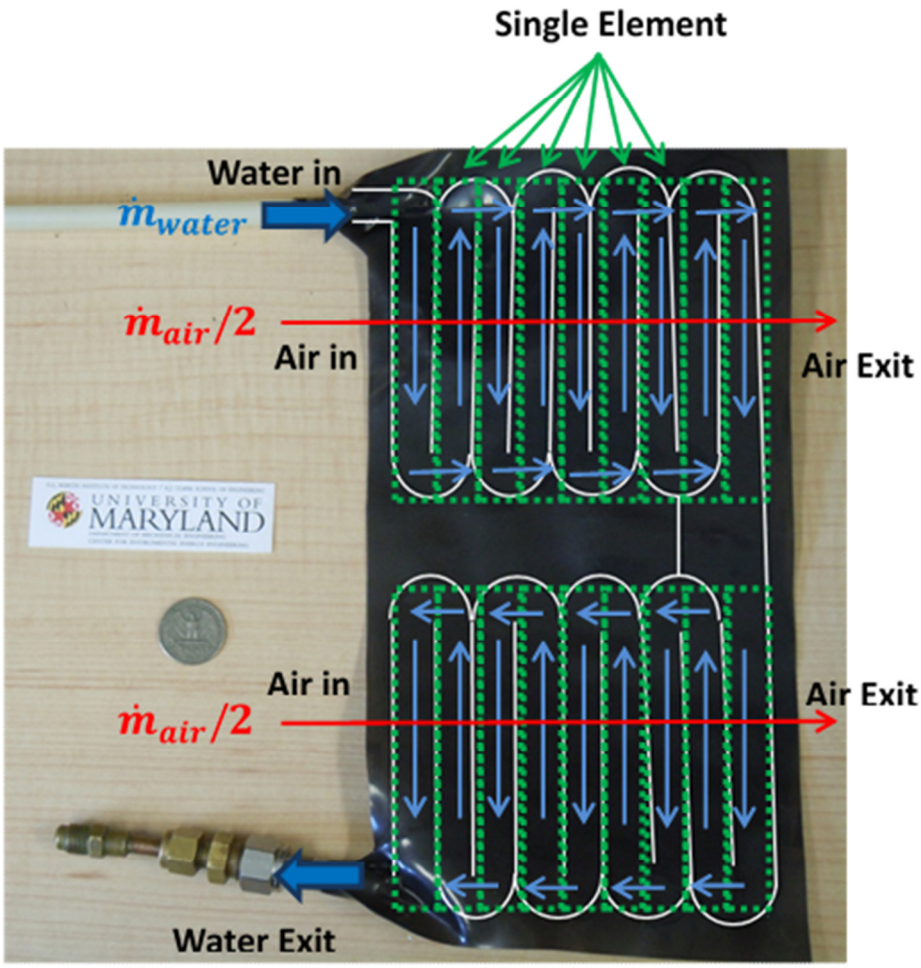

Figure 81: Polymer heat exchanger computational domain

Considering the symmetric geometry of the heat exchanger and the similar flow conditions (both air-side and water-side) for all the segments, the overall heat transfer coefficient (U) of the entire heat exchanger can be assumed as equivalent to the overall heat transfer coefficient in each segment. The overall heat transfer coefficient per segment can be evaluated using the unmixed cross flow NTU method, as previously shown in Eqs. (10) and (11), where U was evaluated based on heat transfer area per segment ($A_{H,seg}$), which is calculated as 28.8 cm^2.

In order to calculate the air-side heat transfer coefficient, the overall heat transfer coefficient is related with air-side and water-side heat transfer coefficient, as shown in Eqs (75)-(79):

$$\frac{1}{UA_{H,seg}} = R_{tot} \tag{75}$$

$$R_{tot} = R_{air} + R_{wall} + R_{water} \tag{76}$$

$$R_{air} = \frac{1}{h_{air}A_{H,seg}} \tag{77}$$

$$R_{wall} = \frac{\ln\left(\frac{r_{out}}{r_{in}}\right)}{2\pi L_{water,seg}k} \tag{78}$$

$$R_{water} = \frac{1}{h_{water}A_{H,seg}} \tag{79}$$

where R is thermal resistance, r_{out} and r_{in} is the channel outer and inner radius, $L_{water,seg}$ is the water flow length per segment (calculated as 9 cm), and k is the HDPE thermal conductivity (k=0.5 W/mK). As the thickness of the of the polymer layer is only 0.15 mm, the heat transfer area in the air-side and water-side can be assumed to be the same, and defined as $A_{H,seg}$, which is also used to evaluate overall heat transfer area.

The water-side convective heat transfer coefficient (h_{water}) was calculated using the analytical solution for a circular channel described in Ref. [157] based on the assumption that the water-side channel is fully expanded. This assumption is justified, as water-side thermal resistance is not the limiting factor on the air-water heat exchanger. As a result, a small deviation in the water-side heat transfer coefficient will not significantly affect the

calculation. To justify this assumption, in the next section a chart will be provided to compare the percentage of the water-side thermal resistance compared to the wall and air-side thermal resistance. Thereafter, the air-side heat transfer coefficient can be calculated using Eqs. (75)-(79).

Lastly, the overall heat exchanger effectiveness (ε_{HX}) can be evaluated as a function of heat exchanger capacity, air-side flow rate and inlet temperature, and water-side flow rate and inlet temperature as previously shown in Eq. (52).

For repeatability analysis, the experiments were run twice. The heat transfer and pressure drop performances were evaluated to be within 10% for both runs.

8.5. Uncertainty Analysis

Uncertainty propagation analysis was performed to calculate the inaccuracy in the heat exchanger performance ($Q, h, U, \Delta p, \varepsilon_{HX}$) due to inaccuracy in the measurements. A list of measurement equipment with their corresponding accuracies is shown in Table 30. The uncertainties for all heat exchanger performance parameters ($Q, h, U, \Delta p, \varepsilon_{HX}$) were calculated based on the method explained in NIST Technical Note 1297 [177]. The error bars are included in the results presented in the next chapter.

Table 30: List of measurement equipment and their accuracy

Equipment Function	Equipment Name	Accuracy
Air-side flow rate	Fischer Porter F Rotameter (Model#: 10A4557SS)	$\pm 2\%$
Water-side flow rate	FCI FlexCor mass flowmeter compact (Model#: CMF-CNQOAOAID-C00000)	$\pm 1\%$
Temperature	T-type thermocouple	$\pm\ 0.5^{o}C$
Air-side pressure drop	Setra pressure transducer (Model#: 239)	0.14% FS of 5 inch H20
Water-side pressure drop	Validyne P55 general purpose pressure transducer (Model#: P55D 4-N-1-36-S-4-S)	0.25% FS of 35kPa

8.6. Experimental Results

8.6.1. Heat Transfer Performance

The heat transfer performance of the polymer heat exchanger for a constant water flow rate is shown in Figure 82. The results are plotted as functions of air-side volumetric flow rate and Reynolds number (Re_{air}). Re_{air} is defined as:

$$Re_{air} = \frac{D_{air}\dot{m}_{air}/2}{A_{front,air}\mu_{air}} \tag{80}$$

where $A_{front,air}$ is air-side frontal area evaluated as the frontal area of the header as shown in Figure 77(b) ($0.13m \times 0.012m$) and D_{air} is air-side hydraulic diameter also evaluated at the frontal area of the header ($D_{air} = 0.022m$). The air-side mass flow rate was divided by two, as the heat exchanger consists of two identical sections, as shown in Figure 81.

Figure 82(a) shows the capacity of the polymer heat exchanger at 27.5 ^{o}C temperature difference between inlet air and water ($\Delta T_{water-air}$). The graph shows that up to 225 W heat exchanger capacity is possible. The air-side heat transfer coefficient is between 35 to 135 W/m^{2}K as shown in Figure 82(b). The overall heat transfer coefficient of the polymer heat exchanger is in the range of 35-120 W/m^{2}K, as shown in Figure 82(c). This number is higher than typical fin-tube heat exchanger U, which typically ranges from 25-50 W/m^{2}K [158]. Up to 60% heat exchanger effectiveness is noted, as shown in Figure 82(d), which is lower than the design required heat exchanger effectiveness of 72%. This is because the polymer heat exchanger was a different design from the proposed design due to the failure on the expansion process of the proposed polymer heat exchanger design. Analyzing the trend, as expected, heat exchanger capacity, air-side heat transfer coefficient, and overall heat transfer coefficient increase with increase in air-side Reynolds number.

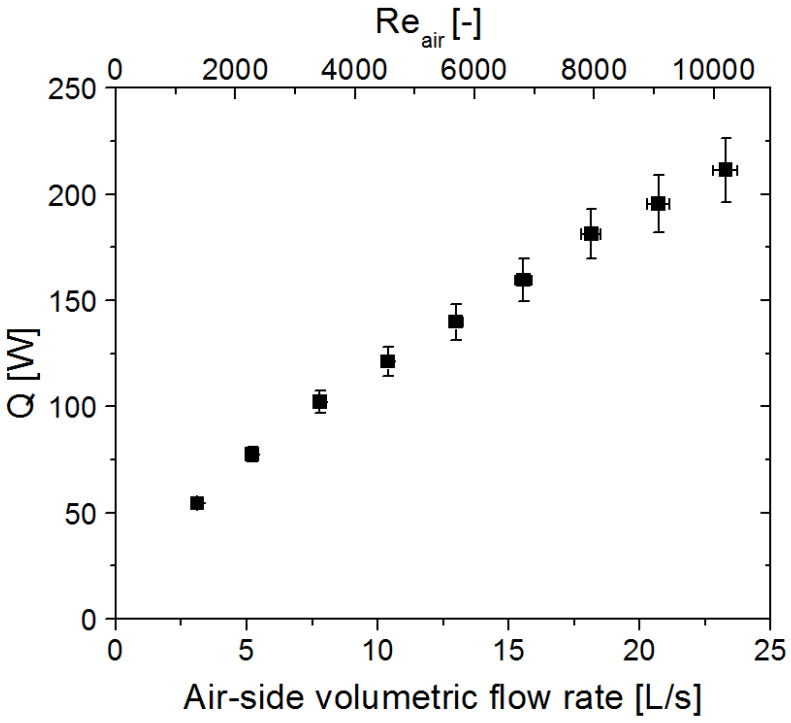

(a)

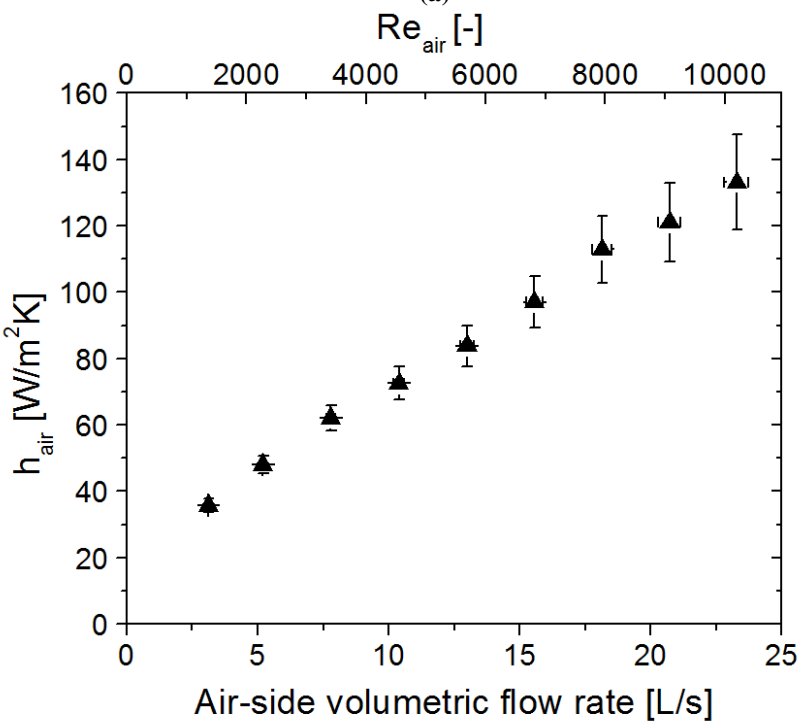
Re air [-]
0
2000
4000
6000
8000
10000
h air [W/m2K]
0
20
40
60
80
100
120
140
160
0
5
10
15
20
25
Air-side volumetric flow rate [L/s]

(b)

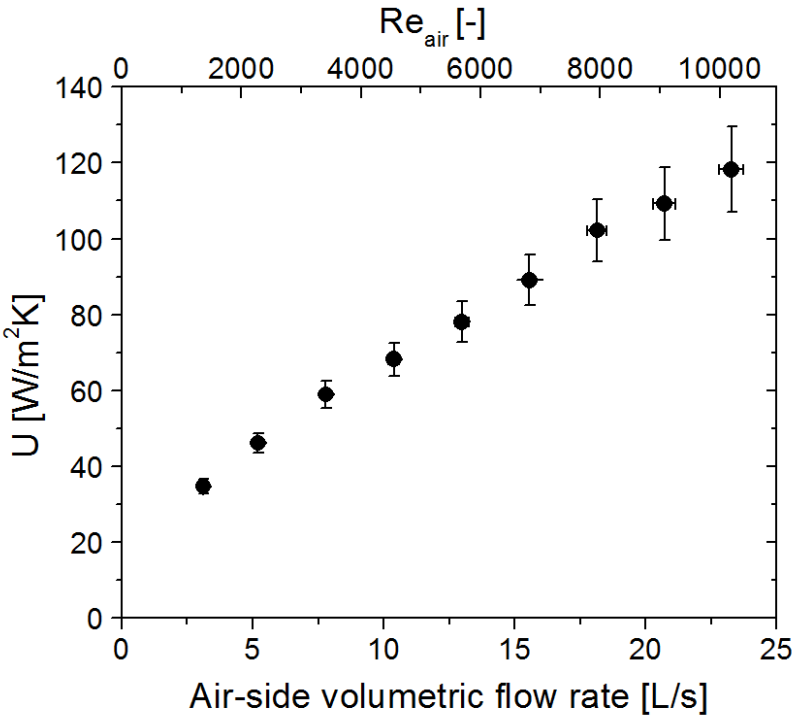
Re air [-]
0
2000
4000
6000
8000
10000
U [W/m2K]
0
20
40
60
80
100
120
140
0
5
10
15
20
25
Air-side volumetric flow rate [L/s]

(c)

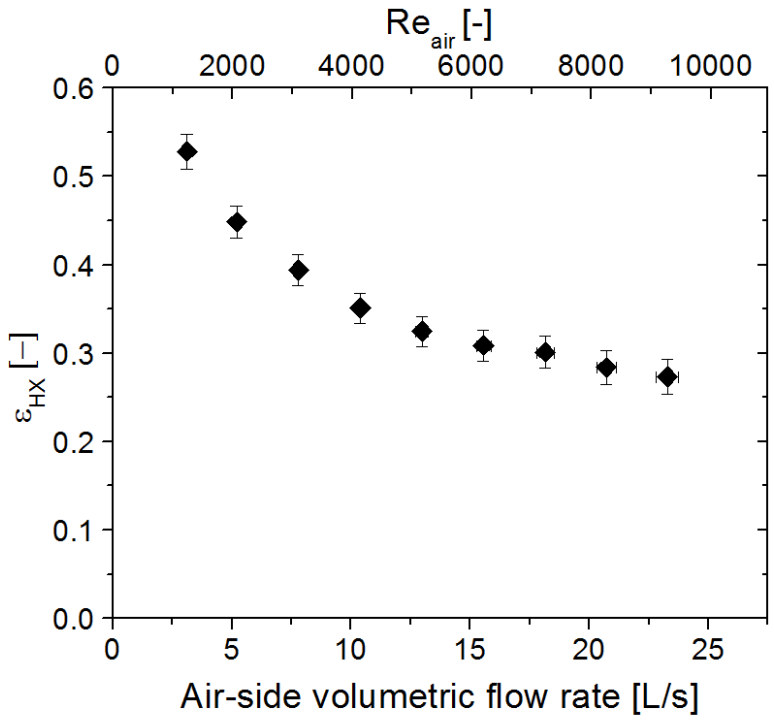

(d)

Figure 82: Heat transfer performance (varying-air side and constant water flow rate of 12.5 mL/s): (a) Heat capacity, (b) Air-side heat transfer coefficient, (c) Overall heat transfer coefficient, (d) Heat exchanger effectiveness

Similarly, the heat transfer performance results for the polymer heat exchanger for varying water-side flow rate and nominal Reynolds number are shown in Figure 83. Nominal Reynolds number ($Re_{nom,water}$) is calculated based on assuming a fully circular water tube and given as:

$$Re_{nom,water} = \frac{D_{water}\dot{m}_{water}}{A_{front,water}\mu_{water}} \tag{81}$$

where D_{water} and $A_{front,water}$ are water-side hydraulic diameter and frontal area with corresponding value of 0.87 cm and 0.59 cm^2, respectively.

The heat transfer performance of the polymer heat exchanger for a constant air flow rate is shown in Figure 83. There is a slight increasing trend in overall heat transfer coefficient as the water flow rate increase. However, the overall heat transfer coefficient

is not significantly dependent on the water-side flow rate. This shows that the water-side thermal resistance contributes only a small portion of the total thermal resistance.

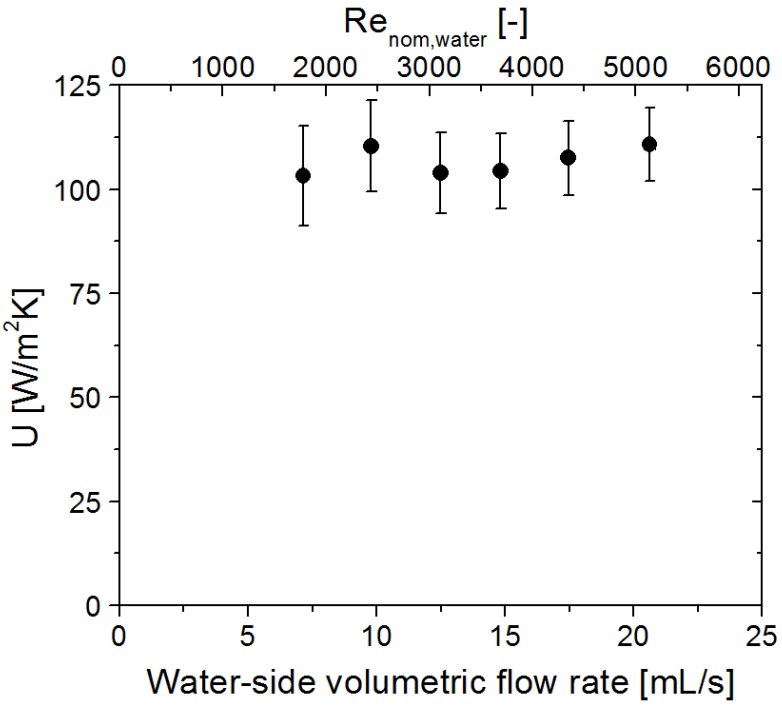

Figure 83: Overall heat transfer coefficient vs water flow rate and Reynolds number (constant air volume flow rate of 20 L/s)

The percentage distribution of the thermal resistance for three different air-side Reynolds number values are shown in Figure 84. These are based on the minimum, middle value, and maximum air-side flow rates set during the experiment. The water-side flow rate is the same for all three cases (12.5 mL/s). Comparison of the water side thermal resistance (R_{water}), air-side thermal resistance (R_{air}), and wall thermal resistance (R_{wall}), as evaluated from Eqs. (77) - (79), is shown in Figure 84. As can be seen in the figure, despite being built out of low thermal conductivity material, the wall thermal resistance is very low (max 3%) as compared to the air-side thermal resistance, which is the dominant resistance in all three cases. This shows that the thickness of the heat exchanger can be

further increased for higher pressure heat exchangers without significantly changing the thermal performance of the heat exchanger.

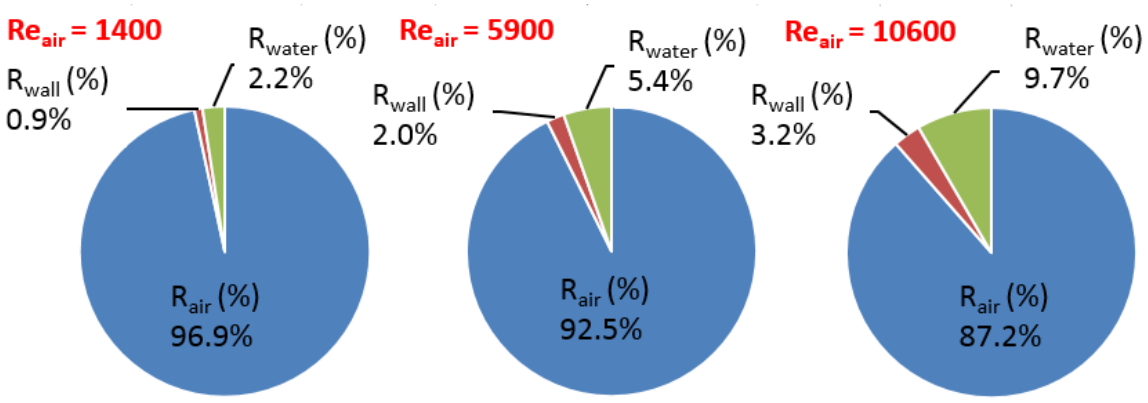

Figure 84: Distribution of the thermal resistance for three different air-side Reynolds numbers (all cases evaluated at the same water flow rate of 12.5 mL/s)

8.6.2. Pressure Drop Performance

Air-side pressure drop performances as a function of air-side Reynolds number for three different water flow rates are shown in Figure 85. The trend is as expected where pressure drop increases with air-side Reynolds number. Interestingly, it was found that the air-side pressure drop slightly increased as water-side flow rate was increased. This was because when water side flow rate was increased, the water channels started to expand further, restricting the airflow path. At water side volumetric flow rate of 12.5 mL/s, the air side pressure drop was in the range of 13-530 Pa.

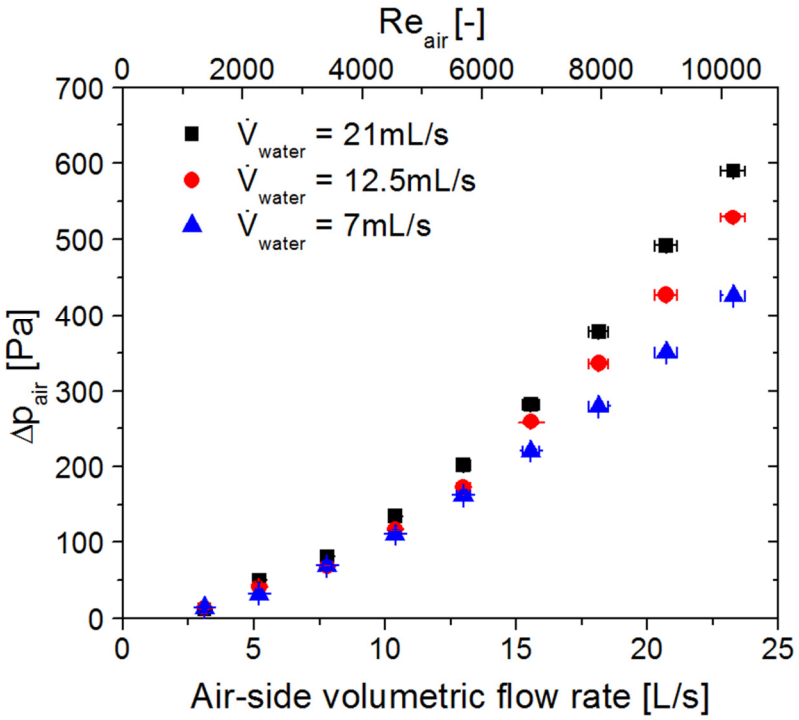

Figure 85: Experimental results – Air-side pressure drop

The water-side pressure drop experimental result is shown in Figure 86, which shows increasing trend as water-side nominal Reynolds number increase. This variation was attributed to deformation of water tubes as water flow rate increased. Numerical analysis of water flow in an elliptical pipe was done for different values of the ratio of major to minor axes of the ellipse (Z). $Z = 1$ corresponds to a circle. Experimental results matched the numerical values of pressure drop at Z=0.4 for low flow rates; however, the experimental results were closer to the numerical values at Z=0.5 at higher flow rates. This shows that the water-side pressure drop is closer to elliptical pipe performance rather than circular pipe performance. It should be noted that the actual hydraulic diameter decreases as the value of Z decreases. The hydraulic diameter was varied from 0.87 cm to 0.62 cm as Z varied from 1 to 0.4. While the elliptical tube is one reason for the high water-side pressure drop, there is also another factor than can cause high water-

side pressure drop. Some bending was noted on the water channel, especially close to the connection between the heat exchanger and water supply/collection pipes as shown in Figure 75(b), which can cause additional pressure drop.

Although the water-side pressure drop results show that the actual water channel is an ellipse, our assumption on using circular channel analytical solution to evaluate the water side heat transfer coefficient can still be justified, as the thermal resistance on the air side is much more dominant than on the water side, as shown in Figure 84. As a result, a slight change in water-side heat transfer coefficient will not significantly affect the overall heat transfer performance. Recalculating the air-side heat transfer coefficient using elliptical pipe (Z=0.5) for water-side heat transfer coefficient changes the air-side heat transfer coefficient values only up to 2%.

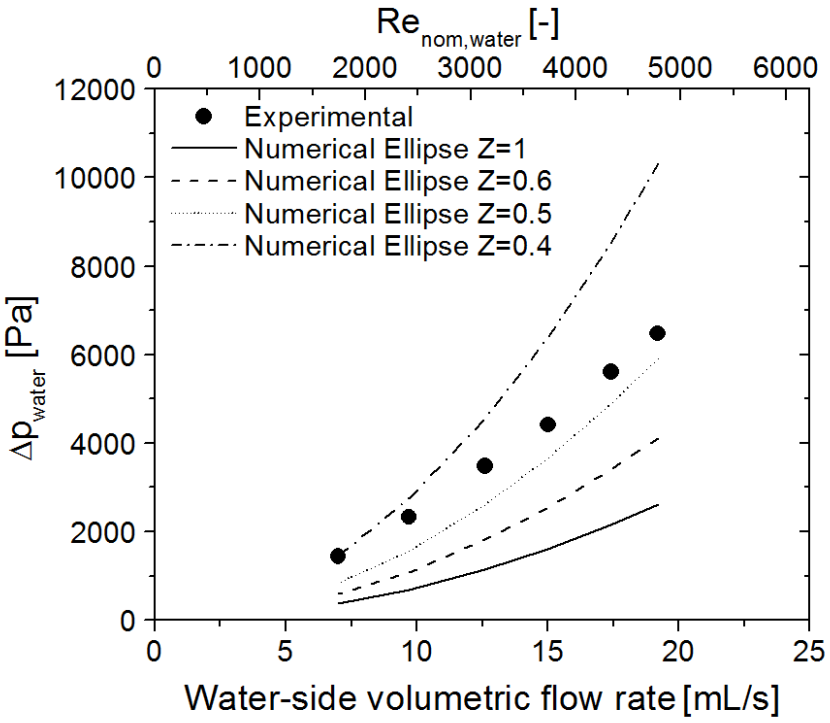

Figure 86: Experimental results – Water-side pressure drop vs. water flow rate

8.6.3. Comparison with Conventional Technology

The air-side performance of the polymer heat exchanger was compared with the performance of five commercially available plain plate fin surfaces commonly used for metal based heat exchangers. The plain plate fin surface performances (pressure drop and heat transfer coefficient) were calculated based on the friction factor and Colburn j-factor test data provided by Kays and London [5]. The flow lengths for all five plain plate fin heat exchangers were set to be the same as the polymer heat exchanger air flow length of 0.11 m as shown in Figure 74(a). The geometries for all five plain plate fin surfaces are listed in Table 31. For a more detailed dimension specifications please refer to Ref. [5].

Table 31: Plain plate fin surface geometries [5]

	Fin Pitch (fin/cm)	Plate Spacing (cm)
Plain Plate Fin 1	7.8	0.635
Plain Plate Fin 2	4.4	0.635
Plain Plate Fin 3	5.9	1.06
Plain Plate Fin 4	4.0	1.38
Plain Plate Fin 5	5.8	8.38

The performance comparison of the polymer heat exchanger with plain plate fin heat exchangers is shown in Figure 87. The performance of the polymer heat exchanger was equal or even superior to some of the plain plate fin heat exchanger performances. This shows that the polymer heat exchanger shows promise to compete with conventional metallic heat exchanger in terms of heat transfer performance. In addition, the major advantages of polymer heat exchangers compared to conventional metallic heat

exchangers are their lower weight, lower cost, and anti-fouling and anticorrosion properties, which are not shown in the figure.

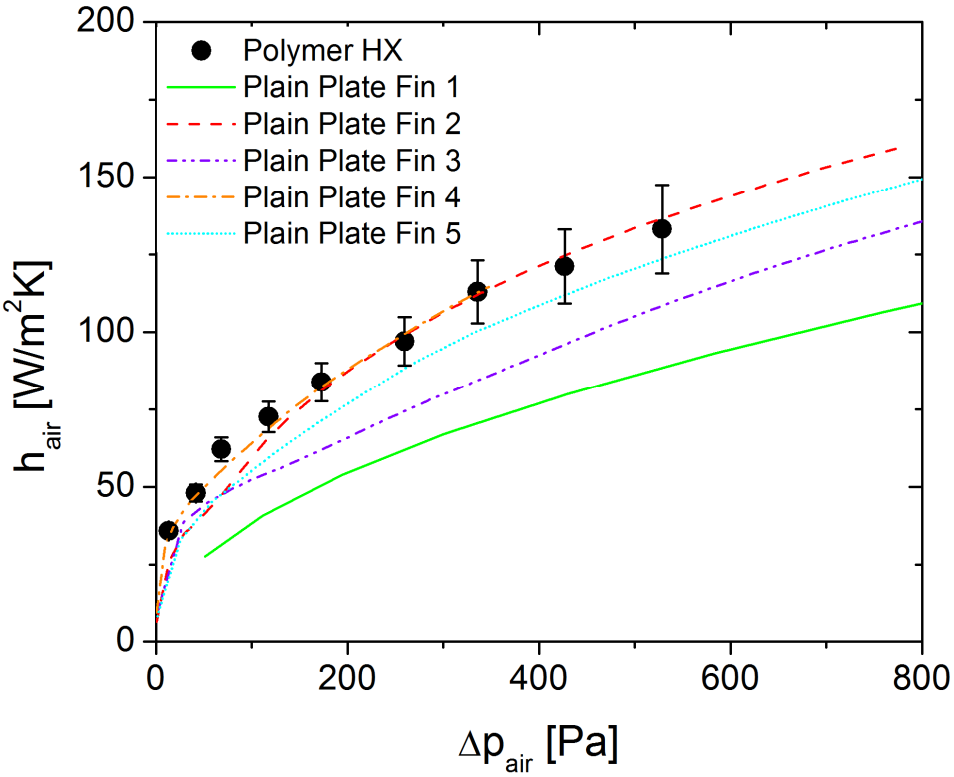

Figure 87: Performance comparison with conventional heat transfer surfaces

8.6.4. Scaled Up Performance Model and Mass Saving Estimation

In order to apply these results to power plant cooling, the heat exchanger was scaled up to 12.2 MW. One baseline requirement for the 12.2 MW design is that air-side and water-side mass flow rates need to be close to 600 kg/s, as shown previously in Table 7. As a result, the experimental data when $\dot{m}_{air} = \dot{m}_{water} = 0.0125$ kg/s was selected as the single element model, as it has the same mass flow rate ratio as the 12.2 MW baseline. The single element model can be scaled up using two methods:

1. Full scale 1 => by increasing the number of elements to match the total mass flow rate to the baseline of 600 kg/s
2. Full scale 2 => by increasing the number of elements to match the heat capacity to the baseline of 12.2 MW

Table 32 shows the scaled up results of the polymer heat exchanger using both methods. As the number of elements is the only variable that can be varied for the scaling up, it is not possible to get a design which matches both mass flow rate and heat capacity at the same time.

Table 32: Scaled up results for polymer heat exchanger

	Single Element	**Full Scale 1 (Matching Flow rate)**	**Full Scale 2 (Matching Q)**
Q [MW]	0.000125	6.0	12.2
$Q/(m\Delta T)$ [W/kgK]	267.8	267.8	267.8
$Q/(V\Delta T)$ [W/m3K]	8480	8480	8480
Δp_{air} [Pa]	117.6	117.6	117.6
Δp_{water} [Pa]	3486	3486	3486
COP [-]	95	95	95
$\dot{m}_{air}$ [kg/s]	0.0125	600	1224
$\dot{m}_{water}$ [kg/s]	0.0125	600	1224
$T_{in,air}$ [C]	40	40	40
$T_{in,water}$[C]	67.5	67.5	67.5
$\#\ of\ element$	1	48000	97945

Comparison of the scaled up polymer heat exchanger with the baseline (stainless steel wavy fin 12.2 MW) is shown in Table 33. Comparing the full scale #1 with the baseline, 903% increase in gravimetric energy density is possible at a cost of 50% reduction in capacity and 45% reduction in COP. Comparing the full scale #2 with the baseline, 903% increase in gravimetric energy density is possible at a cost of 45% reduction in COP and two times increase in flow rate.

Table 33: Comparison with baseline

	Full Scale 1 (Matching Flow rate)	Full Scale 2 (Matching Q)	Baseline (Wavy-fin)	% Variation (Full Scale 1)	% Variation (Full Scale 2)
Material	High-Density Polyethylene	High-Density Polyethylene	Stainless Steel	-	-
Q [MW]	6.0	12.2	12.2	**-51%**	**0.00%**
$Q/(m\Delta T)$ [W/(kgK)]	267.8	267.8	26.7	**903%**	**903%**
$Q/(V\Delta T)$ [W/(m^{3}K)]	8480	8480	27217	**-69%**	**-69%**
Δp_{air} [Pa]	117.6	117.6	121	**-3%**	**-3%**
Δp_{water} [Pa]	3486	3486	5050	**-31%**	**-31%**
COP [-]	95	95	171	**-45%**	**-45%**
$\dot{m}_{air}$ [kg/s]	600	1224	608	**0%**	**101%**
$\dot{m}_{water}$ [kg/s]	600	1224	584	**0%**	**110%**
$T_{in,air}$ [C]	40	40	40	-	-
$T_{in,water}$[C]	67.5	67.5	67.5	-	-

The scaled up polymer heat exchanger cannot meet all of the design requirements (heat capacity of mass flow rate). This is because unlike the proposed design, the simplified model was not designed for 12.2 MW from the beginning. As a result, it is possible that it cannot be scaled up to meet all of the design requirements. However, as this is the first time a polymer heat exchanger based on prime surface was successfully fabricated and tested in the lab with favorable heat transfer performance, this work can count as a proof of concept to show the potential for prime surface polymer heat exchangers fabricated using additive manufacturing. In addition, although the scaled up design does not meet all of design requirements, a mass reduction close to one order of magnitude is possible, as shown in the previous table.

8.7. Summary

In summary, the polymer heat exchanger based on the proposed design was not fabricated successfully, as water channels could not be expanded properly. However, instead a simplified design with larger channel hydraulic diameter was successfully fabricated. The

experimental test of the simplified design shows that overall heat transfer coefficient in the range of 35-120 W/m^2K and air-side heat transfer coefficient in the range of 35-135 W/m^2K are possible. The air-side performance of the polymer heat exchanger is equal or superior to common plain plate fin surfaces. In addition, the wall thermal resistance is not significant compared to the total thermal resistance, which shows that the prime surface polymer heat exchanger was not limited by low thermal conductivity of the polymer material. The heat exchanger was then scaled up to a 12.2 MW unit according to the design requirements. But, as the heat exchanger is a simplified model that was not designed for 12.2 MW from the beginning, unlike the case of the proposed design, the heat exchanger could not be scaled up to meet all the design requirements. However, the experimental results show that, in addition to already having advantage on low weight, low cost, antifouling, and anticorrosion property compared to the metallic heat exchanger, the prime surface polymer heat exchanger can also compete with the metallic heat exchanger in terms of thermal performance.

Chapter 9: Conclusion and Proposed Future Work

9.1. Conclusions

In this dissertation, additive manufacturing technique was used to fabricate and successfully test metallic and polymer heat exchangers which benefited from an advanced design optimization scheme to meet the air side heat transfer requirements for dry cooling of power plants. Although the study focused on dry cooling applications for power plants, results can be of significance to other industries that rely on air side cooling for various applications. These include air cooled condensers (heat pump, refrigeration), air cooled heat sinks (electronic cooling), air-to-air heat exchangers (economizers), and other air-water heat exchangers (car radiators).

9.1.1. Advance Metallic Heat Exchanger

The advance metallic heat exchanger was composed of manifold-microchannel surface on the air side and mini channels on the water side. In order to predict its performance, a novel numerical modeling method that can be used in conjunction with optimization was developed. Water-side performance was evaluated based on available correlations while the air-side performance was calculated by the modified hybrid method developed as part of this study. The overall performance of the heat exchanger was evaluated using a control-volume-base method that specifically developed for this unique type of heat exchanger. Using the developed numerical model, multi objective optimization was performed to identify designs that could lead to the highest gravimetric heat transfer density ($Q/m\Delta T$) and coefficient of performance ($COP/\Delta T$). The optimization constraints were defined such that all possible solutions would meet the geometrical, manufacturing and performance constraints. For comparison purpose, multi-objective

optimizations were also performed on conventional heat exchangers (e.g., wavy fin, louvered fin, plain plate fin) for the same performance constraints. The results showed that the manifold-microchannel heat exchanger offers significant performance advantage over conventional heat exchangers. Compared to the wavy-fin baseline, 59% increase in gravimetric heat transfer density was achieved for the same coefficient of performance. The heat exchanger design was scaled down to develop a subscale prototypes that can be used for fabrication and experimental testing.

The manifold-microchannel heat exchanger prototypes were fabricated using the direct metal laser sintering (DMLS) technique. Using this method, the manifold and the fins were built together as a single piece, which eliminated the need to bind both parts together. Five scaled down prototype manifold-microchannel heat exchangers were fabricated out of three different materials: titanium alloy (Ti64), stainless-steel (SS17-4), and aluminum (AlSi10Mg). Detailed inspection of the fabricated coupons revealed some fabrication inaccuracies in one or more parameters, especially on the air-side fin thickness. Experimental testing was performed on all five prototype heat exchangers. The experimental results were compared with the numerical modeling for the same fin thickness, which showed good agreement between both results. The average percentage errors between both results were calculated as 18% and 12% for pressure drop and base conductance, respectively. Compared to the conventional heat exchangers, despite fabrication inaccuracy, higher performance was achieved for Ti64 prototype heat exchangers. Compared to wavy-fin surfaces, a 45% to 100% increase in base conductance and 15% to 50% increase in heat transfer coefficient for the same pressure drop were observed. It was demonstrated that if the fin fabrication resolution can be

improved, so that all fins are built uniformly with 150 micron thickness, then an even higher performance enhancement is possible. However, the performance of SS17-4 and AlSi10Mg heat exchangers were lower than some of the conventional heat exchangers. This was attributed to the higher fabrication inaccuracies in both SS17-4 and AlSi10Mg heat exchangers as compared to the Ti64 heat exchanger.

Using the experimental data, the titanium alloy metallic heat exchanger performance was scaled up to 12.2 MW, which is suitable for power plant cooling applications. The performance of the scaled models turned out to be lower than what was predicted numerically. Compared to the stainless steel baseline 20% mass reduction is noted. However compared to the baseline with the same material (titanium alloy), both heat exchangers' mass were identic. This is because the design of metallic prototype heat exchanger had deviated from their initial optimized design due to additional fabrication constraints and fabrication inaccuracies. Despite some fabrication inaccuracy in this first round of fabrication, the study demonstrated the potential of additive manufacturing to realize successful fabrication of a high-performance manifold-microchannel heat exchanger design that would have been very difficult and cost prohibitive with conventional manufacturing techniques. In addition, the experimental results successfully validated the respective numerical models. This confirms that if the fabrication inaccuracy can be reduced, the predicted performance enhancements should be achievable. 30% reduction in mass was predicted compared to titanium alloy baseline. Since additive manufacturing is in its infancy stages for applications in heat/mass transfer enhancement, it show promises to overcome its current limitations.

9.1.2. Advance Polymer Heat Exchanger

The polymer heat exchanger was based on prime surface heat transfer technology. A geometry that met all of the performance requirements was proposed based on CFD modeling. Comparing the performance of the proposed polymer heat exchanger with the wavy-fin baseline, 680% increase in gravimetric heat density ($Q/(m\Delta T)$) is possible because polymer yields significantly lower density compared to metal. However, the aforementioned increase in gravimetric heat density was accompanied by a slight reduction, 12%, in volumetric heat transfer density ($Q/V\Delta T$) due to polymer's low thermal conductivity. The polymer heat exchanger design was scaled down to develop a prototype for fabrication and experimental testing.

The first attempt of fabrication of the proposed design was unsuccessful as the water channels could not expand properly. As a result, a modified design was proposed with larger channel size. The new coupon heat exchanger was successfully fabricated. Experimental tests were performed on the heat exchanger. Experimental results show that due to low thickness of the wall, the wall thermal resistance was not the limiting factor of its performance. The wall resistance only contributes up to 3% of the total resistance. Comparing the air-side heat transfer coefficient with plain plate fin surfaces, higher performance was noted compared to most of the surfaces. The polymer heat exchanger performance was scaled up to 12.2 MW, which is suitable for power plant cooling applications. But, as the heat exchanger is a simplified model that was not designed for 12.2 MW from the beginning, unlike the case of the proposed design, the scaled up heat exchanger could not meet all the design requirements. However, this work has shown that

a lightweight and low cost polymer heat exchanger can be fabricated with additive manufacturing techniques.

9.2. Proposed Future Work

Several directions for future work in the areas of numerical modeling of manifold microchannel heat exchangers, additive manufacturing, and also continuity of the project are proposed here.

9.2.1. Numerical Modeling

The modified hybrid method proposed in this dissertation did not take into account the effect of tapered manifold on pressure drop calculation. As the main function of the tapered manifold is to reduce flow maldistribution, for cases where maldistribution is already low, like the one proposed in this study, the tapered manifold will not significantly affect the performance. However, it will be beneficial to be able to evaluate how much flow maldistribution can be reduced by using tapered manifold for cases with high flow maldistribution. In addition, optimum designs which were not selected during the optimization due to high maldistribution may become available due to this tapered manifold design. In order to take into account the effect of the tapered manifold on the heat exchanger performance, the modified hybrid method can be modified further by varying the manifold frontal area (A_{mnd}) as a function of distance from the entrance (x-axis) and recalculating the mass and momentum equations. However, as both velocity (v) and manifold frontal area would vary as a function of x, the differential equations may be highly non-linear and could not be solved using standard method.

9.2.2. Additive Manufacturing

In the field of additive manufacturing, work is needed to improve the fabrication quality of DMLS. The numerical results have shown that in order for the performance of manifold-microchannel heat exchanger to be marginally superior compared to conventional surfaces, the fin thickness needs to be 150 μm or lower. Current DMLS techniques are still unable to fabricate fins with thickness of 150 μm or lower. However, as the additive manufacturing is still in the development stage, there are still many ways that it can be improved. Several research areas that can improve the DMLS technique include: laser resolution, finer powder, and sensor controlled process.

9.2.3. Project Continuity

For continuity of the project, it is proposed that second generation of manifold-microchannel and polymer heat exchanger were fabricated. Based on the lessons learned from first fabrication attempt, a new set of fabrication constraints could be drawn, such as inclined fin angle for the metallic heat exchanger and minimum channel width for polymer heat exchanger. The optimization can be re-run by taking into account of all of these criteria. Based on the new optimized design, a second-generation prototype could be fabricated, tested, and scaled up.

References

[1] Acharya, S., Bushart, S., and Shi, J., 2013, "NSF/EPRI Joint Solicitation Informational Webcast," EPRI and NSF.
[2] Feeley, T. J. I., Green, L., and Murphy, J. T., 2005, "Department of Energy/Office of Fossil Energy's Power Plant Water Management R&D Program ", U.S. Department of Energy.
[3] Fleischill, S., and Hayat, B., 2014, "Power Plant Cooling and Associated Impacts: The Need to Modernize U.S. Power Plants and Protect Our Water Resources and Aquatic Ecosystems ", NRDC - National Resources Defense Council.
[4] Dorjets, V., 2014, "Today in Energy," U.S. Energy Information Administration, https://www.eia.gov/todayinenergy/detail.cfm?id=14971 , (Retrieved: January 2016)
[5] Kays, W. M., and London, A. L., 1984, Compact Heat Exchangers 3rd Edition, Krieger Publishing Company, Malabar, FL.
[6] Wang, C. C., Lee, C. J., Chang, C. T., and Lin, S. P., 1998, "Heat transfer and friction correlation for compact louvered fin-and-tube heat exchangers," International Journal of Heat and Mass Transfer, 42(11), pp. 1945-1956.
[7] Sheik Ismail, L., Velraj, R., and Ranganayakulu, C., 2010, "Studies on pumping power in terms of pressure drop and heat transfer characteristics of compact plate-fin heat exchangers—A review," Renewable and Sustainable Energy Reviews, 14(1), pp. 478-485.
[8] Yan, W. M., and Sheen, P. J., 2000, "Heat transfer and friction characteristics of fin-and-tube heat exchangers," International Journal of Heat and Mass Transfer, 43(9), pp. 1651-1659.
[9] Lee, Y., Lee, P., and Chou, S., 2013, "Numerical study of fluid flow and heat transfer in the enhanced microchannel with oblique fins," Journal of Heat Transfer, 135(4), pp. 041901.
[10] Morimoto, K., Suzuki, Y., and Kasagi, N., 2008, "High performance recuperator with oblique wavy walls," Journal of Heat Transfer, 130(10), pp. 101801.
[11] Arie, M. A., Shooshtari, A. H., Dessiatoun, S. V., Al-Hajri, E., and Ohadi, M. M., 2015, "Numerical modeling and thermal optimization of a single-phase flow manifold-microchannel plate heat exchanger," International Journal of Heat and Mass Transfer, 81, pp. 478-489.
[12] Cetegen, E., 2010, "Force fed microchannel high heat flux cooling utilizing microgrooved surface," Ph.D. Thesis, University of Maryland, College Park.
[13] Andhare, R. S., 2013, "Experimental heat transfer and pressure drop characteristic of A single phase manifold-microchannel plate heat exchanger," M.S. Thesis, University of Maryland, College park.
[14] Kim, Y. H., Chun, W. C., Kim, J. T., Pak, B. C., and Baek, B. J., 1998, "Forced air cooling by using manifold microchannel heat sinks," Journal of Mechanical Science and Technology, 12(4), pp. 709-718.
[15] Boteler, L., Jankowski, N., McCluskey, P., and Morgan, B., 2012, "Numerical investigation and sensitivity analysis of manifold microchannel coolers," International Journal of Heat and Mass Transfer, 55(25), pp.7698-7708.

[16] Wang, Y., and Ding, G. F., 2008, "Numerical analysis of heat transfer in a manifold microchannel heat sink with high efficient copper heat spreader," Microsystem Technologies, 14(3), pp. 389-395.
[17] Joardar, A., and Jacobi, A., 2008, "Heat transfer enhancement by winglet-type vortex generator arrays in compact plain-fin-and-tube heat exchangers," International Journal of Refrigeration, 31(1), pp. 87-97.
[18] Leu, J. S., Wu, Y. H., and Jang, J. Y., 2004, "Heat transfer and fluid flow analysis in plate-fin and tube heat exchangers with a pair of block shape vortex generators," International Journal of Heat and Mass Transfer, 47(19), pp. 4327-4338.
[19] Yazdani, M., and Yagoobi, J. S., 2014, "Heat transfer enhancement of backstep flow by means of EHD conduction pumping," International Journal of Heat and Mass Transfer, 73, pp. 819-825.
[20] Morcos, V., and Shafey, H. M., 1995, "Performance analysis of a plastic shell-and-tube heat exchanger," Journal of Elastomers and Plastics, 27(2), pp. 200-213.
[21] Liu, W., Davidson, J., and Mantell, S., 2000, "Thermal analysis of polymer heat exchangers for solar water heating: a case study," Journal of Solar Energy Engineering, 122(2), pp. 84-91.
[22] Wang, Y., Davidson, J., and Francis, L., 2005, "Scaling in polymer tubes and interpretation for use in solar water heating systems," Journal of Solar Energy Engineering, 127(1), pp. 3-14.
[23] Zarkadas, D. M., and Sirkar, K. K., 2004, "Polymeric hollow fiber heat exchangers: An alternative for lower temperature applications," Industrial & Engineering Chemistry Research, 43(25), pp. 8093-8106.
[24] Zarkadas, D. M., Li, B., and Sirkar, K. K., 2005, "Polymeric hollow fiber heat exchangers (PHFHEs): A new type of compact heat exchanger for lower temperature applications," Proceedings of the ASME 2005 Summer Heat Transfer Conference collocated with the ASME 2005 Pacific Rim Technical Conference and Exhibition on Integration and Packaging of MEMS, NEMS, and Electronic Systems, San Francisco, CA, USA, pp. 429-438.
[25] Song, L., Li, B., Zarkadas, D., Christian, S., and Sirkar, K. K., 2010, "Polymeric hollow-fiber heat exchangers for thermal desalination processes," Industrial & Engineering Chemistry Research, 49(23), pp. 11961-11977.
[26] Yan, X., Li, B., Liu, B., Zhao, J., Wang, Y., and Li, H., 2014, "Analysis of improved novel hollow fiber heat exchanger," Applied Thermal Engineering, 67(1), pp. 114-121.
[27] Cevallos, J. G., Bergles, A. E., Bar-Cohen, A., Rodgers, P., and Gupta, S. K., 2012, "Polymer heat exchangers—History, opportunities, and challenges," Heat Transfer Engineering, 33(13), pp. 1075-1093.
[28] Burns, J., and Jachuck, R., 2001, "Condensation studies using cross-corrugated polymer film compact heat exchanger," Applied Thermal Engineering, 21(4), pp. 495-510.
[29] Cheng, L., and Van Der Geld, C. W. M., 2005, "Experimental study of heat transfer and pressure drop characteristics of air/water and air-steam/water heat exchange in a polymer compact heat exchanger," Heat Transfer Engineering, 26(2), pp. 18-27.
[30] Harris, C., Kelly, K., Wang, T., McCandless, A., and Motakef, S., 2002, "Fabrication, modeling, and testing of micro-cross-flow heat exchangers," Journal of Microelectromechanical Systems, 11(6), pp. 726-735.

[31] Robinson, F., Cevallos, J. G., Bar-Cohen, A., and Bruck, H., 2011, "Modeling and validation of a prototype thermally-enhanced polymer heat exchanger," Proceedings of ASME 2011 International Mechanical Engineering Congress and Exposition, Denver CO, pp. 597-606.
[32] Bourell, D., Beaman, J., Leu, M., and Rosen, D., 2009 "A brief history of additive manufacturing and the 2009 roadmap for additive manufacturing: looking back and looking ahead," Proceedings of US-Turkey Workshop on Rapid Technologies, Istanbul, Turkey, pp. 5-11
[33] Kawamoto, H., 2007, "Electronic circuit printing, 3D printing and film formation utilizing electrostatic inkjet technology," NIP & Digital Fabrication Conference, Anchorage, Alaska, USA, pp. 961-964.
[34] Wang, H., Masood, S., Iovenitti, P., and Harvey, E. C., 2001, "Application of fused deposition modeling rapid prototyping system to the development of microchannels," Proceeding of International Symposium on Microelectronics and MEMS, Adelaide, Australia, pp. 213-220.
[35] Ikuta, K., Hirowatari, K., and Ogata, T., 1994, "Three dimensional micro integrated fluid systems (MIFS) fabricated by stereo lithography," Proceeding of Micro Electro Mechanical Systems (MEMS) 1994, Oiso, pp. 1-6.
[36] Zein, I., Hutmacher, D. W., Tan, K. C., and Teoh, S. H., 2002, "Fused deposition modeling of novel scaffold architectures for tissue engineering applications," Biomaterials, 23(4), pp. 1169-1185.
[37] Hutmacher, D. W., Schantz, T., Zein, I., Ng, K. W., Teoh, S. H., and Tan, K. C., 2001, "Mechanical properties and cell cultural response of polycaprolactone scaffolds designed and fabricated via fused deposition modeling," Journal of Biomedical Materials Research, 55(2), pp. 203-216.
[38] Cao, T., Ho, K. H., and Teoh, S. H., 2003, "Scaffold design and in vitro study of osteochondral coculture in a three-dimensional porous polycaprolactone scaffold fabricated by fused deposition modeling," Tissue Engineering, 9(4, Supplement 1), pp. 103-112.
[39] Cheng, X., Gurkan, U. A., Dehen, C. J., Tate, M. P., Hillhouse, H. W., Simpson, G. J., and Akkus, O., 2008, "An electrochemical fabrication process for the assembly of anisotropically oriented collagen bundles," Biomaterials, 29(22), pp. 3278-3288.
[40] Schuck, H., Bauerfeld, F., Sauer, D., Harzic, R., Velten, T., Riemann, I., and König, K., 2007, "Rapid prototyping of 3D micro-nanostructures to explore cell behavior," Proceedings of 4M Conference, Ingbert, Germany, pp. 16-23.
[41] Vaezi, M., Seitz, H., and Yang, S., 2013, "A review on 3D micro-additive manufacturing technologies," The International Journal of Advanced Manufacturing Technology, 67(5-8), pp. 1721-1754.
[42] Levy, G. N., Schindel, R., and Kruth, J. P., 2003, "Rapid manufacturing and rapid tooling with layer manufacturing (LM) technologies, state of the art and future perspectives," CIRP Annals-Manufacturing Technology, 52(2), pp. 589-609.
[43] Zhang, X., Jiang, X., and Sun, C., 1999, "Micro-stereolithography of polymeric and ceramic microstructures," Sensors and Actuators Part A: Physical, 77(2), pp. 149-156.
[44] Liu, B., Gong, X., and Chappell, W. J., 2004, "Layer-by-layer polymer stereolithography fabrication for three-dimensional RF components," Microwave

Symposium Digest 2004 IEEE MTT-S International, Fort Worth, TX, USA, pp. 481-484.
[45] Pede, D., Serra, G., and De Rossi, D., 1998, "Microfabrication of conducting polymer devices by ink-jet stereolithography," Materials Science and Engineering, 5(3), pp. 289-291.
[46] Chartier, T., Chaput, C., Doreau, F., and Loiseau, M., 2002, "Stereolithography of structural complex ceramic parts," Journal of Materials Science, 37(15), pp. 3141-3147.
[47] Halloran, J. W., Griffith, M., and Chu, T. M., 2000, "Stereolithography resin for rapid prototyping of ceramics and metals," U.S. Patent No. 6,117,612.
[48] Lee, J. W., Lee, I. H., and Cho, D. W., 2006, "Development of micro-stereolithography technology using metal powder," Microelectronic Engineering, 83(4), pp. 1253-1256.
[49] Imbaby, M., Jiang, K., and Chang, I., 2008, "Fabrication of 316-L stainless steel micro parts by softlithography and powder metallurgy," Materials Letters, 62(26), pp. 4213-4216.
[50] Atwel, C., 2014, "The stereolithography process in a 2D breakdown,"SolidSmack, http://www.solidsmack.com/fabrication/stereolithogrphy-110-micron-old-world-laboratories-nano-3d-printer/. (Retrieved: February 2016)
[51] Simchi, A., Petzoldt, F., and Pohl, H., 2003, "On the development of direct metal laser sintering for rapid tooling," Journal of Materials Processing Technology, 141(3), pp. 319-328.
[52] Kathuria, Y., 1999, "Microstructuring by selective laser sintering of metallic powder," Surface and Coatings Technology, 116, pp. 643-647.
[53] Tsopanos, S., Sutcliffe, C., and Owen, I., 2005, "The manufacture of micro cross-flow heat exchangers by selective laser melting," Proceedings of ECI: Fifth International Conference on Enhanced, Compact and Ultra Compact Heat Exchangers, Hoboken, NJ, USA, pp. 410-417.
[54] Bertrand, P., Bayle, F., Combe, C., Gœuriot, P., and Smurov, I., 2007, "Ceramic components manufacturing by selective laser sintering," Applied Surface Science, 254(4), pp. 989-992.
[55] Shishkovsky, I., Yadroitsev, I., Bertrand, P., and Smurov, I., 2007, "Alumina–zirconium ceramics synthesis by selective laser sintering/melting," Applied Surface Science, 254(4), pp. 966-970.
[56] Gibson, I., and Shi, D., 1997, "Material properties and fabrication parameters in selective laser sintering process," Rapid Prototyping Journal, 3(4), pp. 129-136.
[57] "Selective laser sintering process," https://en.wikipedia.org/wiki/Selective_laser_sintering. (Retrived February 2016)
[58] Masood, S. H., and Song, W. Q., 2004, "Development of new metal/polymer materials for rapid tooling using fused deposition modelling," Materials & Design, 25(7), pp.587-594.
[59] "Fused deposition modelling," https://en.wikipedia.org/wiki/Fused_deposition_modeling. (Retrived February 2016)
[60] Mueller, B., and Kochan, D., 1999, "Laminated object manufacturing for rapid tooling and patternmaking in foundry industry," Computers in Industry, 39(1), pp. 47-53.

[61] Zhang, Y., He, X., Du, S., and Zhang, J., 2001, "Al2O3 ceramics preparation by LOM (laminated object manufacturing)," The International Journal of Advanced Manufacturing Technology, 17(7), pp. 531-534.
[62] Klosterman, D., Chartoff, R., Graves, G., Osborne, N., and Priore, B., 1998, "Interfacial characteristics of composites fabricated by laminated object manufacturing," Composites Part A: Applied Science and Manufacturing, 29(9), pp. 1165-1174.
[63] Himmer, T., Nakagawa, T., and Anzai, M., 1999, "Lamination of metal sheets," Computers in Industry, 39(1), pp. 27-33.
[64] Mueller, B., and Kochan, D., 1999, "Laminated object manufacturing for rapid tooling and patternmaking in foundry industry," Computers in Industry, 39(1), pp. 47-53.
[65] Palermo, E., 2013, "Laminated Object Manufacturing," LiveScience, http://www.livescience.com/40310-laminated-object-manufacturing.html. (Retrieved February 2016)
[66] Baum, T. H., Larson, C. E., and Jackson, R. L., 1989, "Laser-induced chemical vapor deposition of aluminum," Applied physics letters, 55(12), pp. 1264-1266.
[67] Baum, T. H., and Jones, C. R., 1985, "Laser chemical vapor deposition of gold," Applied Physics Letters, 47(5), pp. 538-540.
[68] Houle, F., Jones, C., Baum, T., Pico, C., and Kovac, C., 1985, "Laser chemical vapor deposition of copper," Applied Physics Letters, 46(2), pp. 204-206.
[69] Besling, W. F. A., Goossens, A., Meester, B., and Schoonman, J., 1998, "Laser-induced chemical vapor deposition of nanostructured silicon carbonitride thin films," Journal of Applied Physics, 83(1), pp. 544-553.
[70] Ito, A., Kadokura, H., Kimura, T., and Goto, T., 2010, "Texture and orientation characteristics of α-Al2O3 films prepared by laser chemical vapor deposition using Nd: YAG laser," Journal of Alloys and Compounds, 489(2), pp. 469-474.
[71] You, Y., Ito, A., Tu, R., and Goto, T., 2010, "Low-temperature deposition of α-Al2O3 films by laser chemical vapor deposition using a diode laser," Applied Surface Science, 256(12), pp. 3906-3911.
[72] Mazumder, J., and Kar, A., 2013, Theory and Application of Laser Chemical Vapor Deposition, Springer Science & Business Media, New York, USA
[73] Calvert, P., 2001, "Inkjet printing for materials and devices," Chemistry of Materials, 13(10), pp. 3299-3305.
[74] Everton, S. K., Hirsch, M., Stravroulakis, P., and Leach, R. K., 2016, "Review of in-situ process monitoring and in-situ metrology for metal additive manufacturing," Materials & Design, 95, pp. 431-445.
[75] Nassar, A. R., Keist, J. S., Reutzel, E. W., and Spurgeon, T. J., 2015, "Intra-layer closed-loop control of build plan during directed energy additive manufacturing of Ti–6Al–4V," Additive Manufacturing, 6, pp. 39-52.
[76] Ding, Y., Warton, J., and Kovacevic, R., 2016, "Development of sensing and control system for robotized laser-based direct metal addition system," Additive Manufacturing, 10, pp. 24-35.
[77] Hagqvist, P., Heralić, A., Christiansson, A. K., and Lennartson, B., 2015, "Resistance based iterative learning control of additive manufacturing with wire," Mechatronics, 31, pp. 116-123.

[78] Flynn, J. M., Shokrani, A., Newman, S. T., and Dhokia, V., 2016, "Hybrid additive and subtractive machine tools–Research and industrial developments," International Journal of Machine Tools and Manufacture, 101, pp. 79-101.
[79] Kumar, V., Manogharan, G., and Cormier, D. R., 2009, "Design of periodic cellular structures for heat exchanger applications," Proceeding of Solid Freeform Fabrication Symposium, Austin, TX, pp. 738-748.
[80] Wong, M., Owen, I., Sutcliffe, C. J., and Puri, A., 2009, "Convective heat transfer and pressure losses across novel heat sinks fabricated by selective laser melting," International Journal of Heat and Mass Transfer, 52(1), pp. 281-288.
[81] Ramirez, D. A., Murr, L. E., Li, S. J., Tian, Y. X., Martinez, E., Martinez, J. L., Machado, B. I., Gaytan, S. M., Medina, F., and Wicker, R. B., 2011, "Open-cellular copper structures fabricated by additive manufacturing using electron beam melting," Materials Science and Engineering: A, 528(16), pp. 5379-5386.
[82] Hutter, C., Büchi, D., Zuber, V., and Von Rohr, P. R., 2011, "Heat transfer in metal foams and designed porous media," Chemical Engineering Science, 66(17), pp. 3806-3814.
[83] Cormier, Y., Dupuis, P., Farjam, A., Corbeil, A., and Jodoin, B., 2014, "Additive manufacturing of pyramidal pin fins: Height and fin density effects under forced convection," International Journal of Heat and Mass Transfer, 75, pp. 235-244.
[84] Cevallos, J. G., 2014, "Thermal and Manufacturing Design of Polymer Composite Heat Exchangers," Ph.D. Thesis, University of Maryland, College Park.
[85] Thompson, S. M., Aspin, Z. S., Shamsaei, N., Elwany, A., and Bian, L., 2015, "Additive manufacturing of heat exchangers: A case study on a multi-layered Ti–6Al–4V oscillating heat pipe," Additive Manufacturing, 8, pp. 163-174.
[86] Harper, R. R., and Brown, W. B., 1922, "Mathematical equations for heat conduction in the fins of air-cooled engines," NACA Annual Report 8, pp. 677-708.
[87] Kuppan, T., 2013, Heat Exchanger Design Handbook 2nd Edition, CRC Press, Boca Raton, FL.
[88] Shah, R. K., and London, A. L., 1978, Laminar Flow Forced Convection in Ducts: A Source Book for Compact Heat Exchanger Analytical Data, Academic Press, New York.
[89] Taylor, M. A., 1987, Plate-Fin Heat Exchangers: Guide to Their Specification and Use, Heat Transfer and Fluid Flow Services.
[90] Webb, R., 1981, "Enhancement for Extended Surface Geometries used in Air Cooled Heat Exchangers," NATO Advanced Study Institute, Middle East Technical Univ., Ankara, Turkey.
[91] Xia, G., Zhai, Y., and Cui, Z., 2013, "Numerical investigation of thermal enhancement in a micro heat sink with fan-shaped reentrant cavities and internal ribs," Applied Thermal Engineering, 58(1), pp. 52-60.
[92] Yeom, T., Simon, T. W., Huang, L., North, M. T., and Cui, T., 2012, "Piezoelectric translational agitation for enhancing forced-convection channel-flow heat transfer," International Journal of Heat and Mass Transfer, 55(25), pp. 7398-7409.
[93] Nawaz, K., Bock, J., and Jacobi, A. M., 2012, "Thermal-hydraulic performance of metal foam heat exchangers." International Refrigeration and Air Conditioning Conference, Lafayette, IN, Paper 1283.

[94] Ribeiro, G. B., and Barbosa Jr, J., 2012, "Experimental assessment of metal foam and louvered fins as air-side heat transfer enhancement for miniaturized condensers." International Refrigeration and Air Conditioning Conference, Lafayette, IN, Paper 1236.
[95] Noh, J. S., Lee, K. B., and Lee, C. G., 2006, "Pressure loss and forced convective heat transfer in an annulus filled with aluminum foam," International Communications in Heat and Mass Transfer, 33(4), pp. 434-444.
[96] Wong, K. C., and Indran, S., 2013, "Impingement heat transfer of a plate fin heat sink with fillet profile," International Journal of Heat and Mass Transfer, 65, pp. 1-9.
[97] Mahalingam, R., and Glezer, A., 2005, "Design and thermal characteristics of a synthetic jet ejector heat sink," Journal of Electronic Packaging, 127(2), pp. 172-177.
[98] Yang, L., Tan, H., Du, X., and Yang, Y., 2012, "Thermal-flow characteristics of the new wave-finned flat tube bundles in air-cooled condensers," International Journal of Thermal Sciences, 53, pp. 166-174.
[99] Pongsoi, P., Pikulkajorn, S., and Wongwises, S., 2014, "Heat transfer and flow characteristics of spiral fin-and-tube heat exchangers: A review," International Journal of Heat and Mass Transfer, 79, pp. 417-431.
[100] Tang, L., Zeng, M., and Wang, Q., 2009, "Experimental and numerical investigation on air-side performance of fin-and-tube heat exchangers with various fin patterns," Experimental Thermal and Fluid Science, 33(5), pp. 818-827.
[101] Moore, J., Grimes, R., Walsh, E., and O'Donovan, A., 2014, "Modelling the thermodynamic performance of a concentrated solar power plant with a novel modular air-cooled condenser," Energy, 69, pp. 378-391.
[102] Kim, S. Y., Kang, B. H. and Kim, J. H., 2001, "Forced convection from aluminium foam materials in an asymmetrically heated channel," International Journal of Heat and Mass Transfer, 44(7), pp. 1451-1454.
[103] Harpole, G. M., and Eninger, J. E., 1991, "Micro-channel heat exchanger optimization," Semiconductor Thermal Measurement and Management Symposium, Phoenix, AZ, pp. 59-63.
[104] Arie, M. A., Shooshtari, A., Dessiatoun, S., and Ohadi, M., 2014, "Thermal optimization of an air-cooling heat exchanger utilizing manifold-microchannels," Proceedings of IEEE Intersociety Conference on Thermal and Thermomechanical Phenomena in Electronic Systems (ITherm), Orlando, FL, pp. 807-815.
[105] Arie, M. A., Shooshtari, A. H., Dessiatoun, S. V., Ohadi, M. M., and Hajri, E. A., 2012, "Simulation and thermal optimization of a manifold microchannel flat plate heat exchanger," ASME 2012 International Mechanical Engineering Congress and Exposition, Houston, Texas, USA, pp. 209-220.
[106] Arie, M. A., Shooshtari, A., Dessiatoun, S., Al-Hajri, E., and Ohadi, M., 2015, "Numerical modeling and thermal optimization of a single-phase flow manifold-microchannel plate heat exchanger," International Journal of Heat and Mass Transfer, 81, pp. 478-489.
[107] Arie, M. A., 2012, "Numerical modeling and optimization of single phase manifold-microchannel plate heat exchanger," M.S. Thesis, University of Maryland, College park.
[108] Jha, V., Dessiatoun, S., Ohadi, M., Shooshtari, A., and Al-Hajri, E., "High performance micro-grooved evaporative heat transfer surface for low grade waste heat recovery applications," Proceeding of ASME 2011 Pacific Rim Technical Conference

and Exhibition on Packaging and Integration of Electronic and Photonic Systems, Portland, OR, pp. 277-283.
[109] Jha, V., Dessiatoun, S., Shooshtari, A., Al-Hajri, E. S., and Ohadi, M. M., 2015, "Experimental characterization of a nickel alloy-based manifold-microgroove evaporator," Heat Transfer Engineering, 36(1), pp. 33-42.
[110] Boyea, D., Shooshtari, A., Dessiatoun, S. V., and Ohadi, M. M., 2013, " Heat transfer and pressure drop characteristics of a liquid cooled manifold-microgroove condenser," Proceedings of the ASME 2013 Heat Transfer Summer Conference, Minneapolis, MN, USA.
[111] Ohadi, M. M., Choo, K., Dessiatoun, S., and Cetegen, E., 2012, Next Generation Micro Channel Heat Exchanger 1st edition, Springer Publishing Co., New York.
[112] Kermani, E., Dessiatoun, S., Shooshtari, A., and Ohadi, M. M., 2009, "Experimental investigation of heat transfer performance of a manifold microchannel heat sink for cooling of concentrated solar cells," IEEE 59th Electronic Components and Technology Conference, San Diego, CA, pp. 453-459.
[113] Copeland, D., Behnia, M., and Nakayama, W., 1997, "Manifold microchannel heat sinks: isothermal analysis," IEEE Transactions on Components, Packaging, and Manufacturing Technology – Part A, 20(2), 96-102.
[114] Poh, S. T., and Ng, E. Y. K., 1999, "Investigative study of manifold microchannel heat sinks for electronic cooling design," Journal of Electronics Manufacturing, 9(2), pp. 155-166.
[115] Poh, S. T., and Ng, E. Y. K., 1998, "Heat transfer and flow issues in manifold microchannel heat sinks: a CFD approach," 2nd Electronics Packaging Technology Conference, Singapore, pp. 246-250.
[116] Ryu, J. H., Choi, D. H., and Kim, S. J., 2003, "Three-dimensional numerical optimization of a manifold microchannel heat sink," International Journal of Heat and Mass Transfer, 46(9), pp. 1553-1562.
[117] Kermani, E., Dessiatoun, S., Shooshtari, A., and Ohadi, M. M., 2009, "Experimental investigation of heat transfer performance of a manifold microchannel heat sink for cooling of concentrated solar cells," IEEE 59th Electronic Components and Technology Conference, San Diego, CA, pp. 453-459.
[118] Escher, W., Brunschwiler, T., Michel, B., and Poulikakos, D., 2010, "Experimental investigation of an ultrathin manifold microchannel heat sink for liquid-cooled chips," Journal of Heat Transfer, 132, pp. 081402-081401.
[119] Yang, K., and Zuo, C., 2015, "A novel multi-layer manifold microchannel cooling system for concentrating photovoltaic cells," Energy Conversion and Management, 89, pp. 214-221.
[120] Hu, H., Ren, F., Kuravi, S., and Hsu, P. F., 2014, "Liquid metal flows in manifold microchannel heat sink," Proceedings of the ASME 2014 International Mechanical Engineering Congress and Exposition, Montreal, Quebec, Canada, pp. V010T13A085.
[121] Andhare, R. S., Shooshtari, A., Dessiatoun, S. V., and Ohadi, M. M., 2016, "Heat transfer and pressure drop characteristics of a flat plate manifold microchannel heat exchanger in counter flow configuration," Applied Thermal Engineering, 96, pp. 178-189.
[122] Zhou, F., Liu, Y., Joshi, S. N., Liu, Y., and Dede, E. M., 2015, "Modular flow structure design for a single-phase manifold microchannel cold plate," Proceedings of the

ASME 2015 International Technical Conference and Exhibition on Packaging and Integration of Electronic and Photonic Microsystems, San Francisco, California, USA, pp. V003T04A008.
[123] Mandel, R., Dessiatoun, S., McCluskey., P., and Ohadi, M., 2015, "Embedded two-phase cooling of high flux electronics via micro-enabled surface and fluid delivery system (FEEDS)," Proceedings of the ASME 2015 International Technical Conference and Exhibition on Packaging and Integration of Electronic and Photonic Microsystems, San Francisco, California, USA, pp. V003T10A012.
[124] "Folded Fins," Enertron, http://www.enertron-inc.com/resources-folded-fins.aspx. (Retrieved January 2016)
[125] "Folded Fin," Cooler Master, http://odm.coolermaster.com/manufacture.php?page_id=6. (Retrieved January 2016)
[126] "Aluminium Plate-Fin Heat Exchangers," Lindeus-engineering, http://www.lindeus-engineering.com/internet.le.le.usa/en/images/P_3_2_e_12_150dpi136_5772.pdf. (Retrieved January 2016)
[127] Kandlikar, S. G., and Grande, W. J., 2003, "Evolution of microchannel flow passages -thermohydraulic performance and fabrication technology," Heat Transfer Engineering, 24(1), pp. 3-17.
[128] Liao, Y. S., Chen, S. T., Lin, C. S., and Chuang, T. J., 2005, "Fabrication of high aspect ratio microstructure arrays by micro reverse wire-EDM," Journal of Micromechanics and Microengineering, 15(8), p. 1547.
[129] Mahabunphachai, S., and Koc, M., 2008, "Fabrication of micro-channel arrays on thin metallic sheet using internal fluid pressure: Investigations on size effects and development of design guidelines," Journal of Power Sources, 175(1), pp. 363-371.
[130] Mei, F., Parida, P. R., Jiang, J., Meng, W. J., and Ekkad, S. V., 2008, "Fabrication, assembly, and testing of Cu-and Al-based microchannel heat exchangers," Journal of Microelectromechanical Systems, 17(4), pp. 869-881.
[131] Joo, Y., Dieu, K., and Kim, C. J., 1995, "Fabrication of monolithic microchannels for IC chip cooling," Proceedings IEEE Micro Electro Mechanical Systems (MEMS'95), Amsterdam, Netherlands, pp. 362-367.
[132] "Choose the Right Process for Your Job," ChemART, http://www.chemart.com/Choose-the-Right-Process-For-Your-Job_ep_125-1.html. (Retrieved January 2016)
[133] Lohner, A., 1997, "Laser sintering ushers in new route to PM parts," Metal Powder Report (MPR), 52(2), pp. 24-30.
[134] J. Cornelus, Additive manufacturing: industrial applications of direct metal printing, In InterPACK2015/ICNMM2015, 7 July 2015.
[135] Deisenroth, D. A., Arie, M. A., Shooshtari, A., Dessiatoun, S., and Ohadi, M., 2015, "Review of most recent progress on development of polymer heat exchangers for thermal management applications," Proceeding ASME 2015 International Technical Conference and Exhibition on Packaging and Integration of Electronic and Photonic Microsystems InterPACK2015, San Francisco, CA, USA, pp. V003T03A003.
[136] T'Joen, C., Park, Y., Wang, Q., Sommers, A., Han, X., and Jacobi, A., 2009, "A review on polymer heat exchangers for HVAC&R applications," International Journal of Refrigeration, 32(5), pp. 763-779.

[137] "MONOBLOCK - The Polymer Heat Exchanger," Monoblock, http://www.segerfrojd.com/. (Retrieved January 2016)
[138] "Plastic Interchange Heat Exchanger," Ail Research, inc., http://ailr.com/our-technology/plastic-interchange-heat-exchanger/. (Retrieved January 2016)
[139] "Plastic heat exchanger core," Alibaba, http://www.alibaba.com/product-detail/PLASTIC-HEAT-EXCHANGER-CORE_430338703.html. (Retrieved January 2016)
[140] Han, Z., and Fina, A., 2011, "Thermal conductivity of carbon nanotubes and their polymer nanocomposites: a review," Progress in Polymer Science, 36(7), pp. 914-944.
[141] Wang, X., Yong, Z., Li, Q., Bradford, P. D., Liu, W., Tucker, D. S., Cai, W., Wang, H., Yuan, F. G., and Zhu, Y., 2013, "Ultrastrong, stiff and multifunctional carbon nanotube composites," Materials Research Letters, 1(1), pp. 19-25.
[142] Khan, M. O., Leung, S. N., Chan, E., Naguib, H. E., Dawson, F., and Adinkrah, V., 2013, "Effects of microsized and nanosized carbon fillers on the thermal and electrical properties of polyphenylene sulfide based composites," Polymer Engineering & Science, 53(11), pp. 2398-2406.
[143] Balachander, N., Seshadri, I., Mehta, R. J., Schadler, L. S., Borca-Tasciuc, T., Keblinski, P., and Ramanath, G., 2013, "Nanowire-filled polymer composites with ultrahigh thermal conductivity," Applied Physics Letters, 102(9), pp. 093117.
[144] Zhou, W., Wang, C., Ai, T., Wu, K., Zhao, F., and Gu, H., 2009, "A novel fiber-reinforced polyethylene composite with added silicon nitride particles for enhanced thermal conductivity," Composites Part A: Applied Science and Manufacturing, 40(6), pp. 830-836.
[145] Sinh, L. H., Hong, J. M., Son, B. T., Trung, N. N., and Bae, J. Y., 2012, "Thermal, dielectric, and rheological properties of aluminum nitride/liquid crystalline copoly (ester amide) composite for the application of thermal interface materials," Polymer Composites, 33(12), pp. 2140-2146.
[146] Dogruoz, M. B., and Arik, M., 2010, "On the conduction and convection heat transfer from lightweight advanced heat sinks," IEEE Transactions on Components and Packaging Technologies, 33(2), pp. 424-431.
[147] Harpole, G. M., and Eninger, J. E., 1991, "Micro-channel heat exchanger optimization," Proceedings of 7th Annual IEEE Semiconductor Thermal Measurement and Management Symposium, Phoenix, AZ, pp. 59-63.
[148] Beaver, A., 2014, Baltimore Aircoil Company, private communication.
[149] Denkenberger, D. C., Brandemuehl, M. J., Pearce, J. M., and Zhai, J., 2012, "Expanded microchannel heat exchanger: design, fabrication, and preliminary experimental test," Proceedings of the Institution of Mechanical Engineers, Part A: Journal of Power and Energy, pp. 0957650912442781.
[150] "Direct Metal Laser Sintering (DMLS) Technology," Solid Concept, https://www.youtube.com/watch?v=bgQvqVq-SQU. (Retrieved February 2016)
[151] "Direct Metal Laser Sintering Materials," Stratasys, https://www.stratasysdirect.com/materials/direct-metal-laser-sintering/. (Retrieved February 2016)
[152] "Direct Metal laser Sintering," Proto Labs, https://www.protolabs.com/additive-manufacturing/direct-metal-laser-sintering. (Retrieved February 2016)

[153] "Materials," Layerwise, http://www.layerwise.com/technology/materials/. (Retrieved February 2016)
[154] 2015, "3D printing materials: choosing the right material for your application," Stratasys, https://www.stratasysdirect.com/content/white_papers/STR_7463_15_SDM_WP_3D_MATERIALS.PDF. (Retrieved February 2016)
[155] Carter, A., 2014, Stratasys Ltd., private communication.
[156] Cornelus, J., 2015, "Additive Manufacturing: Industrial applications of Direct Metal Printing," InterPACKICNMM2015, San Francisco.
[157] Nellis, G. F., and Klein, S. A., 2009, Heat Transfer, Cambridge University Press, New York, NY.
[158] Bergman, T. L., Lavine, A. S., Incropera, and F. P., Dewitt, D. P., 2011, Fundamentals of heat and mass transfer, John Wiley & Sons, Hoboken NJ.
[159] Petukhov, B., 1970, "Heat transfer and friction in turbulent pipe flow with variable physical properties," Advances in Heat Transfer, 6(503), p. i565.
[160] Bajura, R., 1971, "A model for flow distribution in manifolds," Journal of Engineering for Gas Turbines and Power, 93(1), pp. 7-12.
[161] Sarker, R., and Ray, T., 2009, "An improved evolutionary algorithm for solving multi-objective crop planning models," Computers and Electronics in Agriculture, 68(2), pp. 191-199.
[162] Ziolkowski, M., and Gratkowski, S., 2009, "Genetic algorithm-based multi-objective optimization of an exciter for magnetic induction tomography," COMPEL: The International Journal for Computation and Mathematics in Electrical and Electronic Engineering, 28(5), pp. 1121-1128.
[163] Takahama, T., and Sakai, S., 2009, "Efficient constrained optimization by the ε constrained differential evolution using an approximation model with low accuracy," Transactions of the Japanese Society for Artificial Intelligence, 24(1), pp. 34-45.
[164] Holland, J. H., 1992, "Genetic algorithms," Scientific American, 267(1), pp. 44-50.
[165] Xie, G., Sunden, B., and Wang, Q., 2008, "Optimization of compact heat exchangers by a genetic algorithm," Applied Thermal Engineering, 28(8), pp. 895-906.
[166] Hilbert, R., Janiga, G., Baron, R., and Thévenin, D., 2006, "Multi-objective shape optimization of a heat exchanger using parallel genetic algorithms," International Journal of Heat and Mass Transfer, 49(15), pp. 2567-2577.
[167] Amanifard, N., Nariman-Zadeh, N., Borji, M., Khalkhali, A., and Habibdoust, A., 2008, "Modelling and pareto optimization of heat transfer and flow coefficients in microchannels using GMDH type neural networks and genetic algorithms," Energy Conversion and Management, 49(2), pp. 311-325.
[168] Ravagnani, M., Silva, A., Arroyo, P., and Constantino, A., 2005, "Heat exchanger network synthesis and optimisation using genetic algorithm," Applied Thermal Engineering, 25(7), pp. 1003-1017.
[169] Aute, V., Abdelaziz, O., Azarm, S., and Radermacher, R., 2008, "Cross-validation based single response adaptive design of experiments," 12th AIAA/ISSMO Multidisciplinary Analysis and Optimization Conference, Victoria, Canada, paper. 6067
[170] Saleh, K., Abdelaziz, O., Aute, V., Radermacher, R., and Azarm, S., 2010, "Microchannel approximation assisted design optimization and CFD verification."

International Refrigerant and Air Conditioning Conference, West Lafayette, USA, paper. 1088.
[171] Li, M., Li, G., and Azarm, S., 2008, "A kriging metamodel assisted multi-objective genetic algorithm for design optimization," Journal of Mechanical Design, 130(3), paper. 31401.
[172] Mistree, F., Korte, J. J., Mauery, T. M., and Simpson, T. W., 2012, "Kriging models for global approximation in simulation-based multidisciplinary design optimization," AIAA Journal, 39(12).
[173] Simpson, T. W., Martin, J. D., Booker, A. J., Giunta, A. A., Haftka, R. T., Renaud, J. E., and Kleijnen, J. P. C., 2005, "Use of kriging models to approximate deterministic computer models," AIAA Journal, 43(4), pp. 853-863.
[174] Lophaven, S. N., Nielsen, H. B., and Søndergaard, J., 2002, DACE: A Matlab kriging toolbox, Citeseer.
[175] "Direct Metal Laser Sintering (DMLS) Design Guidline," Stratasys, https://www.stratasysdirect.com/resources/direct-metal-laser-sintering-dmls/. (Retrieved February 2016)
[176] Rose, J. W., 2004, "Heat-transfer coefficients, Wilson plots and accuracy of thermal measurements," Experimental Thermal and Fluid Science, 28(2), pp. 77-86.
[177] Taylor, B.N., and Kuyatt, C. E., 1994, "Guidelines for evaluating and expressing the uncertainty of NIST measurement results." NIST Technical Note 1297
[178] 2007, “Materials for direct metal laser-sintering (DMLS),” EOS, http://www.detekt.com.tw/download/eos/7%EF%BC%AD%E6%8A%80%E8%A1%93%E5%8F%8A%E7%95%B0%E5%9E%8B%E6%B0%B4%E8%B7%AF/EOSINT%20M%20Materials%20for%20Direct%20Metal%20Laser-Sintering%20%28DMLS%29.pdf (Retrieved March 2016)
[179] 2011, “Material data sheet - EOS Aluminium AlSi10Mg for EOSINT M 270,” EOS, https://www.anubis3d.com/documents/dmls/datasheets/Aluminum-AlSi10Mg.pdf (Retrieved March 2016)
[180] Hudak, R., Sarik, M., Dadej, R., Zivcak, J., and Harachova, D., 2013, "Material and thermal analysis of laser sinterted products," Acta Mechanica et Automatica, 7(1), pp. 15-19.